

In situ IR spectroscopic studies
of the CO oxidation reaction
over a ruthenium model catalyst

im Fachbereich Chemie und Biologie
der Justus-Liebig-Universität Gießen

genehmigte Dissertation

von

Attila Farkas

aus

Baia de Arama

Gießen 2008

Die vorliegende Arbeit wurde in der Zeit von Februar 2003 bis März 2008 am Physikalisch-Chemischen Institut der Justus-Liebig-Universität Gießen unter der Anleitung von Prof. Dr. Herbert Over und Dr. Georg Mellau angefertigt.

Erster Gutachter: Prof. Dr. Herbert Over

Zweiter Gutachter: Prof. Dr. Peter Klar

Acknowledgments

I thank Prof. Dr. Herbert Over for accepting me as his student and for entrusting me with this beautiful and challenging research topic. I owe him, as a teacher, my introduction to the science, but I could equally well say *magic* of Surface Science. His constant support and unwavering confidence in my abilities have helped me, more than once, out of the difficult moments of my research. I confess that I am indebted to him not only as a teacher, but also as a friend. Herbert and his wonderful family have compensated for the absence of my own family, which I have left many years ago in order to acquire science abroad.

Without the help of Dr. Georg Mellau, the first FTIR spectra measured with the newly built setup would have come only much too late. My familiarization with the theory and practice of FTIR spectroscopy would have been far less instructive and exciting without his constant attention and patient advice.

I thank Dr. Marcus Knapp for generously sharing with me his experimental knowledge, and for acquainting me with the finer details and intricacies of the system of ruthenium dioxide.

Valuable support, constant encouragement and many relaxing moments I owe to my colleagues Daniela Crihan, Dr. Yunbin He, Jan Philipp Hofmann, Stefan Zweidinger and Carl Hubbe.

Besonders möchte ich mich bei Jenny Schäfer, Manuela Kellner, Fabian Hofmann und Nico Erdmann bedanken, die mir über die letzten Jahre so etwas wie ein Zuhause gegeben haben.

The workmanship and practical expertise of the *Feinmechanische Werkstatt* led by Harry Heidt were instrumental in completing the experimental setup to the necessary standards. All problems concerning electronic devices have been promptly and elegantly solved by Harald Weigand. I thank them on this occasion.

I thank Hansjörg Ruppender and the companies Omnivac and Prevac for substantial help in the testing phase of the experimental setup, as well as for kindly providing me the construction drawings shown in the present thesis.

I thank Prof. Dr. Peter Klar for accepting to referee the present thesis.

Lebenslauf

Persönliche Angaben

Name	Attila Farkas
Geboren	am 14.06.1971 in Baia de Arama, Rumänien
Staatsangehörigkeit	rumänisch
Familienstand	ledig.

Ausbildung

1990-1995	Diplom-Physikstudium an der Universität Timisoara, Rumänien
1989-1990	Wehrdienst, Rumänien
1985-1989	Gymnasium, Timisoara, Rumänien.

Beruflicher Werdegang

2003-2008	Wissenschaftlicher Mitarbeiter, Justus-Liebig Universität Gießen. Dissertation unter der Leitung von Prof. Dr. H. Over.
1995-2003	Wissenschaftlicher Mitarbeiter, Institutul de Cercetare a Materiei Condensate Timisoara, Rumänien.

Publikationsliste

1. H. Over, Y. B. He, A. Farkas, G. Mellau, C. Korte, M. Knapp, M. Chandhok, and M. Fang. Long-term stability of Ru-based protection layers in extreme ultraviolet lithography: A surface science approach. *J. Vac. Sci. Technol. B*, **25**, 1123-1138, 2007.
2. Y. B. He, A. Goriachko, C. Korte, A. Farkas, G. Mellau, P. Dudin, L. Gregoratti, A. Barinov, M. Kiskinova, A. Stierle, N. Kasper, S. Bajt and H. Over. Oxidation and Reduction of Ultrathin Nanocrystalline Ru Films on Silicon: Model System for Ru-Capped Extreme Ultraviolet Lithography Optics. *J. Phys. Chem. C*, **111**, 10988-10992, 2007.
3. J. Assmann, V. Narkhede, N. A. Breuer, M. Muhler, A. P. Seitsonen, M. Knapp, D. Crihan, A. Farkas, G. Mellau, and H. Over. Heterogeneous oxidation catalysis on ruthenium: bridging the pressure and materials gaps and beyond. *J. Phys.: Condens. Matter*, **20**, 184017, 2008.

Persönliche Beiträge zu den zitierten Artikeln:

1. *In situ* Röntgen-Reflektivitätsmessungen an nanometer-dünnen Schichten von Ru auf amorphem Siliciumoxid während der Oxidation und Reduktion der Proben, zusammen mit Y.B. He, ANKA Synchrotron Karlsruhe, Juni 2006.
2. *In situ* IR-Reflektions-absorptionsspektroskopische (RAIRS) Messungen an den im Artikel 1. untersuchten Proben, zusammen mit G. Mellau. Die RAIRS Anlage wurde als Teil dieser Dissertation konzipiert und in Betrieb genommen.
3. *In situ* RAIRS Messungen am RuO₂(110) Modellkatalysator während der Hochdruck-Oxidation von CO. Die Ergebnisse bilden einen Teil dieser Dissertation.

Zusammenfassung

Im Rahmen dieser Dissertation wurde eine komplexe Ultrahochvakuum-(UHV)-Anlage für die *in situ* IR-Spektroskopie an Modellkatalysatoren konzipiert, aufgebaut und in Betrieb genommen. Das Verbindungsglied zwischen UHV-System und FTIR-Spektrometer bildet eine UHV-Reaktionskammer mit IR-optischen Fenstern, die auch für höhere Drücke einsetzbar ist. Dieser Aufbau erlaubt die Präparation und *in situ* IR-Spektroskopie an Modellkatalysatoren über einen weiten Druck (10^{-10} -1 mbar) und Temperaturbereich (100-1200 K).

Bei dem hier untersuchten Modellkatalysator handelt es sich um einen dünnen $\text{RuO}_2(110)$ -Film, der epitaktisch auf $\text{Ru}(001)$ aufgewachsen wurde. Die Kohlen-Monoxid-Oxidation wurde auf diesem Modellsystem mittels *in situ* Reflektions-Absorptions-IR-Spektroskopie (RAIRS) in der C-O Streckschwingungsregion (1800 - 2200 cm^{-1}) untersucht. Die RAIRS Experimente bei 350 K zeigen, dass die Oberfläche sowohl unter stöchiometrischen als auch oxidierenden Bedingungen im Druckbereich von 10^{-6} - 10^{-3} mbar mit Inseln von dicht gepacktem CO bedeckt ist, die durch IR-Banden im Bereich von 2060 bis 2080 cm^{-1} charakterisiert werden können. Außerdem beweisen die RAIR-Spektren die Existenz von dicht gepackten Sauerstoffinseln. Die Oxidation der CO-Inseln geht sehr langsam von statten, da die Aktivierungsenergie für die Diffusion von CO und O auf $\text{RuO}_2(110)$ mit cca. 1.2 eV vergleichsweise hoch ist. Es lässt sich schließen, dass diese praktisch inaktive CO-Phase den Katalysator zumindest partiell vergiftet.

Weitere RAIRS-Untersuchungen in dieser Arbeit befassen sich mit der Reoxidation einer mild reduzierten $\text{RuO}_2(110)$ -Fläche und der Reduktion von $\text{RuO}_2(110)$ zu metallischem $\text{Ru}(001)$ unter hohen CO-Dosen.

Abstract

As part of the present thesis, a complex ultrahigh vacuum (UHV) system for *in situ* IR spectroscopic studies of model catalysts was designed, built and made operational. The interface between the UHV system and the FTIR spectrometer is formed by an UHV reaction chamber with high-pressure capabilities, equipped with IR-transparent viewports. The setup allows the preparation and the *in situ* IR-spectroscopic study of single-crystal model catalysts over an extended pressure range (10^{-10} -1 mbar) at temperatures in the 100-1200 K range.

The model catalyst studied in the present thesis was an ultrathin RuO₂(110) film epitaxially grown on the Ru(001) surface. The oxidation of CO on the model catalyst was studied by *in situ* reflection-absorption IR spectroscopy (RAIRS) in the spectral region of the C-O bond stretch vibrations (1800-2200 cm⁻¹). Our *in situ* RAIRS experiments at 350 K indicate that under stoichiometric and oxidizing conditions in the 10^{-6} - 10^{-3} mbar range, areas of the RuO₂(110) surface are covered by clusters of densely packed CO molecules, characterized by IR absorption bands in the range 2060-2080 cm⁻¹. The RAIR spectra also indicate the existence of densely packed clusters of O atoms on the RuO₂(110) surface. The oxidation of the aggregated CO molecules is very slow due the high activation energies (1.2 eV) for CO and O diffusion on the RuO₂(110) surface. We conclude that this practically inactive CO species is partly poisoning the catalyst surface.

Further results include a RAIRS study of the process of reoxidation of a mildly reduced RuO₂(110) surface and an *in situ* RAIRS study concerning the reduction of the RuO₂(110) film to metallic ruthenium under intense exposure to CO.

Contents

1	Introduction	5
2	UHV system for <i>in situ</i> RAIRS	13
2.1	The UHV system	14
2.1.1	The analysis chamber	16
2.1.2	Sample docking system and the sample holder	18
2.1.3	The UHV/high-pressure cell	22
2.1.4	Fast entry system	24
2.2	Fourier transform IR spectroscopy	25
2.2.1	The Michelson interferometer	27
2.2.2	Phase correction	28
2.2.3	Finite resolution	29
2.2.4	Apodization	30
2.2.5	Digitization of the interferogram	33
2.2.6	Measurement of an FT-RAIR spectrum	33
2.3	The FTIR spectrometer and the optical setup	36
2.4	Detection limit of the RAIRS setup	38
3	C-O vibration and IR absorption	43
3.1	Macroscopic models of absorption in molecular layers	43
3.1.1	Fresnel coefficients for the three-layer dielectric system	44
3.1.2	Reflectivity change due to absorbing thin films	45
3.1.3	Reflectivity change and the molecular polarizability	47
3.2	Single diatomic adsorbate	48
3.2.1	Shift of the C-O stretch frequency upon chemisorption	48
3.2.2	Force constants of a chemisorbed CO molecule	50
3.2.3	Dynamics of a single chemisorbed CO molecule	53

3.3	Dynamics of an adsorbed CO layer	58
3.3.1	Coupling between adsorbates	58
3.3.2	Dynamics of a chemisorbed layer in external field	64
3.3.3	From adsorbate dynamics to RAIR spectra	67
4	The RuO₂(110) surface	71
4.1	Oxidation of the Ru(001) surface	71
4.2	RuO ₂ (110) films on Ru(001)	74
4.3	Chemical activity of the RuO ₂ (110) film	78
4.3.1	Adsorption of CO on reduced RuO ₂ (110)	78
4.3.2	Adsorption of O ₂ on RuO ₂ (110)	80
4.4	Preparation and characterisation by RAIRS	82
5	CO on the stoichiometric RuO₂(110) surface	87
5.1	The Langmuir model of adsorption	87
5.2	Experiment and results	89
5.3	Vibrational coupling between the CO _{ot} molecules	90
5.4	Computer simulations of the RAIR spectra	93
6	CO on the reduced RuO₂(110) surface	97
6.1	Reduction under UHV conditions	98
6.1.1	Reduced RuO ₂ (110) surface terminated by asymmetric bridging CO	98
6.1.2	CO on reduced RuO ₂ (110) under UHV conditions	101
6.1.3	Reduced RuO ₂ (110) surface terminated by symmetric bridging CO	101
6.2	Coadsorption of CO and O on RuO ₂ (110)	105
6.2.1	Adsorption of O on the reduced RuO ₂ (110) surface	105
6.2.2	Adsorption of CO on the O-saturated stoichiometric RuO ₂ (110) surface	108
6.3	Adsorption of CO on RuO ₂ (110) at high pressure	109
6.4	Structural transformations of RuO ₂ (110)	113
6.4.1	Partial restoration of r-RuO ₂ (110)	113
6.4.2	Heavy reduction of the RuO ₂ (110)/Ru(001) film by CO exposure at high temperature and pressure	122

7	<i>In situ</i> RAIRS of the RuO₂(110) model catalyst	131
7.1	In situ RAIRS in the 10 ⁻⁷ -10 ⁻⁶ mbar domain	133
7.2	In situ RAIRS in the 10 ⁻⁶ -10 ⁻² mbar domain	137
7.2.1	RuO ₂ (110) model catalyst under stoichiometric feed of CO and O ₂	137
7.2.2	RuO ₂ (110) model catalyst under oxidizing reaction conditions	146
7.3	Characteristic IR frequencies	148
7.3.1	Vibrational polarizabilities of isolated CO molecules ad- sorbed on RuO ₂ (110)	150
7.3.2	Simulated IR spectra of ordered CO _{br} /CO _{ot} phases	159
8	Summary and Outlook	163
A	Life cycle of a catalyst	169
B	Reflection of light at metal surfaces	171
C	Quantum theory of IR absorption	179
D	One-dimensional adsorbates	189
E	Computation of RAIR spectra	193

Chapter 1

Introduction

Heterogeneous catalysis has been a central process in the chemical industry for almost a century now. World agriculture has been supplied with fertilizers rich in nitrogen since 1913 due to the discovery of the Haber-Bosch process, in which nitrogen from air is converted to ammonia using an iron-based catalyst. Today, every car has a catalyst that converts carbon monoxide to carbon dioxide and eliminates other pollutants from the exhaust gas. Heterogeneous catalysis is involved in most of the processes leading to the production of industrial chemicals, fuels and pharmaceuticals. It has been estimated that more than 80% of the products of chemical industry must have been in contact with solid catalysts.

A catalyst is conveniently defined [1] as a substance that transforms reactants into products through an uninterrupted and repeated cycle of elementary steps, in which the catalyst participates while being regenerated in its original form at the end of each cycle. In heterogeneous catalysis, the catalytic substance consists of active sites at the surface of a solid. Although the catalyst does not appear in the net balance of the catalyzed reaction, it may nevertheless be strongly affected during the catalytic process, to the extent that one can properly speak of a catalyst life cycle [1, 2] (see also Appendix A).

The *in situ* characterisation of commercial heterogeneous catalysts under reaction conditions is a difficult task, due to their complex structure and to the fact that only few investigation methods are applicable at high reactant pressure. For instance, the kinetics of a catalytic reaction may be readily investigated by measuring the dependence of reaction rates on pressure and temperature. The disadvantage of such a purely 'macroscopic' approach is that no atomic details

of the reaction mechanism can be understood this way. A catalyzed reaction involves more types of elementary processes, like adsorption, dissociation, diffusion and reaction of molecules at the catalyst surface. Due to the complex interplay of these processes, even seemingly simple catalytic reactions are not easily understood in microscopic detail.

During the past four decades, the development of ultrahigh vacuum (UHV) technology has offered the researchers instruments for the preparation of atomically clean, well defined surfaces of single crystals. An understanding of the elementary steps involved in a catalytic reaction has been subsequently achieved within the so called *surface science* approach, which entails the study of the catalytic reaction on a *model catalyst* consisting most frequently of a well defined plane of a single crystal of the catalyst material, at reactant pressures in the UHV range (10^{-10} - 10^{-7} mbar). The controlled adsorption of minute quantities of gas and the study of the emerging surface structures has been possible due to the development of surface-sensitive spectroscopic techniques (HREELS, XPS, AES) [3]. Most of these techniques depend on the strong interaction of electrons with the sample and are effective only under UHV conditions, where the mean free path of the electrons is large enough. The scope of the surface science studies of catalysts has been therefore traditionally limited to the UHV domain.

The surface science approach to real catalysis necessarily brings up two questions which cannot be answered in a general manner but must be studied for each system separately. First, it is not a priori clear if the reaction mechanism, as unraveled by surface science studies at reactant pressures in the UHV range, continues to remain effective under practical reaction conditions, at pressures typically 10^{13} - 10^{15} times higher. The results of a surface science approach are thus inevitably separated from the realm of industrial catalysis by a so called 'pressure gap' (Fig.1.1). The information obtained in a surface science study on a model catalyst under UHV conditions concerns the structure of the surface, the adsorption sites, sticking coefficients, binding geometries and energies of the reactants, the elementary reaction steps and their activation energies. In the ideal case, it would be possible to recover the reaction rates measured in an industrial catalytic process at high pressure (1-100 bar) from a microkinetic model based on the reaction mechanism and the parameters obtained in UHV experiments. For a given catalytic system, this kind of extrapolation of experimental results from the UHV to the high pressure domain is referred to as a 'bridging' of the

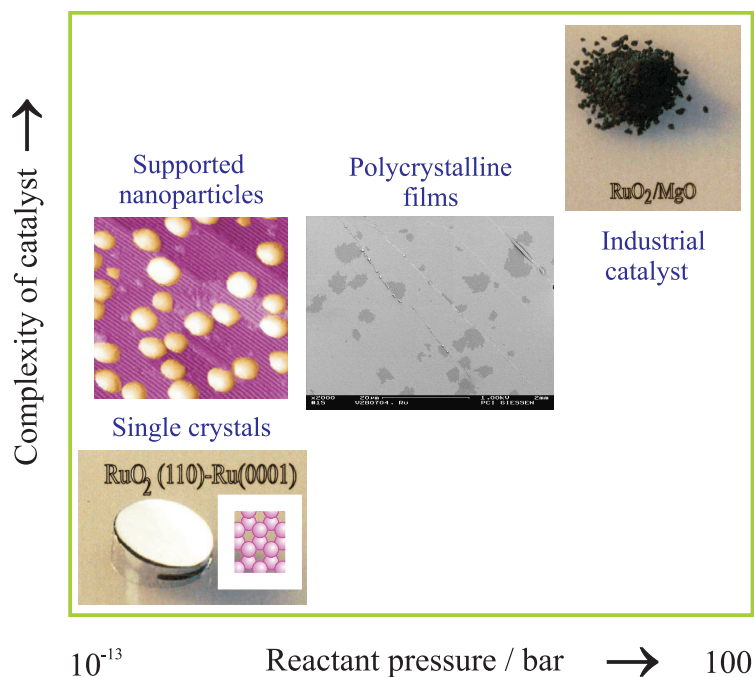


Figure 1.1: The surface science approach to catalysis is separated from the realm of practical catalysis by a *pressure gap* of 13-15 orders of magnitude and by a marked difference in the complexity of the catalyst, referred to as a *material gap*.

pressure gap. A classic example of such a successful extrapolation was given in the case of ammonia synthesis over iron [4, 5].

The second question concerns the suitability of a single crystalline, low complexity model catalyst, for modeling a complex commercial catalyst. It has been frequently observed that a catalyst is able to 'adapt' to the catalyzed reaction by changing its surface structure, a process called *reconstruction*. This kind of structural transformations of a catalyst, in response to the reaction conditions, open the possibility that elementary reaction steps, which have been identified as the most active on a model catalyst in the UHV domain, play only a minor role with the real catalyst under industrially relevant reaction conditions. The model catalyst investigated in the surface science approach is thus separated by a second, so called 'material gap' from the realm of industrial catalysis.

The object of the present thesis, the oxidation of carbon monoxide over a ruthenium catalyst, may serve as an instructive illustration of the pressure and material gaps. Particular interest in the CO oxidation over Ru was originally triggered by work on supported catalysts by Cant *et al.* [6]. Under UHV con-

ditions their 'ruthenium' catalyst exhibited by far the lowest activity among the studied late transition metals, while under atmospheric reactant pressure the situation was reversed, and a superior activity of Ru compared with Pt, Rh or Pd was measured. Practically identical activities were subsequently obtained for the Ru(001) single crystal surface by Peden and Goodman [7]. These intriguing results could be understood after Over *et al.* [8] have shown that at high oxygen partial pressure an atomically thin ruthenium dioxide (RuO_2) layer develops on the surface of the Ru model catalyst. The high catalytic activity of the RuO_2 film in the oxidation of CO has been traced back to a significantly weaker binding energy of oxygen on this surface comparatively to the Ru metal surface. The apparent pressure gap in the catalytic activity of Ru is thus shown to be in fact a material gap. Since the reaction rates for CO oxidation over RuO_2 under UHV conditions can be extrapolated to obtain the reaction rates over a Ru catalyst at high pressure [9, 10] the pressure gap in the catalytic activity of Ru has been bridged from the point of view of reaction kinetics, by identifying the RuO_2 film as the catalytically active state.

The present thesis aims to demonstrate more directly the bridging of the pressure gap for the case of the CO oxidation reaction over a Ru-based model catalyst. The underlying concept was to monitor the CO oxidation reaction on the same sample of the model catalyst, in the same chamber (*in situ*) over a broad pressure range extending from UHV to about one mbar, by using a suitable spectroscopic technique. For this purpose, we have designed an UHV system to complement the Bruker IFS 120 HR high resolution fourier transform infrared (FTIR) spectrometer, in use at the Physical Chemistry department of the University of Giessen. The reaction was conducted in an UHV cell with high pressure capabilities and viewports for IR spectroscopy. Our model catalyst was a thin ruthenium dioxide layer grown under UHV conditions on the atomically clean (001) plane of a Ru single crystal. On the high pressure / high complexity side of the gap, diffuse reflectance IR spectroscopic (DRIFTS) studies of the CO oxidation reaction over a more complex Ru model catalyst (supported nanometer-size Ru clusters) due to Assmann *et.al.* [11, 12] may serve as a basis of comparison for our results.

Among the IR spectroscopic techniques applied in the study of solid catalysts, reflection-absorption IR spectroscopy (RAIRS) is best suited for the study of submonolayer quantities of molecules adsorbed on the surfaces of single crystals

[13, 14]. We shall consider only *metallic* single crystals and note that, due to its metallic conductivity, ruthenium dioxide qualifies as such. In RAIRS, the IR beam is directed to the sample surface at grazing incidence ($80\text{-}85^\circ$), a geometry by which the normal component of the electric field at the surface is enhanced by a factor of two, partly compensating for the weak IR absorption signal of the chemisorbed molecules. Specific for RAIRS is the rather stringent dipole selection rule, which states that only those vibrational modes of the chemisorbed molecule can be excited, for which the surface-normal component of the dipole moment changes [15]. The internal vibration modes of a molecule, if they are not forbidden by the dipole selection rule, can be relatively easily measured by RAIRS. The detection of adsorbate-substrate vibrations ($300\text{-}500\text{ cm}^{-1}$) is much more difficult, due to the sensitivity loss of IR detectors at low frequencies [16].

Up to the millibar range, the gas phase absorbs IR photons only weakly, such that RAIRS is particularly suited for studies of adsorbates on single crystals at high pressure. By implementing RAIRS with the UHV/high pressure reaction cell, we were in a comfortable position to monitor *in situ* the adsorbed CO molecules at the model catalyst surface, from the UHV range up to 10^{-2} mbar.

Since there can be no more than 10^{15} adsorbed molecules in a layer on a metal sample of 1 cm^2 area, preferentially molecules with high dipole moment are recommended for a RAIRS study. It is not surprising that, due to the strong dipole moment associated with the C-O bond, CO adsorbed on metal surfaces is the system most studied by RAIRS. The stretch frequency of the CO molecule is very sensitive to the coordination and electronic properties of its adsorption site, and to the presence of coadsorbates which act as electron donors or acceptors. The CO molecule is therefore ideally suited as an IR probe (test molecule) for the investigation of chemically active sites on the sample surface. On the other hand, the large dipole moment of the CO test molecules leads to strong dipole-dipole coupling at higher coverages. In this case, although the test molecules occupy inequivalent adsorption sites, a single collective resonance¹ band is detected by RAIRS. The interpretation of RAIRS spectra is relatively straightforward only at low coverages, when the CO test molecules are well separated and their coupling not too strong (typically at few percent of a monolayer).

¹The standard experimental method to minimize the influence of the dipole-dipole coupling between CO test molecules implies the use of isotopic mixtures of ^{12}CO and ^{13}CO , which due to their reciprocally shifted ($\sim 50\text{ cm}^{-1}$) vibration frequencies do not resonate [17].

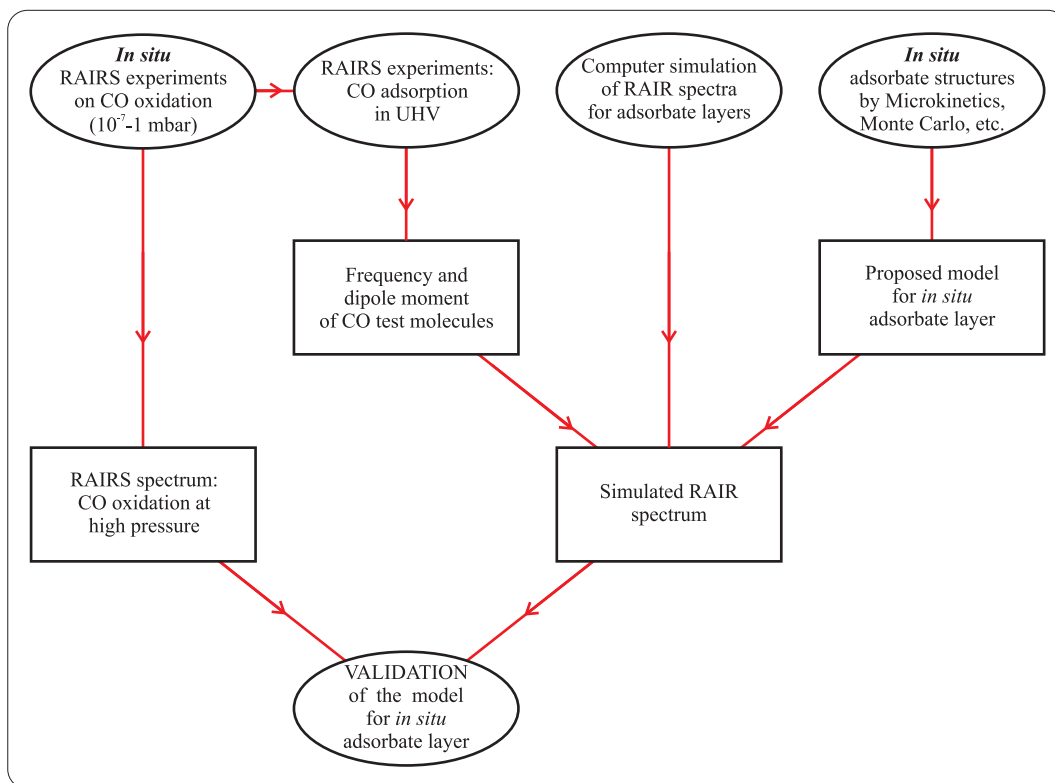


Figure 1.2: Proposed approach to the IR-spectroscopic bridging of the pressure gap for the CO oxidation reaction over RuO₂(110).

It is not possible to maintain low coverages in all situations when using CO as a test molecule. In our RAIRS study of CO oxidation at high pressure, the CO molecule plays the role of an IR probe but is at the same time a reactant. According to the reaction conditions, the CO coverage of the sample can vary from isolated molecules to complete coverage. Moreover, RAIRS is the only method by which the *in situ* CO coverage can be estimated. With a more or less complete adsorbed layer, CO plays the role of an IR probe molecule in a vibrational regime dominated by dipole-dipole coupling.

In order to gain as much information as possible from the RAIR spectra measured under reaction conditions, we propose an approach which combines RAIRS experiments under UHV conditions with the *computation* of IR spectra for *models* of the adsorbed layer under reaction conditions (Fig.1.2). The models of the adsorbed layer indicate the positions of the reactants (CO, O, vacant sites) *in situ* on the catalyst surface. RAIRS measurements of well characterised adsorbate structures under UHV conditions provide the vibrational parameters

(characteristic frequencies, dipole moments) of the CO test molecules adsorbed at different active sites of the model catalyst. Using the theory of dipole-dipole coupling, the RAIR spectrum of the proposed *model* adsorbate layer is computed based on the CO vibrational parameters determined in the UHV experiments. The model proposed for the *in situ* adsorbed layer is evaluated by comparing its computed RAIR spectrum with the experimental RAIR spectrum under reaction conditions. We note that our proposed approach is yet another example of a 'bridging the gap' strategy, since data obtained by RAIRS on pure adsorption systems under UHV conditions are used to compute RAIR spectra under reaction conditions at high pressure.

The present thesis is structured as follows. A description of the experimental setup, consisting of the UHV system and the FTIR spectroscopic system is given in Chap.2. The physical principles of reflection-absorption IR spectroscopy, the dynamics of CO vibrations at a metal surface and the theory of dipole-dipole coupling are presented in Chap.3. The structure, chemical activity and the preparation of the RuO₂(110) model catalyst are presented in Chap.4. An extensive RAIRS study of the adsorption system CO on RuO₂(110) is described in Chap.5 and Chap.6. The *in situ* RAIRS study of the CO oxidation reaction over RuO₂(110) (10^{-7} - 10^{-2} mbar, 350 K) is discussed in Chap.7. A summary of the results is given in Chap.8, page 163.

Chapter 2

UHV system for *in situ* RAIRS studies of model catalysts

In the present chapter we describe a complex UHV system designed for the study of single crystalline model catalysts by surface science methods (in the UHV regime) and by *in situ* reflection-absorption IR spectroscopy in the high pressure regime. The UHV system has been conceived from the outset as an extension to the Bruker IFS 120 HR high resolution fourier-transform IR (FTIR) spectrometer in use at the Physical Chemistry department of the University of Giessen. The UHV system and the FTIR spectrometer are coupled by means of an additional UHV chamber with high pressure (HP) capability and equipped with IR-transparent viewports. This UHV/HP chamber (cell) plays simultaneously the role of a batch reactor and that of a spectroscopic cell for *in situ* IR measurements under controlled conditions, in the pressure range 10^{-10} -1 mbar.

The main blocks of the experimental setup are indicated in Fig.2.1. The setup consists essentially of a complete UHV system *A* and the Bruker IFS 120 HR spectrometer *B*. The optics and mechanical parts of the FTIR spectrometer are housed in a vast vacuum chamber *B*, evacuated to 10^{-2} - 10^{-1} mbar in order to minimize absorption of the IR beam in air. The IR beam exits from the spectrometer *B* and enters chamber *C*, which hosts the UHV/HP cell with the sample and the optical components for the transfer of the IR beam to the sample surface (transfer optics). After reflection at the sample surface, the IR beam is guided to chamber *D* which contains the IR detectors. The vacuum chambers *C* and *D* are merely extensions of the evacuated volume of the FTIR spectrometer.

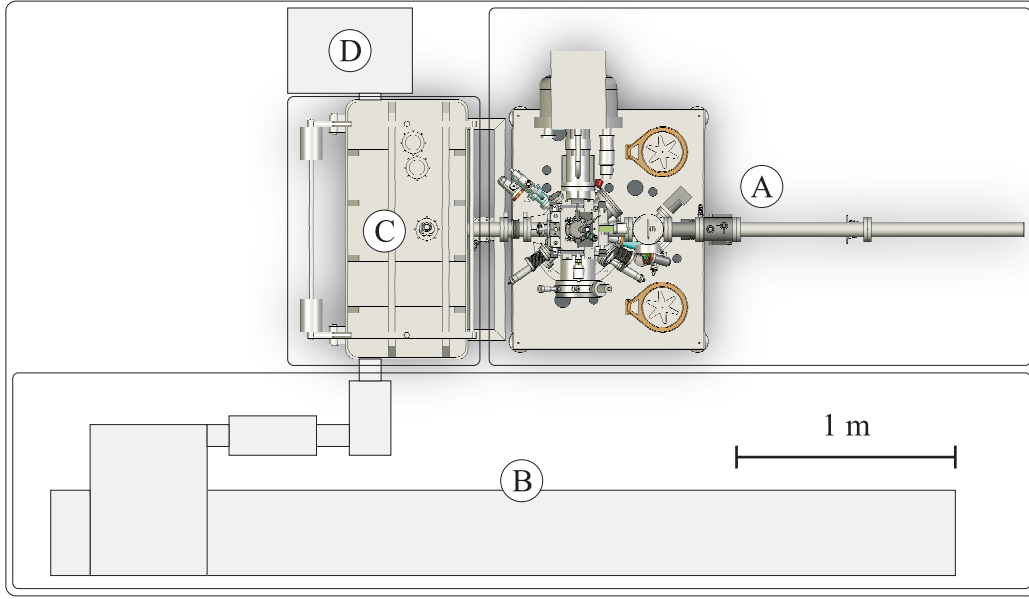


Figure 2.1: Overview of the experimental setup: A-UHV system, B-FTIR spectrometer (Bruker IFS 120 HR), C-chamber for transfer optics and the UHV/high-pressure cell, D-chamber for IR detectors.

2.1 The UHV system

To obtain a quick overview of the UHV system we shall briefly discuss Fig.2.2. The central part of the system is the Analysis Chamber (AC), a standard UHV chamber equipped with instruments for the preparation and characterization of the sample. The AC is separated from the Fast Entry System by a gate valve *b*. The sample is introduced through the load lock *1*, which is subsequently evacuated such that the sample can be moved, by means of a transfer rod, from the load lock into the AC without breaking the UHV conditions. In the AC the sample is transferred into the manipulator *7*, which serves to position the sample in front of the preparation and characterization instruments. Following preparation the sample is moved, by means of the transfer rod, into the UHV/HP cell *11* for *in situ* IR spectroscopic measurements. Here, the sample is supported by the manipulator *12*, which serves to position the sample in the focus of the IR beam. The IR beam enters the UHV system and reaches the sample surface through the IR-transparent viewport *13*. In the next sections we shall discuss each part of the UHV system in detail.

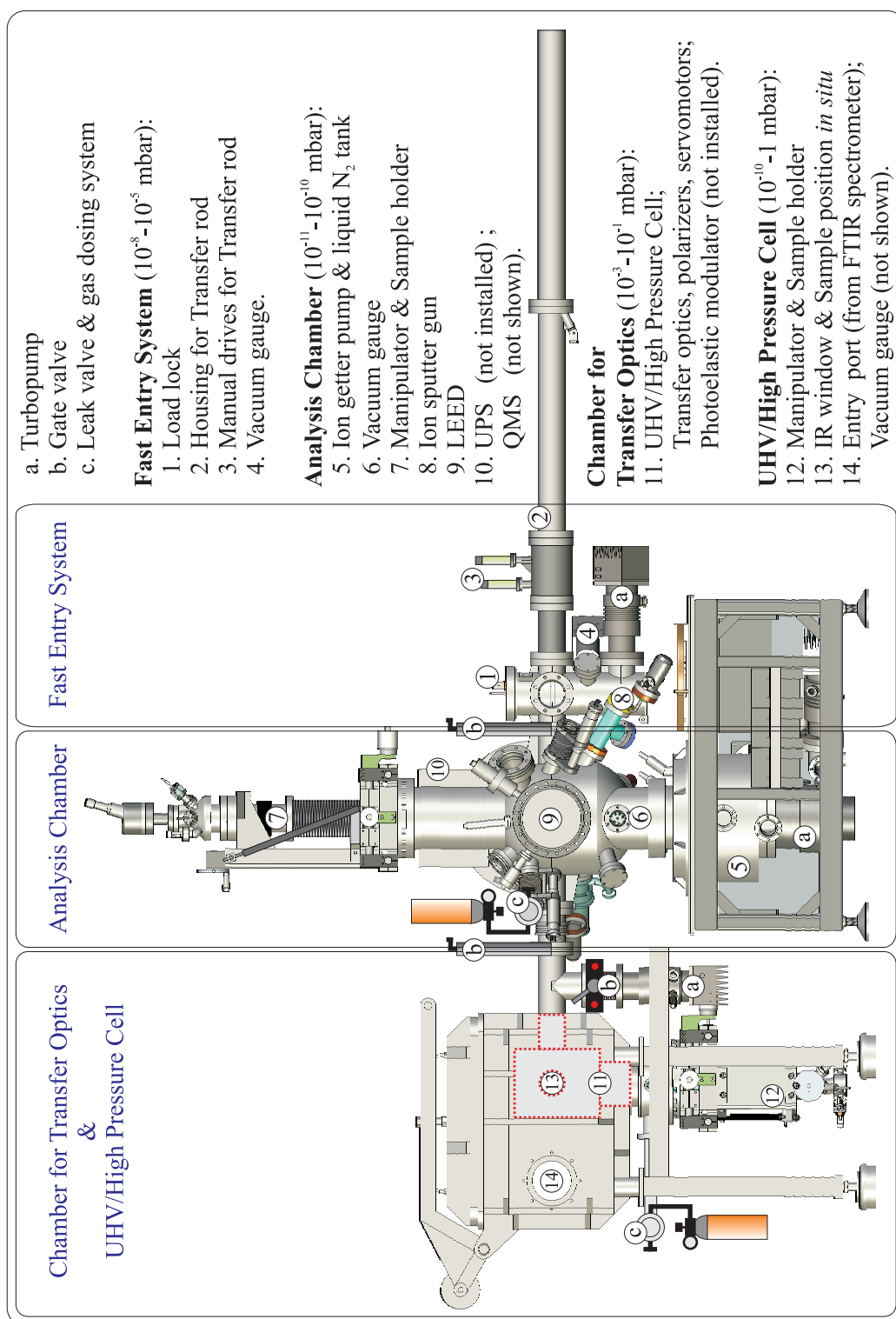


Figure 2.2: Overview of the UHV system. Only the instruments used in the present work are shown.

2.1.1 The analysis chamber

The design of the analysis chamber has been led by the idea to implement a large variety of surface science methods and instruments. Thus, the design of the analysis chamber has been determined mainly by the necessity to accommodate a collection of sometimes bulky instruments around a relatively small volume UHV chamber. Most critical was the position of the hemispherical analyzer for X-ray photoelectron spectroscopy (XPS) and of the X-ray and UV sources, which must be located on flanges positioned under a well defined angle¹ relatively to the hemispherical analyzer. Further analysis instruments include a LEED setup and a quadrupole mass spectrometer (QMS) for monitoring the composition of the residual gas and for temperature-programmed desorption measurements. An ion-sputter gun must be provided for cleaning the sample. For the controlled deposition of monolayers of other metals at the sample surface, additional flanges must be foreseen for a Knudsen cell and for an electron-bombardment evaporator.

We have adopted the design of an essentially spherical UHV chamber, with a cylindrical segment intercalated between both hemispheres (Fig.2.3). The inclusion of the cylindrical segment was necessary in order to provide room for grouping the instruments on different levels. The preparation and analysis instruments are focused on the principal axis of the chamber ($\beta = 90^\circ$), but each instrument is focused into a different plane, numbered from F1 to F5, in order to avoid collisions and to gain more interior space for the sample. For instance, the sample transfer rod, the LEED and the ion-sputter gun are contained in the plane F1, while the plane F2 located 70 mm lower is dedicated to the instruments for photoelectron spectroscopy (electron analyzer, X-ray and UV sources). The dimensions and flange allocation of the analysis chamber are given in Fig.2.3.

The sample is positioned within the analysis chamber by means of a manipulator (Fig.2.2, position 7) equipped with an XY translation stage (± 25 mm) and a Z translation of 170 mm (the distance between the focal planes F3 and F4 is 165 mm). The manipulator permits rotation and tilt of the sample. The analysis chamber is separated by gate valves (Fig.2.2, positions *b*) from both the fast entry system and from the UHV/HP cell. This design brings up the problem that the sample must be freely transferable between the chambers, without attachments

¹The surface sensitivity of XPS can be enhanced by placing the analyzer at the so-called take-off angle of the photoelectrons (54°) [15].

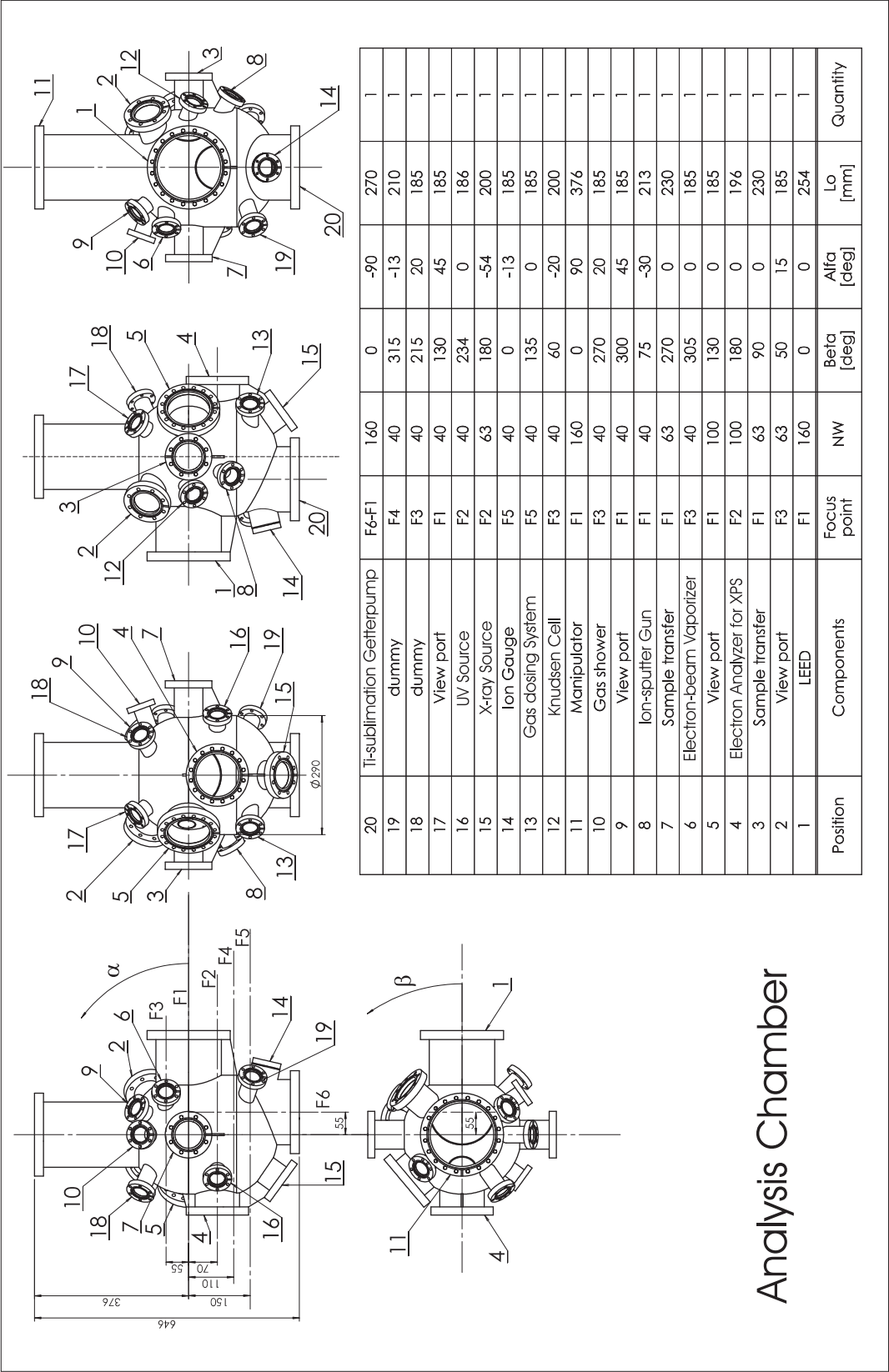


Figure 2.3: Dimensions and flange allocation of the analysis chamber.

for cooling and heating. The solution was an elaborate sample docking system fastened on the manipulator rod, which permits cooling and heating the sample while keeping the sample detachable.

2.1.2 Sample docking system and the sample holder

The sample docking system of the manipulator is shown in Fig.2.4.a. The sample holder is shown in Fig.2.4.b and Fig.2.4.c. The sample holder (in the position shown in Fig.2.4.c) is transferred into the sample dock 1 by means of the transfer rod, following the direction of the arrow. The movable plate 2 holds the contacts for heating (3), thermocouple (4) and grounding (5) of the sample. When put under pressure (4 bar) from outside, the bellows 6 expand and, by acting on a lever mechanism, press the movable plate 2 against the back side of the sample holder (Fig.2.4.b). The contacts 3, 4 and 5 on plate 2 engage then the corresponding contacts on the back side of the sample holder and the sample can be heated (radiatively or by electron bombardment) and its temperature measured. To cool the sample, greater pressure (6 bar) must be applied to the bellows 6. While the contacts on plate 2 remain further engaged, a cooling finger 7 (which moves independently of plate 2) is now pressed against the back side of the sample holder. The cooling finger 7 is terminated by a sapphire ball (Fig.2.4.a) which fits into the dip on the cooling finger 8 of the sample holder (Fig.2.4.b). The cooling finger 8 is in direct thermal contact with the sample. With the cooling finger 7 pressed against the cooling finger 8 of the sample holder, the sample can be simultaneously heated and cooled.

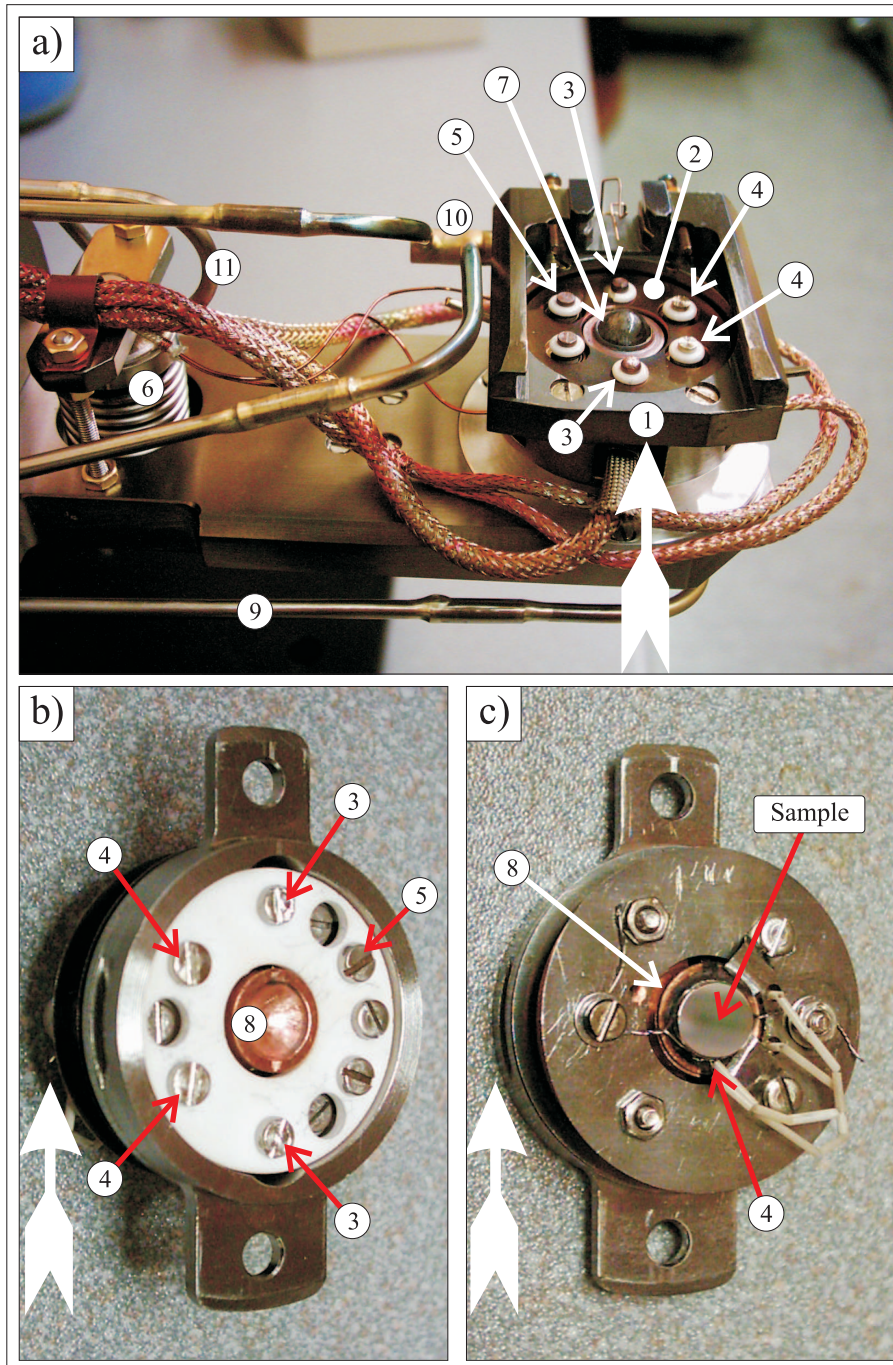


Figure 2.4: a) Sample docking system, b) sample holder (back side), c) sample holder (front side). Constructive parts: 1-sample dock, 2-movable plate, 3-contacts for heating the sample, 4-contacts for thermocouple, 5-contact for grounding the sample, 6-bellows, 7-cooling finger, 8-cooling finger (to sample), 9-tubing for liquid nitrogen (to 7), 10-cooling finger (to 1), 11-tubing for compressed air (to 6). Details are explained in the text.

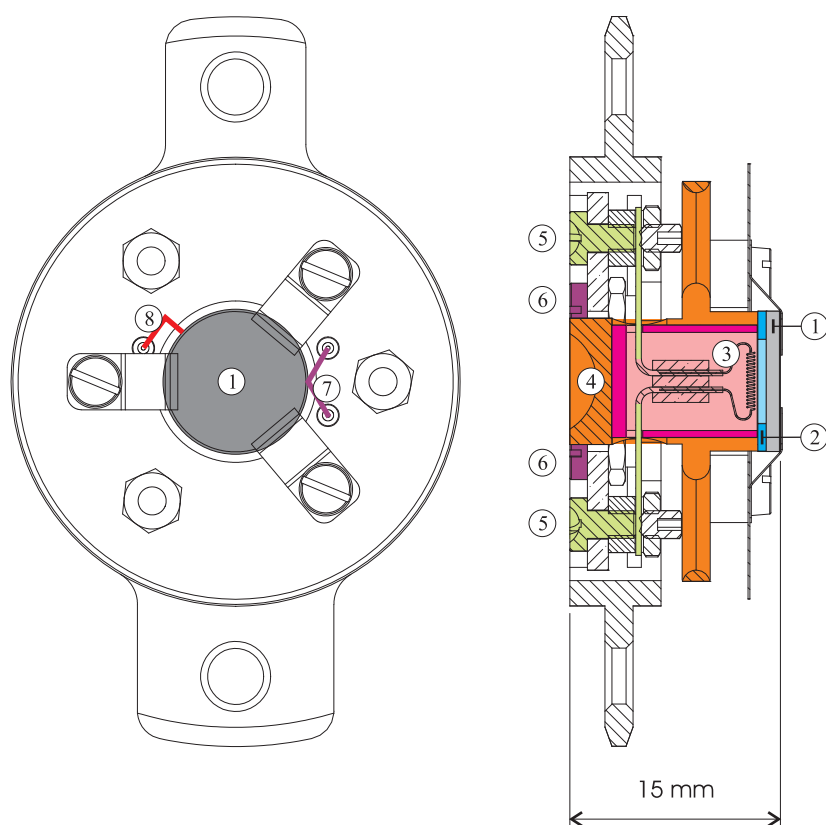


Figure 2.5: Constructive parts of the sample holder: 1-sample, 2-sapphire ring, 3-filament for heating the sample, 4-cooling finger, 5-electrical contacts (to 3), 6-electrical contacts for thermocouple, 7-thermocouple, 8-grounding of the sample.

Constructive details of the sample holder are shown in Fig.2.5. The sample *1* is kept in thermal contact with the cooling finger *4* by means of a sapphire plate *2*, shaped as a ring in order to permit the electrons emitted from filament *3* to reach the back side of the sample. When the sample is heated, the thermal conductivity of the warmed sapphire plate *2* decreases and the sample *1* is thermally isolated from the cooling finger *4*. When heating of the sample is interrupted, the sapphire plate cools down and its thermal conductivity increases, facilitating the cooling of the sample. The design permits to efficiently heat the sample while keeping the cooling finger (Fig.2.4, position *7*) engaged to the sample holder. This feature is an advantage during a RAIRS measurement, since the repeated disengagement of the cooling finger would lead to a small drift of the sample position relatively to the IR beam, which could disturb the adjustment of the optical system.

Heating of the sample can occur either through radiation from the filament (efficient up to about 800 K) or through electron bombardment on the back of the sample (for warming rates up to 20 K/s and temperatures up to 1300 K). By applying a small voltage at the contacts *5* (Fig.2.5), the filament *3* is brought to incandescence and starts to emit thermoelectrons. High voltage (100-1000 V) applied between the sample *1* (grounded) and the filament *3* accelerates the thermoelectrons toward the sample. The current passing from the filament into the sample is routinely in the 10-20 mA range.

For discussing the cooling of the sample, let us now return to Fig.2.4. In the manipulator, the flux of liquid nitrogen is transported to the cooling finger of the sample *7* along the line *9*. The transport lines for liquid nitrogen are built of thin, flexible metal tubing such as not to hinder the rotation of the manipulator. A second cooling finger (*10*) protects the sample dock *1* against the heat radiated by the sample holder.

In conclusion, the sample docking system and the sample holder permits to cool the sample to 100 K by pumping liquid nitrogen through cooling lines built into the manipulator, and to heat the sample up to 1300 K by electron bombardment under a voltage bias up to 1000 V. The power transferred to the sample during electron bombardment is in the 10-20 W range. The sample is completely detachable from the manipulator and can be transferred under UHV conditions between separate chambers.

Some cautionary remarks about the choice of materials for the sample holder are in place. Prior to the use of a sample holder equipped with electron bombard-

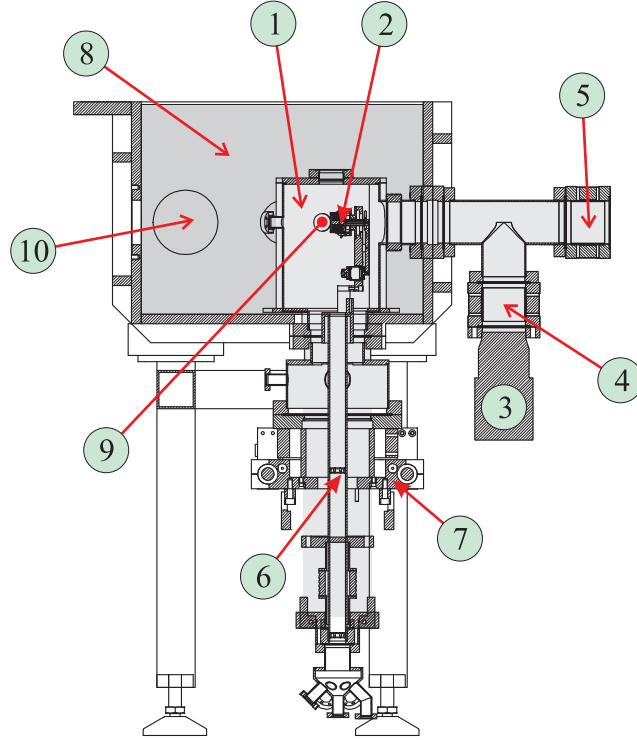


Figure 2.6: Chamber for the transfer optics with the UHV/high-pressure cell. 1-UHV/high-pressure cell, 2-sample holder, 3-turbopump (to 1), 4-gate valve, 5-gate valve (to the analysis chamber), 6-manipulator rod, 7-translation stage of the manipulator, 8-chamber for transfer optics (10^{-2} mbar), 9-IR transparent viewport, 10-exit port for IR beam (to IR detector chamber). The volume marked in light gray is part of the UHV system.

ment, we have extensively experimented with a resistively heated sample holder of similar construction. The disadvantage of that design was that the power could not be concentrated to the sample but was instead consumed to heat the bulk of the sample holder. Over longer periods of use in the UHV chamber, a blueish film has covered the molybdenum heating filament and has spread over the sample holder. Auger electron spectroscopy of the Ru sample has revealed a high content of Mo, which could explain why our surface science experiments involving 'clean' Ru(001) surfaces were in the beginning unsuccessful.

2.1.3 The UHV/high-pressure cell

A section through the block consisting of the vacuum chamber for transfer optics and the UHV/high-pressure cell is shown in Fig.2.6. The sample is introduced

into the UHV/HP cell 1, from the analysis chamber, through the gate valve 5 by means of the transfer rod. The UHV/HP cell contains a manipulator 6 of similar design to the manipulator in the analysis chamber, described in the previous section. After insertion of the sample holder 2 into the docking system on the manipulator rod 6, the transfer rod is withdrawn and the gate valve 5 may be closed, isolating the UHV/high-pressure cell from the rest of the UHV system.

The UHV conditions in the UHV/HP cell 1 are maintained by the turbo molecular pump 3. During high pressure experiments, the gate valve 4 is closed in order to protect the turbo molecular pump 3. When both gate valves 4 and 5 are closed, the UHV/HP chamber may be used to study reactions at high pressure and may be assimilated to a *batch reactor*.

The IR beam exits the FTIR spectrometer through the port 10, from where it is guided by a system of mirrors to the IR-transparent viewports 9. The manipulator 6 is supported on the XY translation stage 7, which permits a translation of ± 25 mm in both directions. The Z-translation of the manipulator 6 is limited to 30 mm. The manipulator permits also rotation of the sample. The sample holder 2 can thus be exactly positioned relatively to the IR viewports 9, such that it occupies the focus of the IR beam.

The IR-transparent viewports 9 are one of the most delicate points of the design. Since the stretch vibrations of the CO molecule (2000 cm^{-1}) fall into the mid-IR range, the material chosen for the viewports has to be transparent in this region. The viewports are therefore made from single crystals such as KBr, CaF₂ and sealed with Viton O-rings in grooves machined into the wall of the chamber. In order to minimize unwanted interference effects, the two sides of the single crystalline discs are cut along the same crystal plane, but are intentionally misaligned by about 1° . Since the whole UHV/HP cell is contained in the vacuum chamber for transfer optics at 10^{-2} mbar, these viewports are in fact differentially pumped feedthroughs for IR radiation. The design has made possible a base pressure of 1×10^{-9} mbar in the UHV/HP chamber after bakeout.

The bakeout of such IR viewports is a well known problem since the first designs of *in situ* IR cells [18]. To bake out the UHV/HP cell, we have used heating ribbons (250 W) wrapped around the chamber. During the first attempts, the heating ribbons passed very close above the salt viewports, and a uniform temperature of about 130°C at the chamber surface was achieved. However, these attempts were unsuccessful because the surface of the viewport single crystal KBr

(intentionally miscut to a small angle) has roughened by developing terraces, due to the high bakeout temperature. These terraces have expanded over the surface of the crystal until they reached the Viton O-ring sealings, and no perfect sealing could be achieved. We have therefore wrapped the UHV/HP chamber with heating ribbons such that they pass at a few cm from the IR viewports, keeping them exposed to ambient air for cooling. The temperature of the CaF_2 viewport did not exceed this time 80°C and the bakeout was successful.

Another problem we met with the salt crystal IR-viewports was their hygroscopicity. When the chamber for transfer optics 8 (Fig.2.6) has not been pumped for a longer time, we have noticed a worsening of the pressure in the UHV/HP cell and an elevated water content in the residual gas. In order to avoid diffusion of water from ambient air, through the viewports into the UHV/HP chamber, it has proved necessary to keep rough vacuum in the chamber for transfer optics 8.

2.1.4 Fast entry system

The fast entry system has the role to make possible the rapid introduction of samples into the UHV system, without breaking the UHV conditions. The time consuming bakeout of the chamber, necessary if the UHV chamber would have been opened, can thus be avoided.

The load lock is a small UHV chamber equipped with a turbo-molecular pump and with a lid sealed by a Viton O-ring for the introduction of the sample. The sample holder is inserted into a fork fastened on the inner side of the lid. After closing the load lock, the turbo molecular pump is started and within 30 minutes a pressure of 5×10^{-6} mbar is achieved, which permits the safe transfer of the sample into the analysis chamber (base pressure 1×10^{-10} mbar). After longer periods the base pressure in the load lock stabilizes at 1×10^{-8} mbar.

The transfer is made by means of a transfer rod, housed in a long extension of the load lock chamber. The transfer rod is of the *rack-and-pinion* type (TLI Thermionics), and is manoeuvred from outside by means of two rotary feedthroughs. These permit translation of the transfer rod (100 cm) and rotation around its axis ($\pm 90^\circ$), necessary because of the position of the sample holder during the transfer into both manipulators.

Note

The UHV system described in the present section was designed and manufactured by the firma Prevac². The sample docking system and the sample holder described in Section 2.1.2 were developed by the firma Prevac.

2.2 Fourier transform IR spectroscopy

Fourier transform IR spectrometers (FTIR) present attributes which recommend them for the measurement of reflection-absorption spectra from surface species. In the 1950's the first IR spectroscopic studies of adsorbed species [18] were carried out mostly with grating or prism IR spectrometers and their sensitivity was not particularly large. In the 1960's new methods emerged due to the development of fourier transform spectrometers, in parallel with computers and the fast-fourier-transform algorithm necessary for the transformation of the interferogram to an IR spectrum [16, 19].

The most important advantage of FTIR spectrometers rests in the use of a Michelson interferometer as spectral analyzer, which increases the signal-to-noise ratio for any measurement, compared to dispersive techniques (prisms, gratings). This has been understood due to the work of Jacquinot [20] and Fellgett [21].

The *throughput* or Jacquinot advantage states that in a lossless optical system, like a Michelson interferometer, the brightness of an object equals the brightness of an image. Therefore, the flux throughput and brightness are constant at any point in a Michelson interferometer, from the source to the sample to the detector. Whereas the only radiation reaching the detector of a dispersive spectrometer has passed through the entrance and exit slits of the monochromator, there is no such obstruction in an interferometer, except the size of the mirrors [22].

The *multiplex* or Fellgett advantage may be stated as follows [19]. Let us suppose we are interested in measuring a broad spectrum between the wavenumbers ν_1 and ν_2 with a resolution $\Delta\nu$. The number of spectral elements M in the broad band is then $M = (\nu_2 - \nu_1)/\Delta\nu$. If a grating or prism instrument is being used, each spectral element $\Delta\nu$ can be measured for a time T/M , where T is the total time required for the measurement of the spectrum from ν_1 to ν_2 . One can say that the integrated signal measured for the element $\Delta\nu$ is proportional to T/M .

²Prevac sp. z o.o., Raciborska 61, PL-44362 Rogow, www.prevac.eu

If the noise is random and independent of the signal level, the signal-to-noise ratio for the grating instrument would be

$$\left(\frac{S}{N}\right)_{grating} \sim \sqrt{\frac{T}{M}} \quad . \quad (2.1)$$

The situation for the interferometer is different because it detects all elements $\Delta\nu$ in the broad band $\nu_2 - \nu_1$ all the time. The integrated signal measured for the element $\Delta\nu$ is therefore proportional to T . If the noise is random and independent of the signal level, the signal-to-noise ratio for the interferometer would be

$$\left(\frac{S}{N}\right)_{FTIR} \sim \sqrt{T} \quad , \quad (2.2)$$

with the same proportionality factor as in Eq.2.1. Comparing the signal-to-noise ratios of interferometers to that of grating spectrometers we get

$$\frac{(S/N)_{FTIR}}{(S/N)_{grating}} = \sqrt{M} \quad . \quad (2.3)$$

To measure a spectrum with high resolution (M large) an interferometer is much more suited than a grating spectrometer, due to its signal-to-noise ratio which is better by a factor \sqrt{M} . For instance, if the resolution must be as high as to have $M = 10^4 - 10^6$, the signal-to-noise ratio of the interferometer could be better by a factor of $10^2 - 10^3$ than that of the grating spectrometer. For the *same* value of the signal-to-noise ratio, the acquisition time of a spectrum is therefore much shorter in the case of FTIR. In the context of the spectroscopy of adsorbed molecules, the detection of transient surface species becomes thus possible.

Further advantages [22] stem from the optical properties of the light beams in an interferometer. Greenler has shown that bands due to surface species are enhanced when very high angles of incidence are used [23]. Since the beam at the exit of the interferometer is highly collimated, the incident angle is well-defined and angles approaching the optimal theoretical value of 87° may be realized. Greenler has further shown that only radiation polarized parallel to the surface normal is absorbed by the surface species. The beam emerging from an interferometer shows substantially less polarization than that from a grating monochromator.

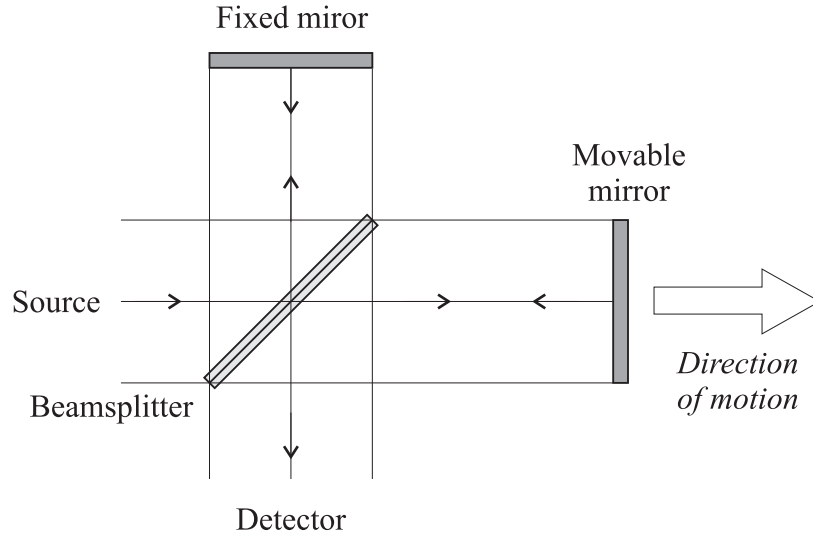


Figure 2.7: Schematic representation of a Michelson interferometer.

We shall next review the basic ideas of FTIR spectroscopy by following the clear and concise exposition in Ref.[22].

2.2.1 The Michelson interferometer

The Michelson interferometer is shown schematically in Fig. 2.7. It consists of two perpendicular plane mirrors, one of which is stationary, while the other moves at a constant velocity v cm/s in the direction shown. Between the two is a semi-reflecting film, or beam splitter, at which the incident beam is divided and later recombined after a path difference has been introduced between the two beams.

If the incoming radiation is monochromatic of frequency ν cm^{-1} , the signal measured at the detector (interferogram) goes through a series of intensity maxima and minima, corresponding to constructive and destructive interference. The expression for the intensity $I(\delta)$ transmitted by the interferometer is a function of the optical path difference (δ cm) of the beam which has been reflected off both mirrors

$$I(\delta) = 0.5 H(\nu) I(\nu) (1 + \cos(2\pi \nu \delta + \theta_\nu)) \quad (2.4)$$

where $I(\nu)$ is the intensity of the radiation incident into the interferometer, $H(\nu)$ is a factor less than unity which represents the departures from the actual spectral intensity $I(\nu)$ due to the instrument characteristics, and θ_ν is a phase shift introduced by the beamsplitter and detector electronics. The detector signal varies

sinusoidally with a frequency f_ν given by

$$f_\nu = 2\nu\delta \quad \text{Hz} \quad (2.5)$$

The factor of two arises from the fact that a displacement $\delta/2$ of the moving mirror changes the optical path difference (retardation) by an amount of δ cm. The optical frequency is therefore encoded in the form of an oscillation of much lower frequency, which is usually in the audiofrequency range.

Each input frequency from a polychromatic source can be treated independently, and the output is the summation of all the sinusoidal oscillations due to each optical frequency in the source. At one point in the mirror travel, all the waves are in phase and their sum is large. Elsewhere, they are not in phase, their sum is smaller, and the variations in signal are almost imperceptible compared to the variations around zero retardation. The resulting AC fraction of the signal is then given by

$$I(\delta) = \int_{-\infty}^{+\infty} B(\nu) \cos(2\pi \nu \delta + \theta_\nu) d\nu \quad (2.6)$$

where

$$B(\nu) = 0.5 H(\nu) I(\nu) \quad . \quad (2.7)$$

Mathematically, Eq.2.6 is similar to one-half of a cosine Fourier transform pair, where the other half is given by

$$B(\nu) = \int_{-\infty}^{+\infty} I(\delta) \cos(2\pi \nu \delta) d\delta \quad . \quad (2.8)$$

2.2.2 Phase correction

The phase shift θ_ν in Eq.2.6 results from an asymmetry in the instrument, in sampling, from dispersion in the beam splitter, or from the finite time constant of the detector amplifier. Two common examples which may lead to a nonzero phase shift are sampling of the first data point before the zero retardation point, and a wavenumber-dependent phase lag on each cosinusoidal component due to the electronic filters designed to remove high-frequency noise from the interferogram [16]. In this case, the spectrum is connected to the interferogram by means of

the complex fourier transform

$$B(\nu) = \int_{-\infty}^{+\infty} I(\delta) e^{-2\pi i \nu \delta} d\delta \quad . \quad (2.9)$$

In order to eliminate these instrumental effects, one has to perform the process of phase correction in the spectral computations. The first operation is the elimination of the phase shift due to the interferogram peak being located off-center from zero, and the second is that which generates the real phase-corrected spectrum from the complex, uncorrected spectrum. The corrected phase should then be near zero or 2π . Usually, this computation is carried out by investigating a small region of the interferogram around both sides of the point of stationary phase, and determining θ_ν from this interferogram according to

$$\theta_\nu = \arctan \left\{ \frac{\text{Im } B(\nu)}{\text{Re } B(\nu)} \right\} \quad . \quad (2.10)$$

In this way, only one side of the interferogram needs to be sampled for the full retardation, while on the other side of zero retardation only a few points need to be measured.

2.2.3 Finite resolution

In the foregoing discussion the interferogram has been assumed to be of infinite extent. An infinitely long mirror travel and sampling of an infinitely large number of points by passing perfectly collimated light through the interferometer would lead to perfect resolution in the measured spectra.

In practice there are several factors which affect the resolution of the computed spectra. The first and most important of these is the *length* of the mirror travel. The effect of mirror travel can be understood intuitively by considering a spectrum consisting of two closely separated spectral lines ν_1 and $\nu_2 \text{ cm}^{-1}$. The interferogram consists of the addition of the two cosine waves generated by these lines, and the closer in frequency are the lines, the greater the retardation needed before these cosine waves become out of phase. For complete separation of the two spectral lines, the retardation ($X \text{ cm}$) must equal $1/(\nu_2 - \nu_1)$. The resolution

$\Delta\nu$ of a Michelson interferometer is given by

$$\Delta\nu \sim 1/X \text{ cm}^{-1}. \quad (2.11)$$

The second criterion determining resolution is the *divergence* of the beam through the interferometer. If there is a difference in optical path between the center of the beam passing through the interferometer and the extreme ray, interference will occur between these rays, and the intensity of the signal for any frequency in the interferogram will decrease as the retardation increases. After a certain point in mirror travel, there is no further gain in resolution on increasing the retardation. The maximum half-angle of the beam, γ_{max} , depends on the resolution given by Eq.2.11, and on the highest frequency in the spectrum ν_{max}

$$\gamma_{max} = \sqrt{\frac{\Delta\nu}{\nu_{max}}} \text{ radians}. \quad (2.12)$$

The quality of the drive of the mirror is a limiting factor for the achieved resolution and the highest measurable frequency, since tilting of the movable mirror beyond a certain tolerance will have the same effect as a diverging beam.

2.2.4 Apodization

If one could determine an interferogram completely for δ varying between $+\infty$ and $-\infty$, the spectrum could be reproduced exactly. However, since in practice δ has a maximum value X , the value $B'(\nu_1)$ computed for a particular frequency $\nu_1 \text{ cm}^{-1}$ will only approximate the true value of $B(\nu_1)$. In this case, Eq.2.8 may be put in the form

$$B'(\nu_1) = \int_{-\infty}^{+\infty} I(\delta) D(\delta) \cos(2\pi \nu \delta) d\delta \quad (2.13)$$

where $D(\delta)$ is a boxcar function such that

$$D(\delta) = \begin{cases} 1 & \text{if } -X < \delta < X \\ 0 & \text{if } \delta < -X \text{ or } X < \delta \end{cases} \quad (2.14)$$

The cosine transform of the product of two even functions, such as $I(\delta)$ and $D(\delta)$, is the convolution of the cosine transform of each function. The cosine

transform of $I(\delta)$ is the 'true' spectrum $B(\nu)$, while the transform of $D(\delta)$ imparts the shape to a computed spectral line. In this case, the intensity at any frequency ν_1 in the spectrum is computed to be

$$B'(\nu_1) = \int_{-\infty}^{+\infty} B(\nu) f(\nu_1 - \nu) d\nu \quad (2.15)$$

where $f(\nu)$ is the cosine transform of the boxcar function Eq.2.14

$$f(\nu) = \int_{-\infty}^{+\infty} D(\delta) \cos(2\pi \nu \delta) d\delta \quad (2.16)$$

or explicitly

$$f(\nu) = 2X \left[\frac{\sin(2\pi \nu X)}{2\pi \nu X} \right] \quad (2.17)$$

The function $f(\nu)$ appearing in Eq.2.15 is sometimes referred to as the instrument line shape. By introducing the notations

$$y = 2\pi \nu X$$

and the so-called *sinc* function

$$\text{sinc}(y) = \sin(y)/y \quad ,$$

it is useful to rewrite Eq.2.17 as

$$f\left(\frac{y}{2\pi X}\right) = 2X \text{sinc}(y) \quad (2.18)$$

If we would measure a strictly monochromatic source with an ideal interferometer, the interferogram would be a pure cosine wave. The cosine transform $f(\nu)$ given in Eq.2.17 may then be interpreted as the spectrum $B'(\nu)$ of the monochromatic source, calculated from the pure cosine interferogram according to Eq.2.15. The shape of $f(\nu)$ is shown in Fig.2.8 (black curve) and shows some large secondary maxima.

According to the Rayleigh criterion, two adjacent spectral lines of equal intensity are considered just resolved when the center of one line is at the same frequency as the first zero value of the instrument line shape $f(\nu)$ of the other line [16]. While two close spectral features of equal intensity can be easily distin-

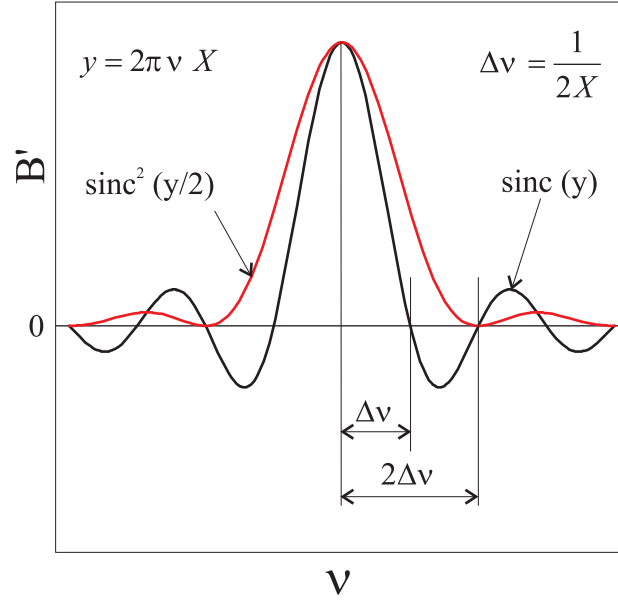


Figure 2.8: The spectrum $B'(\nu)$ of a strictly monochromatic source, computed from the pure cosine interferogram, with boxcar apodization $D(\delta)$ (black curve) and with triangular apodization $A(\delta)$ (red curve).

guished with the instrument line shape generated by the boxcar function (black curve, Fig.2.8), in the case where one line is much stronger than the other, it is difficult to distinguish the weak line from the sidelobes of the stronger line. In this situation it is preferable to have a line shape which does not show these secondary features. This is achieved by a numerical process known as *apodization*.

In the apodization process, the function $D(\delta)$ is replaced by another function $A(\delta)$, which gives more weight to the values of $I(\delta)$ near $\delta = 0$, and tends to zero in the vicinity of $\delta = X$. One example is the triangular apodization function

$$A(\delta) = 2 \cdot \begin{cases} 1 - |\delta/X| & \text{if } -X < \delta < X \\ 0 & \text{if } \delta < -X \text{ or } X < \delta \end{cases}, \quad (2.19)$$

where the factor 2 has been inserted in order to have the *mean* value of $A(\delta)$ over the interval $(-X, X)$ equal to the mean value of the original boxcar function $D(\delta)$. The cosine transform $f_A(\nu)$ of $A(\delta)$ is

$$f_A(\nu) = 2X \left[\frac{\sin(\pi \nu X)}{\pi \nu X} \right]^2 \quad (2.20)$$

or equivalently

$$f_A\left(\frac{y}{2\pi X}\right) = 2X \operatorname{sinc}^2(y/2) \quad . \quad (2.21)$$

The instrument line shape $f_A(\nu)$ generated by $A(\delta)$ is shown in Fig.2.8 (red curve). It may be seen that although the sidelobes are reduced substantially, there is an increase in the width of the line. The effect of apodizing with the triangular apodization function $A(\delta)$ is to reduce the resolution $\Delta\nu$ by a factor of approximately two.

2.2.5 Digitization of the interferogram

In order to preserve all the information from an interferogram unambiguously, it should be sampled at a frequency which is at least twice the maximum audio frequency f_{max} in the interferogram. This is known as the Nyquist criterion. If the sampling frequency is $2F$, all of the frequencies below F will be transferred through the sampling process unambiguously. Frequencies higher than F will appear at frequencies below F . This phenomenon is known as *folding* or *aliasing*. If information at a frequency f_1 slightly greater than F is present, its amplitude will be added to the information at $(2F - f_1)$, giving incorrect intensity data at this frequency. Therefore, all the information (both optical signal and electronic noise) for frequencies greater than F must be severely attenuated. This means that it is necessary to filter out all frequencies in the spectrum which correspond to frequencies in the interferogram greater than F , i.e. we must have $f_{max} < F$.

2.2.6 Measurement of an FT-RAIR spectrum

Reflection-absorption spectroscopy of adsorbed species is a so-called two-channel method, as shown in Fig.2.9. This means that in order to obtain a RAIR spectrum it is necessary to measure two separate (single-channel) spectra, one for the reflecting substrate (denoted $S_0(\nu)$) and one for the substrate with the adsorbed molecules (denoted $S(\nu)$), where ν denotes the wavenumber of the incident light.

The acquisition of a single-channel spectrum begins with the recording of an interferogram. For this purpose, the movable mirror of the interferometer is translated at constant speed, which results in a series of maxima and minima of different intensity at the detector. The exact positioning of the mirror is achieved by means of laser ray passing through the interferometer. The equally

spaced interference maxima of the laser ray along the path of the mirror serve as a precise reference frame, making possible a localization of the mirror within half the wavelength of the laser (633 nm). The position of the mirror and the corresponding detector signal are recorded in the so-called interferogram, which is subsequently stored on the computer. To obtain the single-channel spectrum proper, the interferogram is fourier-transformed in the computer. The result is the single-channel spectrum $S(\nu)$ of the sample.

The single-channel spectrum $S(\nu)$ is a so-called reflection-absorption spectrum of the sample. By means of the reflectivity $R(\nu)$ of the sample, the measured spectrum can be written as

$$S(\nu) = I(\nu) R(\nu) \quad (2.22)$$

where $I(\nu)$ is the intensity of the light beam incident on the sample surface.

The reflectivity of the substrate $R_0(\nu)$ changes to $R(\nu)$ after the adsorption of molecules. Since the molecules absorb energy from the incident light beam, the change of reflectivity

$$\Delta R = R_0 - R$$

is obviously positive, i.e. the reflectivity must diminish upon adsorption. The quantity ΔR is called the *reflectivity change* of the surface due the adsorbed molecules. In order to obtain this quantity from the measured single-channel spectra $S(\nu)$ and $S_0(\nu)$, we form the quotient

$$\frac{S(\nu)}{S_0(\nu)} = \frac{R(\nu)}{R_0(\nu)} \quad (2.23)$$

whereby the factor $I(\nu)$ has the same value for both single-channel spectra and cancels out. By writing Eq.2.23 as

$$\frac{S(\nu)}{S_0(\nu)} = 1 - \frac{\Delta R(\nu)}{R_0(\nu)} \quad (2.24)$$

we see that our spectroscopic measurement provides actually the *relative reflectivity change* spectrum of the substrate due to the adsorbed molecules

$$[\text{Relative Reflectivity Change}] (\nu) = \frac{\Delta R(\nu)}{R_0(\nu)} \quad (2.25)$$

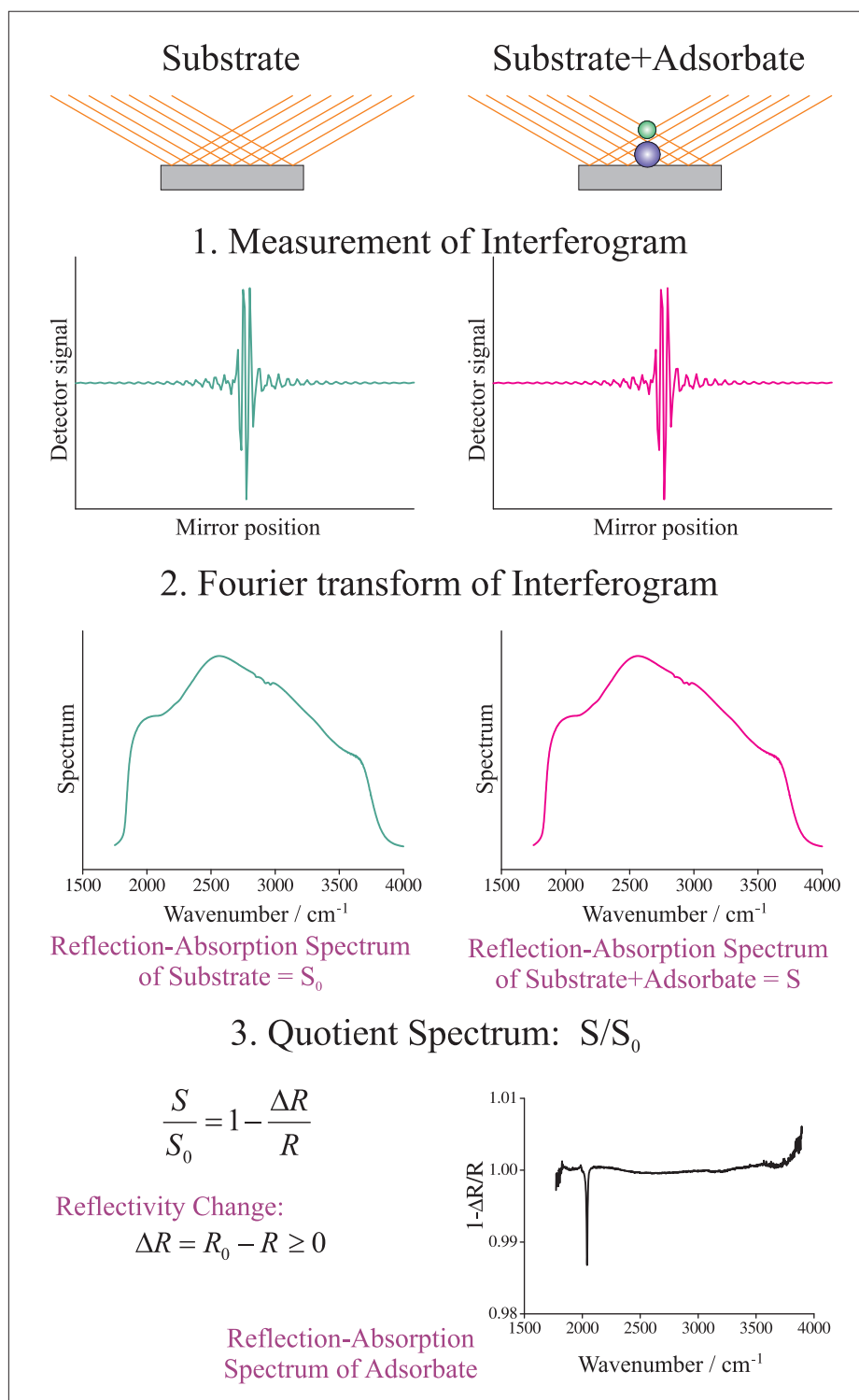


Figure 2.9: Acquisition of the reflection-absorption IR spectrum of an adsorbate.

For the rest of the present thesis, we make the convention to represent the RAIR spectra in the shorthand notation

$$\frac{S}{S_0} = 1 - \frac{\Delta R}{R} \quad . \quad (2.26)$$

2.3 The FTIR spectrometer and the optical setup

The design of the optical setup has been determined by the characteristics of the Bruker IFS 120 HR spectrometer. In order to take advantage of the high throughput of the instrument, we have designed the mirror system such as to keep, from the exit port of the spectrometer, the IR beam at its original section (76 mm) and its divergence as low as possible (see also Chap.2.2).

In order to realize these conditions, we have adopted the design of a spacious chamber for housing the mirror system (Fig.2.10). The mirrors are held on supports fastened to a breadboard on the chamber floor, which permits a precise adjustment. For the IR domain of interest we have chosen Al-coated mirrors. After exiting the FTIR spectrometer, the beam is reflected by plane mirrors onto a concave spherical mirror *b* (diameter 76 mm, focal distance 457 mm) which focuses the beam on the sample *5*. The default angle of incidence at the surface has been set to 9°, but this value can easily be modified by moving the mirrors on the breadboard. The diameter of the beam at the viewport *e* is 10 mm. At the sample position, in the longitudinal direction, the light pencil has approximately the dimensions of the sample (8 mm). After reflection from the sample, the beam leaves the UHV/HP cell through viewport *e*. After reflection at the spherical mirror *c* (identical to *b*) the light bundle is parallel again. The plane mirror *6* is mounted on a motion feedthrough which permits to adjust the optical path, after the rough vacuum (10^{-2} mbar) has been established in the spectrometer chambers³. The plane mirror *6* reflects the parallel beam to the spherical mirror *d*, from where it is focused to the IR detector *8*.

The detector used during the present thesis was an InSb photodiode (Infrared Associates Inc.) cooled by liquid nitrogen. The beamsplitter (*2*) was Si/CaF₂

³Since the vacuum chambers are large, changes in the relative positions of the mirrors during evacuation are inevitable.

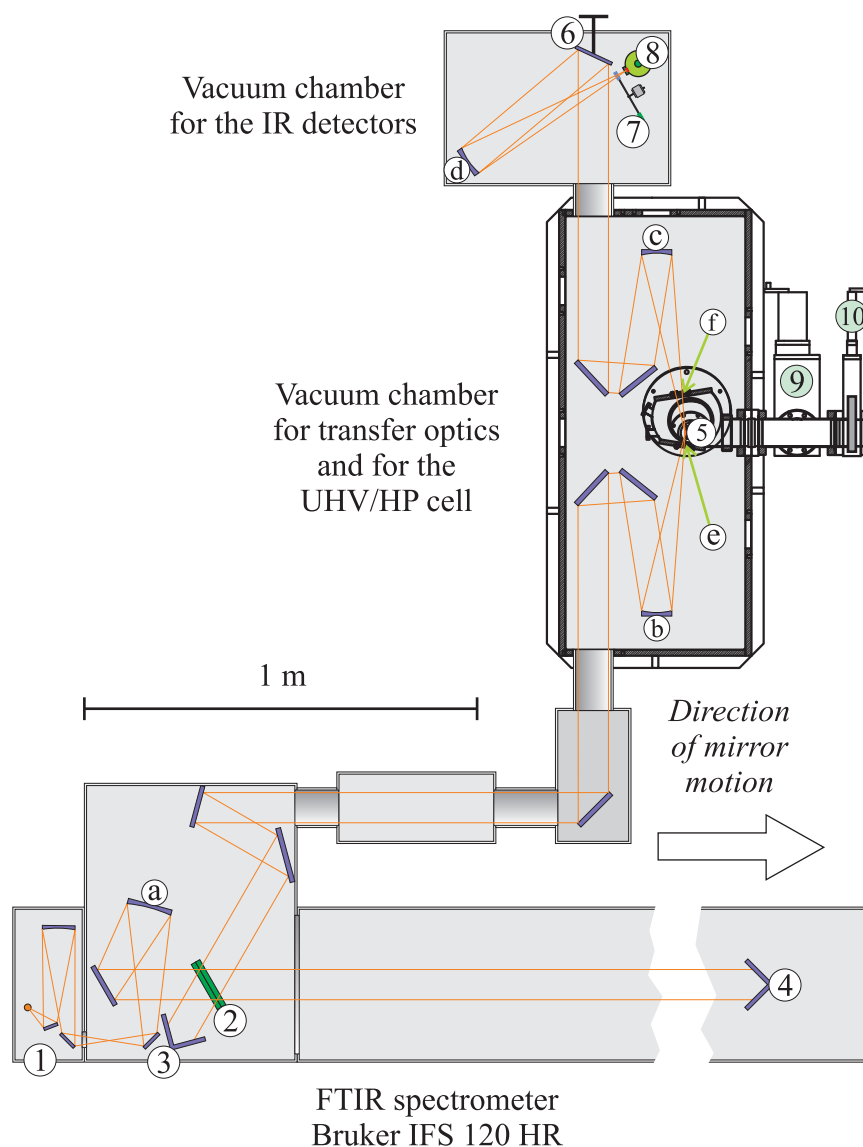


Figure 2.10: The optical system of the FTIR spectrometer Bruker IFS 120 HR and its coupling to the UHV/HP cell. The spherical mirrors are denoted by *a-d*, all other mirrors are plane. The IR-transparent viewports (CaF_2) are denoted by *e* and *f*. Parts of the FTIR spectrometer: 1-source chamber, 2-beamsplitter, 3-fixed cube-corner mirror, 4-movable cube-corner mirror. Parts in the rest of the setup: 5-sample holder (in the UHV/HP cell), 6-plane mirror with motion feedthroughs for adjustment, 7-motorized filter changing, 8-IR detector. Other parts: 9-gate valve, 10-gate valve (to analysis chamber).

(1200-10,000 cm^{-1}), part of the standard accessories of the Bruker IFS 120 HR spectrometer.

2.4 Detection limit of the RAIRS setup

In order to evaluate the sensitivity of our RAIRS setup, we have made a series of test measurements on the CO-Ru(001) adsorption system, well studied in the work of Pfnur *et al.* [24]. The stretch frequency of the C-O bond shifts continuously from 1984 cm^{-1} to 2061 cm^{-1} as a function of increasing CO coverage, which is attributed mainly to dipole-dipole coupling. The frequency versus coverage relation is influenced by the ordering of the CO layer into well defined adsorbate structures, like the $(\sqrt{3} \times \sqrt{3})$ R30° phase at the coverage of 0.33 monolayers (ML). The shape and half-width of the absorption band depend also on the ordering of the CO layer. A linear relationship between coverage and integrated IR absorption intensity exists only below 0.33 ML. At larger CO coverages the absorption intensity falls, with the result that at saturation coverage the absorption per adsorbed molecule is only 35-40% of the absorption at 0.33 ML. This effect is also ascribed to strong lateral interactions in the CO layer [24].

A clean Ru(001) surface was prepared by sputtering the sample for ten minutes with Ar^+ ions (background pressure 1×10^{-5} mbar Ar, acceleration potential 1.5 kV, sample temperature 920 K) followed by a short annealing to 1100 K. The LEED pattern has shown that the resulting Ru(001) surface is clean and smooth. For the IR measurements the sample was transferred from the Analysis Chamber, where the preparation took place, to the UHV/HP cell. In order to desorb eventual contaminants from the residual gas, which could have adsorbed in the minutes following the transfer, the sample was held at 500 K for 30 minutes.

We have prepared a high coverage CO layer by exposing the sample to 1×10^{-8} mbar CO at 283 K. After a total exposure of 30 langmuir⁴ of CO the saturation coverage was reached, characterized by an IR band at 2046 cm^{-1} . This band corresponds to the ordered $(2\sqrt{3} \times 2\sqrt{3})$ R30° phase at a CO coverage of 0.58 ML [24, 25].

⁴The *langmuir* (denoted L) is the unit of exposure of a surface to a gas atmosphere. During an exposure of one langmuir, the surface is hit by a number of molecules equal to the content of one monolayer. It may be shown that exposure of a surface for one second at about 1×10^{-6} mbar corresponds to one langmuir ($1 \text{ L} = 1.33 \times 10^{-6} \text{ mbar} \cdot \text{s}$).

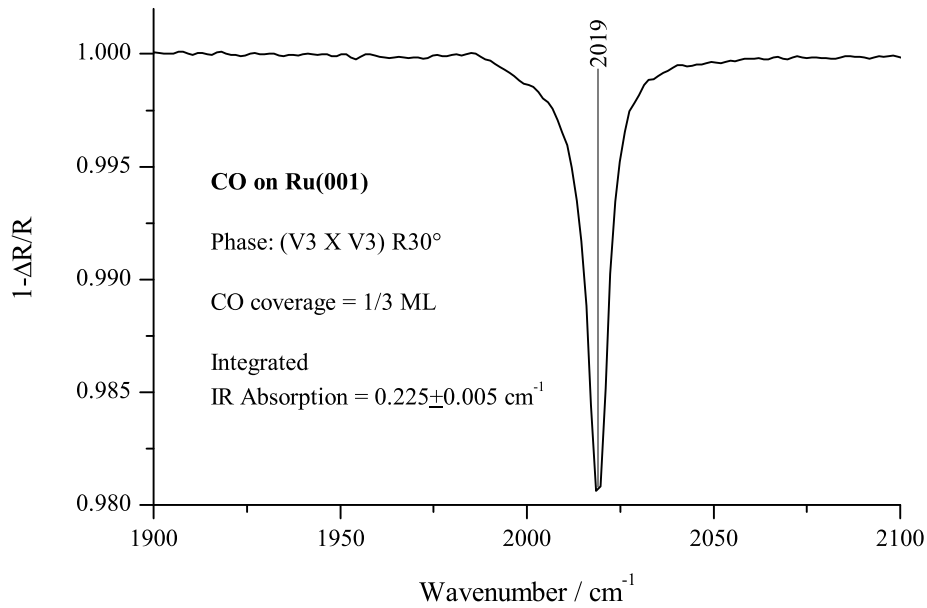


Figure 2.11: RAIR spectrum of the $(\sqrt{3} \times \sqrt{3})\text{-R}30^\circ\text{-CO-Ru(001)}$ phase, with CO coverage of 0.33 ML. The integrated IR absorption of the band can be used for calibrations of the coverage up to 0.3 ML.

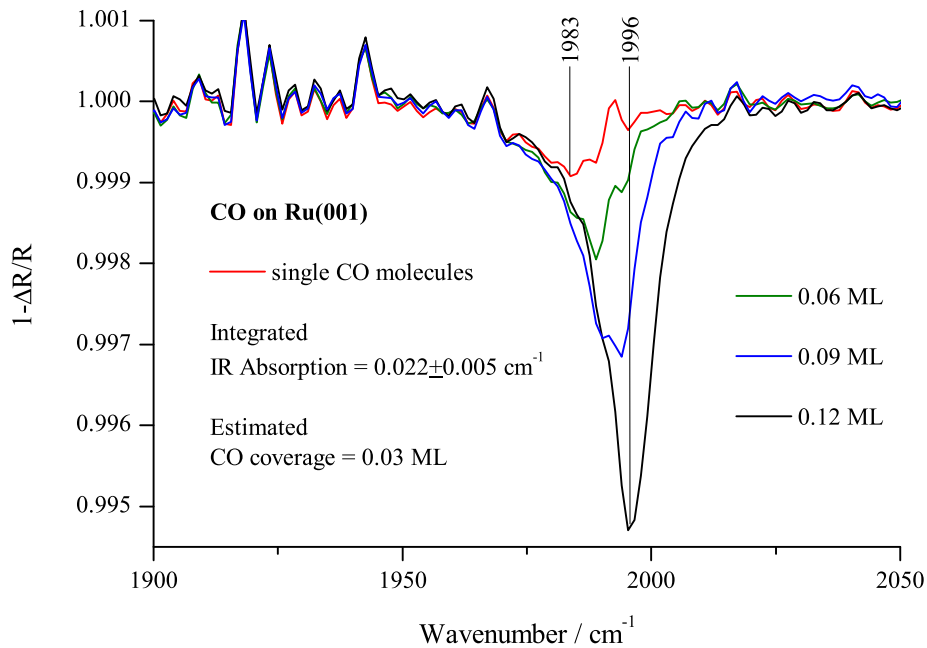


Figure 2.12: RAIR spectra of CO on Ru(001) at low coverage. The coverages have been calibrated against the integrated IR absorption in the $(\sqrt{3} \times \sqrt{3})\text{-R}30^\circ\text{-CO-Ru(001)}$ phase (0.33 ML). CO coverages of 0.12, 0.09, 0.06 and 0.03 ML have been prepared by successively annealing a saturated CO layer to 418 K, 423 K, 428 K and 433 K, respectively.

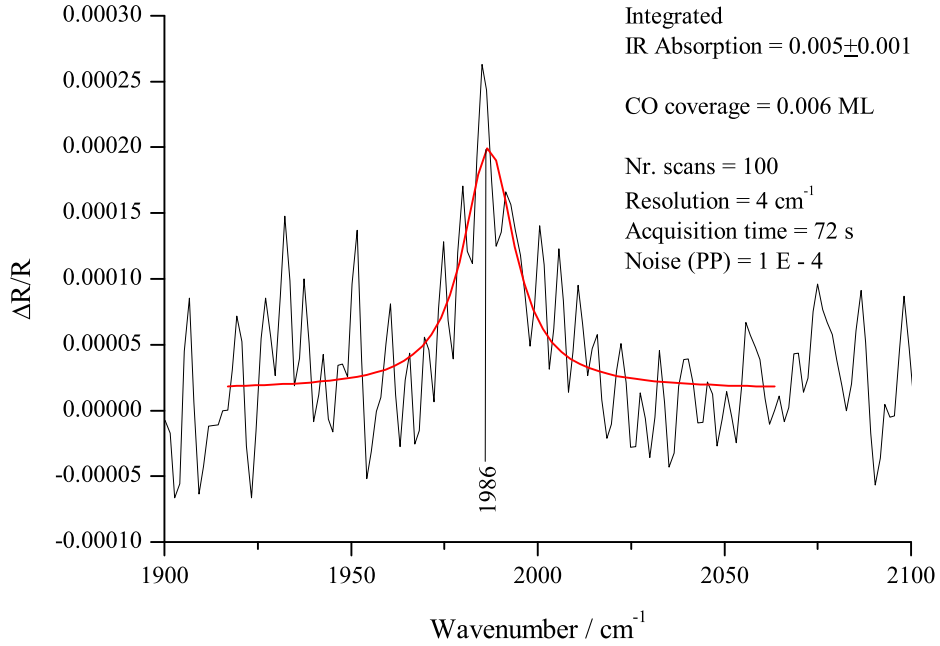


Figure 2.13: RAIR spectra of 0.006 ML CO on Ru(001) obtained after an estimated exposure of 0.03 L CO from the residual gas. The sample temperature was 333 K.

The high coverage CO layer was next annealed by slowly increasing the temperature in 10 K steps followed by recording of the RAIR spectrum. After annealing the sample to 360 K the intensity of the IR band has reached a well noticeable maximum. This intensity maximum is typical of the emergence of the $(\sqrt{3} \times \sqrt{3})\text{R}30^\circ$ phase at 0.33 ML, characterized by a band at 2019 cm^{-1} (Fig.2.11). The integrated IR absorption of this band can be used for calibrations of the coverage, the absorption versus coverage dependence being linear up to about 0.3 ML [24].

In order to test the detection limit of our RAIRS setup, we have prepared low-coverage CO layers by further annealing the sample to progressively increasing temperatures. After successively annealing to 418 K, 423 K, 428 K and 433 K, we have obtained layers with coverages estimated to 0.12, 0.09, 0.06 and 0.03 ML, respectively (Fig.2.12). In the work of Pfnur *et al.* [24] the band position at the lowest measurable coverage (indicated by the authors as 0.003 ML) was 1984 cm^{-1} . In our experiment, the IR band measured at 0.03 ML CO can be well fitted with a lorentzian line centered at $1983\text{-}1984 \text{ cm}^{-1}$. We note that the FWHM of this band (17 cm^{-1}) is very much larger than the typical values at coverages greater than 0.33 ML ($7\text{-}9 \text{ cm}^{-1}$).

We have measured lower CO coverages by observing the adsorption of CO molecules from the residual gas on the clean Ru(001) surface. In the UHV chamber, the residual gas consists mostly of hydrogen and water but CO is also present. During the experiments, the pressure of residual gas in our chamber was 2×10^{-9} mbar. From the mass spectrum measured with the QMS we have estimated the CO content in the residual gas to 6%. Fig.2.13 shows the ratio of two IR spectra measured 300 seconds apart while keeping the sample at 333 K. From the integrated IR absorption of the 1986 cm^{-1} band we infer a coverage of 0.006 ML CO, in reasonable agreement with the estimated CO exposure of 0.03 L.

The spectra presented in the current section have been measured by averaging of 100 scans, at 4 cm^{-1} resolution the average acquisition time being 0.72 seconds/scan. In Fig.2.13 the peak-to-peak (PP) noise is 1×10^{-4} . We note that the 1986 cm^{-1} band is still distinguishable against a noise level as high as half the absorption signal at the band center. We conclude that the detection limit of our RAIRS setup is about 0.5% of a monolayer of CO on Ru(001).

Chapter 3

Vibrations and IR absorption by chemisorbed CO molecules

Considerable understanding of the vibration spectra of adsorbed molecules can be gained from models which treat the adsorbed molecules as coupled oscillating dipoles. In the present chapter we shall present models of coupled oscillators which allow to compute RAIR spectra by taking into account the long range dipole-dipole interactions within the adsorbed layer.

3.1 Macroscopic models of absorption in molecular layers

As a particularly simple approximation to the physical situation of interest, that of a monolayer of molecules adsorbed on a metal surface, we shall next consider the reflection of light at a metal surface covered by a thin but macroscopic, plane parallel absorbing dielectric slab. An adsorbed layer of only one molecule thickness would correspond in this model to the limiting case of a plane parallel dielectric slab of only few Å thickness, a size domain in which attributing the layer a macroscopic dielectric constant is questionable. On the other hand, many important results needed in the course of the present thesis can be derived in this simplified, macroscopic setting.

3.1.1 Fresnel coefficients for the three-layer dielectric system

Let us consider a stratified dielectric system composed of three phases: a vacuum half space (medium 1) separated through a plane parallel absorbing dielectric slab (medium 2) from a metal half space (medium 3). At this stage the absorbing slab is of unspecified macroscopic thickness d .

A monochromatic s -polarized plane wave (the derivation holds unchanged for an p -polarized wave, so that we shall drop the polarization index) incides from the vacuum on the absorbing dielectric slab giving rise to multiple reflections at the dielectric/metal and dielectric/vacuum interfaces. After each dielectric/vacuum reflection a wave is transmitted from the slab into the vacuum, each of these waves contributing coherently to the observed reflected wave. The Fresnel coefficient (B.23) of the reflected wave is therefore a sum of contributions composed of factors for transmission, reflection and wave propagation

$$\begin{aligned} t &= (t_{12} e^{i\beta}) [1 + r_{23} r_{21} e^{2i\beta} + (r_{23} r_{21} e^{2i\beta})^2 + \dots] t_{23} \\ r &= r_{12} + (t_{12} e^{i\beta}) [1 + r_{23} r_{21} e^{2i\beta} + (r_{23} r_{21} e^{2i\beta})^2 + \dots] (r_{23} e^{i\beta}) t_{21} \end{aligned}$$

Here r_{AB} are the Fresnel amplitude coefficients Eqs.B.20-B.23 specified for the respective two phase systems. The complex phase angle represents wave propagation and absorption in the slab between two consecutive reflections

$$\beta = \frac{2\pi d}{\lambda} \sqrt{\epsilon_2 - \sin^2(\varphi)} \quad (3.1)$$

where φ is the angle of incidence of light on the surface, λ is the wavelength of light in vacuum and ϵ_2 is the complex dielectric permittivity of the dielectric slab. By performing the sum and by using the identities $r_{21} + r_{12} = 0$ and $t_{12} t_{21} - r_{12} r_{21} = 1$, the Fresnel coefficients are put under the standard form

$$t = \frac{t_{12} t_{23} e^{i\beta}}{1 + r_{12} r_{23} e^{2i\beta}} \quad r = \frac{r_{12} + r_{23} e^{2i\beta}}{1 + r_{12} r_{23} e^{2i\beta}}. \quad (3.2)$$

The Fresnel coefficients lead, upon insertion into Eqs.B.37 resp.B.39, to the exact expression of the reflectivity $R(d)$ of a metal surface covered by a macroscopic, absorbing dielectric layer of thickness d .

3.1.2 Reflectivity change due to absorbing thin films

We shall consider next the reflectivity of a very thin surface film of thickness d , much less than the wavelength λ of the monochromatic radiation incident on the surface. Following McIntyre and Aspnes [26] we shall see that by making simple linear approximations valid for $d \ll \lambda$, the exact reflectivity $R(d)$ of the three-phase stratified system is reduced to a relatively simple form, directly connected to the physical quantities measurable in an IR surface spectroscopy measurement.

The reflectivity $R(d)$ of the metal surface covered by an absorbing layer of thickness d and the reflectivity $R(0)$ of the bare metal surface are not easily measured separately with accuracy. The errors which affect the separate measurement of the reflectivities cancel out in the ratio $R(d)/R(0)$, a quantity measured in IR reflection spectroscopy with good accuracy and relative ease. According to this observation, we make the convention to express the effects of an adsorbed layer in IR reflection spectroscopy in terms of the so called *reflectivity change* of the substrate

$$\frac{\Delta R}{R} = \frac{R(0) - R(d)}{R(0)} \quad . \quad (3.3)$$

Useful analytic expressions for $R(d)/R(0)$ have to relate the reflectivity change of the metal substrate to the volume of the adsorbed layer, i.e. the reflectivity change should be manifestly proportional to the thickness d of the adsorbed layer. The limiting case of a very thin film ($d/\lambda \ll 1$) puts in evidence the required proportionality.

In the so-called thin film approximation, the complex phase factor $e^{i\beta}$ in the expression Eq.3.2 of the exact Fresnel reflection coefficient is expanded to first order in d/λ (or β)

$$r(d) = \frac{r_{12} + r_{23}(1 + 2i\beta)}{1 + r_{12}r_{23}(1 + 2i\beta)} \quad . \quad (3.4)$$

The limit of zero film thickness

$$r(0) = \frac{r_{12} + r_{23}}{1 + r_{12}r_{23}} \quad (3.5)$$

correctly reproduces the Fresnel r -coefficient of the bare substrate. Expanding to

first order in in the film thickness β we get

$$\frac{r(d)}{r(0)} = 1 + 2i\beta \left[\frac{r_{23}(1 - r_{12}^2)}{(r_{12} + r_{23})(1 + r_{12}r_{23})} \right] . \quad (3.6)$$

The ratio of the reflectivities is

$$\frac{R(d)}{R(0)} = \left| \frac{r(d)}{r(0)} \right|^2 \quad (3.7)$$

which leads to the reflectivity change

$$\frac{\Delta R}{R} = 4 \operatorname{Im} \left(\beta \left[\frac{r_{23}(1 - r_{12}^2)}{(r_{12} + r_{23})(1 + r_{12}r_{23})} \right] \right) . \quad (3.8)$$

Inserting the explicit expressions of r_{12} and r_{23} into the last equation we get the reflectivity formulas of McIntyre and Aspnes

$$\frac{\Delta R_s}{R_s} = -\frac{8\pi d}{\lambda} \cos(\varphi) \operatorname{Im} \left(\frac{\epsilon_2 - \epsilon_3}{1 - \epsilon_3} \right) \quad (3.9)$$

$$\frac{\Delta R_p}{R_p} = -\frac{8\pi d}{\lambda} \cos(\varphi) \operatorname{Im} \left\{ \left(\frac{\epsilon_2 - \epsilon_3}{1 - \epsilon_3} \right) \left[\frac{1 - (1/\epsilon_2 + 1/\epsilon_3) \sin^2(\varphi)}{1 - (1 + 1/\epsilon_3) \sin^2(\varphi)} \right] \right\} , \quad (3.10)$$

for s and p polarizations, respectively. Here ϵ_2 is the complex dielectric function of the adsorbed layer and ϵ_3 is the dielectric function of the metal, the incidence medium (1) being vacuum.

Taking into account that $|\epsilon_3| \gg |\epsilon_2| \sim 1$ in the IR domain, Eq.3.9 shows that the reflectivity change in s -polarized light is negligibly small. For the reflectivity change in p -polarized light Eq.3.10 we get in the same limit the simple expression

$$\frac{\Delta R_p}{R_p} = -\frac{8\pi d}{\lambda} \left(\frac{\sin^2 \varphi}{\cos \varphi} \right) \operatorname{Im} \left(-\frac{1}{\epsilon_2} \right) , \quad (3.11)$$

valid as long as the angle of incidence φ is not extremely flat ($\cos^2(\varphi) < 1/|\epsilon_3|$). A typical example is Pt(111) covered by 0.25 monolayers of CO, in which case $\epsilon_2 = 1 + 2i$ and $\epsilon_3 = -120 + 340i$ at $\lambda^{-1} = 2200 \text{ cm}^{-1}$. For the platinum surface Eq.3.11 holds at incidence angles under 87° , a condition satisfied in most experimental situations [13].

3.1.3 Reflectivity change and the molecular polarizability

The most important shortcoming of Eq.3.11, with reference to monomolecular adsorbed layers, is that it assumes that the layer can be characterized by a macroscopic dielectric constant ϵ_2 . In the case of a layer of CO molecules adsorbed on a metal surface, this assumption is questionable. However, Eq.3.11 is almost universally accepted in the RAIRS literature, being used with success in the interpretation of RAIR spectra for very different systems. We shall further express Eq.3.11 with reference only to microscopic quantities, in a form more useful for the purposes of the present work.

Let us consider a dielectric layer on a metal surface, which is still thin on the scale of the wavelength of the light, in order that Eq.3.11 applies, but is thick on the scale of molecular dimensions. For the bulk material composing this layer we can apply the Clausius-Mosotti relation [27] to connect the macroscopic dielectric constant ϵ_2 of the layer to the polarizability of the individual molecules

$$\frac{\epsilon_2(\omega) - 1}{\epsilon_2(\omega) + 2} = \frac{4\pi}{3} n \alpha(\omega) \quad (3.12)$$

where n is the number of molecules / cm^3 and $\alpha(\omega)$ is the frequency dependent electrical polarizability of a molecule. If the dielectric constant of the layer is not much different from unity ($\epsilon_2 \approx 1$), then Eq.3.12 reduces to

$$\epsilon_2(\omega) = 1 + 4\pi n \alpha(\omega) \quad . \quad (3.13)$$

In the limiting case of a monomolecular dielectric layer, the last equation can be interpreted as [14]

$$\epsilon_2(\omega) = 1 + \frac{4\pi}{d} \left(\frac{N}{A} \right) \alpha(\omega) \quad , \quad (3.14)$$

where N/A is the number of molecules adsorbed per cm^2 and the parameter d would correspond to the thickness of the monomolecular adsorbate. Fortunately, the ill-defined parameter d cancels out upon insertion of Eq.3.14 into the reflectivity change formula Eq.3.11. The reflectivity change can therefore be expressed in the final form [13, 14]

$$\left(\frac{\Delta R}{R} \right) (\omega) = -\frac{16\pi}{c} \left(\frac{N}{A} \right) \left(\frac{\sin^2 \varphi}{\cos \varphi} \right) \omega \text{Im} \alpha(\omega) \quad , \quad (3.15)$$

where c is the speed of light in vacuum, N is the number of molecules adsorbed over a surface area A of the metal surface, φ is the angle of incidence of the light beam relatively to the surface normal and $\alpha(\omega)$ is the total electrical polarizability of a molecule in the layer. Eq.3.15 is customarily applied in the literature for the interpretation of the RAIR spectra of a large variety of adsorbates. In the present work, it will form the starting point for the simulation of RAIR spectra of CO molecules adsorbed on the RuO₂(110) surface.

3.2 Single diatomic adsorbate

3.2.1 Shift of the C-O stretch frequency upon chemisorption

When a CO molecule adsorbs on a metal surface, the force constant of the C-O bond is diminished relatively to its gas-phase value. Thus, the CO stretch frequency is 2143 cm⁻¹ in the gas phase but it shifts to 1984 cm⁻¹ upon chemisorption on the Ru(001) surface [24]. Several factors determine the frequency shift of a single adsorbed CO molecule from its gas phase value: i) mechanical renormalization due to the formation of the Ru-CO bond, ii) interaction of the vibrating molecular dipole with its image in the metal, iii) chemical effects, such as back-donation, which change the C-O bond strength upon chemisorption [13, 28].

Mechanical renormalization

Within a purely mechanistic picture, we can treat the bond of the CO molecule to the rigid Ru substrate as an elastic spring of force constant k_{RuC} . If we suppose that the internal force constant of the C-O bond is not influenced by the adsorption of the CO molecule, we get two vibration eigenfrequencies for this Ru-C-O 'molecule' [28]. One of the eigenfrequencies corresponds to the Ru-CO vibration, where the CO molecule is regarded as a rigid body, the other frequency corresponds to the internal C-O vibration, when the center of mass of the CO molecule is considered fixed. This second frequency, denoted as ω_s , is blue shifted relatively to the gas phase frequency ω_g

$$\left(\frac{\omega_s}{\omega_g}\right) \approx 1 + \frac{k_{\text{RuC}}}{k_{\text{CO}}} \frac{\mu^2}{M_{\text{C}}^2} \quad , \quad (3.16)$$

where μ is the reduced mass of the CO molecule and M_C is the mass of the carbon atom. By taking physically plausible values for the force constants k_{RuC} and k_{CO} , Bradshaw and Schweizer [28] have obtained, for CO adsorbed on transition metals, typical shifts of about $+50 \text{ cm}^{-1}$ to higher frequencies.

Self-image effect

Due to the screening of electric fields in a metal by the conduction electrons, the dipole moment of the adsorbed molecule will induce an electrostatic image dipole in the metal. The interaction of the adsorbate dipole with its electrostatic image leads, in case of a perfectly conductive substrate, to a red shift of the C-O internal stretch frequency

$$\left(\frac{\omega_s}{\omega_g}\right) = 1 - \frac{\alpha_V(0)}{4z^3 - \alpha_e} \quad , \quad (3.17)$$

where z denotes the distance from the CO molecular dipole to its electrostatic image, $\alpha_V(\omega)$ is the vibrational polarizability and α_e is the electronic polarizability of the CO molecule (see also the next section). Bradshaw and Schweizer [28] have shown that, for CO adsorbed on transition metals, the self-image effect leads to a shift of about -50 cm^{-1} to lower frequencies. Thus, the blue shift induced by mechanical renormalization is more or less compensated by the red shift due to the self-image effect.

Chemical shift. The Blyholder model

The weakening of the C-O internal bond in the chemisorbed CO molecule has been traditionally explained within the backbonding model proposed by Blyholder [29]. This model assumes that the chemical bond between CO and the metal (Ru) is formed by charge transfer from the 5σ molecular orbital (MO) of CO into the metal and by 'backdonation' of electrons from the metal d -bands into the unoccupied $2\pi^*$ MO of CO, as shown in Fig.3.1. Since the 5σ MO is only weakly bonding, but the $2\pi^*$ strongly antibonding, the C-O internal bond is weakened by the formation of the C-Ru chemisorption bond. The amount of backdonation into the $2\pi^*$ MO is reflected by a lowering of the C-O stretching frequency [13].

Further support for the strong influence of backdonation on the CO stretch frequency is provided experimentally by coadsorption experiments. If CO is

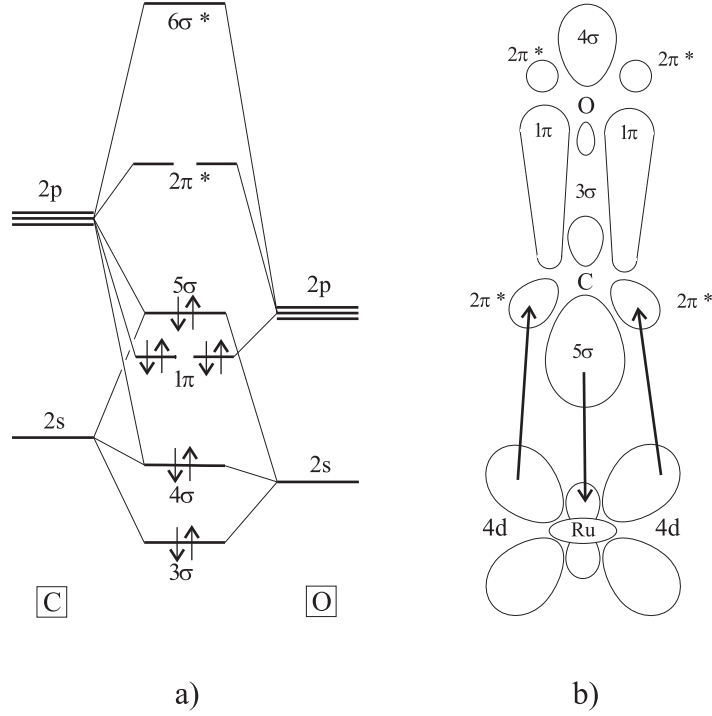


Figure 3.1: Chemisorption of CO on Ru. a) Schematic molecular orbital diagram for CO [31], b) Schematic representation of the Blyholder model (after Ref. [13]).

coadsorbed with strong 'electron donors' such as hydrocarbons, shifts to lower frequencies of up to -100 cm^{-1} are observed [30], a fact which is consistent with an increased backdonation to the CO molecule as charge from the co-adsorbate is transferred to the metal. On the other hand, coadsorption of 'electron acceptors', such as oxygen, reduces backdonation to the CO molecule and hence cause a shift to higher frequencies. Later in this work we shall have the opportunity to apply these important observations in the interpretation of the IR spectra of CO adsorbed on the ruthenium dioxide surface.

3.2.2 Force constants of a chemisorbed CO molecule

The potential energy of a gas-phase diatomic molecule like CO is accurately approximated by the Morse potential

$$v(r) = D_{CO} \left[1 - \exp \left(-\frac{r - r_{CO}^0}{\alpha_{CO}} \right) \right]^2 \quad (3.18)$$

where D_{CO} is the dissociation energy of the CO molecule, r_{CO}^0 is the equilibrium distance between the nuclei and α_{CO} is a parameter related to the force constant

$$k_{CO}^{gas} = \frac{2D_{CO}}{\alpha_{CO}^2} \quad (3.19)$$

of internal stretching in the gas-phase CO molecule. The Morse potential accounts for the ground state energy of the electronic system in the coulombian field of the nuclei as well as for the coulombian repulsion between the nuclei. To take advantage of the simplicity of the Morse potential description of molecular energies and to extend its applicability to the case of atomic and molecular chemisorption, the so called *bond order conserved* Morse potential (BOC-MP) framework was proposed by Shustorovich [32].

For definiteness let us consider, according to the main ideas of this method, the case of CO chemisorption onto Ru(001). Chemisorbed CO can in principle take on Ru(001) an adsorption site of single (on-top one of the Ru atoms), double (bridging two neighboring Ru atoms) or triple (hollow site) coordination. To get the potential energy of the chemisorbed molecule, we have to add to the Morse potential describing the C-O bond of the gas phase molecule one new Morse potential for each of the m ($m = 1, 2, 3$) C-Ru chemisorption bonds

$$U_m(X_C, Z_{CO}) = mQ(1 - X_C)^2 + D_{CO}(1 - Z_{CO})^2 \quad (3.20)$$

where Q is the dissociation energy of the C-Ru bond and D_{CO} is the gas phase dissociation energy of the CO molecule. The molecular coordinates

$$X_C = \exp\left(-\frac{x - x_0}{\alpha_{C-Ru}}\right) \quad Z_{CO} = \exp\left(-\frac{r - r_0}{\alpha_{CO}}\right)$$

where x is the actual C-Ru bond length and x_0 is the equilibrium length of a C-Ru bond, are referred to as *bond orders* of the respective bonds, by analogy with the Pauling rule on the relationship between bond order n and bond length R in metallic systems

$$R(n) = R(1) - 0.300 \ln(n).$$

After the postulate of a Morse-type analytic form of the chemisorption potential, the second postulate of the BOC-MP framework is the principle of bond order conservation (BOC) which, for this special case, states that the bond order of the

chemisorbed CO molecule equals the bond order of the gas phase CO molecule

$$m X_C + Z_{CO} = 1 \quad (3.21)$$

where the bond order of the gas phase CO molecule is unity (the nuclei are localized at the equilibrium distance r_0). Use of the BOC principle with the adsorbate Morse potential Eq.3.20 leads to

$$U_m(X_C, Z_{CO}) = \frac{1}{m} Q((m-1) + Z_{CO})^2 + D_{CO}(1 - Z_{CO})^2. \quad (3.22)$$

Minimization of the potential Eq.3.22 and use of the bond order conservation constraint lead to the constrained minima of the Morse potential Eq.3.20 of the chemisorbed CO molecule

$$X_C^1 = \frac{Q}{mD_{CO} + Q} \quad Z_{CO}^1 = \frac{m(D_{CO} - Q) + Q}{mD_{CO} + Q} \quad , \quad (3.23)$$

which constitute the bond orders of the C-O and C-Ru bonds after chemisorption.

The stretch frequency of the chemisorbed CO molecule is evaluated [33] directly from the expression of the potential energy Eq.3.22 by expansion of the C-O bond length coordinate r around the equilibrium value corresponding to Z_{CO}^1 (Eq.3.23)

$$U_m(r) = \text{const.} + \left(D_{CO} + \frac{Q}{m} \right) \left(\frac{Z_{CO}^1}{\alpha_{CO}} \right)^2 (r - r_1)^2$$

which by reference to Eq.3.19 may be written

$$U_m(r) = \text{const.} + \frac{1}{2} k_{CO}^{gas} \left(1 + \frac{Q}{mD_{CO}} \right) (Z_{CO}^1)^2 (r - r_1)^2$$

to obtain the expression of the C-O bond force constant k_{CO}^{ad} in the chemisorbed CO molecule

$$k_{CO}^{ad}(m) = k_{CO}^{gas} \left(1 + \frac{Q}{mD_{CO}} \right) (Z_{CO}^1)^2 \quad . \quad (3.24)$$

By use of Eq.3.23 the force constant k_{CO}^{ad} can be expressed as a function of the gas phase dissociation energy of the CO molecule D_{CO}^{gas} and the heat of adsorption Q of the CO molecule

$$k_{CO}^{ad}(m) = k_{CO}^{gas} \frac{1}{mD_{CO}} \frac{(m(D_{CO} - Q) + Q)^2}{mD_{CO} + Q} \quad . \quad (3.25)$$

The stretch frequency of the chemisorbed CO molecule coordinated to m Ru atoms results directly from the expression of k_{CO}^{ad}

$$\nu_{CO}^{ad}(m) = \nu_{CO}^{gas} \left[\frac{1}{mD_{CO}} \frac{(m(D_{CO} - Q) + Q)^2}{mD_{CO} + Q} \right]^{1/2}. \quad (3.26)$$

Using the standard parameters [34]

$$\begin{aligned} \nu_{CO}^{gas} &= 2143 \text{ cm}^{-1} \\ D_{CO} &= 9.8 \text{ eV} \\ Q &= 1.7 \text{ eV} \quad , \end{aligned}$$

from Eq.3.26 we find 1978 cm^{-1} and 1877 cm^{-1} for the stretch frequencies of a CO molecule in the on-top and the bridge positions on the Ru(001) surface, in agreement with the respective experimental values 1983 cm^{-1} and 1867 cm^{-1} .

We close this brief discussion of the force constants by mentioning that, for a large number of diatomic molecules, useful empirical relations between the force constants and other parameters, like the dissociation energy or the bond order, have been proposed and verified in the literature. For a comprehensive review of these results the reader is referred to the book by Ibach [35], Chap. 6.3.2.

3.2.3 Dynamics of a single chemisorbed CO molecule

We start by considering the dynamics of a single CO molecule, first in free space and subsequently in a chemisorbed state. The Lagrange function of the molecule in free space is

$$\mathcal{L}_{free} = \frac{M_O}{2} \dot{\mathbf{r}}_O^2 + \frac{M_C}{2} \dot{\mathbf{r}}_C^2 - U(|\mathbf{r}_O - \mathbf{r}_C|) \quad (3.27)$$

where U is the interaction potential of the C and O atoms. In the free molecule the rotation and vibration degrees of freedom are decoupled from the translation of the molecule by a transformation to the center of mass and relative coordinates, respectively

$$\begin{aligned} \mathbf{R} &= \frac{M_O \mathbf{r}_O + M_C \mathbf{r}_C}{M_O + M_C} \\ \boldsymbol{\rho} &= \mathbf{r}_O - \mathbf{r}_C \end{aligned} \quad (3.28)$$

by which the Lagrange function reads

$$\mathcal{L}_{free} = \frac{M}{2} \dot{\mathbf{R}}^2 + \frac{\mu}{2} \dot{\boldsymbol{\rho}}^2 - U(|\boldsymbol{\rho}|) \quad (3.29)$$

showing explicitly the separation of rotation and vibration from the translation movement of the molecule as a whole. Here $M = M_O + M_C$ is the total mass of the CO molecule and μ is its reduced mass, defined as

$$\mu = \frac{M_O M_C}{M_O + M_C} \quad .$$

If the molecule does not dissociate upon chemisorption then both atoms will continue to interact with each other and additionally, with the substrate. We shall neglect the vibrations of the substrate and consider it totally rigid. As explained in Chap.3.3.1, this proves to be a gross approximation in general, but it turns out to be sufficient for the treatment of the high frequency adsorbate modes, like the C-O stretching. The atom-substrate interaction can be modeled by selecting suitable interaction potentials, for example of the Morse type. Let the molecule adsorb upright, connecting to the substrate through the C atom. We shall consider only the movements of the two atoms along the surface normal. In the natural coordinates z_O and z_C representing the distance of the O and C atoms to the substrate respectively, the Lagrange function of the adsorbed molecule is

$$\mathcal{L}_{ads} = \frac{M_O}{2} \dot{z}_O^2 + \frac{M_C}{2} \dot{z}_C^2 - U(|z_O - z_C|) - v_O(z_O) - v_C(z_C) \quad (3.30)$$

where U is the free-space intramolecular potential and the subscripts on the atom-substrate interaction potential v show that these can be different for each of the atoms. The Lagrange function of the chemisorbed molecule reads, in the relative and center of mass coordinates defined according to Eq.3.28

$$\mathcal{L}_{ads} = \frac{M}{2} \dot{R}^2 + \frac{\mu}{2} \dot{\rho}^2 - U(\rho) - v_O(R - \frac{M_C}{M} \rho) - v_C(R + \frac{M_O}{M} \rho) \quad , \quad (3.31)$$

showing that the atom-substrate potentials couple the internal vibration coordinate ρ to the translation coordinate R . Performing a Taylor expansion to second order about the equilibrium position, we can arrange the result to obtain

$$\mathcal{L}_{ads} = \frac{M}{2} (\dot{r}^2 - \Omega_r^2 r^2) + \frac{\mu}{2} (\dot{u}^2 - \Omega_u^2 u^2) + \sqrt{M\mu} G r u \quad (3.32)$$

where r and u denote the small displacements of the center of mass R and of the C-O separation ρ from their respective equilibrium positions, and G is a coupling constant determined by the explicit analytic form of the potentials v_O and v_C .

The Lagrange function of Eq.3.32 represents a pair of coupled oscillators. Neglecting the coupling term we get the following picture of the two oscillator modes: coordinate r represents a rigid molecule (no internal vibration) oscillating against the substrate while coordinate u represents a molecule having a fixed center of mass and showing only an internal oscillation. A shortcoming of this rather intuitive picture is that the neglect of the coupling term precludes the excitation of the molecule-substrate vibration by an external electric field. On the other hand, it follows from the derivation that the oscillator frequencies Ω_r and Ω_u and the strength of the mode coupling G are functions of the parameters entering the model potentials v_O , v_C and U and accordingly are not independent. In particular, neglecting the coupling term may not always be consistent with the model Eq.3.30.

We shall next use standard methods of molecular vibration analysis to decouple the internal stretching mode u from the adsorbate-substrate vibration mode r . First we rescale the coordinates to formally represent harmonic oscillators of the same mass. Replacing r through

$$v = r \sqrt{\frac{M}{\mu}} \quad (3.33)$$

we can rewrite Eq.3.30 to represent a pair of coupled oscillators of mass μ

$$\mathcal{L}_{ads} = \frac{\mu}{2}(\dot{u}^2 + \dot{v}^2) - \frac{\mu}{2}(\Omega_u^2 u^2 + \Omega_r^2 v^2 - 2G uv). \quad (3.34)$$

Writing the last equation in the 'rotated' frame

$$u' = \cos(\varphi) u - \sin(\varphi) v \quad (3.35)$$

$$v' = \sin(\varphi) u + \cos(\varphi) v \quad (3.36)$$

the coupling term will vanish if the rotation parameter φ is set

$$\varphi = \frac{1}{2} \arctan \left(\frac{2G}{\Omega_u^2 - \Omega_r^2} \right). \quad (3.37)$$

The Lagrange function of Eq.3.34 is reduced to a pair of independent oscillators

$$\mathcal{L}_{ads} = \frac{\mu}{2}(\dot{u}'^2 - \Omega_u'^2 u'^2) + \frac{\mu}{2}(\dot{v}'^2 - \Omega_r'^2 v'^2) \quad (3.38)$$

whose eigenfrequencies Ω_u' and Ω_r' lie above Ω_u and below Ω_r respectively.

Let us next turn to the case of the CO molecule in a time-dependent external electric field. In the gas phase, the molecule couples the electric field *via* its electric dipole moment

$$V_{ext} = -q_0 (\mathbf{r}_C - \mathbf{r}_O) \cdot \mathbf{E}(t) \quad (3.39)$$

where q_0 is the absolute value of the electric charge on the C and O atoms in the gas phase CO molecule. We assume a similar interaction potential for the chemisorbed molecule

$$V_{ext} = -q_{ad} (z_C - z_O) E_z(t) = q_{ad} (\rho_0 + u(t)) E_z(t) \quad (3.40)$$

where q_{ad} is the electric charge on the atoms C and O in the chemisorbed state, ρ_0 and $u(t)$ are the equilibrium distance between the C and the O atoms and its oscillation respectively, and E_z is the surface-normal component of the local electric field at the molecule. Tangential components of the electric field vanish at the surface because of the electrical conductivity of the metallic substrate. The term due to the static dipole moment $q_{ad} \rho_0$ of the chemisorbed molecule merely shifts the equilibrium position of the atoms and is otherwise not dynamically relevant. Recalling that the internal coordinate u is a linear combination of the normal coordinates u' and v' we write the Lagrange function of the chemisorbed molecule Eq.3.38 as the sum of two independent harmonic oscillators, separately driven by the external field $E_z(t)$

$$\mathcal{L}_{ads}^{ext} = \frac{\mu}{2}(\dot{u}'^2 - \Omega_u'^2 u'^2) - q_u^* u' E_z(t) + \frac{\mu}{2}(\dot{v}'^2 - \Omega_r'^2 v'^2) - q_r^* v' E_z(t) \quad (3.41)$$

where the effective dipole charges of the normal modes are

$$\begin{aligned} q_u^* &= q_{ad} \cos(\varphi) \\ q_r^* &= q_{ad} \sin(\varphi) \end{aligned} \quad (3.42)$$

We note in particular that the mode v' , which can be seen as a perturbation of the rigid molecule to substrate vibration r , acquires an effective dipole charge as a result of its coupling to the internal vibration u . The equations of motion of the adsorbate are the Euler-Lagrange equations derived from Eq.3.41

$$\ddot{u}' + \Gamma_u \dot{u}' + \Omega_u'^2 u' = -\frac{q_u^*}{\mu} E_z(t) \quad (3.43)$$

$$\ddot{v}' + \Gamma_r \dot{v}' + \Omega_r'^2 v' = -\frac{q_r^*}{\mu} E_z(t) \quad (3.44)$$

At this point the damping coefficients Γ were introduced, to account for the energy loss of the vibrating molecule to the substrate by coupling its continuous-spectrum excitations (phonons) or by excitation of electron-hole pairs. The damping coefficients are connected to the measured width of the IR absorption line.

With the external field representing a monochromatic wave of frequency ω

$$E_z(t) = E_z(\omega) \exp(-i\omega t) \quad ,$$

the normal modes of the adsorbate are harmonic oscillations of the same frequency

$$u'(t) = \hat{u}'(\omega) \exp(-i\omega t) \quad (3.45)$$

$$v'(t) = \hat{v}'(\omega) \exp(-i\omega t) \quad (3.46)$$

where the complex amplitudes \hat{u}' and \hat{v}' satisfy Eqs.3.43 and 3.44, now written

$$(-\omega^2 - i\omega\Gamma_u + \Omega_u'^2) \hat{u}'(\omega) = -\frac{q_u^*}{\mu} E_z(\omega) \quad (3.47)$$

$$(-\omega^2 - i\omega\Gamma_r + \Omega_r'^2) \hat{v}'(\omega) = -\frac{q_r^*}{\mu} E_z(\omega) \quad (3.48)$$

By inserting the solutions \hat{u}' and \hat{v}' into the definition of the dipole moment of the adsorbed molecule

$$\hat{p}(\omega) = -q_{ad} \hat{u}(\omega) = -q_u^* \hat{u}'(\omega) - q_r^* \hat{v}'(\omega) = \alpha(\omega) E_z(\omega)$$

we obtain the polarizability of the single chemisorbed molecule

$$\alpha(\omega) = \frac{q_u^{*2}/\mu}{\Omega_u'^2 - \omega^2 - i\omega\Gamma_u} + \frac{q_r^{*2}/\mu}{\Omega_r'^2 - \omega^2 - i\omega\Gamma_r} \quad . \quad (3.49)$$

We conclude the discussion of the single adsorbate by rewriting, for further reference, the polarizability α of Eq.3.49 as a function of the 'natural' parameters of Eq.3.32

$$\alpha(\omega) = \frac{q_{ad}^2}{\mu} \frac{\Omega_r^2 - \omega^2 - i\omega\Gamma_r}{(\Omega_r^2 - \omega^2 - i\omega\Gamma_r)(\Omega_u^2 - \omega^2 - i\omega\Gamma_u) - G^2} \quad (3.50)$$

3.3 Dynamics of an adsorbed CO layer

3.3.1 Coupling between adsorbates

We consider a CO layer chemisorbed on the surface of a metal, a large but finite cluster. Since there is essentially no difference between the nuclei of the chemisorbed molecules and those of the metal substrate, we shall treat them on an equal footing. The system we are going to study consists therefore of only two components: all the nuclei on one side and the electrons on the other. Central to our discussion is the assumption that the adiabatic approximation is valid, i.e. that the wave function of the complete system may be approximated as the product of a nuclear wave function and an electronic wave function. The electronic wave function accounts for the movement of the electrons in the coulombian field of the immobile nuclei. The nuclear wave function describes the vibrations of the nuclei around their equilibrium positions with the potential energy

$$U(\mathbf{R}) = \sum_{i < j} \frac{Z_i Z_j}{|\mathbf{R}_i - \mathbf{R}_j|} + \mathcal{E}_{el}(\mathbf{R}) \quad (3.51)$$

where the total energy of the electrons \mathcal{E}_{el} appears as an additional coupling between the nuclei. In the harmonic approximation, the smooth potential energy function $U(\mathbf{R})$ is expanded in a Taylor series around the equilibrium position of the nuclei \mathbf{R}_0 , which is a minimum

$$U(\mathbf{R}) = U(\mathbf{R}_0) + \frac{1}{2} \sum_{ij} \sum_{\alpha\beta} K_{ij}^{\alpha\beta}(\mathbf{R}_0) (R_i^\alpha - R_{0i}^\alpha)(R_j^\beta - R_{0j}^\beta)$$

where the indices α, β refer to the cartesian components of the respective quantities. At this point, by distinguishing between the nuclear coordinates \mathbf{r} of the adsorbate molecules and those of the lattice nuclei \mathbf{R} proper, the potential energy

splits into three distinct contributions

$$U(\mathbf{r}, \mathbf{R}) = U_{ads}(\mathbf{r}) + U_{phonon}(\mathbf{R}) + U_{ads-phonon}(\mathbf{r}, \mathbf{R})$$

representing the potential energy of the CO vibrations in the adsorbed layer, the potential energy of the harmonic lattice vibrations (phonons) and the coupling between adsorbate vibrations and phonons, respectively. Writing the Lagrange function for the adsorbates-and-lattice system

$$\mathcal{L} = \frac{1}{2} \sum_i M_i \dot{\mathbf{r}}_i^2 + \frac{1}{2} \sum_A M_A \dot{\mathbf{R}}_A^2 - U(\mathbf{r}, \mathbf{R})$$

the equations of motion for both $(\mathbf{r} - \mathbf{r}_0)$ and $(\mathbf{R} - \mathbf{R}_0)$ can be set up. If we consider that all lattice vibrations are excited by the motions of the externally perturbed adsorbate, then it follows that they are connected to the adsorbate vibrations through a causal linear relationship

$$[\mathbf{R}_A(t) - \mathbf{R}_{0A}] = \int_0^t \sum_i G_{Ai}(t - t') [\mathbf{r}_i(t') - \mathbf{r}_{0i}] dt'$$

where G is the Green function¹ of the harmonic lattice vibrations. The last expression leads, upon insertion into the adsorbate equations of motion, to a closed set of equations which contain only the adsorbate coordinates $(\mathbf{r} - \mathbf{r}_0)$ [35]. Equally well, we may insert the expression for $(\mathbf{R} - \mathbf{R}_0)$ into the Lagrange function of the complete adsorbate-and-lattice system to obtain an *effective* Lagrange function, which depends explicitly only on the adsorbate coordinates $(\mathbf{r} - \mathbf{r}_0)$ but nevertheless includes effects due to the lattice vibrations.

Since in the present work we are not going to explicitly consider lattice vibrations (phonons) or their coupling to adsorbate vibrations, without loss of generality we shall formally drop the phonon contributions to the potential energy. At the same time we note that, whenever an expression for the potential energy shall be written, involving the adsorbate degrees of freedom alone, this is to be understood as an approximation to the *effective* quantities, defined by including the lattice degrees of freedom as described above. The parameters appearing in the potential energy of the adsorbate are therefore to be considered effective in

¹The Green function G_{Ai} describes the propagation of the movement of the adsorbate nucleus at \mathbf{r}_i through the lattice to the nucleus located at \mathbf{R}_A .

the sense that they already include effects due to the lattice vibrations. These effects may influence² the low-frequency modes of an atomic or molecular adsorbate, like the O-substrate (550 cm^{-1}) or the CO-substrate vibration (320 cm^{-1}) on $\text{RuO}_2(110)$. On the other hand, the frequencies of internal modes like the C-O stretching ($1850\text{-}2150 \text{ cm}^{-1}$) are much higher than the Debye frequency of the metal (410 cm^{-1} for Ru) and consequently lattice vibrations may be considered as completely decoupled in this case.

The foregoing discussion shows that, in the harmonic approximation, it is possible to express the potential energy of the adsorbate nuclei in a closed form without reference to the lattice degrees of freedom

$$U_{ads}(\mathbf{r}) = \frac{1}{2} \sum_{ij} \sum_{\alpha\beta} k_{ij}^{\alpha\beta}(\mathbf{r}_0) (r_i^\alpha - r_{0i}^\alpha) (r_j^\beta - r_{0j}^\beta) \quad (3.52)$$

where the coefficients k are the effective force constants. We note that the effective force constants are frequency dependent since they include the vibrational response of the lattice to adsorbate excitations³. In the spirit of this remark, experimental values of the force constants have to be compared to theoretical values calculated on the relaxed lattice [36].

We continue our discussion with the special assumption [35] that Eq.3.52 may be obtained as the harmonic approximation to a potential built up entirely of pairwise contributions

$$\sum_{i < j} \varphi_{ij}(\mathbf{r}_i, \mathbf{r}_j) \quad . \quad (3.53)$$

Since with immobile lattice atoms (as reflected by the incorporation of their degrees of freedom in the effective force constants) the center of mass of an adsorbed CO molecule is a constant during molecular vibration, we shall pass from the original coordinates $\mathbf{r}_a^{(C)}, \mathbf{r}_a^{(O)}$ of the nuclei in molecule number a to the center of mass coordinates

$$\left. \begin{aligned} \mathbf{x}_a &= (\mu/M_O) \mathbf{r}_a^{(C)} + (\mu/M_C) \mathbf{r}_a^{(O)} \\ \mathbf{u}_a &= \mathbf{r}_a^{(O)} - \mathbf{r}_a^{(C)} \end{aligned} \right\} \quad \text{where} \quad \mu = \frac{M_C M_O}{M_C + M_O}$$

²The frequency of O vibrations above a hollow site on Ni(111) is computed 514 cm^{-1} when the underlying Ni atoms are rigidly held in place. When the Ni atoms are allowed to move as the oxygen vibration is being excited, an upward frequency shift of 64 cm^{-1} results, in agreement with the experimental frequency of 580 cm^{-1} . The Debye frequency of Ni is 395 cm^{-1} [35].

³For a detailed treatment please consult the book by Ibach [35], pp.146-151.

is the reduced mass of the CO molecule. In the new coordinates we have

$$\left. \begin{aligned} \mathbf{r}_a^{(C)} &= \mathbf{x}_a - (\mu/M_C) \mathbf{u}_a \\ \mathbf{r}_a^{(O)} &= \mathbf{x}_a + (\mu/M_O) \mathbf{u}_a \end{aligned} \right\} .$$

Considering the pairwise character of the interaction Eq.3.53, the analytical form of the potential Eq.3.52 reduces to

$$\begin{aligned} U_{ads}(\mathbf{u}, \mathbf{x}) &= \frac{1}{2} \sum_a \left(\sum_{\alpha\beta} k_{CO}^{\alpha\beta}(\mathbf{x}_a) u_a^\alpha u_a^\beta \right) \\ &\quad + \sum_{a<b} \left(\sum_{\alpha\beta} V^{\alpha\beta}(\mathbf{x}_a, \mathbf{x}_b) u_a^\alpha u_b^\beta \right) \end{aligned} \quad (3.54)$$

where the first term accounts for the internal potential energy of a CO molecule adsorbed at position \mathbf{x} and the second term contains the (pairwise) interaction between different adsorbed CO molecules.

Having clarified the general form of the adsorbate potential energy, we are now confronted with the task to find workable approximations for its coefficients. Confining our discussion to C-O bond displacements in the direction of the surface normal $\hat{\mathbf{e}}_3$, we subsequently put

$$\mathbf{u}_a = u_a \hat{\mathbf{e}}_3 \quad .$$

Denoting by μ the reduced mass of the CO molecule, k_{CO}^{33}/μ is now identified with the *measured* stretching frequency of an isolated adsorbate, the so-called 'singleton' frequency. To construct the coefficients V , we shall make the following assumptions regarding the nature of the interactions they describe

$$V^{\alpha\beta}(\mathbf{x}_1, \mathbf{x}_2) \text{ is } \begin{cases} \text{pure } dipole-dipole \text{ for } |\mathbf{x}_1 - \mathbf{x}_2| \longrightarrow \infty, \\ 'chemical' \text{ and } dipole-dipole \text{ for next neighbors.} \end{cases}$$

At first sight there seem to be little justification in designating a part of the potential as 'chemical', as long as its origin and analytical form are not known. However, we shall show that the difference between the two postulated contributions becomes apparent when the electronic polarizability of the adsorbates

is considered, as the dipole-dipole coupling is severely screened by the electrons whereas the 'chemical' coupling is affected differently and only to a lesser extent. Chemical couplings of this type have been first proposed for chemisorbed CO by Moskovits and Hulse [37] inspired by the valence force field of Cotton and Kraihanzel [38] developed for C-O bonds in metal carbonyls. More recently, a model similar in many respects to the present one was applied to the system CO on Pt(111), where short-range chemical couplings were introduced in addition to dipole-dipole coupling in order to account for the vibrational polarizability of CO molecules in the dense Pt(111) (2×2) -3CO structure [39].

The analytical expression of the electrostatic (dipole-dipole) potential for adsorbed CO molecules has been a subject of debate. Elaborate analyses in earlier work [40, 41] have called attention to the highly idealized character of the widespread approach based on treating the adsorbates as 'pointlike' dipoles within the classical theory of electrostatic images. Notwithstanding such cautionary remarks, the classical approach remains enduringly popular. Because of the simplicity and familiarity of its concepts, we shall continue our discussion within the classical framework. For an excellent review of the theory and of many experimental results concerning the dipole-dipole coupling, the reader is referred to the classic paper by Hollins and Pritchard [17].

The electrostatic properties of adsorbed CO molecules are subsequently idealized through pointlike dipoles

$$\mathbf{p} = e^* \mathbf{u}$$

located at the molecule center of mass \mathbf{x} and oriented along the molecular axis. Both nuclei of an adsorbed CO molecule possess a localized effective charge of absolute value e^* . We may expect the value of the effective charge e^* to be sensitive to the chemical nature of the adsorption site and to the presence of neighboring coadsorbates.

The total electrostatic energy of the molecular pointlike dipoles consists of a direct through-vacuum contribution and an indirect one, mediated by the substrate electrons and described in the formalism of electrostatic images [42, 43]. To the

familiar trough-vacuum dipole-dipole potential⁴

$$\frac{\mathbf{p}_1 \cdot \mathbf{p}_2 - 3(\hat{\mathbf{n}}_{21} \cdot \mathbf{p}_1)(\hat{\mathbf{n}}_{21} \cdot \mathbf{p}_2)}{|\mathbf{x}_1 - \mathbf{x}_2|^3} \quad \text{with} \quad \hat{\mathbf{n}}_{21} = \frac{\mathbf{x}_1 - \mathbf{x}_2}{|\mathbf{x}_1 - \mathbf{x}_2|} \quad ,$$

which for surface-normal stretching of the C-O bond reduces to

$$\frac{p_1 p_2}{|\mathbf{x}_1 - \mathbf{x}_2|^3} \quad , \quad (3.55)$$

we have to add potentials for the interaction of the dipole with the electrostatic image of its neighbor (first term) and for the interaction of both electrostatic images with each other (second term)

$$\left[\frac{1}{(|\mathbf{x}_1 - \mathbf{x}_2|^2 + 4d^2)^{3/2}} - \frac{12d^2}{(|\mathbf{x}_1 - \mathbf{x}_2|^2 + 4d^2)^{5/2}} \right] p_1 p_2$$

where $2d$ is the distance of the neighbor dipole to its own electrostatic image. More specifically, the parameter d is interpreted as the distance between the center of mass of the adsorbate-induced electronic charge density and the 'jellium edge' as given in the treatment of Lang and Kohn [43]. For CO on transition metals, $d = 0.7\text{-}0.8$ Å. It has been pointed out [44] that the interaction of the dipole with its own image should not be explicitly included since the molecular chemisorption potential (or equivalently, the force constants of the chemisorbed molecule) do already account for the electrostatic molecule-substrate interactions. Summing the electrostatic contributions and adding the short-range 'chemical' potential χ we arrive at our full model potential

$$\left. \begin{aligned} V^{33}(\mathbf{x}_1, \mathbf{x}_2) &= \chi(\mathbf{x}_1, \mathbf{x}_2) + e_1^* e_2^* v(|\mathbf{x}_1 - \mathbf{x}_2|) \\ v(x) &= \frac{1}{x^3} + \frac{1}{(x^2 + 4d^2)^{3/2}} - \frac{12d^2}{(x^2 + 4d^2)^{5/2}} \end{aligned} \right\} \quad . \quad (3.56)$$

We note at this point that for the trough-metal vibrational coupling of a pair of chemisorbed CO molecules, similar in nature to the 'chemical' effects we intend to describe by introducing the χ term, an analytical expression was derived by Persson [45]. Approximating the metal by a jellium, this coupling turns out to

⁴In the present work we consistently use gaussian cgs units. The coulombian energy of two unit charges 1 cm apart is 1 erg.

be very small for the rather common situation $k_F R \geq 4$, where R is the distance between the molecules and k_F is the Fermi wavenumber of the metal. For CO on Cu(100) the relative contribution of this coupling term to the total shift of the CO stretch frequency was evaluated to at most few percent of the observed total shift. Despite this negative result, it shall prove useful to keep the short-range 'chemical' potential χ as a useful fit parameter in further applications.

3.3.2 Dynamics of a chemisorbed layer in external field

To derive the dynamics of a chemisorbed layer of CO molecules we shall start by writing the Lagrange function in the 'natural' center of mass and relative position coordinates of Eq.3.32 instead of using the normal mode lagrangian Eq.3.41 of the previous section. The reason for this choice lyes in the fact that in the 'natural' coordinates only the stretching mode couples the electric field, the resulting equations of motion being thus much simpler.

The total Lagrange function of the adsorbed layer in an external electric field

$$\mathcal{L} = \mathcal{L}_{ads} + \mathcal{L}_{int} + \mathcal{L}_{ext} \quad (3.57)$$

consists of terms accounting for the noninteracting dipoles

$$\mathcal{L}_{ads} = \frac{M}{2} \sum_i (\dot{z}_i^2 - \Omega_z^2 z_i^2) + \frac{\mu}{2} \sum_i (\dot{u}_i^2 - \Omega_u^2 u_i^2) + \sqrt{M\mu} G \sum_i z_i u_i$$

where $z_i = \mathbf{x}_i \cdot \hat{\mathbf{e}}_3$ is the height of the molecule center of mass above the surface and M is the total mass of the CO molecule, their pairwise electrostatic-chemical coupling according to Eq.3.56

$$\mathcal{L}_{int} = - \sum_{i < j} V^{33}(\mathbf{x}_i, \mathbf{x}_j) u_i u_j$$

and finally the energy due to the applied electric field $\mathbf{E}_i^{ext}(t) = \hat{\mathbf{e}}_3 E_i^{ext}(t)$

$$\mathcal{L}_{ext} = \sum_i e_i^* u_i \left[E_i^{ext}(t) - \sum_{j \neq i} v(|\mathbf{x}_i - \mathbf{x}_j|) p_j^{el} \right]$$

where E_i^{ext} denotes the applied field at site i and the second term is a depolarizing contribution directed against it, due to the electronic polarization of each

adsorbate under the *local* electric field at the respective site. A key quantity of the present model, the local electric field E_i^{loc} is the field that actually induces both electronic and vibrational dynamic dipole moments of the adsorbate

$$p_i^{el}(t) = \alpha_e E_i^{loc}(t)$$

where α_e is the electronic polarizability of the adsorbed molecule, nearly frequency independent in the IR range of interest. The value of α_e is 2.6-2.8 Å³ for gas phase CO and may be of the order of a few Å³ for chemisorbed CO.

Writing the Euler-Lagrange equations for the Lagrange function Eq.3.57 we arrive at the equations of motion of the adsorbed layer

$$\begin{aligned} \mu(\ddot{u}_i + \Omega_u^2 u_i) + \sum_{j \neq i} \left[\chi(\mathbf{x}_i, \mathbf{x}_j) + e_i^* e_j^* v(|\mathbf{x}_i - \mathbf{x}_j|) \right] u_j &= \sqrt{M\mu} G z_i \\ &+ e_i^* \left[E_i^{ext}(t) - \sum_{j \neq i} v(|\mathbf{x}_i - \mathbf{x}_j|) p_j^{el} \right] \\ M(\ddot{z}_i + \Omega_z^2 z_i) &= \sqrt{M\mu} G u_i \end{aligned} \quad (3.58)$$

We note that the second equation is very simple, as a consequence of the rigid molecule-to-substrate vibration mode z having no effective charge of its own.

The monochromatic IR beam of frequency ω

$$E_i^{ext}(t) = \hat{E}_i^{ext} \exp(-i\omega t)$$

has the same amplitude \hat{E}_i^{ext} at each site, according to the fact that in IR spectroscopy the wavelength is in μm range. The local electric field has the same harmonic time dependence as the external field

$$E_i^{loc}(t) = \hat{E}_i^{loc} \exp(-i\omega t)$$

and consequently we can put

$$p_i^{el}(t) = \hat{p}_i^{el} \exp(-i\omega t) \quad \text{with} \quad \hat{p}_i^{el} = \alpha_e \hat{E}_i^{loc} \quad .$$

The solutions z and u to the system of coupled equations are to be sought in the

form of harmonic oscillations of the same frequency

$$\begin{aligned} z_i(t) &= \hat{z}_i(\omega) \exp(-i\omega t) \\ u_i(t) &= \hat{u}_i(\omega) \exp(-i\omega t) \end{aligned}$$

where \hat{u} and \hat{r} are complex amplitudes satisfying

$$\begin{aligned} \mu(\Omega_u^2 - \omega^2) \hat{u}_i + \sum_j \chi(\mathbf{x}_i, \mathbf{x}_j) \hat{u}_j &= \sqrt{M\mu} G \hat{z}_i \\ &+ e_i^* \left[\hat{E}_i^{ext} - \sum_{j \neq i} v(|\mathbf{x}_i - \mathbf{x}_j|) (\hat{p}_j^{el} + e_j^* \hat{u}_j) \right] \\ M(\Omega_r^2 - \omega^2) \hat{z}_i &= \sqrt{M\mu} G \hat{u}_i \end{aligned}$$

The equation of motion for the stretching mode \hat{u} is obtained in closed form after elimination of the center of mass coordinates \hat{z} by means of the second equation

$$\begin{aligned} \mu \left(\Omega_u^2 - \omega^2 - G^2 \frac{1}{\Omega_r^2 - \omega^2} \right) \hat{u}_i + \sum_j \chi(\mathbf{x}_i, \mathbf{x}_j) \hat{u}_j &= \\ e_i^* \left[\hat{E}_i^{ext} - \sum_{j \neq i} v(|\mathbf{x}_i - \mathbf{x}_j|) (\hat{p}_j^{el} + e_j^* \hat{u}_j) \right] \end{aligned} \quad (3.59)$$

Taking into account the expression of the vibrational polarizability of a single chemisorbed CO molecule, which exhibits poles (absorption peaks) for the stretch as well as for the rigid molecule to substrate vibration modes

$$\alpha(\omega) = \left(\frac{e^{*2}}{\mu} \right) \frac{\Omega_r^2 - \omega^2}{(\Omega_r^2 - \omega^2)(\Omega_u^2 - \omega^2) - G^2}$$

and identifying the vibrational dipole moment $e_i^* u_i = p_i$, Eq.3.60 is now written

$$\frac{1}{\alpha_i(\omega)} \hat{p}_i + \sum_j \frac{\chi(\mathbf{x}_i, \mathbf{x}_j)}{e_i^* e_j^*} \hat{p}_j = \hat{E}_i^{ext} - \sum_{j \neq i} v(|\mathbf{x}_i - \mathbf{x}_j|) (\hat{p}_j^{el} + \hat{p}_j) \quad . \quad (3.60)$$

Eq.3.60 is the key equation of the present model. It describes the dynamics of a collective stretching mode in a layer of chemisorbed CO molecules excited by an external harmonic field, taking self-consistently into account the dynamical coupling between the molecules (dipole-dipole and an additional, non-electrostatic short range coupling) and the screening of the molecular vibrational dipole mo-

ments by the molecular electronic polarizability.

To cast this result into a more familiar form let us note that, in the absence of the non-electrostatic coupling χ , Eq.3.60 would reduce to the couple

$$\text{for } \chi = 0 \quad \left\{ \begin{array}{l} \hat{p}_i = \alpha_i(\omega) \hat{E}_i^{loc} \quad ; \quad \hat{p}_i^{el} = \alpha_e \hat{E}_i^{loc} \\ \hat{E}_i^{loc} = \hat{E}_i^{ext} - \sum_{j \neq i} v(|\mathbf{x}_i - \mathbf{x}_j|) (\hat{p}_j^{el} + \hat{p}_j) \end{array} \right.$$

which admits an immediate, intuitive interpretation. Under an externally applied harmonic field \hat{E}_i^{ext} each vibrational dipole moment \hat{p}_i is excited by the local field \hat{E}_i^{loc} at the adsorbate site. The same applies for the molecular electronic dipole moments \hat{p}_i^{el} . At each site, the applied field \hat{E}_i^{ext} is diminished by the *depolarizing* field due to the total dipole moments $(\hat{p}_i^{el} + \hat{p}_i)$ induced in the adsorbates. In this way, the electronic and vibrational dipole moments are being induced by the local field, which in its turn is self-consistently determined by the induced dipole moments.

3.3.3 From adsorbate dynamics to RAIR spectra

In calculations of RAIR spectra based on the dynamic equation 3.60 we shall proceed by first solving the equivalent matrix equation

$$\hat{E}_i^{loc} + \sum_{j \neq i} \left\{ \frac{\chi(\mathbf{x}_i, \mathbf{x}_j)}{e_i^* e_j^*} \alpha_j(\omega) + v(|\mathbf{x}_i - \mathbf{x}_j|) [\alpha_e + \alpha_j(\omega)] \right\} \hat{E}_j^{loc} = \hat{E}_i^{ext} \quad (3.61)$$

to obtain the local field \hat{E}_i^{loc} , the vibrational dipole moments being then simply

$$\hat{p}_i = \alpha_i(\omega) \hat{E}_i^{loc} \quad .$$

The RAIR spectrum as a function of the frequency ω of the exciting light is given by Eq.3.15

$$\left(\frac{\Delta R}{R} \right) (\omega) = -\frac{16\pi}{c} \left(\frac{N}{A} \right) \left(\frac{\sin^2 \varphi}{\cos \varphi} \right) \omega \text{Im } \tilde{\alpha}(\omega)$$

where c is the speed of light in vacuum, N is the number of molecules adsorbed over a surface area A of the sample, φ is the angle of incidence of the light beam relatively to the surface normal and $\tilde{\alpha}(\omega)$ is the *effective* vibrational polarizability

of a CO molecule in the fully coupled layer, defined according to

$$\sum_i \hat{p}_i = N \tilde{\alpha}(\omega) \hat{E}^{ext} \quad . \quad (3.62)$$

The effective polarizability $\tilde{\alpha}$ of the CO molecule in an adsorbate layer of a given structure is obtained from the last equation by inserting the solution \hat{E}_i^{loc} of the dynamical equation 3.61 calculated for that structure

$$\tilde{\alpha}(\omega) = \frac{1}{N \hat{E}^{ext}} \sum_i \alpha_i(\omega) \hat{E}_i^{loc} \quad . \quad (3.63)$$

From a principle point of view, the investigation of a system by RAIRS proceeds in two distinct stages. In the first stage we aim at the determination of dynamical parameters, which are intrinsic to the CO molecule adsorbed on the studied surface and account for its interaction with the IR radiation. These parameters enter the vibrational polarizability of the adsorbed CO molecule and are essentially the dynamic charge e^* and the singleton frequency Ω , each specified for the different adsorption sites available. The next steps are necessary:

1. preparation under UHV (and eventually at low temperature) of well known, possibly highly ordered CO adsorbate structures;
2. recording of the respective RAIR spectra under UHV conditions;
3. setting up a structural model of the adsorbate, guided by extensive prior knowledge;
4. simulation of the RAIR spectra for the given adsorbate structure, by means of a dynamical model of adsorbate interactions. The dynamical parameters are obtained by fitting the proposed (structural *and* dynamical) model to the experimental RAIR spectrum.

Once this program has been completed for a number of well defined CO adsorbate structures, it becomes possible to assign dynamical parameters (vibrational polarizabilities) to the different CO species (adsorption sites) present on the surface. Variants of the proposed program would include the study of ordered adsorbed layers containing different chemical species. In view of a study of the CO oxidation reaction, investigations of layers of CO coadsorbed with O seem necessary.

Detailed knowledge of the dynamical parameters of the adsorbed CO molecule (here seen mainly as a test molecule) in various contexts is a prerequisite for the second stage of the RAIRS study.

In the qualitatively different second stage we use RAIRS as an analytical tool in situations where other (UHV-specific) spectroscopic methods become impracticable. A typical case is the *in situ* monitoring of adsorbates during a catalyzed reaction under pressure reactants feed. Our aim is to propose structure models of the adsorbed layer under reaction conditions, the experimental evidence at hand being mostly the *in situ* recorded RAIR spectrum. Unlike during the first stage under UHV conditions, our prior knowledge of the adsorbate structure under stable reaction conditions is scarce. It is therefore possible that more than one structure model can be proposed in order to simulate the measured RAIR spectrum, additional arguments being requested to arrive at an unequivocal physical picture. Simulation of RAIR spectra for these practically unknown adsorbate structures has a substantially better chance to succeed when the knowledge of the adsorbate dynamical parameters, gained in the first stage, is more detailed.

Computer implementation

In order to facilitate the application of the formalism presented in the current chapter, we have implemented it as a computer program. In Chap.5 we have successfully applied the program for the interpretation of the RAIR spectra of on-top CO on the stoichiometric RuO₂(110) surface. As an application example, a listing of the program used for this calculation is given in App.E.

Chapter 4

The RuO₂(110) surface: properties and preparation

The present chapter is intended as a brief review of the principal results in the literature concerning the RuO₂(110) surface. The first section presents the oxidation the Ru(001) surface, leading to the formation of the so-called 'oxygen-rich' Ru surfaces, much more active in the oxidation of CO than the original metallic Ru surface. The structure of the catalytically active phase of these 'oxygen-rich' Ru surfaces, the ultrathin epitaxial RuO₂(110) film, is described in Section 2. The chemical activity of the RuO₂(110) surface towards CO and O₂ is summarized in Section 3. We conclude with a presentation of our results concerning the preparation of the sample and its characterisation by RAIRS.

4.1 Oxidation of the Ru(001) surface

Ruthenium forms only one stable solid oxide phase, namely ruthenium dioxide. The growth of a ruthenium dioxide layer on the surface of a ruthenium single crystal is a complex process which was clarified mostly during the past decade [8, 10, 46]. Ruthenium dioxide (RuO₂) crystallizes in a rutile-type structure (Fig.4.3.a), the crystalline structure of the mineral rutile (titanium dioxide). In the bulk structure of RuO₂ the Ru atoms bind to six O atoms, forming a slightly distorted RuO₆ octahedron, while the O atoms are coordinated to three Ru atoms in a planar way, consistent with an sp² hybridization of the oxygen atoms. The ruthenium dioxide surfaces studied in the present work are ultrathin

epitaxial RuO_2 *films* grown under intensive oxygen exposure on the facets of Ru single crystals, rather than facets of a bulk RuO_2 single crystal. By denoting the ruthenium dioxide films as *epitaxial* we indicate that there exists a well defined orientation of the film relatively to the lattice of the Ru substrate. The orientation of an epitaxially grown RuO_2 film is conditioned in the first place by the orientation of the single crystalline Ru substrate. For instance, the epitaxial RuO_2 layer exposes preferentially the (110) facet when grown on Ru(001) and the (100) facet when grown on Ru(10 $\bar{1}$ 0). The structures of these two ruthenium dioxide layers are denoted $\text{RuO}_2(110)$ and $\text{RuO}_2(100)$ respectively.

Exposing the Ru(001) surface at room temperature to molecular oxygen under UHV conditions, a (2 \times 2)-O [47] and a (2 \times 1)-O overlayer are formed [48], containing 0.25 and 0.50 monolayers of chemisorbed oxygen, respectively. The dissociative sticking coefficient of O_2 drops, from about 1 on the clean Ru(001) surface, to less than 10^{-3} on the chemisorbed O overlayers, such that under UHV conditions the (2 \times 1)-O phase was considered to be the saturation phase. It has been subsequently shown that by dosing much more oxygen (10^3 - 10^6 L), the Ru(001) surface can accommodate two additional phases with even higher content of chemisorbed oxygen, namely (2 \times 2)-3O with 0.75 monolayers of O [49] and (1 \times 1)-O with one monolayer of O [50]. The dissociative sticking coefficient of O_2 over the Ru(001)-(1 \times 1)-O surface is estimated to be less than 10^{-6} [51]. Consequently, oxygen uptake beyond the coverage of one monolayer becomes the rate determining step in the initial oxidation of Ru(001). However, as soon as an oxide nucleus is formed on the Ru(001)-(1 \times 1)-O surface, oxide formation proceeds in an autocatalytic way [52], given that the dissociative sticking coefficient of O_2 on the oxide nucleus is as high as 0.7 [51]. Autocatalytic oxidation implies that the surface produces the 'catalyst' for its own oxidation, in the form of small oxide nuclei which, by efficiently dissociating the O_2 molecules, lead to a self-acceleration of the oxidation process. The threshold temperature for the oxidation of Ru(001) by molecular oxygen turns out to be 540 K. Below this temperature, $\text{RuO}_2(110)$ cannot be formed on Ru(001), as shown by *in situ* SXRD measurements performed at oxygen pressures up to 0.1 mbar [53]. Below 400 K only chemisorbed oxygen can be stabilized on Ru(001).

Exposure of the Ru(001) surface to O_2 at 580-630 K in a wide pressure range (10^{-5} - 10^{-1} mbar) results in the growth of a 1.6 nm thick $\text{RuO}_2(110)$ epitaxial film on Ru(001), as shown by *in situ* SXRD measurements [53]. The thickness of the

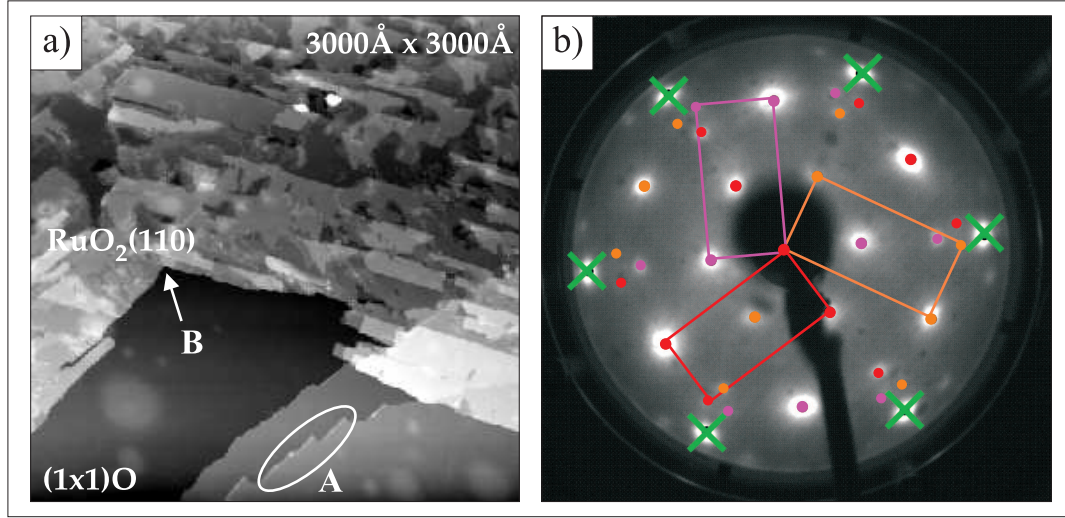


Figure 4.1: RuO₂(110) epitaxial film grown on the Ru(001) surface. a) Large scale STM images [54] show the coexistence of the RuO₂(110) film with the (1 × 1)-O phase of chemisorbed oxygen. The RuO₂(110) film is broken up into multiple patches, few hundreds of Å wide each. The oxide film grown at the step edges of the (1 × 1)-O area is indicated by A. The intersection of two RuO₂(110) domains, rotated 120° relative to each other, is marked by B. b) The LEED pattern consists in the superposition of a hexagonal pattern (indicated by crosses) due to the (1 × 1)-O areas and of three rectangular patterns rotated by 120° (each indicated by dots of a different color) stemming from RuO₂(110) patches of the three orientations. Image adapted after Refs.[55, 56].

RuO₂(110) film was practically independent of the preparation conditions in the indicated range, being limited to five RuO₂(110) crystal planes. The growth of the RuO₂(110) film on Ru(001) may be briefly characterised as *autocatalytic* and *self-limited*. In addition, the RuO₂(110) and the Ru(001) lattices are *incommensurate*. SXRD data have indicated the dimensions 3.12 Å × 6.38 Å [53] for the unit cell of the RuO₂(110) epitaxial film, which are incommensurate to the lattice constant of 3.71 Å of the Ru(001) substrate.

Large-scale STM images [54] show that, due to its incommensurate growth relatively to the Ru(001) substrate, the RuO₂(110) epitaxial film breaks up into separate patches several hundreds of Å in size, rotated 120° to each other (Fig.4.1.a). The coexistence of distinct RuO₂(110) domains of different orientations is most directly observed by low-energy electron diffraction (LEED). Instead of the rectangular LEED pattern characteristic of the RuO₂(110) *structure*, the LEED pattern of the epitaxially grown RuO₂(110) *film* on Ru(001) presents hexagonal symme-

try, consisting of the superposition of three separate rectangular patterns rotated 120° relatively to each other (Fig.4.1.b). Furthermore, STM images [8, 54] have shown the coexistence of $\text{RuO}_2(110)$ patches with areas occupied by the $(1 \times 1)\text{-O}$ phase, both several hundreds of Å wide (Fig.4.1.a). The presence of the $(1 \times 1)\text{-O}$ phase on the oxidized $\text{Ru}(001)$ surface is easily recognized in the LEED pattern, given that its characteristic diffraction spots (marked by crosses in Fig.4.1.b) are distinct from those of the $\text{RuO}_2(110)$ patches [55]. The $(1 \times 1)\text{-O}$ phase is chemically inert, neither CO nor O_2 adsorption being observed at temperatures higher than 50 K [57].

The observation of a self-limited growth mechanism of the $\text{RuO}_2(110)$ layers does not exclude the growth of thicker ruthenium dioxide films on $\text{Ru}(001)$. Oxidation of the $\text{Ru}(001)$ surface at higher temperature (670-720 K) leads to the growth of thicker RuO_2 films consisting of 7-11 $\text{RuO}_2(110)$ crystal planes [53]. The thicker RuO_2 films present roughened surfaces, exposing other facets in addition to the favoured (110) plane. In STM images taken during the initial stages of the roughening of a $\text{RuO}_2(110)$ film, the catalytically inactive $c(2 \times 2)$ -reconstructed $\text{RuO}_2(100)$ facet has been identified [58]. This observation has proved of key importance in understanding the puzzling deactivation of Ru-based catalysts under oxidizing conditions [59, 60], first reported by Cant *et al.* [6].

4.2 Surface structure of the epitaxially grown $\text{RuO}_2(110)$ films on $\text{Ru}(001)$

The literature data presented in the previous section have shown that exposure of the $\text{Ru}(001)$ surface to large doses (10^6 L) of molecular oxygen, at sample temperatures exceeding 540 K, results in the formation of a so called oxygen-rich $\text{Ru}(001)$ surface, accommodating a quantity of oxygen equivalent to 3-6 times the content of the $(1 \times 1)\text{-O}$ phase on $\text{Ru}(001)$. On these oxygen-rich $\text{Ru}(001)$ surfaces, the $(1 \times 1)\text{-O}$ phase coexists with an epitaxially grown, ultrathin $\text{RuO}_2(110)$ film.

Following the identification of the catalytically active phase of an oxygen-rich $\text{Ru}(001)$ surface, with the ultrathin $\text{RuO}_2(110)$ epitaxial film [8, 62], two structure models have been investigated in order to establish the atomic geometry at the surface of a $\text{RuO}_2(110)$ film in pristine condition [55]. The models, represented in Fig.4.2.a and Fig.4.2.b, are truncations of the bulk RuO_2 structure along the

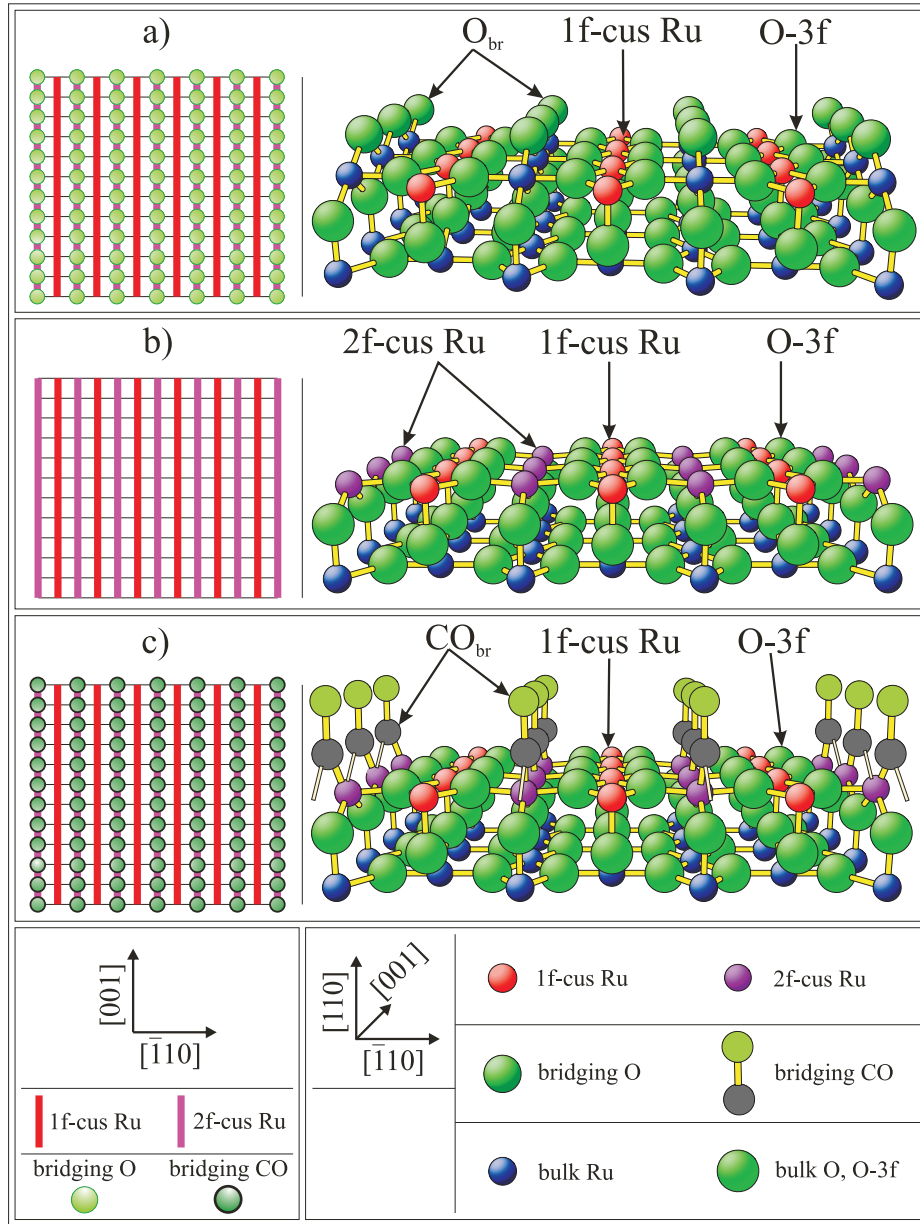


Figure 4.2: Schematic representation (left column) and ball-and-stick model [8] (right column) of the $\text{RuO}_2(110)$ surface. *a)* On the *stoichiometric* (pristine) surface, pairs of Ru atoms are bridged by oxygen atoms (O_{br}). *b)* The *mildly reduced* surface is obtained after removal of the O_{br} atoms from the stoichiometric surface. *c)* The vacant bridge sites on the mildly reduced surface can be occupied by other adsorbates, for example CO_{br} . The O-3f oxygen atoms keep their bulk like coordination to three Ru atoms and are not chemically active. The active sites are the O_{br} atoms and the one- and twofold coordinatively unsaturated (cus) Ru atoms, denoted 1f-cus-Ru and 2f-cus-Ru respectively.

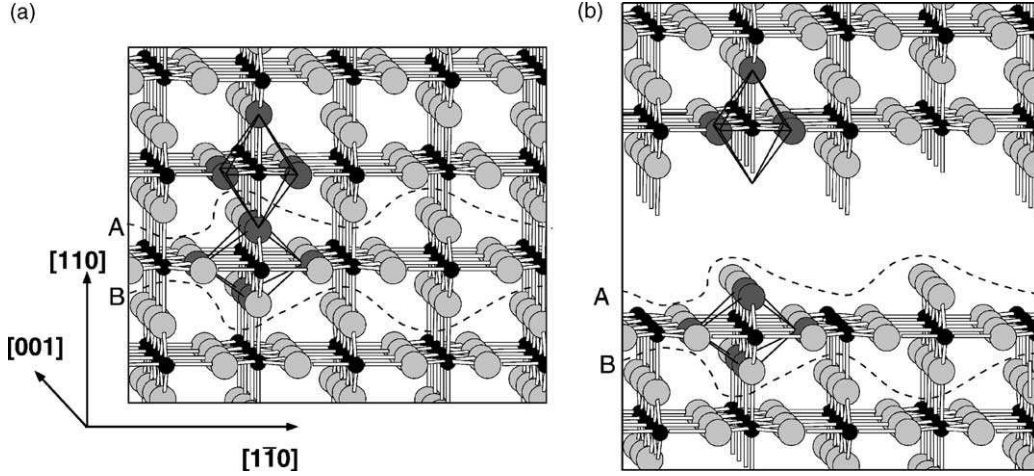


Figure 4.3: a) Ball-and-stick model of the rutile crystal structure. It is composed of slightly distorted octahedra, two of which are indicated. Along the $[110]$ direction these octahedra are stacked with their long axes alternating by 90° . Open channels are visible along the $[001]$ direction. The dashed lines A and B enclose a charge-neutral repeat unit. b) The crystal is cut along line A . The same number of Ru-O and O-Ru bonds are broken. The resulting $\text{RuO}_2(110)$ surface is autocompensated (see text) and stable. *Figures from Ref. [61].*

(110) crystal plane. In the model of Fig.4.2.a, during the present work termed the *stoichiometric* $\text{RuO}_2(110)$ surface, oxygen atoms (O_{br}) are bridging over pairs of Ru atoms, forming ordered rows oriented in the $[001]$ direction. The model in Fig.4.2.b, in the following termed the *mildly reduced* $\text{RuO}_2(110)$ surface, is obtained from model *a* after removal of the O_{br} atoms. In the rest of this work, the $\text{RuO}_2(110)$ surfaces in Fig.4.2.a (stoichiometric) and in Fig.4.2.b (reduced) will be denoted as s- $\text{RuO}_2(110)$ and r- $\text{RuO}_2(110)$, respectively.

In Ref.[55], a combined LEED-DFT analysis was applied to an oxygen-rich Ru(001) surface in order to discriminate between the models s- $\text{RuO}_2(110)$ and r- $\text{RuO}_2(110)$ (Fig.4.2.a, b) of the pristine $\text{RuO}_2(110)$ epitaxial film. The Ru(001) sample was exposed to 6×10^6 L O_2 at 600 K, which led to the accumulation of 6 monolayers of oxygen at the sample surface. The LEED data recorded on the freshly prepared sample have unambiguously indicated that s- $\text{RuO}_2(110)$ (Fig.4.2.a) rather than r- $\text{RuO}_2(110)$ (Fig.4.2.b) is the structure of the pristine $\text{RuO}_2(110)$ epitaxial film. Moreover, DFT optimization of the s- $\text{RuO}_2(110)$ structure has reproduced the LEED-determined geometry to within 0.04 \AA accuracy. In contrast, the disagreement between the DFT-optimized r- $\text{RuO}_2(110)$ structure

and the LEED data was found too large [55].

The bridging oxygen atoms (O_{br}) contribute essentially to the stability of the s-RuO₂(110) surface, as may be shown with reference to the concept of charge autocompensation on ionic surfaces [63, 61]. While truncating the bulk RuO₂ structure such as to expose the s-RuO₂(110) surface, the same number of coordinatively unsaturated (cus) O atoms and Ru atoms are formed, by breaking the respective O-Ru and Ru-O bonds (Fig.4.3.b). Each of these cus atoms has an unsaturated valence, also referred to as a dangling bond [8]. Transferring electrons from the dangling bonds on the Ru cations will exactly compensate the missing charge in the dangling bonds on the O_{br} anions. Thus, due to the presence of the bridging O_{br} atoms, the s-RuO₂(110) surface is stabilized *via* the autocompensation mechanism [55].

The RuO₂(110) surface (Fig.4.2.a) presents two different kinds of Ru atoms. Along the [001] direction, rows of six-fold coordinated (bulk like) Ru atoms alternate with rows of five-fold coordinated (or one-fold coordinatively unsaturated) Ru atoms. The two kinds of Ru atoms are denoted as 2f-cus-Ru and 1f-cus-Ru, respectively. Two kinds of O atoms are present as well. Similarly to the oxygen atoms in the bulk, the oxygen atoms denoted as O-3f (Fig.4.2.a) maintain a planar coordination to three Ru atoms, consistent with an sp² hybridization of the oxygen atom [8]. The bridging O_{br} atoms are coordinated to two instead of three Ru atoms, their unsaturated valence being oriented perpendicularly to the surface. Together with the 1f-cus-Ru atoms, which also expose dangling bonds oriented perpendicularly to the surface, the O_{br} atoms are the chemically active centers on the stoichiometric s-RuO₂(110) surface. The O-3f atoms are not chemically active during the CO oxidation reaction [64].

The *mildly reduced* r-RuO₂(110) surface (Fig.4.2.b) is obtained after removal of all O_{br} atoms from the stoichiometric s-RuO₂(110) surface (Fig.4.2.a), for example by exposure to CO at room temperature. We must stress that the reduced r-RuO₂(110) surface, as represented in Fig.4.2.b, is not stable and has not been prepared experimentally. DFT calculations have shown that its surface energy would be in the range 90-120 meV/Å², far less favourable than that of the stoichiometric s-RuO₂(110) surface (71 meV/Å²) [10, 55]. The mildly reduced RuO₂(110) surface can be stabilized by populating the vacant bridge sites with CO molecules. Fig.4.2.c shows the r-RuO₂(110) surface with the bridge positions occupied by so-called *asymmetric* bridging CO molecules (see next section).

4.3 Chemical activity of the $\text{RuO}_2(110)$ film

On the atomic scale, the extraordinarily high activity of stoichiometric $\text{RuO}_2(110)$ toward CO oxidation was demonstrated to be controlled by the presence of 1f-cus-Ru sites [8, 62]. It must be emphasised that, unlike with other oxide surfaces, not the defects but rather the regular under-coordinated surface atoms determine the activity of RuO_2 [65].

4.3.1 Adsorption of CO on reduced $\text{RuO}_2(110)$

On the stoichiometric $\text{RuO}_2(110)$ surface the CO molecules adsorb strongly (1.2 eV [62]) on-top of the 1f-cus-Ru atoms, from where the actual oxidation reaction takes place by recombination with the bridging O_{br} to form CO_2 . A complete replacement of O_{br} by CO would be facilitated by the adsorption energy of 1.73 eV for a single CO molecule substituting a bridging O_{br} .

HREELS measurements [66] have shown that exposure of the stoichiometric $\text{RuO}_2(110)$ surface to CO at room temperature leads to the gradual depletion of the bridging O_{br} population, until at a cumulative exposure of about 1 L CO all bridging O atoms are consumed. The stoichiometric $\text{RuO}_2(110)$ turns into a reduced $\text{RuO}_2(110)$ surface where the 2f-cus Ru atoms are, at least partially, capped by bridging CO molecules. Seitsonen *et al.* [64] have obtained the reduced $\text{RuO}_2(110)$ surface by exposing several times (typically, five to ten times) 0.25 L CO at 170 K and annealing to 550 K while monitoring the CO_2 signal with a quadrupole mass spectrometer. They have considered the vanishing of the CO_2 signal as indicative of the complete removal of the O_{br} species, i.e. of the mild reduction of the $\text{RuO}_2(110)$ surface.

The adsorption geometry of CO on the reduced $\text{RuO}_2(110)$ surface depends critically on the CO coverage. This point is well illustrated by the thermal desorption spectrum (TDS) of CO from the reduced $\text{RuO}_2(110)$, shown in Fig.4.4. The low-temperature desorption states β and α , and a high-temperature desorption state γ' can be clearly discriminated. Based on DFT calculations, Seitsonen *et al.* have proposed well defined adsorption sites and binding geometries for these thermal desorption (TD) states [64].

The TDS measurement can be described as follows. The reduced surface has been saturated with CO by exposure at 170 K, i.e. the bridge and on-top sites

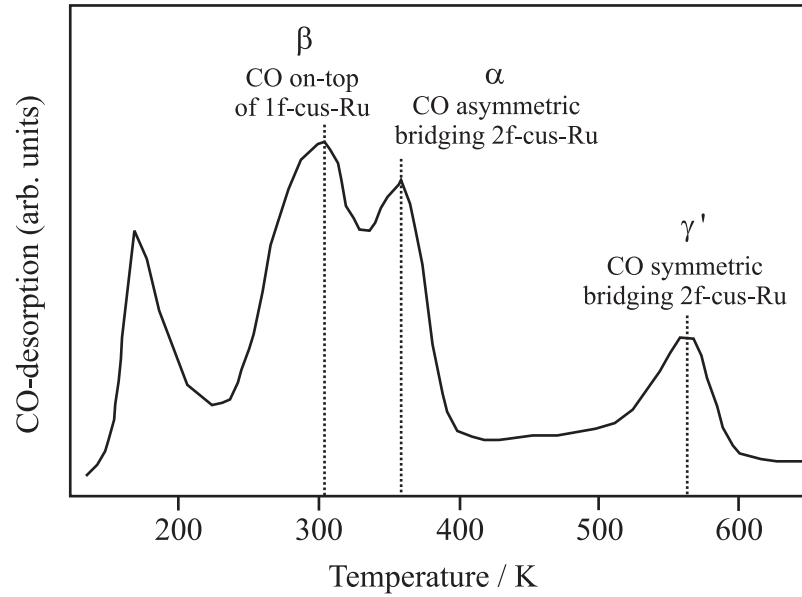


Figure 4.4: Thermal desorption spectrum of CO from a mildly reduced $\text{RuO}_2(110)$ surface (all O_{br} have been previously removed) [64].

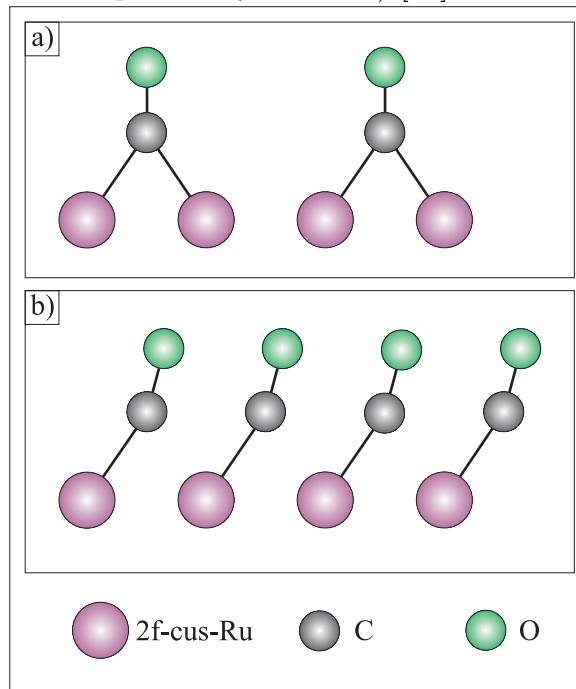


Figure 4.5: Two adsorption geometries for bridging CO_{br} molecules on the mildly reduced $\text{RuO}_2(110)$ surface. a) *Symmetric bridging* CO_{br} molecules occupy the bridge positions above every second pair of 2f-cus-Ru atoms. b) *Asymmetric bridging* CO_{br} molecules bind in a tilted geometry to a single 2f-cus-Ru atom.

are in the beginning occupied by CO. By increasing the sample temperature with a constant rate, the different species of adsorbed CO molecules start to desorb, provided the sample temperature is high enough for the CO molecule to overcome the energy barrier for desorption. The TD spectrum represents in principle the number of desorbed CO molecules as a function of the sample temperature.

At 300 K the on-top CO_{ot} leaves the surface, as reflected by the desorption state β . Now the on-top sites are vacant but the bridge sites are still saturated with CO. For this state, Seitsonen *et al.* have proposed the model depicted in Fig.4.5.b, characterised by a complete row of CO_{br} molecules coordinated in a tilted geometry to each 2f-cus-Ru atom. In the rest of the present thesis we shall denote this kind of bridging CO molecules as *asymmetric* CO_{br} .

At 360 K half of the asymmetric bridging CO_{br} molecules of the β state leave the surface. The remaining CO_{br} molecules change their coordination to the 2f-cus-Ru atoms, from single and tilted to double and upright, as shown in Fig.4.5.a. In the rest of the present thesis we shall denote this kind of bridging CO_{br} molecules as *symmetric* CO_{br} or CO_{br}^{II} . Desorption of the symmetric CO_{br} molecules at 560 K is manifested in the high-temperature desorption state γ' .

It is interesting to note that, according to LEED experiments and DFT calculations [64], the 2f-cus-Ru atoms attached to the symmetric CO_{br} molecules are drawn towards the CO molecule by as much as 0.2 Å. This lateral relaxation of the 2f-cus-Ru atoms allows for a much better overlap of the CO molecular frontier orbitals with those of the substrate.

The binding energies of CO on reduced $\text{RuO}_2(110)$ have been calculated by DFT. For low coverages, when on the average only every second 2f-cus Ru atom is occupied, the symmetric bridge position above 2f-cus Ru atoms is the preferred adsorption site with 1.85 eV, followed by the on-top position above 1f-cus Ru atoms with 1.61 eV. With CO capping all dangling bonds of the 2f-cus Ru atoms, the preference changes from the symmetric bridge position to the asymmetric bridge position above the 2f-cus Ru atoms, with 1.59 eV [64].

4.3.2 Adsorption of O_2 on $\text{RuO}_2(110)$

Like reduction, an equally important process is the facile reoxidation of the partially reduced $\text{RuO}_2(110)$ surface by oxygen supplied in the gas phase. The case of CO oxidation over $\text{RuO}_2(110)$ is an example of the Mars-van-Krevelen catalytic

mechanism [8]. The characteristic feature of this mechanism is that the product leaves the catalyst surface with one or more constituents of the catalyst lattice [67, 68] (in our case O) which has to be subsequently replenished from the gas phase. The latter process is mandatory to keep the oxide catalyst active under reaction conditions.

At temperatures below 140 K, molecular oxygen lies down on the $\text{RuO}_2(110)$ surface as an intact entity, bridging two adjacent 1f-cus-Ru atoms. On increasing the sample temperature, the molecular oxygen dissociates and forms terminal Ru-O bonds to the 1f-cus-Ru atoms. At room temperature, oxygen molecules from the gas phase can efficiently adsorb (sticking probability ~ 0.7) and dissociate.

Exposure of the stoichiometric $\text{RuO}_2(110)$ surface to oxygen at room temperature stabilizes a weakly held oxygen species, which desorbs at about 450 K in molecular form [62]. This species consists of O atoms on-top of the 1f-cus-Ru atoms, in the following denoted as O_{ot} . According to DFT calculations, the binding energy of the on-top O_{ot} atoms is, with only 3.2 eV, much lower than that of the bridging O_{br} species (4.6 eV), which makes O_{ot} a potentially active species.

The diffusion barrier for O_{ot} along the [001] direction has been calculated by DFT as 1.2 eV [65]. From this cause, even at room temperature the on-top O_{ot} atoms are primarily grouped in pairs, as shown by STM [65]. However, if there is an adjacent vacancy in the rows of O_{br} , the diffusion barrier of on-top oxygen to migrate from the on-top site to the bridge site is only 0.6 eV. This diffusion process is very likely at room temperature and accordingly important for the restoration of the mildly reduced $\text{RuO}_2(110)$ surface.

Summary

We conclude by recapitulating the microscopic steps governing the catalytic activity of RuO_2 on the atomic scale [65]. Gas phase CO and O_2 encounter strongly binding adsorption sites on the $\text{RuO}_2(110)$ surface, in the form of the coordinatively unsaturated (cus) Ru atoms. For instance, CO adsorbs on stoichiometric $\text{RuO}_2(110)$ by 1.2 eV (over the 1f-cus-Ru sites), while on the mildly reduced $\text{RuO}_2(110)$ surface the CO binding energy is 1.85 eV for the adsorption over 2f-cus-Ru atoms. The RuO_2 surface provides an active oxygen species to react with CO, i.e. the under-coordinated (bridging) lattice O_{br} atoms. The recombination of adsorbed CO with O_{br} creates vacancies. At room temperature, oxygen

molecules from the gas phase can efficiently dissociate on $\text{RuO}_2(110)$ via a molecular precursor state. This leads to weakly bound O atoms, which adsorb above the 1f-cus-Ru atoms (O_{ot}). Due to their low diffusion barrier (0.6 eV) in the direction of the bridge sites, this weakly held O species is important for the restoration of the mildly reduced $\text{RuO}_2(110)$ surface, where bridging O_{br} atoms have been removed due to recombination with CO molecules.

4.4 Preparation of the $\text{RuO}_2(110)$ epitaxial layer and its characterization by RAIRS

The sample was a commercial (Mateck) Ru(001) crystal 8 mm in diameter and 2 mm thick, cut perpendicularly to the c-axis to a precision of 0.1 degree, the surface roughness after polishing being better than $0.3 \mu\text{m}$. Purity of the crystal was 99.99%, the main contaminants being Os, Ir, Ca and Fe (in the ppm range) and most importantly, carbon. The sample was cleaned by heating in vacuum to 700 K for a cumulated period of 48 hours, interrupted by repeated cycles of sputtering with Ar^+ ions (background pressure 1×10^{-5} mbar argon, ion energy 1.5 keV, sample at 800 K) and flash-annealing to 1100 K in oxygen at 1×10^{-7} mbar background pressure. Flashing in oxygen was necessary in order to eliminate carbon, which during the prolonged annealing segregates from the bulk to the surface, forming graphene layers. The smoothness of the clean Ru(001) surface was qualitatively checked by LEED. Following the initial cleaning procedure, during the experiments the sample had to be occasionally cleaned, two sputtering-annealing cycles having been found sufficient to recover a clear LEED background with sharp diffraction spots.

For the growth of the ultrathin $\text{RuO}_2(110)$ epitaxial film on the Ru(001) surface, the clean sample was transferred to the UHV/HP cell, where it was kept at 600 K for 20 minutes in an oxygen background pressure of 1×10^{-4} mbar O_2 . During the oxidation, the UHV/HP cell was isolated from the rest of the UHV chamber and used in the so-called batch mode (see also Chap.2.1.3). The ordering of the resulting $\text{RuO}_2(110)$ film was visually checked by LEED. The LEED image of the oxide film displayed a rather intense background indicative of a somewhat rough oxide film, at the same time the characteristic diffraction spots of $\text{RuO}_2(110)$ (Fig.4.1.b) being sharply defined. The characteristic reflexes

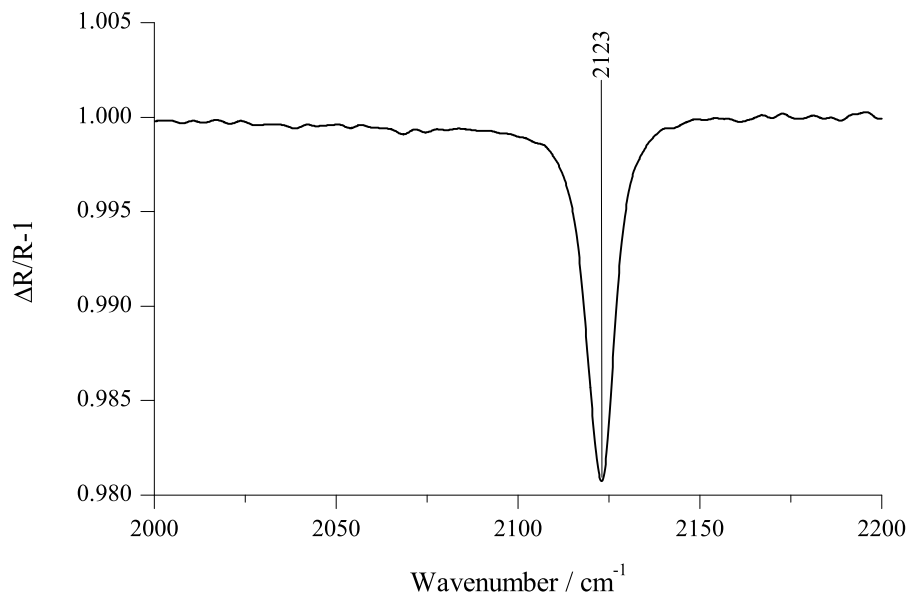


Figure 4.6: RAIR spectrum of the pristine $\text{RuO}_2(110)$ surface, after exposure to 6 L CO at 110 K. The CO molecules occupy the on-top sites, while the bridge sites are occupied by O.

of the $\text{O}(1 \times 1)$ phase were absent, indicating that the sample surface is completely covered by the $\text{RuO}_2(110)$ patches.

In addition to the LEED-check, a protocol based on the RAIR spectrum of CO adsorbed on the pristine $\text{RuO}_2(110)$ film was adopted, and routinely applied during the present work. After cooling the $\text{RuO}_2(110)$ surface to 110 K and subsequent exposure to 6 L CO, a narrow and intense vibrational line emerges in the RAIR spectrum at 2123 cm^{-1} , with FWHM of $8\text{-}10 \text{ cm}^{-1}$ and intensity in the range $1.3\text{-}2.2\%$. We have considered this line (Fig.4.6) as indicative of a clean, well ordered stoichiometric $\text{RuO}_2(110)$ surface, with full rows of O_{br} and with all 1f-cus-Ru sites occupied by on-top CO_{ot} . If the RAIRS line was found wider and less intense than this chosen standard, a substantial improvement could be achieved by repeatedly carrying out the so-called *restoration* procedure: quick annealing (5 to 10 K/s) of the sample to 700 K in 2×10^{-7} mbar oxygen, followed by evacuation of oxygen and quick annealing to 500 K in vacuum. This procedure restores the stoichiometric $\text{RuO}_2(110)$ patches and eliminates eventual contaminants (H, H_2O , CO) from the residual gas, leading to a visibly more intense CO 'signature' line (Fig. 4.7).

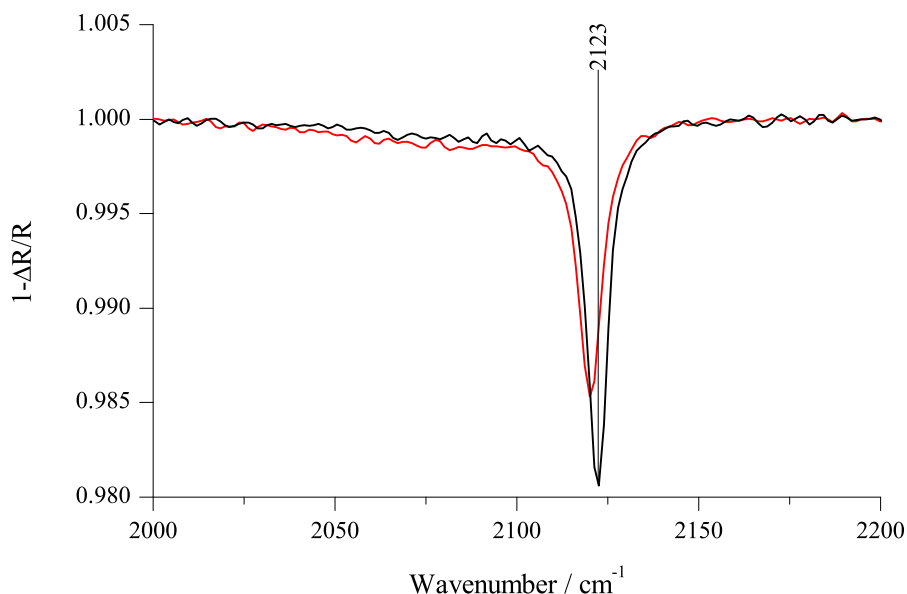


Figure 4.7: Effect of the restoration procedure. CO adsorbed on the stoichiometric $\text{RuO}_2(110)$ film: after holding the film for 12 hour in UHV residual gas at 1×10^{-9} mbar (red curve) and after one restoration procedure (black curve).

The recipe for a standard restoration procedure enables us to exactly reproduce, prior to each RAIRS experiment, the characteristic IR line (2123 cm^{-1}) of CO_{ot} adsorbed on the stoichiometric $\text{RuO}_2(110)$ oxide film. Bringing the oxide film back into this reference state provides us with a well defined starting situation, a necessary condition to obtain reproducible results. Repeating the restoration procedure between the experiments enables us to carry out more experiments on the same oxide film, avoiding thus the time consuming preparation of a new oxide film starting from the clean $\text{Ru}(001)$ surface.

A similar test protocol based on RAIRS has been adopted by Pfnur *et al.* [24]. In their RAIRS study of CO layers on $\text{Ru}(001)$ they have observed that the reproducibility of IR spectra at fixed coverages proved to be the best test of surface cleanliness. Very small quantities of impurities, not detectable with Auger spectroscopy, as well as possibly surface defects, broadened the IR bands or resulted in peak shifting and splitting. This was particularly true near 0.33 ML of CO, where the CO layer orders into the $(\sqrt{3} \times \sqrt{3}) \text{ R}30^\circ$ phase (see also Chap.2.4). These observations show once again that RAIRS is an extremely sensitive tool in the assessment of surface quality and cleanliness.

Note on CO phases, their notation and characteristic IR bands

For an easier lecture of the rest of this thesis, as well as for an overview of the adsorbate layers formed by CO and O on the RuO₂(110) surface and of their characteristic IR bands referred to in the following chapters, please consult on occasions the Synoptic Table on the backflap.

Chapter 5

Adsorption of CO on the stoichiometric RuO₂(110) surface

As an essential prerequisite for the *in situ* RAIRS study of adsorbates under reaction conditions, we shall discuss a class of experiments in which low-temperature adsorption from gas phase is the dominant process, desorption and reaction being negligible. The phases of CO on RuO₂(110) observed under these conditions are characterised by a high degree of ordering and from an experimental point of view, by perfect reproducibility. The circumstance that at low temperatures (100K) the RuO₂ substrate does not react with the adsorbed CO molecules, permits us to assign well defined geometries to the various CO phases identified by IR spectroscopy. The interpretation of RAIR spectra is much simplified under these conditions.

5.1 The Langmuir model of adsorption

The Langmuir model is a highly idealized model of the adsorption/desorption kinetics of molecules at solid surfaces [69, 70]. It is based on a series idealizations: i) all adsorption sites on the surface are equivalent, ii) each site can accommodate at most one molecule, independently of the gas pressure, iii) there are no interactions between the adsorbed molecules, and iv) there is no mechanism for the transport of impinging gas molecules across the surface. We note in passing that the fourth assumption can be relaxed by postulating adsorption via a physisorbed precursor state, as has been elegantly shown by Kisliuk [71].

Let us consider the surface exposed to a gas with temperature T and pressure p . The rate of adsorption is proportional to the particle flux directed towards the surface, i.e. the number of molecules impinging per unit time on the unit surface area. According to kinetic gas theory, this flux is given by the Knudsen formula

$$\frac{p}{\sqrt{2\pi M k_B T}}$$

where k_B is the Boltzmann constant and M is the mass of a gas molecule. The rate of adsorption of molecules at the surface is also proportional to the probability that an impinging particle actually sticks, the so-called *initial* sticking coefficient

$$S_0 = \frac{\text{number of molecules adsorbing / second}}{\text{number of molecules impinging / second}} \quad \text{at low coverage.}$$

Denoting by σ_s the number of molecules adsorbed on the unit surface area, we can write the equation for the rate of adsorption

$$\frac{d}{dt} \sigma_s = \frac{p}{\sqrt{2\pi M k_B T}} \cdot S_0 \cdot \left(1 - \frac{\sigma_s}{\sigma_s^{max}}\right) \quad (5.1)$$

where σ_s^{max} is the maximum possible number of adsorbed particles per unit area. The last factor accounts for the increasing loss of empty sites as the adsorption proceeds. Eq.5.1 is valid only for the case of non-dissociative adsorption.

Introducing the (fractional) coverage $\theta = \sigma_s / \sigma_s^{max}$ and the initial rate of adsorption (i.e. at zero coverage)

$$r_0 = \frac{1}{\sigma_s^{max}} \cdot \frac{p}{\sqrt{2\pi M k_B T}} \cdot S_0 \quad (5.2)$$

we rewrite Eq.5.1 as

$$\frac{d\theta}{dt} = r_0 (1 - \theta) \quad (5.3)$$

whose solution with the initial condition $\theta = 0$ at $t = 0$ is

$$\theta(t) = 1 - e^{-r_0 t}. \quad (5.4)$$

Eq.5.4 applies whenever desorption from the adsorbed layer is negligible, such as in low temperature CO adsorption on RuO₂(110). Since there is only one (on-

top) adsorption site in the unit cell of the $\text{RuO}_2(110)$, which has the dimensions $3.11 \times 6.38 \text{ \AA}^2$, the specific area per adsorption site is

$$\frac{1}{\sigma_s^{max}} = 2.0 \times 10^{-15} \text{ cm}^2.$$

Under the typical conditions of our UHV/HP cell we have $T = 300 \text{ K}$ and $p = 1.0 \times 10^{-9} \text{ mbar}$ as order of magnitude of the pressure in the UHV adsorption experiments. By assuming $S_0 = 1$ for low temperature CO adsorption (each molecule which hits the surface must stick), we get an initial rate of adsorption

$$r_0 = 5.7 \times 10^{-4} \text{ s}^{-1}, \text{ at } 1 \times 10^{-9} \text{ mbar.} \quad (5.5)$$

We shall use Eq.5.4 to estimate the CO coverage on $\text{RuO}_2(110)$ in our low temperature adsorption experiments under UHV conditions.

5.2 Experiment and results

The present section is devoted to a RAIRS study of CO adsorbed on the stoichiometric $\text{RuO}_2(110)$ surface at low temperature under UHV conditions. The stoichiometric $\text{RuO}_2(110)$ surface is terminated by bridging O_{br} atoms, while the 1f-cus-Ru sites are accessible for CO adsorption from the gas phase. In the experiment, the pristine $\text{RuO}_2(110)$ surface was exposed to CO at low pressure, in order to have a low rate of increase of the CO coverage which would permit a detailed, time-resolved monitoring by RAIRS. We could thus monitor the different stages of formation of a saturated CO monolayer on the stoichiometric $\text{RuO}_2(110)$ surface, starting from very small CO coverages.

The $\text{RuO}_2(110)$ surface was prepared starting from a clean $\text{Ru}(001)$ surface, and its cleanliness and ordering were checked by RAIRS according the guidelines set in Chap.4.4. After preparation, the sample was moved from the analysis chamber to the UHV/HP cell and properly aligned to the IR beam. Before starting the adsorption of CO, the sample was flashed in vacuum to 700 K to desorb eventual contaminants from the residual gas. The reference spectrum for the stoichiometric $\text{RuO}_2(110)$ surface was taken after the sample was cooled to 100 K .

The CO pressure in the UHV/HP chamber was set to $3.3 \times 10^{-9} \text{ mbar}$. The

pressure of the residual gas in the chamber was 1×10^{-9} mbar, from which a content of about 6% was CO, as estimated with a quadrupole mass spectrometer. Each spectrum was recorded by averaging of ten intererometer scans, the acquisition time for one complete spectrum being 7.2 seconds. During the acquisition of each spectrum, the CO exposure to the sample increases by 0.02 L. This means that at low coverage the CO coverage of the sample increases by about 0.01 monolayers (ML), but the increase slows down exponentially in time according to Eq.5.4. We have recorded RAIR spectra of the adsorbed CO layer continuously up to a cumulated exposure of 1.2 L CO, where the position and intensity of the RAIRS peak have saturated.

The series of measured RAIR spectra is shown in Fig.5.1. Since the CO molecules adsorb at random over the 1f-cus-Ru atoms, we conclude that the line at 2101 cm^{-1} in the low coverage regime must correspond to isolated on-top CO_{ot} molecules, the so-called *singletons* (spectrum *a*). The 2101 cm^{-1} line can be clearly distinguished up to a coverage of 0.21 (spectrum *c*). Already at 0.05 monolayers CO_{ot}, a new band emerges at 2110 cm^{-1} . The next band is located at 2114 cm^{-1} and becomes distinguishable as a shoulder of the 2110 cm^{-1} band at a coverage of 0.15 monolayers. The 2114 cm^{-1} band remains distinct up to a coverage of 0.23, when it starts to shift to higher frequencies. For coverages in the range 0.25-0.43 the principal band shifts continuously from 2114 cm^{-1} to 2123 cm^{-1} at saturation coverage. We estimate the saturation coverage in our experiment to 40-50 % by means of Eq.5.4 and with 2.3×10^{-9} mbar CO partial pressure.

5.3 Vibrational coupling between the CO_{ot} molecules

With increasing CO exposure the 1f-cus-Ru sites are gradually populated with CO molecules. At coverages of few percent there are mostly isolated CO_{ot} molecules. We intuitively expect that the probability of finding two CO_{ot} molecules occupying neighboring sites increases as even more CO molecules accumulate on the surface. With increasing coverage there is an increasing number of isolated groups consisting of two and more generally of three or four neighboring CO_{ot} molecules. At higher coverages the RuO₂(110) surface must be populated by continuous

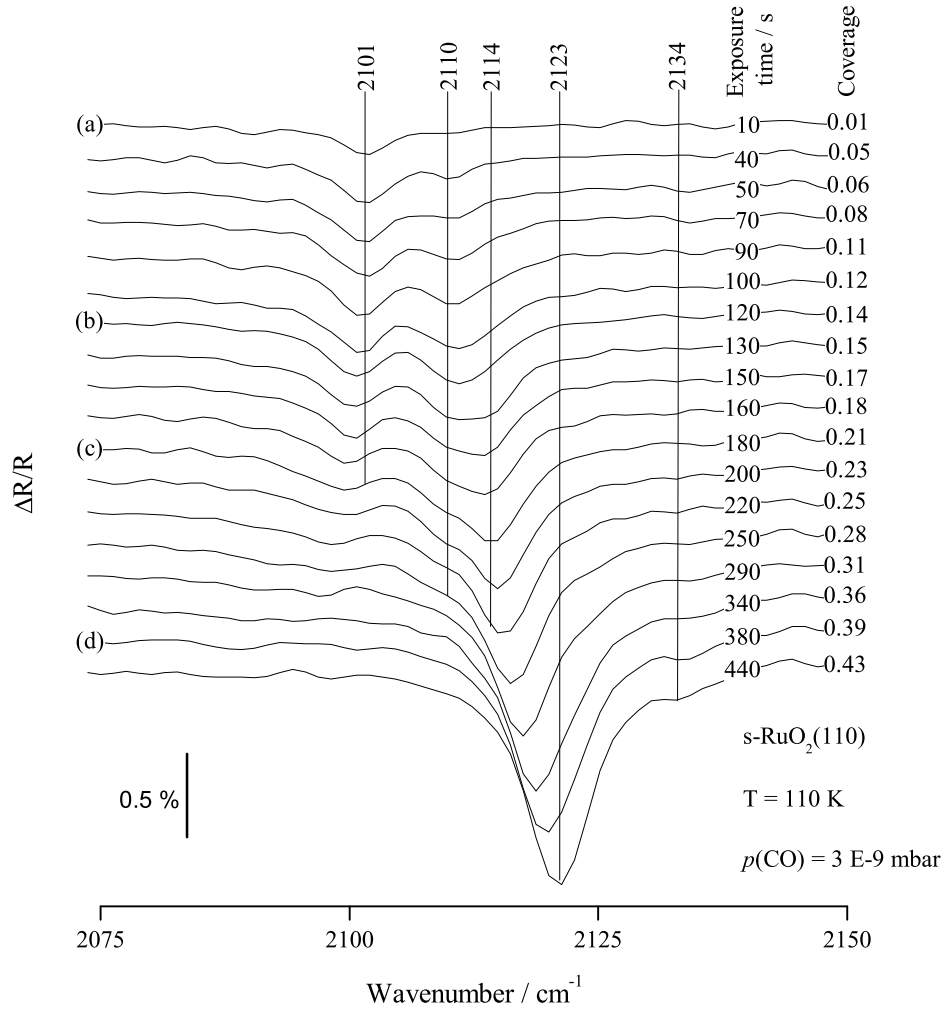


Figure 5.1: Adsorption of CO on the stoichiometric $\text{RuO}_2(110)$ surface at 3×10^{-9} mbar CO and 110 K. With increasing CO coverage of the 1f-cus-Ru sites, distinct vibrational bands develop successively in the 2101-2123 cm^{-1} range.

chains of CO_{ot} molecules of different lengths. More exactly, the number of chains of k neighboring CO_{ot} molecules we might expect to find by inspection of say, 100 on-top sites, is connected to the coverage θ of the surface by the simple statistical formula

$$\text{Nr. of chains of } k \text{ neighboring CO}_{ot} \approx 100 \times (1 - \theta)^2 \theta^k, \quad (5.6)$$

as shown in App.D and also in Ref. [72].

In Fig.5.1 we can observe vibrational lines which are 10-20 cm⁻¹ higher than the frequency of an isolated CO_{ot} molecule (2101 cm⁻¹). As extensively discussed in Chap.3, the electric field of the IR wave excites not the individual CO_{ot} molecules separately but, because of the coupling of vibrations between different adsorbates, it excites a *collective* vibration mode of the adsorbate layer. Most often in the RAIR spectra we see the frequencies of such collective modes, a fact which makes the direct interpretation of the spectra difficult. Our intuitive interpretation of the spectra in Fig.5.1 is, at least at low coverage, that the frequencies of the observed vibrational bands are in fact collective vibration eigenmodi of the chains of neighboring CO_{ot}. With increasing coverage θ , the gradual changes in the RAIR spectrum are then attributed to changing numbers of chains of given length k , as reflected by Eq.5.6.

By assimilating a chain of k neighboring CO_{ot} molecules to a chain of k identical coupled harmonic oscillators, it should be relatively easy to evaluate its eigenfrequencies. Provided just nearest neighbor interactions are considered between the oscillators in the chain, the eigenfrequency $\Omega(k)$ of the mode in which all k oscillators are stretching in phase is given by

$$\Omega(k) = \sqrt{\Omega_1^2 + \Gamma^2 \cos\left(\frac{\pi}{k+1}\right)} \quad (5.7)$$

where Ω_1^2 is the singleton frequency (2101 cm⁻¹) and Γ^2 is the coupling constant between neighboring oscillators in the chain. Tab.5.1 shows that we can find an adequate value for Γ such that the frequencies of the observed IR bands are reproduced by Eq.5.7.

The values in Tab.5.1 suggest that, if the 2101 cm⁻¹ line corresponds to CO_{ot} singletons, then the absorption band at 2110 cm⁻¹ corresponds to pairs of CO_{ot} molecules occupying neighboring on-top sites while the band at 2114 cm⁻¹ is due

Chain length k	$\Omega(k)/\text{cm}^{-1}$	Measured
2	2109.8	2110
3	2113.4	2114
4	2115.2	-
5	2116.2	-
\vdots	\vdots	\vdots
20	2118.3	2123

Table 5.1: Comparison of the experimental frequencies of the CO_{ot} bands in Fig.5.1 with the eigenfrequencies of coupled oscillators as given by Eq.5.7, with $\Omega_1=2101 \text{ cm}^{-1}$ and $\Gamma = 272 \text{ cm}^{-1}$.

to isolated groups of three CO_{ot} molecules. Our discussion also illustrate that, in order to achieve a consistent interpretation of the RAIR spectra, it is necessary to properly include the coupling effects between the adsorbed molecules.

5.4 Computer simulations of the RAIR spectra

In order to give a fully dynamical interpretation to the measured RAIR spectra presented in Fig.5.1, we have undertook computer simulations of the IR spectra in the adsorption experiment. Since there is only one kind of adsorbed CO molecule, namely CO_{ot} , we have only few adjustable parameters in order to reproduce the series of measured, rather complex spectra. The total electric polarizability $\alpha^{ot}(\omega)$ of the adsorbed CO_{ot} molecule is written in the lorentzian parametrization as

$$\alpha^{ot}(\omega) = \alpha_e + \alpha_V^{ot} \frac{\Omega_{ot}^2}{\Omega_{ot}^2 - \omega^2 - i \omega \delta} \quad (5.8)$$

where α_e is the electronic polarizability of the CO_{ot} molecule, α_V^{ot} is the vibrational polarizability, Ω_{ot} is the frequency of the single CO_{ot} molecule and δ is the full width of the IR absorption line of the single CO_{ot} .

From the experiment δ is found to be 6.7 cm^{-1} and Ω_{ot} is 2101 cm^{-1} . In principle, the frequency Ω_{ot} of the isolated molecule can be a function of the CO coverage present on the surface, due to the chemical shift effects entailed by the Blyholder mechanism (see also Chap.3.2.1). In the course of fitting the simulated IR spectra to the measured ones, a practically exact concordance over the entire

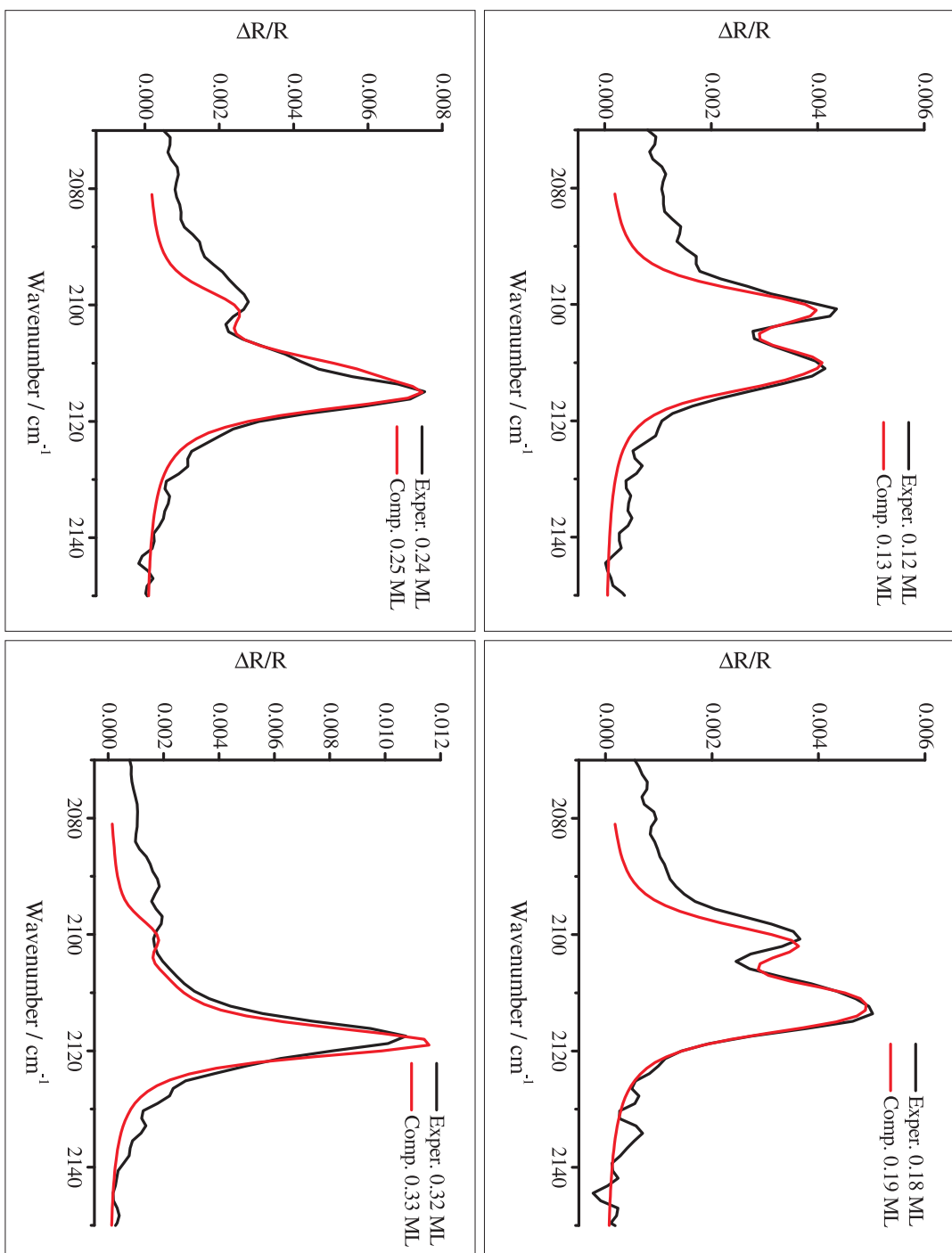


Figure 5.2: RAIIR spectra of CO_{ad} on RuO₂(110): experimental (black curves) and computed (red curves). The computation of the spectra is based on a pure dipole-dipole coupling model. The coverages are indicated in monolayers of CO molecules occupying the on-top sites.

coverage range up to one monolayer was achieved by making the particular choice

$$\Omega_{ot}(\theta) = 2101.5 - 35.2 \theta \quad \text{cm}^{-1} \quad , \quad (5.9)$$

where θ denotes the coverage of on-top sites by CO. For the vibrational polarizability α_V^{ot} of the CO_{ot} molecule we have adopted a value between 0.2-0.3 Å³, rather common in the literature [73] for the absorption bands of CO adsorbed on different transition metals (Ni, Cu, Ru). We have set the distance parameter d between the adsorbed CO molecule and the 'jellium' edge (see also Eq.3.3.1) to 1.7 Å, roughly equal to the geometric distance between the C and Ru atoms.

The electronic polarizability α_e and the vibrational polarizability α_V^{ot} were subsequently adjusted in order to reproduce the series of measured RAIRS spectra. By taking for these parameters the values

$$\begin{aligned} \alpha_e &= 1.12 \text{ Å}^3 \\ \alpha_V^{ot} &= 0.23 \text{ Å}^3 \end{aligned} \quad (5.10)$$

we have computed the series of RAIR spectra shown in Fig.5.2. We note that our best fit value for α_e is about half the value of the electronic polarizability of gas phase CO (2.6 Å³) while α_V^{ot} is practically equal to the vibrational polarizability of CO on other transition metal surfaces, like for instance Cu(100) [73].

In our calculation we have used the vibrational coupling model summarized in Chap.3.3.3, implemented as the computer program listed in App.E. We have considered a pure dipole-dipole coupling according to Eq.3.56, with no short-range chemical coupling ($\chi=0$). We have included the electrostatic image effects by assuming a distance of 3.4 Å between the CO molecule and the plane of image dipoles. Comparison between the experimental and the simulated spectra in Fig.5.2 shows that the dipole-dipole coupling model can fully account for the shapes and positions of the measured absorption bands.

Eq.5.9 is perhaps the most important result of the present simulation. By a careful modeling of the dipole-dipole coupling, we have shown that a downward shift of the single molecule frequency Ω_{ot} from 2101 cm⁻¹ to 2066 cm⁻¹ must accompany an increase in the CO_{ot} coverage. We note that downward chemical shifts of the same magnitude have been experimentally found in CO adsorbed on other oxide surfaces, namely NiO, by using the isotopic dilution method [74].

Chapter 6

RAIRS studies of CO adsorption on the reduced $\text{RuO}_2(110)$ surface

As shown in Chap.4, the stoichiometric $\text{RuO}_2(110)$ surface is characterised by oxygen atoms occupying the bridge positions between a pair of neighboring 2f-cus Ru atoms. During CO oxidation over $\text{RuO}_2(110)$ the bridging oxygen atoms are consumed to an extent regulated by the concentrations of the oxidizing component O_2 and of the reducing component CO in the reactants atmosphere. Under a CO-rich atmosphere, stoichiometric $\text{RuO}_2(110)$ is reduced by the complete replacement of the bridging oxygen atoms by CO molecules. The result is the mildly reduced r- $\text{RuO}_2(110)$ surface.

In order to study the oxidation of CO on RuO_2 by *in situ* RAIRS, it is necessary to make a preliminary RAIRS study of CO adsorption on the reduced $\text{RuO}_2(110)$ surface under UHV conditions.

6.1 Reduction of the $\text{RuO}_2(110)$ surface under UHV conditions

Reduction of the stoichiometric oxide $\text{s-RuO}_2(110)$ to $\text{r-RuO}_2(110)$ under CO exposure at 300 K implies the following elementary reaction steps:

1. adsorption of a CO molecule from gas phase onto a vacant 1f-cus Ru site, in the vicinity of an O_{br} atom;
2. reaction of the adsorbed CO_{ot} molecule with O_{br} to a CO_2 molecule which subsequently desorbs. Removal of O_{br} leaves a vacant bridge site;
3. adsorption of a CO molecule from the gas phase onto the vacant 1f-cus Ru site near the O_{br} vacancy;
4. filling of the O_{br} vacancy by the CO_{ot} molecule adsorbed in the previous step, resulting into a vacant 1f-cus Ru site and a bridging CO_{br} molecule.

By the outlined mechanism all O_{br} can be reduced and the bridge positions completely occupied by CO, provided enough CO is supplied from the gas phase.

6.1.1 Reduced $\text{RuO}_2(110)$ surface terminated by asymmetric bridging CO

The described mechanism suggests a preparation of the reduced oxide film by exposing the surface to several CO adsorption-reaction cycles. Starting with the stoichiometric $\text{RuO}_2(110)$ film, we cool it to 200 K and dose 6 L CO, leading to the complete occupation of the 1f-cus Ru sites, a phase denoted as $\text{O}_{br}/\text{CO}_{ot}$. The $\text{O}_{br}/\text{CO}_{ot}$ phase is identified in the RAIR spectrum by its characteristic CO line at 2123 cm^{-1} (see also the discussion in Chapter 4.4). By heating the $\text{O}_{br}/\text{CO}_{ot}$ phase up to 300 K, most of the O_{br} atoms react with CO_{ot} , the resulting O_{br} vacancies being occupied by CO molecules coming from the 1f-cus Ru sites. The binding energy of the CO molecule in a vacancy of the O_{br} row is as high as 1.74 eV [64]. The CO_{br} molecules occupying such a vacancy are characterized in Fig.6.1 by a C-O stretch band at 1952 cm^{-1} , also measured by HREELS [75].

In Fig.6.1 we assign the 1994 cm^{-1} band to short chains of single-bound neighboring CO_{br} . In the next cycle, by cooling the sample to 200 K and dosing

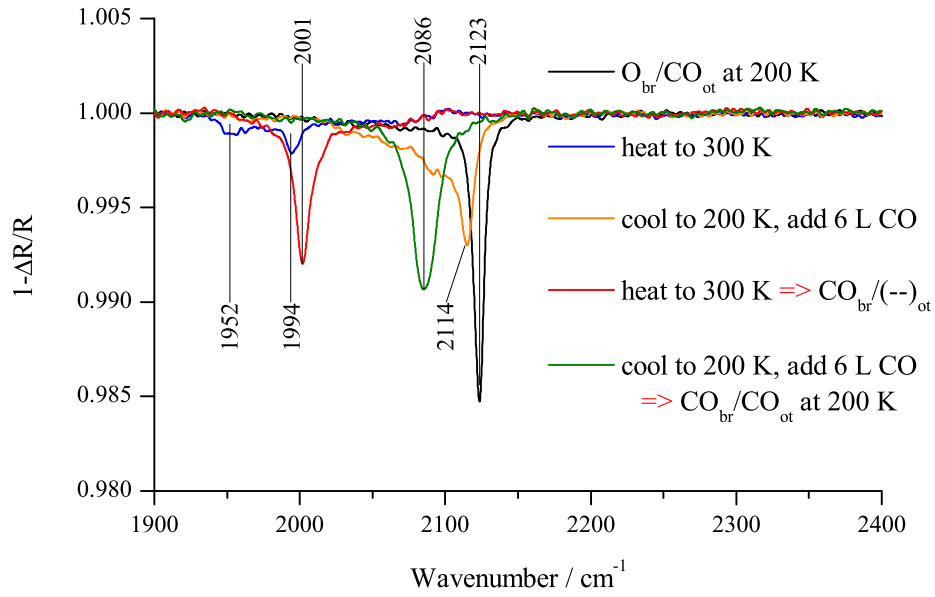


Figure 6.1: Preparation of the $CO_{br}/(-)_{ot}$ phase starting from the O_{br}/CO_{ot} phase on the stoichiometric oxide film through *step-by-step* reduction of O_{br} .

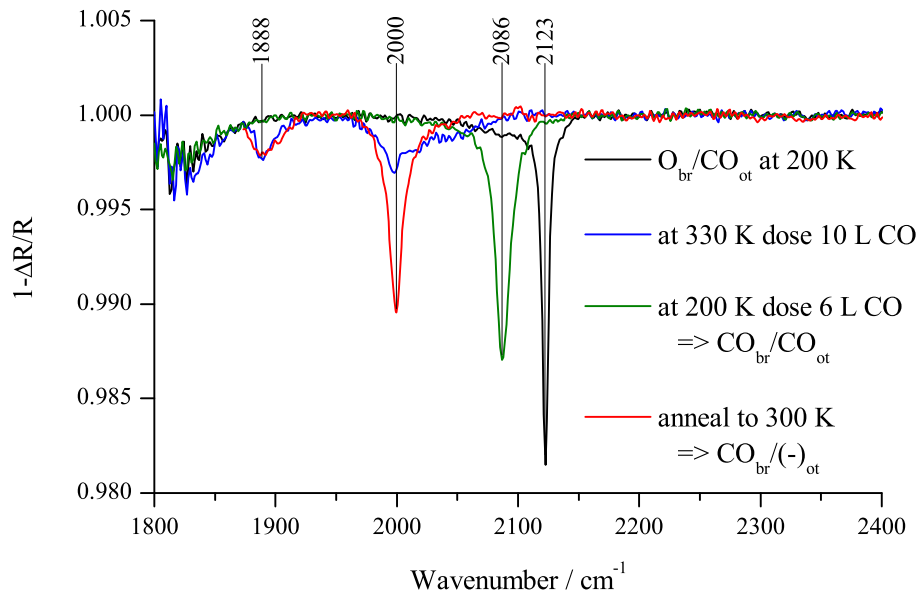


Figure 6.2: Preparation of the $CO_{br}/(-)_{ot}$ phase starting from the O_{br}/CO_{ot} phase on the stoichiometric oxide film through *one-step* reduction of O_{br} .

again 6 L CO, we note that the original CO line has shifted from 2123 cm⁻¹ to 2114 cm⁻¹, indicating that not all O_{br} were reacted away in the first CO exposure cycle. Heating the sample to 300 K, the band at 1994 cm⁻¹ is shifted up to 2001 cm⁻¹ and grows substantially in intensity while the band at 1952 cm⁻¹ disappears. The resulting phase, denoted CO_{br}/(-)_{ot}, is characterised by complete CO_{br} rows and vacant on-top sites. The fact that no O_{br} has remained is easily checked by cooling the sample to 200 K and dosing 6 L CO, when we obtain a band at 2085 cm⁻¹, which is characteristic of a well ordered CO_{br}/CO_{ot} phase (see below).

We have searched for an alternative, more direct procedure based on the total reduction of O_{br} in a single preparation step (Fig.6.2). By exposing the O_{br}/CO_{ot} phase (black curve) to 10 L CO at 330 K, a mildly reduced RuO₂(110) surface is obtained, the bridge positions being now occupied by two CO_{br} species, as identified by the IR bands at 1888 cm⁻¹ and 1998 cm⁻¹ (blue curve). The 1888 cm⁻¹ band corresponds to symmetric bridging CO_{br}. The 2000 cm⁻¹ band is characteristic of complete rows of CO_{br}. By cooling the sample to 200 K and adsorbing CO to saturation we get the 2086 cm⁻¹ band, which is characteristic a phase where the bridge sites are occupied by asymmetric bridging CO and the on-top sites are also occupied by CO. In the following we shall denote this phase as CO_{br}/CO_{ot}. If we wish to prepare a reduced oxide surface exhibiting only asymmetric bridging CO, we have to free up the 1f-cus Ru sites by annealing the CO_{br}/CO_{ot} phase to a temperature high enough to desorb CO_{ot}. By annealing to 300 K we get an asymmetric CO_{br} population (the 2000 cm⁻¹ band on the red curve) much enhanced compared to the original one, but at the same time the population of symmetric bridging CO_{br} (the 1888 cm⁻¹ band) is also exactly restored.

We have tested various other prescriptions for the preparation of a CO layer consisting only of asymmetric CO_{br}, but all of them have at the same time led to a considerable population of symmetric CO_{br}. This observation is in agreement with previous HREELS studies [75] where the peak at 2000 cm⁻¹ was always found accompanied by a band at 1887 cm⁻¹. The authors note that in an ordered chain of asymmetric CO_{br} molecules vacancies can spontaneously occur, in which one of the neighboring CO molecules switches to double coordination.

6.1.2 CO on reduced RuO₂(110) under UHV conditions

The sample was cooled to 110 K, when a reference spectrum was taken at 1×10^{-9} mbar residual gas pressure. The oxide surface was then mildly reduced, as described in Fig.6.1 (red curve). The starting template (curve (a) of Fig.6.3) is therefore a reduced RuO₂(110) surface with the bridge positions occupied by asymmetric bridging CO_{br}. The adsorption experiment was started by setting a constant 3×10^{-9} mbar CO background pressure in the UHV/HP cell. At the same time, FT-RAIR spectra were recorded at 4 cm⁻¹ resolution by averaging of ten scans. Each spectrum was recorded in 7 seconds, which has enabled us to follow in detail the filling of the 1f-cus Ru sites by gas phase CO. The CO layer saturated after 1.8 L CO total exposure, during which 100 spectra were recorded.

At low coverages the formation of small groups of neighboring CO_{ot} adsorbates can be recognized. We assign the very distinct band emerging at 2016 cm⁻¹ (Fig.6.3, after 90 s dosing) to CO_{ot} isolated on the still largely empty rows of 1f-cus Ru sites between complete rows of asymmetric CO_{br}. After 120 s exposure a shoulder has appeared at 2024 cm⁻¹, which in short time is going to outgrow the initial 2016 cm⁻¹ band. As the 2024 cm⁻¹ band reaches its maximal amplitude, the next band appears at 2034 cm⁻¹, after about 200 s. Above this CO exposure (0.45 L) we see only a single, wide band which shifts up to 2048 cm⁻¹ after 280 s exposure, when the band at 2057 cm⁻¹ becomes visible. During the last stages of CO adsorption, the band shifts first to 2074 cm⁻¹ and then reaches its saturation position at 2086 cm⁻¹, with complete rows of CO_{ot} between rows of asymmetric CO_{br}. The shift of the collective IR band from 2074 cm⁻¹ to 2086 cm⁻¹ corresponds to occupation of the on-top sites by CO at coverages between 0.50 to 0.66.

6.1.3 Reduced RuO₂(110) surface terminated by symmetric bridging CO

Quite contrary to the previous case, a reduced RuO₂(110) surface exhibiting only symmetric CO_{br}^{II} and empty 1f-cus-Ru sites has been prepared [64] by exposing the s-RuO₂(110) surface to 5 L CO at 170 K followed by flash annealing to 400 K (repeated three times). The surface has been studied by a combined DFT and

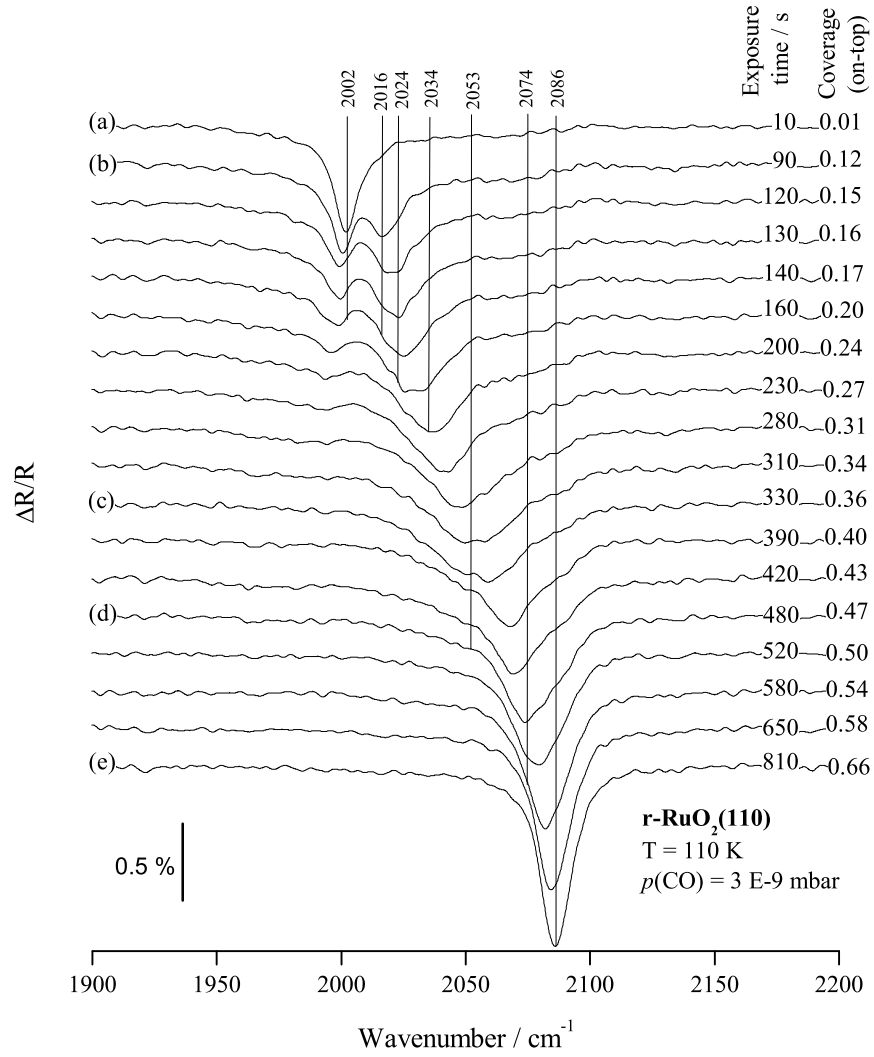


Figure 6.3: Adsorption of CO on the reduced $\text{RuO}_2(110)$ surface at 3×10^{-9} mbar CO and 110 K. The coverage is indicated in monolayers of on-top CO.

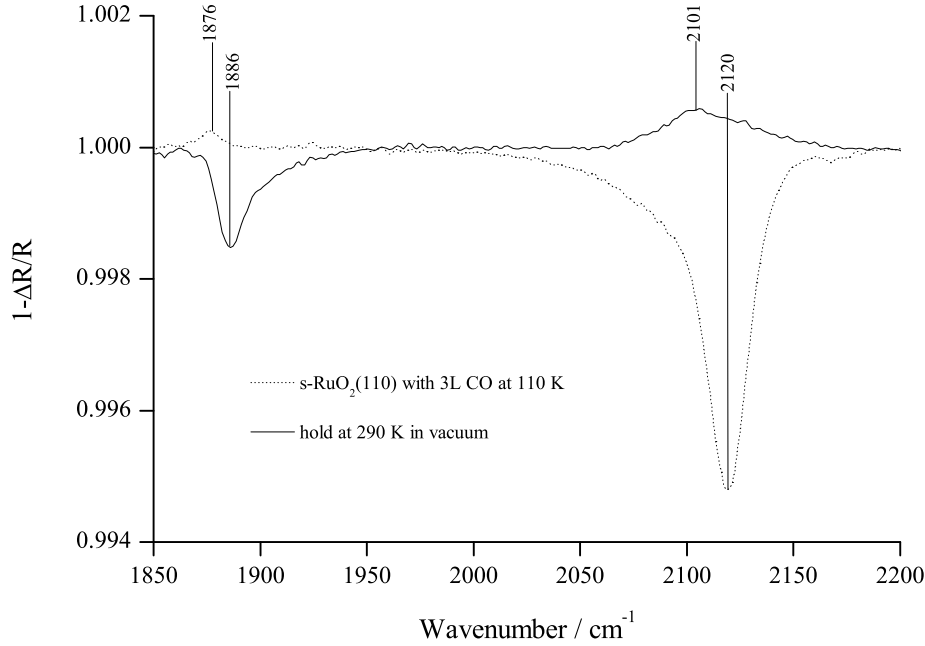


Figure 6.4: Preparation of a reduced $r\text{-RuO}_2(110)$ surface exhibiting only symmetric CO_{br}^{II} . The inverse bands at 1876 cm^{-1} and 2101 cm^{-1} correspond respectively, to isolated CO_{br}^{II} and CO_{ot} on the *reference* $s\text{-RuO}_2(110)$ surface.

LEED approach. The authors notice that symmetric CO_{br}^{II} does not arrange into an ordered (2×1) phase because of the high diffusion barrier of CO along the rows of 2f-cus Ru atoms. The same surface has also been observed by HREELS [75]. After exposing the stoichiometric $s\text{-RuO}_2(110)$ surface to 0.4 L CO at 300 K, a strong line at 2000 cm^{-1} and a much weaker band at 1887 cm^{-1} were observed. The first peak was attributed to asymmetric CO_{br} and the second, to symmetric CO_{br}^{II} . By repeated cycles of annealing to 450 K followed by cooling to 300 K and adsorption of 0.4 L CO, the 2000 cm^{-1} line has gradually disappeared while the 1887 cm^{-1} band has shifted to 1893 cm^{-1} with much enhanced intensity [75].

In the present thesis we have prepared a reduced surface terminated only by symmetric CO_{br}^{II} , and observed it by RAIRS. The stoichiometric $s\text{-RuO}_2(110)$ surface was flash-annealed to 500 K and cooled to 300 K in 2×10^{-7} mbar O_2 . After evacuation of the oxygen no second annealing was made, with the result that the 1f-cus Ru atoms remained capped by O_{ot} , to a percentage of about 80%. Next, the sample was annealed in vacuum to 500 K to desorb O_{ot} then cooled to 110 K, after which the background spectrum was recorded. At 110 K the sample was exposed to 3 L CO, the spectrum (dotted curve, Fig.6.4) showing,

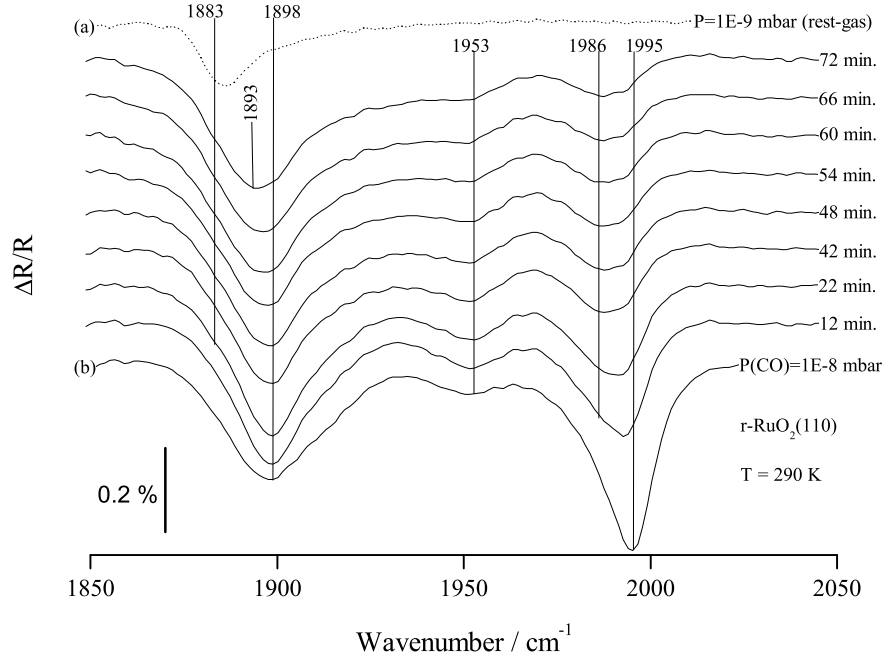


Figure 6.5: Relaxation of CO_{br} species under UHV. On the $\text{CO}^{II}/(-)$ surface (a), adsorbed CO is in equilibrium at 290 K with 1×10^{-8} mbar CO (b) then slowly desorbs after evacuation of the chamber to 1×10^{-9} mbar base pressure.

besides the $\text{O}_{br}/\text{CO}_{ot}$ line at 2120 cm^{-1} , a tiny (0.02%) upward peak at 1876 cm^{-1} corresponding to a small number of CO_{br}^{II} trapped in the otherwise complete O_{br} rows of s- RuO_2 . The line at 1876 cm^{-1} points upwards because it corresponds to a species (CO_{br}^{II}) present on the surface used for measuring the reference spectrum. Finally, by annealing to 290 K (solid curve, Fig.6.4) we end with a $\text{CO}_{br}/(-)_{ot}$ phase consisting mainly of symmetric CO_{br}^{II} , as proved by the shifted, now much enhanced peak at 1886 cm^{-1} .

We consider next CO adsorption on the $\text{CO}_{br}^{II}/(-)_{ot}$ surface at room temperature. We start by exposing the reduced surface as prepared (curve (a) in Fig.6.5) to 1×10^{-8} mbar CO at 290 K for 20 minutes (curve (b) in Fig.6.5). The chamber is then evacuated to base pressure of 1×10^{-9} mbar, after which RAIR spectra are recorded each 6 minutes for about one hour.

The initial surface (curve (a) in Fig.6.5) is the initial $\text{CO}_{br}^{II}/(-)_{ot}$ surface with a population of symmetric CO_{br}^{II} , as shown by the band at 1886 cm^{-1} . As already noted, these adsorbates do not complete an extended (2×1) structure, they can only fill more or less randomly the bridge sites. After reaching the maximal equilibrium CO coverage at room temperature (curve (b) in Fig.6.5) we note that

the initial 1886 cm⁻¹ band has shifted to 1898 cm⁻¹ with a substantial increase in width and amplitude. Additionally, a weak band appears at 1953 cm⁻¹ and a strong and narrow one at 1995 cm⁻¹. After evacuation of the chamber, the CO layer relaxes to a new equilibrium structure characterised mainly by the diminution of the 1995 cm⁻¹ band to a weak remnant at 1986 cm⁻¹. The CO_{br}^{II} band suffers a 5 cm⁻¹ downward shift to 1883 cm⁻¹ but remains, like the 1953 cm⁻¹ band, essentially unchanged. We assign the 1953 cm⁻¹ band to CO adsorbed into the vacancies of the rows of O_{br}, which is compatible to the assignment from HREELS measurements [75].

6.2 Coadsorption of CO and O on RuO₂(110)

The prospect of studying the surface of the RuO₂ catalyst *in-situ* by RAIRS during the CO oxidation reaction requires the identification, based on their IR characteristic frequencies, of complex configurations of CO coadsorbed with O atoms. During the oxidation reaction, the adsorbates are more or less randomly distributed on the surface of the catalyst, their configurations being properly characterised only in statistical terms. Under UHV conditions, these complex configurations cannot be reproduced in a manner precise enough to assign IR lines to certain adsorbate configurations. In the current section we shall study two special cases instead, which can be considered as a guide in assigning IR lines in more complex adsorbate phases under reaction conditions.

6.2.1 Adsorption of O on the reduced RuO₂(110) surface

The O_{br} atoms on the stoichiometric RuO₂(110) surface were reduced and replaced by CO_{br} through exposure to 10 L CO at 330 K. The sample was subsequently flashed to 360 K to desorb eventual remaining on-top CO_{ot}. The reduced RuO₂(110) surface exhibits free 1f-cus Ru sites and rows of CO_{br}, characterised by an IR line at 2000 cm⁻¹ (dotted curve, Fig.6.6). The sample was cooled to 150 K and 3 L O₂ were dosed in order to reach the maximal coverage of the 1f-cus Ru sites, the resulting phase being denoted CO_{br}/O_{ot}. Adsorption of O in the vicinity of the vibrating rows of CO_{br} resulted in a blueshift of the collective IR band up to 2046 cm⁻¹ (solid curve, Fig.6.6). Additionally, a wide but much weaker band was routinely observed about 2080 cm⁻¹.

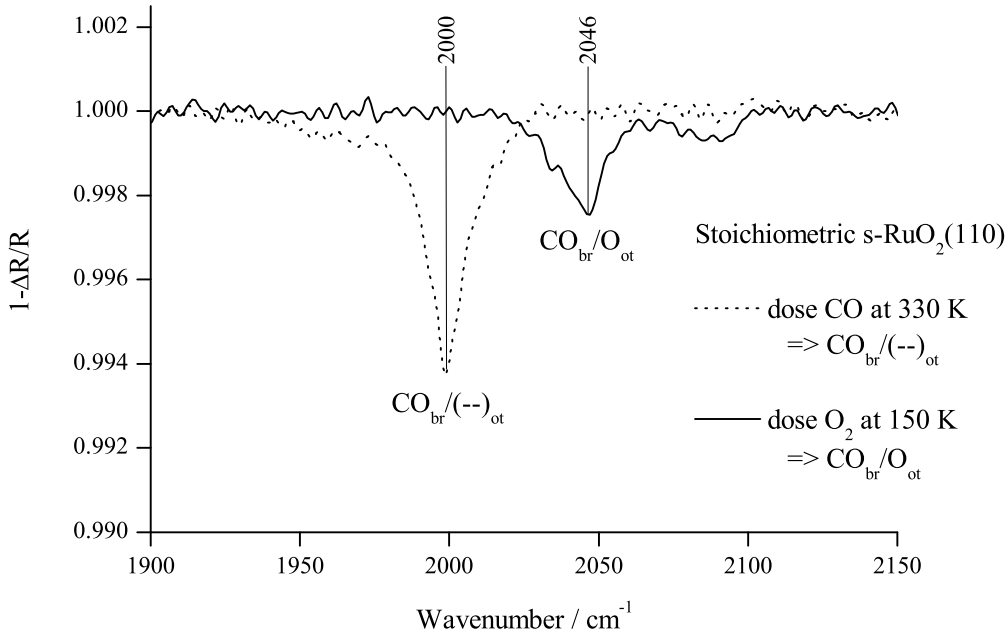


Figure 6.6: Coadsorption of O_{ot} with CO_{br} on the reduced $\text{RuO}_2(110)$ surface. The initial line (2000 cm^{-1}) of CO_{br} suffers a blueshift (2046 cm^{-1}) when O_{ot} occupies the 1f-cus Ru sites.

The reduced $\text{RuO}_2(110)$ surface was exposed to oxygen at low temperature in order to prevent the reaction of oxygen with CO_{br} . The O_2 molecules adsorb dissociatively on pairs of neighboring free 1f-cus Ru sites, where they remain immobile owing to diffusion barriers as large as 1 eV along the rows. At low temperature, this precludes the complete occupation of the 1f-cus Ru sites by O. This intrinsic degree of disorder in the $\text{CO}_{br}/\text{O}_{ot}$ layer manifests in the RAIR spectrum as a low frequency tail of the 2046 cm^{-1} band, due to CO_{br} molecules which have less O_{ot} in their neighborhood. These CO_{br} vibrate at lower frequencies as a consequence of a relatively stronger local $2\pi^*$ backdonation. More precisely, in some instances of the same experiment, the 2046 cm^{-1} $\text{CO}_{br}/\text{O}_{ot}$ band could be resolved into a 2034 cm^{-1} and a 2046 cm^{-1} line (Fig.6.7). The parameters of the individual lorentzian lines composing this RAIR spectrum are given in Tab.6.1. We note that the sum of the integrated intensities of the lines composing the $\text{CO}_{br}/\text{O}_{ot}$ spectrum approximately equals the integrated intensity of the initial $\text{CO}_{br}/(-)_{ot}$ band. Adsorption of O_{ot} in the vicinity of CO_{br} has essentially led to a redistribution of the IR intensity from the initial band to new bands at higher frequencies.

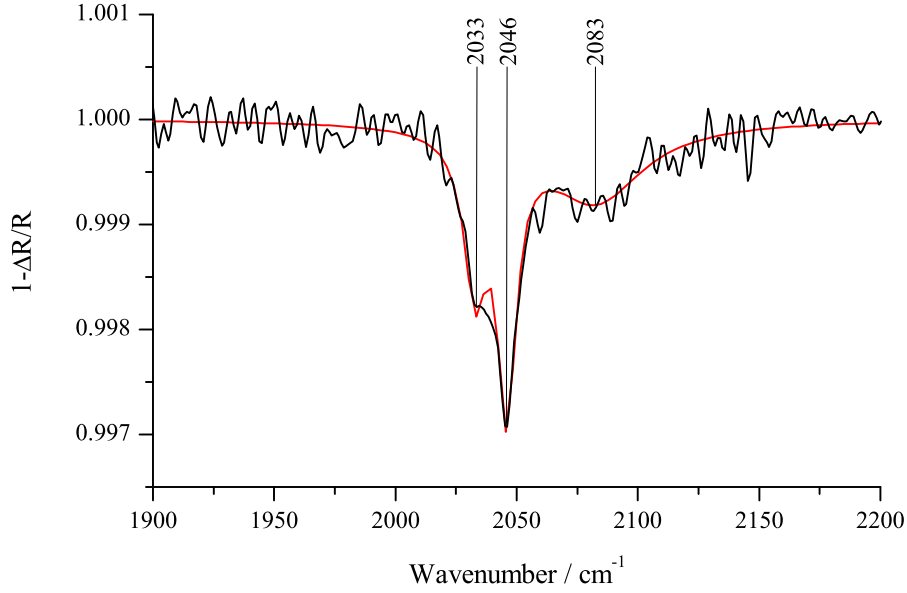


Figure 6.7: RAIR spectrum of a CO_{br}/O_{ot} layer obtained by saturating the reduced r-RuO₂(110) surface with oxygen at 220 K. The red curve is a deconvolution with three lorentzian lines (Tab.6.1.)

Phase	Wavenumber /cm ⁻¹	FWHM /cm ⁻¹	Int. intensity /cm ⁻¹
CO _{br} /(-) _{ot}	2001	14	0.129
CO _{br} /O _{ot}	2033	11	0.025
	2046	9	0.036
	2083	48	0.058

Table 6.1: Lorentzian parameters of the IR lines of CO_{br} on the reduced RuO₂(110) surface before (dotted curve, Fig. 6.6) and after adsorption O_{ot} (Fig.6.7.)

6.2.2 Adsorption of CO on the O-saturated stoichiometric $\text{RuO}_2(110)$ surface

The second CO-O coadsorbate structure we investigated with RAIRS consists of CO adsorbed into the vacancies of a saturated $\text{O}_{br}/\text{O}_{ot}$ layer on stoichiometric $\text{RuO}_2(110)$. Following the standard restoration procedure described in Chap.4.4, the stoichiometric $\text{RuO}_2(110)$ surface was exposed to 20 L O_2 at 400 K. We have dosed oxygen at this particular temperature in order to get a possibly complete saturation of the 1f-cus Ru sites. O_2 adsorbs dissociatively on a pair of neighboring 1f-cus Ru sites, the resulting O_{ot} possessing only a limited mobility along the rows. For this reason, the sample temperature during oxygen exposure had to be set high enough to allow to O_{ot} sufficient mobility to uniformly fill the 1f-cus Ru rows. On the other hand, the sample temperature had to be kept low enough to avoid significant desorption (500 K) of this weakly held species. Subsequent saturation of the surface with 6 L CO at 200 K has confirmed that most of the 1f-cus Ru sites were capped by O_{ot} atoms, the RAIR spectrum showing a rather weak, well profiled line at 2152 cm^{-1} (solid curve, Fig.6.8). We assign this IR line to single CO_{ot} molecules on the O-saturated stoichiometric $\text{RuO}_2(110)$ surface, separated from each other by sequences of O_{ot} . We note that *total* capping of the 1f-cus Ru sites by O was achieved by exposing the stoichiometric $\text{RuO}_2(110)$ surface at 380 K. No adsorbed CO being subsequently detected by RAIRS.

Isolated CO_{ot} molecules (singletons) adsorbed in between full rows of O_{br} on the stoichiometric $\text{RuO}_2(110)$ surface, are characterised by a weak but well defined line at 2100 cm^{-1} (dotted curve, Fig.6.8). When further O_{ot} are adsorbed, up to saturation of the 1f-cus Ru sites, we get an $\text{O}_{br}/\text{O}_{ot}$ layer sparsely populated by CO_{ot} . Each of this isolated CO_{ot} molecules is enclosed in a 'cage' formed by neighboring O_{br} and O_{ot} atoms. On the O-saturated surface, CO_{ot} has two more O_{ot} atoms in its immediate vicinity. A local decrease in the electron density due to the two additional O_{ot} atoms leads to a weaker backdonation into the $2\pi^*$ antibonding orbitals of CO_{ot} and a subsequent stabilization of the internal C-O bond, associated with a 52 cm^{-1} blueshift in the CO stretch frequency (solid curve, Fig.6.8). The lorentzian parameters of the two vibrational lines are given in Tab.6.2. We note that the integrated intensity of the initial CO line remains preserved upon oxygen adsorption in the vicinity of the vibrating CO_{ot} . This observation suggests that the vibrational dipole moment of CO_{ot} or more

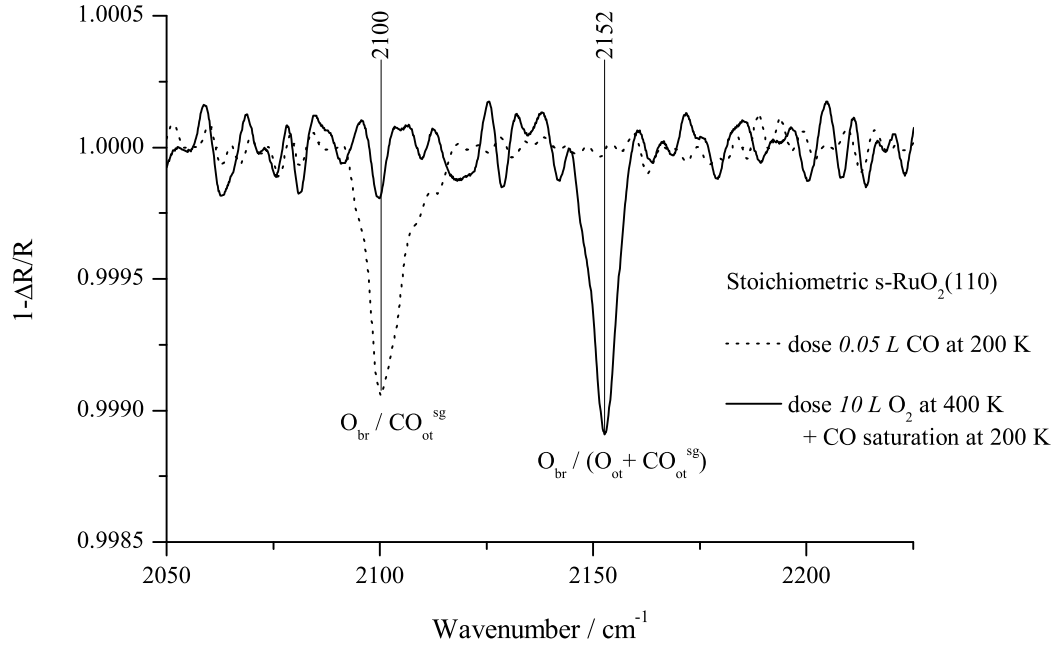


Figure 6.8: IR spectra of isolated CO_{ot} adsorbed on the stoichiometric RuO₂(110) surface (dotted curve) and on the O-precovered RuO₂(110) surface (solid curve). Difference in the noise levels: IR spectra recorded with 100, respectively 10 scans.

Phase	Wavenumber /cm ⁻¹	FWHM /cm ⁻¹	Int. intensity /cm ⁻¹
O _{br} /(-) _{ot}	2100.8	8.7	0.012
O _{br} /O _{ot}	2152.6	6.4	0.012

Table 6.2: Lorentzian parameters of the IR lines (Fig.6.8) of isolated CO_{ot} coadsorbed on the stoichiometric RuO₂(110) surface with the indicated O-phases.

precisely, its vibrational polarizability, remain largely unaffected by coadsorption of oxygen.

6.3 Adsorption of CO on the RuO₂(110) surface at high pressure

We present in the following a RAIRS study of the RuO₂(110) film in a pressure domain usually not directly accessible by standard UHV spectroscopies. In the UHV/HP cell (batch mode) the stoichiometric s-RuO₂(110) film is held at 230 K under 3×10^{-3} mbar constant CO pressure until all O_{br} are reacted off and replaced by CO_{br}. At 230 K the reduction process takes as long as 60 minutes

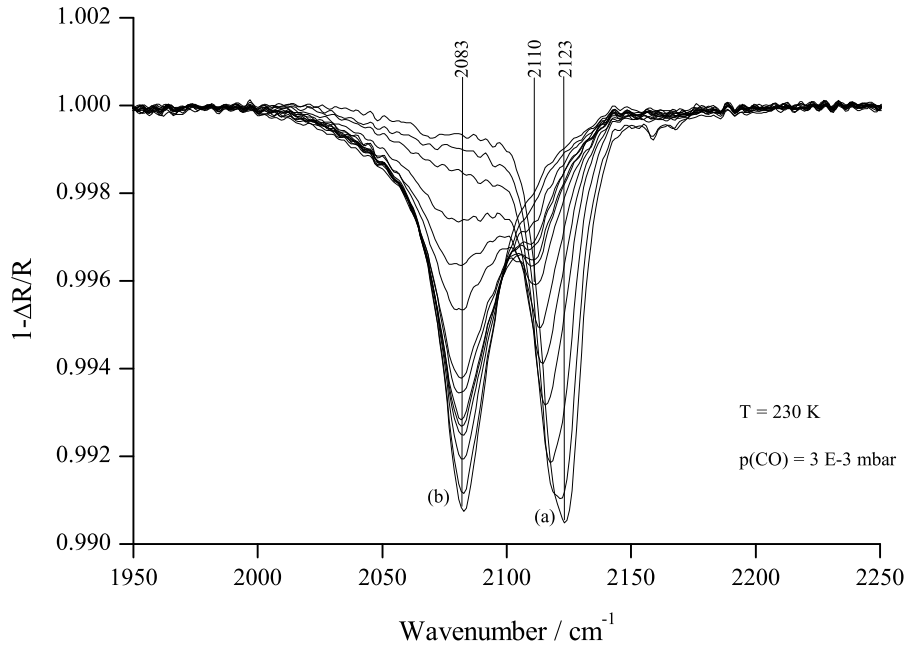


Figure 6.9: Reduction of s- $\text{RuO}_2(110)$ at 230 K under 3×10^{-3} mbar CO. Adsorbed CO on the stoichiometric (a) and after 60 min., on the reduced (b) oxide surface.

to complete, a time interval which permits detailed step by step monitoring by RAIRS (Fig.6.9). Spectra were repeatedly recorded 7.2 s apart with 4 cm^{-1} resolution by averaging of 10 scans/spectrum.

The line at 2123 cm^{-1} corresponds to complete rows of CO_{ot} in between the O_{br} rows of the stoichiometric surface (the $\text{O}_{br}/\text{CO}_{ot}$ phase). When CO_{ot} reacts with O_{br} , vacancies appear in the rows of O_{br} , which are immediately filled by CO molecules stepping in from above the 1f-cus Ru sites. During the whole reduction process, the rows of 1f-cus Ru sites remain practically saturated with CO_{ot} while the rows of O_{br} are gradually depleted and replaced with CO_{br} . Depletion of the O_{br} rows manifests itself in the continuous downward shift of the $\text{O}_{br}/\text{CO}_{ot}$ line from 2123 cm^{-1} to 2110 cm^{-1} . This downward shift can be understood as originating in an increased backdonation into the $2\pi^*$ CO orbitals, following depletion of the more electronegative O_{br} (compared to CO_{br}) species. At 2110 cm^{-1} the downward shift of the $\text{O}_{br}/\text{CO}_{ot}$ line stops but the line diminishes further. Parallel to the involution of the $\text{O}_{br}/\text{CO}_{ot}$ line, the $\text{CO}_{br}/\text{CO}_{ot}$ characteristic line emerges at 2083 cm^{-1} and grows without shifting its position. The $\text{CO}_{br}/\text{CO}_{ot}$ phase consists of CO_{ot} in between full rows of asymmetric CO_{br} .

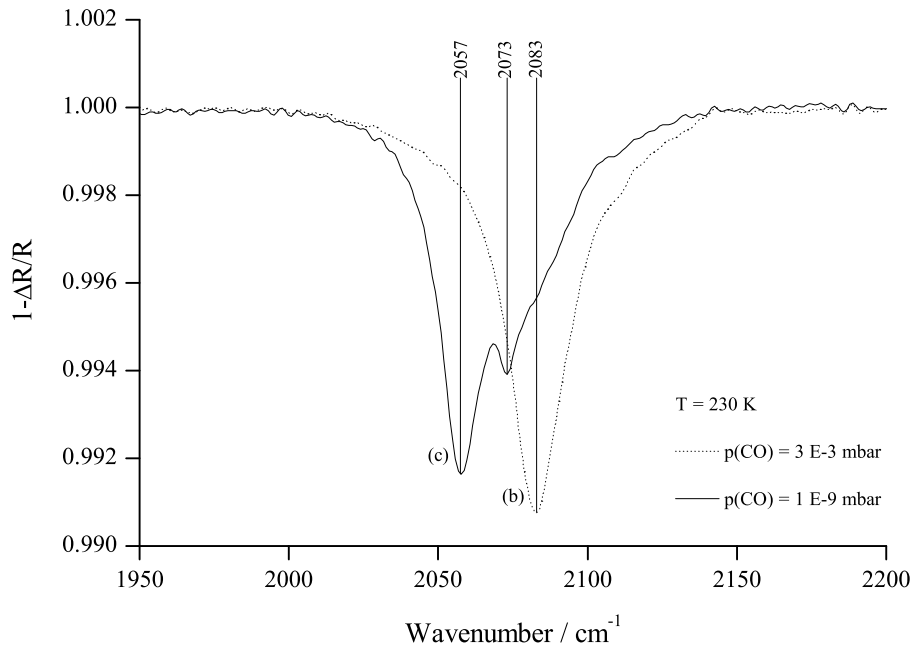


Figure 6.10: At 230 K the saturated CO_{br}/CO_{ot} phase (b) is stable under 3×10^{-3} mbar CO, but it relaxes to the state (c) as the chamber is evacuated to 1×10^{-9} mbar base pressure.

In the second part of the experiment, the UHV/HP cell is evacuated to 1×10^{-9} mbar base pressure (Fig.6.10). Under 3×10^{-3} mbar CO pressure the CO_{br}/CO_{ot} phase (b) is saturated, as shown by the characteristic 2083 cm⁻¹ line. After evacuation of the UHV/HP cell, the CO_{br}/CO_{ot} adsorbate layer has relaxed to a new structure (c). The original 2083 cm⁻¹ line has diminished to an unapparent shoulder while two new lines emerged, a more intense one at 2057 cm⁻¹ and a weaker but well profiled one at 2073 cm⁻¹. The transformation from the saturated (b) to the relaxed CO_{br}/CO_{ot} phase (c) is reversible, as checked by keeping the sample at 230 K and gradually increasing the CO pressure up to 1×10^{-2} mbar (Fig.6.11). It is interesting to note that the relaxed state (c) of the CO adsorbate can also be reached under isobaric conditions, by gradually heating the saturated CO_{br}/CO_{ot} phase up to 340 K under 3×10^{-3} mbar constant CO pressure (Fig.6.12). Despite the relatively high CO pressure during this series of experiments, the RuO₂(110) surface was only mildly reduced, as proved by the fact that the oxide film could subsequently be restored to its reference state (Fig.4.6) by the restoration procedure described in Chap.4.4.

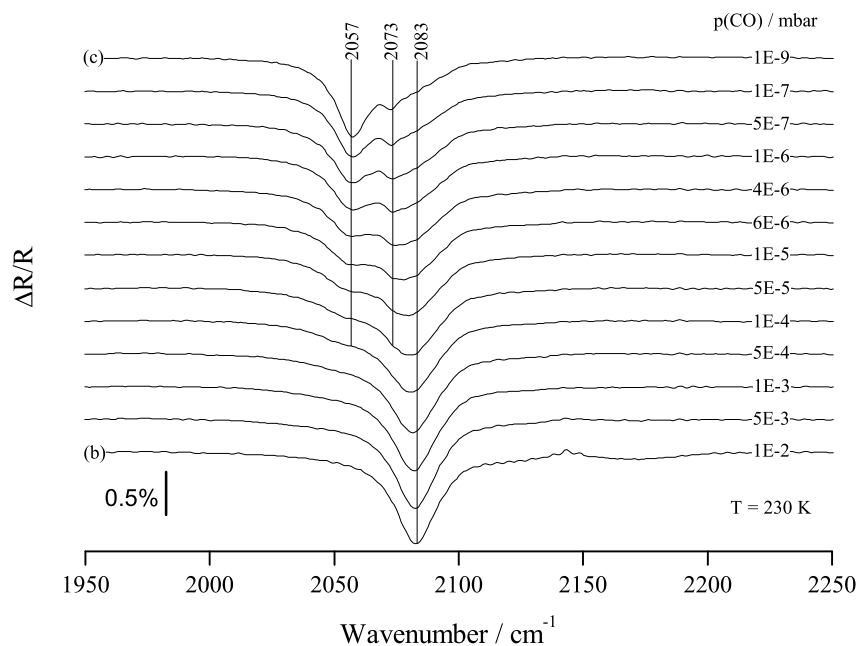


Figure 6.11: The state (c) of the CO adsorbate transforms reversibly into the saturated $\text{CO}_{br}/\text{CO}_{ot}$ phase (b) as the CO pressure is increased isothermally at 230 K.

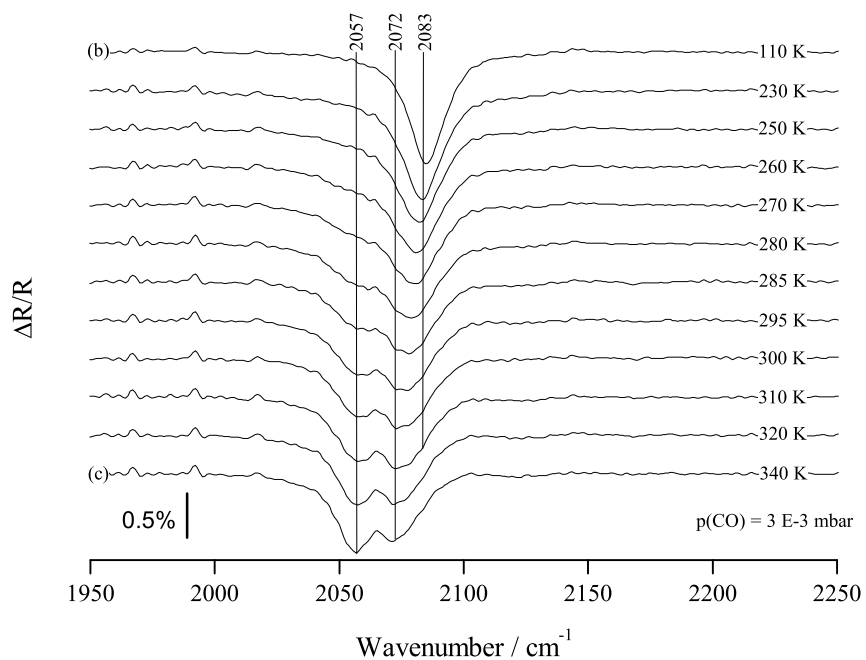


Figure 6.12: The state (c) of the CO adsorbate is reproduced under isobaric conditions by annealing the saturated $\text{CO}_{br}/\text{CO}_{ot}$ phase (b) to 340 K in 3×10^{-3} mbar CO.

6.4 Structural transformations of the reduced $\text{RuO}_2(110)$ surface

The present section contains a RAIRS study of the reduction process of the $\text{RuO}_2(110)$ film. The first part is concerned with the *restoration*, to the stoichiometric structure, of a mildly reduced $\text{RuO}_2(110)$ surface. The second part is devoted to the study of the heavy reduction process of the $\text{RuO}_2(110)$ film to metallic Ru, by exposure to 10^{-3} mbar CO at 400 K.

6.4.1 Partial restoration of the reduced $\text{RuO}_2(110)$ film by diffusion of structure-bound oxygen

Wendt *et al.* [76] have observed that after removing all bridging O_{br} atoms from the stoichiometric s- $\text{RuO}_2(110)$ surface by exposure to CO at 300 K, the resulting mildly reduced r- $\text{RuO}_2(110)$ surface could no longer produce CO_2 when exposed to CO below 400 K. However, annealing the sample to 570 K was found to reactivate the mildly reduced r- $\text{RuO}_2(110)$ surface. The reactivation was manifested in that exposing CO at 170 K to the annealed sample and subsequent cycling of the sample temperature to 500 K has resulted into the formation of CO_2 . The authors [76] have attributed the reactivation of the mildly reduced r- $\text{RuO}_2(110)$ surface to the repopulation of the bridge sites by O_{br} atoms, upon annealing the sample to 570 K. They have pointed out that the oxygen atoms, necessary for the repopulation of the bridge sites, are supplied either by O diffusion from the RuO_2 bulk or by the decomposition of the uppermost $\text{RuO}_2(110)$ layer. The second possibility was suggested by the available STM data [8, 54]. In a series of TPR, LEED and HREELS experiments, Wendt *et al.* have shown that the reactivation of the annealed r- $\text{RuO}_2(110)$ surface is indeed due to the restoration of the O_{br} species [76].

The current section is dedicated to a series of RAIRS experiments aiming at an IR spectroscopic proof of the mentioned restoration process. Within the framework of the present thesis, we see two essential aspects of these experiments. First, they are intended to complement the cited evidence with new experimental data. Their second role is to assess the potential of RAIRS in the study of rather complex surface phenomena, such as the restructuring (restoration) of the $\text{RuO}_2(110)$ surface upon annealing.

Prior to the experiments, the RuO₂(110) film was restored to the ordered stoichiometric structure by flash-annealing to 700 K in 2×10^{-7} mbar O₂ followed by evacuation of oxygen with the sample held at 300 K and a second annealing to 500 K in vacuum (for details see Chap.4.4). The standard RAIRS quality check of the restored oxide consisted in dosing 6 L CO at 170 K (Fig.4.6) all subsequent RAIR spectra being divided by the background taken at this step. The restored RuO₂(110) film was subsequently mildly reduced by exposure to 10 L CO at 330 K (blue curve in Fig.6.2) resulting into a RuO₂(110) surface without O_{br}, as confirmed by the emergence of the CO_{br}/CO_{ot} characteristic peak at 2086 cm⁻¹ after dosing 6 L CO at 200 K (green curve in Fig.6.2). After this step, the oxide film is a reduced r-RuO₂(110) surface five oxide layers (15 Å) thick [53], terminated by a saturated CO_{br}/CO_{ot} layer. This surface is the template of the actual experiment.

Results

The experiment consisted in annealing the template to a preset temperature followed by cooling to 200 K, exposure to 6 L CO and the recording of a RAIR spectrum. The next cycles were completed according to the same prescription for restoration, mild reduction and annealing, each time to a higher preset temperature. Each cycle was ended by cooling the sample to 200 K and dosing 6 L CO, after which a RAIR spectrum was recorded (Fig.6.13). Annealing the reduced surface to 330 K, the IR spectrum shows a single band at 2090 cm⁻¹. Increasing the annealing temperature in steps of 10 K, we could follow the simultaneous development of shoulders at 2083 cm⁻¹ and 2110 cm⁻¹. After annealing the sample to 400 K, the 2083 cm⁻¹ and 2110 cm⁻¹ bands are both fully developed, while the 2090 cm⁻¹ band has vanished. Annealing the sample in the 400-500 K range, we see the 2083 cm⁻¹ band diminishing until disappearance at about 500 K. For annealing temperatures in the 400-600 K range, the high frequency CO band shifts progressively from 2110 cm⁻¹ to 2123 cm⁻¹. After annealing the reduced r-RuO₂(110) surface to 600 K, the RAIR spectrum consists of a single, fully developed band at 2123 cm⁻¹. This band is identical to the absorption band of the ordered O_{br}/CO_{ot} phase on the stoichiometric s-RuO₂(110) surface (Fig.4.6).

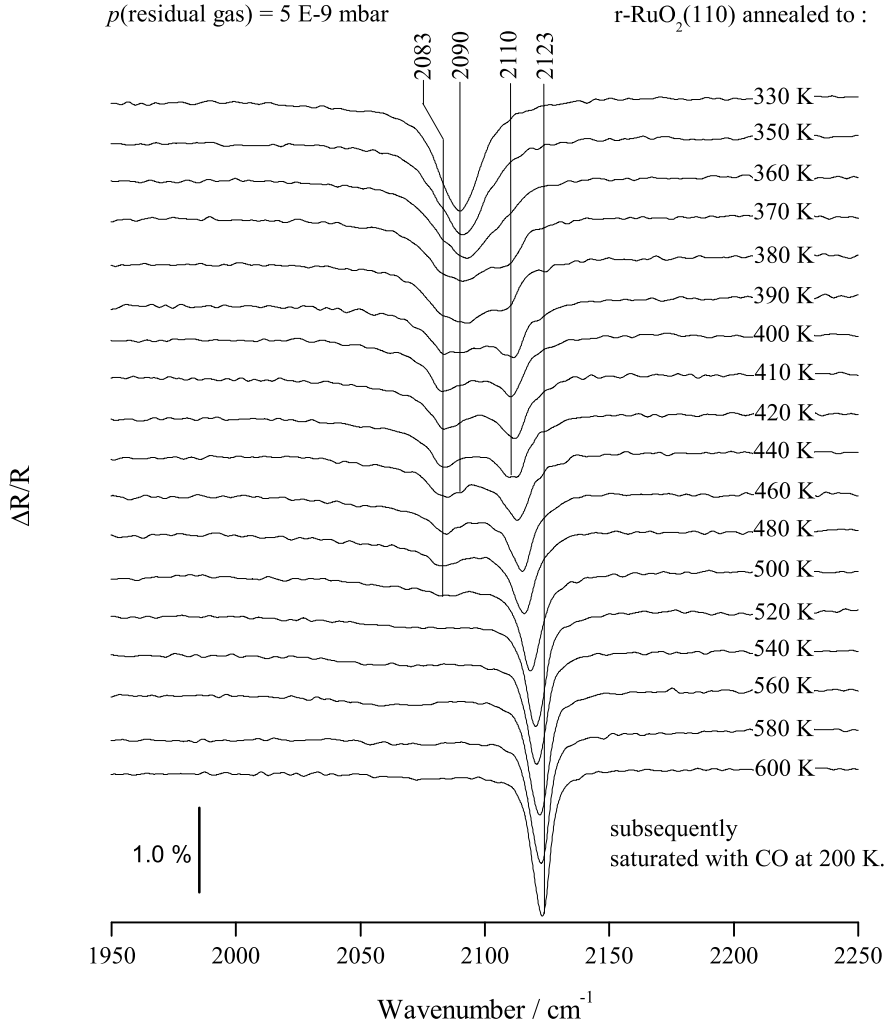


Figure 6.13: Restoration of the mildly reduced $\text{r-RuO}_2(110)$ surface to the stoichiometric $\text{s-RuO}_2(110)$ structure, upon annealing the sample in vacuum. For each measurement, a pristine stoichiometric $\text{RuO}_2(110)$ surface was exposed to 10 L CO at 330 K and subsequently annealed in vacuum to the indicated temperature. The RAIR spectrum was recorded after cooling the sample to 200 K and saturating the surface with 6 L CO. The band at 2090 cm^{-1} corresponds to the saturated $\text{CO}_{br}/\text{CO}_{ot}$ phase. The 2123 cm^{-1} band is characteristic of the $\text{O}_{br}/\text{CO}_{ot}$ phase on the stoichiometric $\text{s-RuO}_2(110)$ surface. Annealing the sample in the 420-600 K range, the $2110\text{-}2123\text{ cm}^{-1}$ shift of the CO band indicates the emergence of increasingly longer O_{br} sequences, proving that the mildly reduced oxide surface is being progressively restored to the stoichiometric $\text{s-RuO}_2(110)$ structure.

Discussion

The 2090 cm⁻¹ frequency of the initial CO band is somewhat higher than the 2083 cm⁻¹ characteristic frequency of the saturated CO_{br}/CO_{ot} phase. This observation suggests the presence of isolated O_{br} atoms in the otherwise saturated CO_{br}/CO_{ot} layer¹. As the annealing temperature is increased up to about 400 K, the 2083 cm⁻¹ and 2110 cm⁻¹ bands are developing while the 2090 cm⁻¹ band is decreasing. The surface processes responsible for these evolutions may be understood with reference to our RAIRS experiments concerning CO adsorption on the stoichiometric s-RuO₂(110) surface, presented in Chap.5. We recall that by exposing the stoichiometric s-RuO₂(110) surface to a small CO dose at low temperature, the CO molecules adsorb onto the 1f-cus Ru sites either as isolated CO_{ot} or by forming short sequences of few CO_{ot} molecules. The RAIR spectra show that isolated CO_{ot} molecules vibrate at 2101 cm⁻¹ while, due to the coupling of vibrations in neighboring molecules, sequences of two and three CO_{ot} molecules vibrate at 2110 cm⁻¹ and 2114 cm⁻¹ respectively (Fig.5.1, Tab.5.1). We stress that these values of the CO_{ot} stretching frequencies are conditioned by the presence of the rows of O_{br} atoms on the stoichiometric s-RuO₂(110) surface².

Based on the interpretation of the CO adsorption experiment on stoichiometric s-RuO₂(110), we assign the development of the CO band at 2110 cm⁻¹ to the formation, following the annealing in the 330-400 K range, of short O_{br} sequences occupying two or three neighboring bridge sites. We identify thus the 2110 cm⁻¹ CO absorption band on the annealed oxide surface, with the IR band due to groups of two CO_{ot} molecules located between the complete O_{br} rows on the stoichiometric s-RuO₂(110) surface (Fig.5.1). The reason for this assignment lies in the fact that, in both cases, the nearest-neighbor vicinity of the CO_{ot} molecules vibrating at 2110 cm⁻¹ is similar (Fig.6.14.b, c). The isolated O_{br} atoms induce in the nearby CO_{ot} molecules an upward chemical shift of 20-30 cm⁻¹ relatively to the vibration frequency of more distant CO molecules which have only CO molecules as neighbors. Although at the beginning of the restoration process

¹The isolated O_{br} atoms bind electronic charge in the substrate, which otherwise would have been backdonated into the antibonding 2π* orbitals of the neighboring CO adsorbates, leading thus to an increase in the CO stretching frequency. Through long range dipole-dipole vibrational couplings, these local effects add up in the entire layer producing a single collective CO stretching mode at a slightly higher position (2090 cm⁻¹ vs. 2083 cm⁻¹).

²Based on our observations, we mention that in the absence of the O_{br} atoms the CO stretching frequency on the RuO₂(110) surface would not exceed 2080-2090 cm⁻¹.

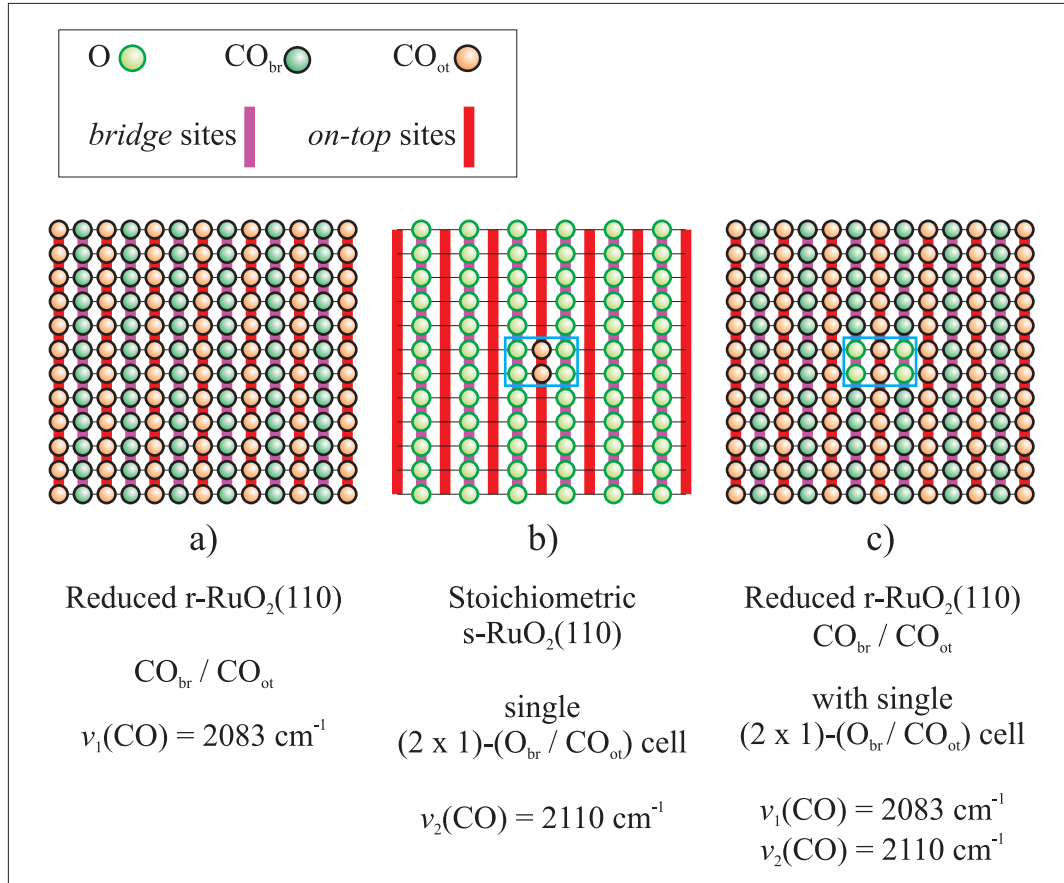


Figure 6.14: Restoration of the mildly reduced $\text{r-RuO}_2(110)$ surface to the stoichiometric $\text{s-RuO}_2(110)$ structure, upon annealing the sample in vacuum: origin of the 2110 cm^{-1} band (Fig.6.13). After annealing to 330-410 K, the RAIR spectrum consists of the $2083\text{-}2090 \text{ cm}^{-1}$ and the 2110 cm^{-1} bands. a) The 2083 cm^{-1} band is characteristic of the $\text{CO}_{\text{br}}/\text{CO}_{\text{ot}}$ phase on the reduced $\text{r-RuO}_2(110)$ surface. b) On the stoichiometric $\text{s-RuO}_2(110)$ surface, the 2110 cm^{-1} band corresponds to pairs of isolated CO_{ot} molecules between complete rows of O_{br} . c) Due to the large separation of frequencies (27 cm^{-1}), the vibrations of the two species of CO molecules (with CO, respectively O_{br} as first neighbors) do not couple significantly, the respective IR absorption bands being present independently. The development of the 2110 cm^{-1} band upon annealing the sample in the 330-410 K range indicates the onset of the restoration process, characterised by an increase in the O_{br} population and hence in the number of pairs of isolated O_{br} atoms occupying neighboring sites.

(when annealing to 330-380 K, Fig.6.13) not many CO molecules are neighbor to isolated pairs of O_{br} atoms, this significant chemical shift gives rise to an easily distinguishable band at 2110 cm^{-1} , clearly separated from the collective band at $2083\text{--}2090\text{ cm}^{-1}$ due to the majority CO molecules ($\text{CO}_{br}/\text{CO}_{ot}$ phase, Fig.6.14.a). Increasing progressively the annealing temperature results into increasingly larger populations of O_{br} atoms. From a statistical point of view, the number of pairs of O_{br} atoms occupying neighboring sites will also increase, resulting into the development of the 2110 cm^{-1} band at the onset of the restoration process.

Annealing the sample in the 410-600 K range, the progressive replenishing of bridge sites with O atoms continues. The increase in the O_{br} population results in the emergence of longer sequences of O_{br} atoms occupying neighboring sites. Accordingly, with the increase of the annealing temperature the areas occupied by the saturated $\text{CO}_{br}/\text{CO}_{ot}$ phase have to diminish. The weakening of the 2083 cm^{-1} band was indeed observed in the 410-500 K range of annealing temperatures (Fig.6.13). The 2083 cm^{-1} band has completely disappeared after annealing the sample to 520 K. Adsorption of CO on the annealed r- $\text{RuO}_2(110)$ surface is increasingly similar to adsorption of CO on the stoichiometric s- $\text{RuO}_2(110)$ surface (see also Fig.5.1). On the stoichiometric s- $\text{RuO}_2(110)$ surface, the $2110\text{--}2123\text{ cm}^{-1}$ shift of the IR band with increasing CO coverage is due to the emergence of progressively longer sequences of neighboring CO_{ot} between the complete rows of O_{br} . The argument illustrated in Fig.6.14 for the case of pairs of neighboring O_{br} atoms can obviously be extended to longer sequences of neighboring O_{br} atoms. Thus, for CO adsorption on the reduced r- $\text{RuO}_2(110)$ surface after annealing in the 410-600 K range, we attribute the continuous $2110\text{--}2123\text{ cm}^{-1}$ shift of the principal CO band (Fig.6.13) to the emergence of increasingly longer sequences of neighboring O_{br} atoms. After annealing the reduced r- $\text{RuO}_2(110)$ surface to 600 K, the restoration of the stoichiometric s- $\text{RuO}_2(110)$ structure is practically complete. The restoration process can be thus considered as proved by RAIRS.

The described RAIRS experiment has proved the restoration of the reduced r- $\text{RuO}_2(110)$ surface to the stoichiometric s- $\text{RuO}_2(110)$ structure, upon annealing the sample to 600 K in vacuum. However, the origin of the oxygen atoms used to restore the O_{br} species could not be identified by RAIRS. We note that our IR spectroscopic results are in complete agreement with the conclusions of earlier STM experiments [54, 58], where in addition the restoration mechanism was also explained. In order to answer the question, where do the oxygen atoms in the

restored O_{br} species originate from and how does the restoration process work, we shall summarize in the following the conclusions of the cited STM investigations.

In the STM study [58] the authors have imaged the stoichiometric $\text{RuO}_2(110)$ surface (Fig.6.15.a), identifying the alternating dark and bright rows as vacant 1f-cus Ru sites and O_{br} atoms, respectively. After exposing the stoichiometric surface to 10 L CO at 300 K, the STM image (Fig.6.15.b) presents the same pattern of alternating dark and bright rows, the difference being that the bright rows appear with reduced intensity and isolated bright features populate the dark rows. The faint bright rows were this time identified as bridging CO_{br} molecules and the bright features between them, as isolated CO_{ot} molecules. Accordingly, the surface imaged in Fig.6.15.b is the mildly reduced $\text{RuO}_2(110)$ surface. After annealing the mildly reduced oxide surface to 600 K, the STM image (Fig.6.15.c) reveals extended areas with a structure identical to the initial, stoichiometric $\text{RuO}_2(110)$ surface imaged in Fig.6.15.a. These STM experiments are therefore an immediate proof of the result due to Wendt *et al.* [76] that by annealing the mildly reduced r- $\text{RuO}_2(110)$ surface to 600 K in vacuum, the oxide layer is restored to the stoichiometric s- $\text{RuO}_2(110)$ structure.

Besides the areas with restored stoichiometric $\text{RuO}_2(110)$ structure, the annealed surface in Fig.6.15.c presents holes of an apparent depth of 3 Å, imaged as dark stripes. At the rims of the holes, bright features of round shape were observed, with an apparent height of 2 Å. The interpretation of these particular features have proved essential for an understanding the mechanism of the restoration process. In Ref. [54] the authors have shown that by annealing the mildly reduced r- $\text{RuO}_2(110)$ surface to 600 K, the stoichiometric s- $\text{RuO}_2(110)$ structure is restored by means of repopulation of the bridge sites with O atoms originating from the threefold-coordinated oxygen species (3f-O) of the $\text{RuO}_2(110)$ structure. Upon heating the sample to 450 K, CO_{br} molecules desorb from the surface, leaving behind a reduced $\text{RuO}_2(110)$ structure with vacant bridge sites and high surface energy³. Increasing the annealing temperature to 500 K results in a restructuring of the $\text{RuO}_2(110)$ surface, in that threefold-coordinated 3f-O surface atoms are liberated from the oxide structure, thereby creating the holes observed in the STM image [58]. These O atoms diffuse subsequently to occupy the bridge positions, leading to the complete restoration of the O_{br} rows. The

³The surface energy of the reduced $\text{RuO}_2(110)$ surface with vacant bridge sites is more than 120 meV/Å², which is to be compared to 74 meV/Å² of the stoichiometric surface [58, 64].

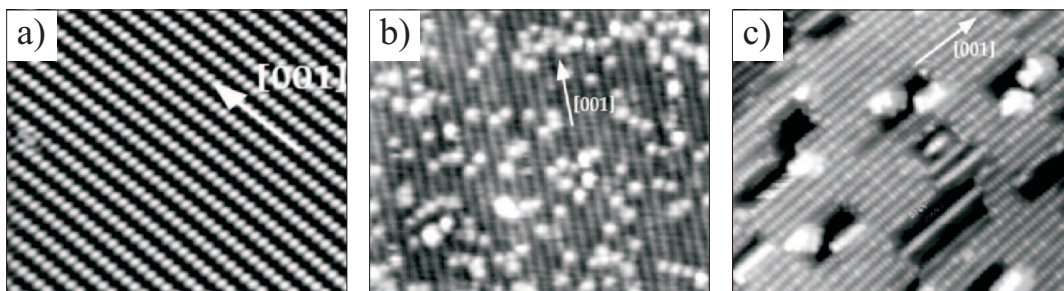


Figure 6.15: Restoration of the mildly reduced $\text{RuO}_2(110)$ surface. STM images [58] of the $\text{RuO}_2(110)$ surface: a) stoichiometric, b) mildly reduced after 10 L CO exposure at 300 K, c) restored after annealing in vacuum to 600 K. The bright rows are: O_{br} in (a), CO_{br} in (b) and O_{br} in (c). In (b): the bright spots between the rows are isolated CO_{ot} molecules. In (c): the bright areas are one-layer thin Ru clusters on stoichiometric $\text{RuO}_2(110)$ while in the dark areas ('holes') the topmost oxide layer is missing.

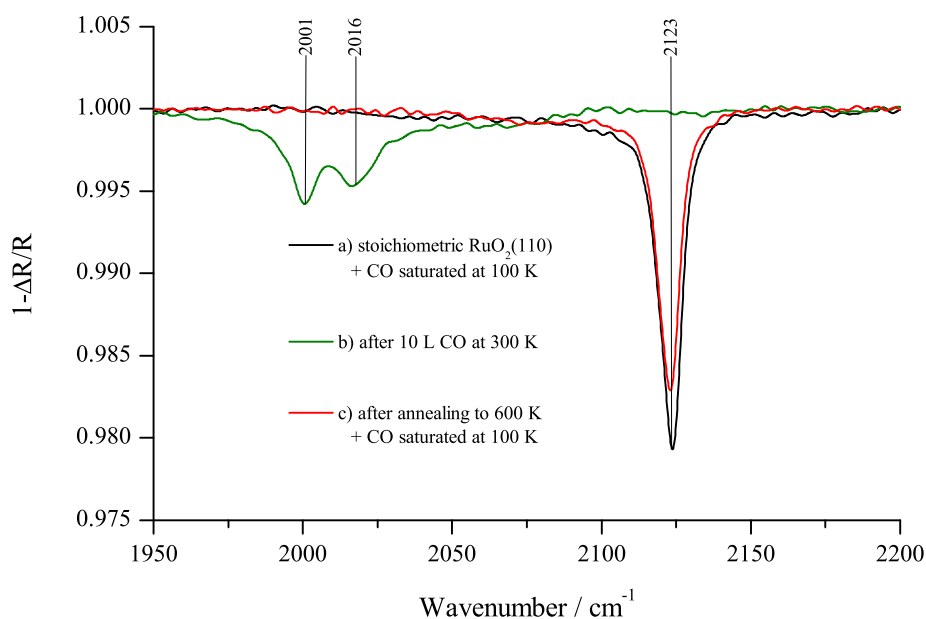


Figure 6.16: Restoration of the mildly reduced $\text{RuO}_2(110)$ surface. RAIR spectra of the $\text{RuO}_2(110)$ surface: a) stoichiometric, saturated with CO at 100 K, b) reduced, after 10 L CO at 300 K, c) restored, after annealing to 600 K in vacuum and subsequent saturation with CO at 100 K. Spectra (a) and (c) show the IR absorption due to CO_{ot} test-molecules, subsequently adsorbed on the surfaces imaged in Fig.6.15 (a) and (c), respectively. For spectrum (b), no additional CO test-molecules were adsorbed on the surface imaged in Fig.6.15.b.

coordinations of the Ru atoms, which initially were attached to the released 3f-O atoms in the oxide structure, are reduced to the extent that they become unstable and agglomerate to small Ru clusters at the rims of the holes, imaged by STM as bright features (Fig.6.15.c). Annealing the sample to 670 K puts in evidence the hexagonal shape of the larger clusters, confirming thus their identification as Ru islands [58, 54]. In summary, the restored oxide surface may be seen as an autocompensated $\text{RuO}_2(110)$ structure with small Ru islands [58].

After the review of the STM studies [58, 54], let us now return to the discussion of the RAIRS spectra in Fig.6.13. It is rather remarkable that the restoration of the O_{br} atoms sets in already after annealing to temperatures as low as 370 K, as indicated by the emergence of the 2110 cm^{-1} band. According to the restoration mechanism proposed in Ref.[58] this would imply that threefold-coordinated oxygen atoms (3f-O) are being liberated from the uppermost $\text{RuO}_2(110)$ layer already at 370 K. Furthermore, annealing to temperatures over 400 K leads to an increasingly efficient completion of the O_{br} rows by the liberated 3f-O atoms, reflected in the RAIR spectra by the $2110\text{-}2123\text{ cm}^{-1}$ shift of the principal CO band. The completion of the O_{br} rows in the 410-600 K range can be ascribed to an increased number of 3f-O atoms liberated during annealing, as well as to the enhanced mobility of these O atoms along the 1f-cus Ru rows. The restoration mechanism proposed in Ref.[58] provides thus the necessary background for a consistent interpretation of our RAIR spectra (Fig.6.13).

To conclude the present section, we note that the STM images in Ref.[58] (Fig.6.15) can be put in a one-to-one correspondence with our RAIR spectra (Fig.6.16). Cooling the pristine stoichiometric s- $\text{RuO}_2(110)$ surface to 100 K and subsequently dosing 6 L CO results in the saturation of 1f-cus Ru sites by CO_{ot} , characterised by an IR band at 2123 cm^{-1} (Fig.6.16.a). The position of the CO_{ot} band at 2123 cm^{-1} is conditioned by the presence of complete rows of O_{br} on the stoichiometric $\text{RuO}_2(110)$ surface, as shown in the STM image Fig.6.15.a. The mildly reduced r- RuO_2 surface is obtained, in both STM and RAIRS experiments, by exposing the s- $\text{RuO}_2(110)$ surface to 10 L CO at room temperature. In the STM image Fig.6.15.b, the reduced surface presents complete rows of CO_{br} molecules and mostly vacant 1f-cus Ru sites, with only few isolated CO_{ot} molecules. The vibrations of these CO molecules can be directly detected by IR spectroscopy, without the need of adsorbing additional CO test molecules like in the case of the s- $\text{RuO}_2(110)$ surface. The RAIR spectrum of the

r-RuO₂(110) surface consists of a 2001 cm⁻¹ and a 2016 cm⁻¹ band, respectively characteristic of complete rows of CO_{br} molecules and of isolated CO_{ot} molecules adsorbed between them. These assignments were inferred from the low-pressure CO adsorption experiments on the mildly reduced r-RuO₂(110) surface, described in Chap.6.1.2 (see also Fig.6.3).

The STM images have shown that annealing the mildly reduced RuO₂(110) surface to 600 K results into an inhomogeneous surface, covered by an oxide film with the structure of stoichiometric RuO₂(110) with holes and small Ru clusters [58]. Restoration of the O_{br} rows (Fig.6.15.c) could be clearly confirmed by RAIRS (Fig.6.16.c). However, the RAIR spectra did not show additional features associated with either the Ru clusters or the holes. This observation is not surprising, since the structure of the oxide layer within the holes is stoichiometric RuO₂(110), located one oxide layer deeper than the rest of the RuO₂(110) surface. The vibration frequency of eventual CO molecules chemisorbed into the holes, on the stoichiometric RuO₂(110) surface, would therefore not be much different from that of the majority CO species, characterised by an IR band at 2123 cm⁻¹ (Fig.6.16, spectra *a* and *c*).

We note that the sensitivity of RAIRS should have been sufficient to detect minute quantities of CO adsorbed on the Ru clusters. Absence of the corresponding IR features, after exposure of the mildly reduced RuO₂(110) surface to 6 L CO at 200 K and 1×10^{-8} mbar CO, indicates that CO did not adsorb on the Ru clusters, presumably due to the blocking of the adsorption sites by O atoms. We expect therefore that RAIRS measurements under high background CO pressure are necessary, in order to reveal the existence of Ru clusters on the reduced RuO₂(110) surface. In the next section, we shall apply these observations to the RAIRS study of a severely reduced RuO₂(110) surface.

6.4.2 Heavy reduction of the RuO₂(110)/Ru(001) film by CO exposure at high temperature and pressure

In the present work we have so far considered only the *mildly* reduced r-RuO₂(110) surface, where the stoichiometric RuO₂(110) structure is essentially preserved with the only difference that the bridge sites in the topmost oxide layer are not terminated by O_{br}, but by CO_{br}. A reduced surface with all bridge positions vacant would possess a surface energy too high to remain stable, the occupation

of the vacant bridge sites by substitute adsorbates being mandatory to ensure stability of the reduced $\text{RuO}_2(110)$ structure. Reduced $\text{r-RuO}_2(110)$ surfaces of high stability were experimentally demonstrated by bridging the 2f-cus Ru sites with CO [64] and with Cl atoms [77]. In the current section we shall discuss RAIR spectra of CO on the reduced $\text{r-RuO}_2(110)$ surface, recorded during an irreversible reduction process under high pressure CO exposure. Interpretation of the RAIR spectra shows close similarities to the SXRD results of He *et al.* [53].

The experiment consists in annealing the restored $\text{RuO}_2(110)$ surface under 3×10^{-3} mbar CO background pressure. The sample is held at constant temperature while RAIR spectra are being recorded each few minutes until stability is reached. Subsequently the temperature is increased by further 5-10 K. The 340-440 K series is plotted in Fig.6.17, starting with spectrum (c) of Fig.6.12.

The initial spectrum (c) consists of two wide bands at 2057 cm^{-1} and 2072 cm^{-1} . In the 340-390 K temperature range (spectra not shown) the 2072 cm^{-1} band remains fixed but loses intensity compared to the 2057 cm^{-1} band, which shifts continuously down to 2048 cm^{-1} with only minor intensity loss. In the 390-415 K range the trend is reversed, the 2072 cm^{-1} band progressively increases in intensity up to exactly its initial value at 340 K (spectrum c) while the 2048 cm^{-1} band steadily diminishes to a mere tail of the restored 2072 cm^{-1} band. At about 420 K the opposite transformation (d)-(e) occurs in roughly 50 minutes, entailing the vanishing of the 2072 cm^{-1} band parallel to the re-emergence of the 2044 cm^{-1} line. During the transformation, the positions of both bands remain rigorously constant. At saturation, the remaining 2044 cm^{-1} line is intense (1.6%) and relatively narrow (14 cm^{-1}) compared to the usual CO bands on $\text{RuO}_2(110)$ ($20\text{-}30 \text{ cm}^{-1}$) and can thus be assigned to a well ordered CO layer, either on RuO_2 or on Ru metal.

Recently, *in situ* SXRD experiments were performed by He *et al.* [53]. The authors have prepared a $\text{RuO}_2(110)$ film 1.6 nm thick (self-limited growth of five oxide layers) by exposure of $\text{Ru}(001)$ to 1×10^{-4} mbar O_2 at 630 K for 20 minutes, the same preparation procedure as followed throughout the present work. The lateral size of the incommensurately grown $\text{RuO}_2(110)$ domains determined from the SXRD peak width was 10 nm. The oxide film was subsequently reduced by exposure to 1×10^{-5} mbar CO at 415 K. Within the experimental time resolution of 100 s, no induction period of the reduction process was found. The progressing reduction of RuO_2 domains was monitored *in situ* by SXRD, the in-

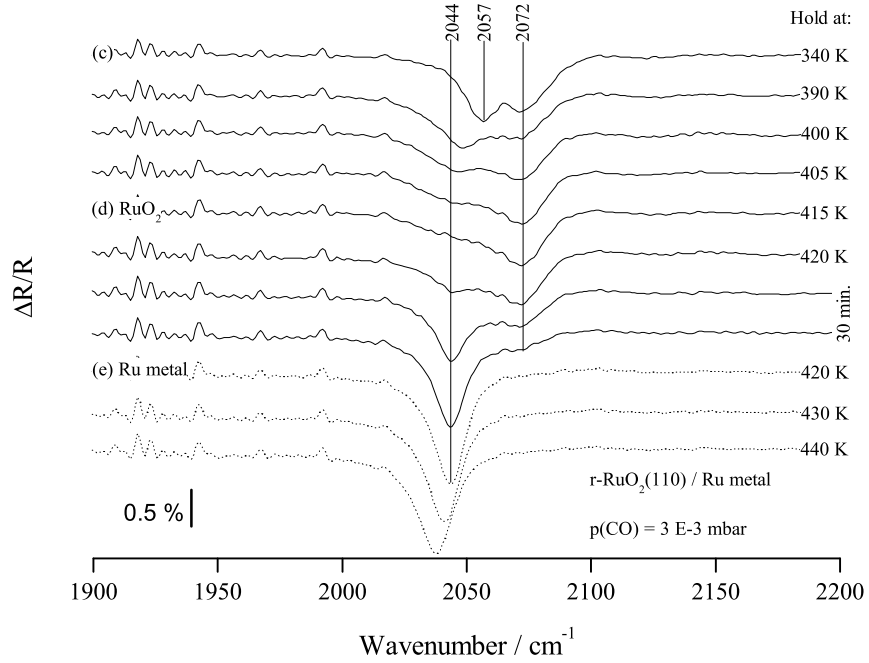


Figure 6.17: RAIR spectra of $\text{RuO}_2(110)$ reduction under 3×10^{-3} mbar CO. The $\text{RuO}_2(110)$ -characteristic 2072 cm^{-1} band disappears at 420 K in about 40 min. Above 420 K, the 2044 cm^{-1} band is attributed to CO on Ru(001).

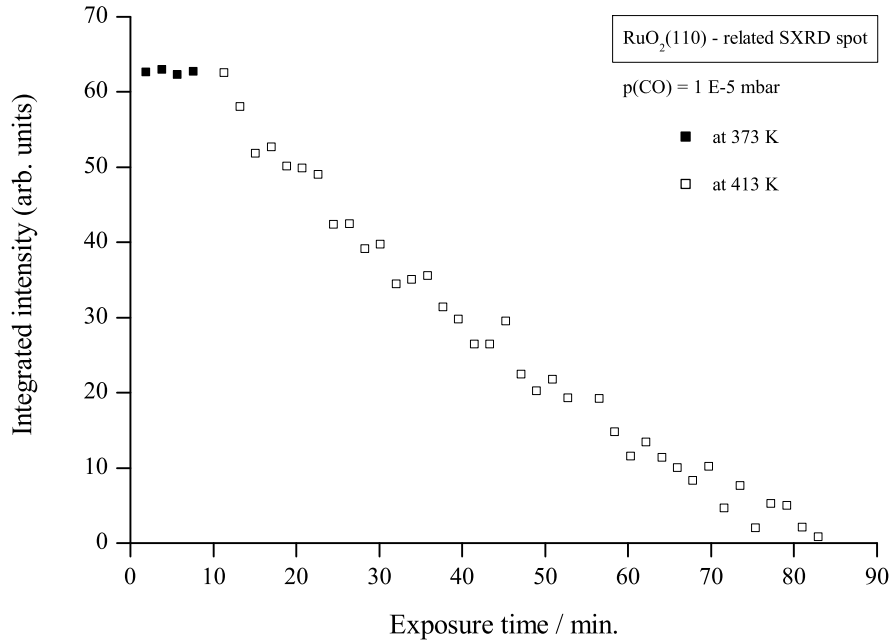


Figure 6.18: Reduction of the $\text{RuO}_2(110)/\text{Ru}(001)$ film by exposure to 1×10^{-5} mbar CO at 413 K. The integrated intensity of a $\text{RuO}_2(110)$ -characteristic SXR D peak is plotted against CO exposure. Data adapted after Fig.4.c in Ref.[53].

tegral intensity of the $\text{RuO}_2(110)$ characteristic SXRD peak⁴ decreasing linearly in time (Fig.6.18). The reduction process was completed within 76 min. Additionally it has been shown that neither the averaged size nor the thickness of the RuO_2 domains varies during the reduction process, which seems to proceed rather through 'annihilation' of complete domains. CO exposure at 373 K has not lead to a significant reduction of the $\text{RuO}_2(110)$ film, the required minimal temperature being thus about 400 K.

In the present RAIRS studies of CO adsorbed, under reaction conditions, on $\text{RuO}_2(110)/\text{Ru}(001)$ up to reactant pressures of 1×10^{-2} mbar, the 2072 cm^{-1} band is the most intense one, being observed during periods of highest catalyst activity. Since the activity of a Ru catalyst is conditioned by the presence of RuO_2 patches, we can consider the presence of the 2072 cm^{-1} band as indicating the presence of a $\text{RuO}_2(110)$ film on the sample surface. The gradual weakening and the subsequent disappearance of the 2072 cm^{-1} band (Fig.6.17) can therefore be seen as reflecting the same process as the disappearance of the $\text{RuO}_2(110)$ -specific SXRD peak in the experiments of He *et al.* (Fig.6.18). Both results are indicative of the *total* reduction of $\text{RuO}_2(110)$ film to metallic Ru, under intense CO exposure at about 400 K. The fact that both the 2072 cm^{-1} and the 2044 cm^{-1} bands remain at constant frequency, as long as the (d)-(e) transformation at 420 K is not complete, may be seen as similar to the *in situ* SXRD result, which indicates the spontaneous 'annihilation' of entire $\text{RuO}_2(110)$ domains, rather than their gradual reduction by CO. The observation that the IR band positions at 2044 cm^{-1} and 2072 cm^{-1} remain constant can be understood by noting that the local environment of each vibrating CO molecule, and thus the central frequency of the IR band, is not affected during the reduction process, provided this process does not change the morphology of the $\text{RuO}_2(110)$ domains on which the vibrating CO probe molecules are adsorbed. The spontaneous annihilation of entire $\text{RuO}_2(110)$ domains is manifested in the decrease (respectively increase) of the IR band intensity, the band position remaining essentially unaffected.

In order to discuss the state of the $\text{RuO}_2(110)/\text{Ru}(001)$ film following the heavy reduction process, we shall briefly review a previous STM and XPS study by Over *et al.* [54]. The authors have prepared a heavily reduced $\text{RuO}_2(110)$ surface by exposing the stoichiometric surface to 100 L CO while keeping the

⁴H=0.733, K=0, L=0.5

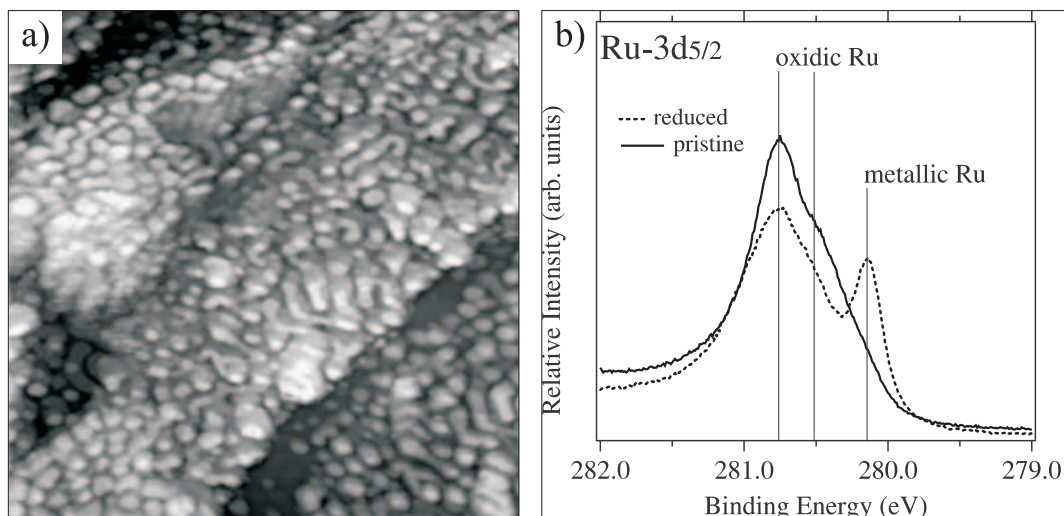


Figure 6.19: Heavily reduced $\text{RuO}_2(110)$ surface, obtained by exposing the stoichiometric surface to 100 L CO at 600 K: a) STM image showing the presence of a metallic Ru overlayer, visualised as round, flat Ru clusters, b) HRCLS spectra of the $\text{Ru-3d}_{5/2}$ level on the heavily reduced $\text{RuO}_2(110)$ surface (dotted curve) showing the coexistence of both metallic and oxidic Ru domains [54].

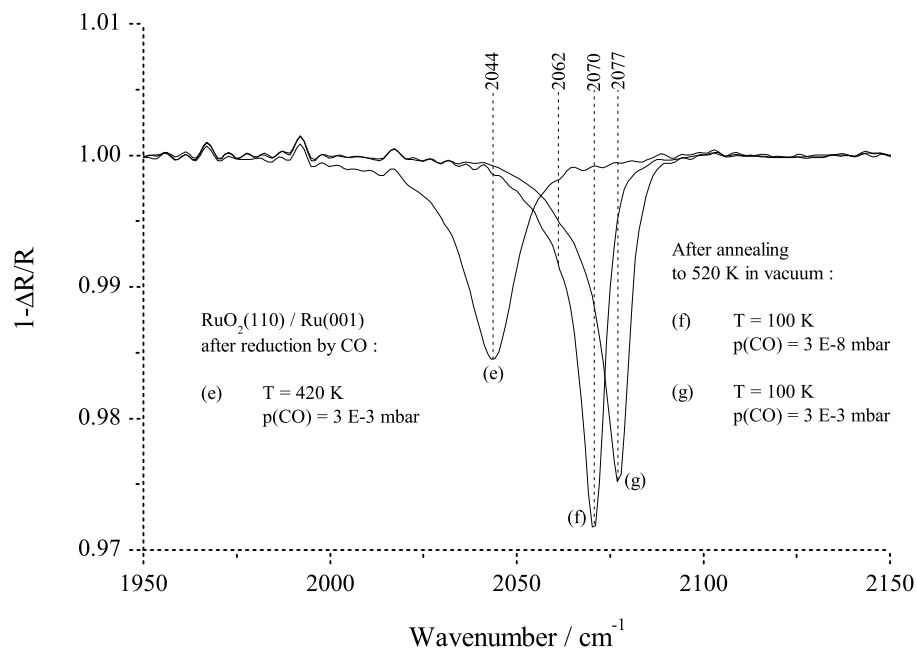


Figure 6.20: Following heavy reduction of the $\text{RuO}_2(110)/\text{Ru}(001)$ film, the IR spectrum (e) is characteristic of CO on $\text{Ru}(001)$ [78]. Annealing to 520 K in vacuum and subsequent CO saturation, at 100 K and different pressures, leads to IR spectra (f)-(g) similar to CO coadsorbed with O on $\text{Ru}(001)$ [79].

sample at 600 K. The sample surface has subsequently become very rough, as indicated by the LEED image with no diffraction spots attributable to RuO_2 . The STM image (Fig.6.19.a) is also very different from that of the stoichiometric $\text{RuO}_2(110)$ surface. Instead of the well ordered rows of O_{br} atoms, characteristic of the pristine $\text{RuO}_2(110)$ film (Fig.6.15.a), the STM images show a disordered surface covered by bright islands of round shape. High-resolution core level shift spectra (HRCLS) of the $\text{Ru-3d}_{5/2}$ and O-1s levels have shown the presence of RuO_2 at the surface, as well as an increase in the area of metallic Ru (Fig.6.19.b). The step height in the STM image (Fig.6.19.a) was about 2 Å much closer to the step height on Ru(001) (2.14 Å) than on $\text{RuO}_2(110)$ (3.11 Å), indicating that the bright, round features are Ru clusters consisting of a single layer of Ru atoms. The authors in Ref. [54] have concluded that the heavily reduced $\text{RuO}_2(110)$ surface consists of rough RuO_2 fully covered by metallic Ru layers. These Ru layers can grow together and completely cover the rests of the RuO_2 layer, giving rise to a so called buried $\text{RuO}_2(110)$ oxide. A similar effect has been observed with bulk RuO_2 , annealing to 700 K being reported to induce a hexagonal LEED pattern indicating the emergence of a thin, crystalline Ru slab on the surface of the bulk RuO_2 crystal [80].

In order to elucidate the state of the surface following the process of heavy reduction of the $\text{RuO}_2(110)/\text{Ru}(001)$ film by CO at 420 K, we have performed RAIRS studies, in which CO plays the role of an IR probe molecule (Fig.6.20). The IR band emerging at 2044 cm^{-1} after completion of the reduction process, with 1.5 % amplitude and 16 cm^{-1} FWHM, is reasonably similar to the IR band reported for CO adsorbed on clean Ru(001) under comparable conditions [78], exposure to 3.3 mbar CO at 500 K leading to a CO stretching band at 2048 cm^{-1} , with 3% amplitude and about 12 cm^{-1} FWHM. This observation suggests that the sample surface is essentially metallic Ru. Following evacuation of the UHV/HP cell to 2×10^{-8} mbar stable residual CO pressure, we have annealed the heavily reduced sample to 520 K and subsequently saturated it with CO at 100 K under 3×10^{-3} mbar CO, obtaining a CO stretch band at 2077 cm^{-1} with an amplitude of 2.4% and 10 cm^{-1} FWHM (Fig.6.20.g). A similar IR band (f) but of lower frequency (2070 cm^{-1}) was obtained after reducing the pressure to 3×10^{-8} mbar CO.

While the amplitude and width of the 2077 cm^{-1} band are typical of CO on Ru(001), its position is significantly higher than the maximal CO stretch

frequency (2060 cm^{-1}) measured on clean Ru(001) at the saturation coverage of 0.67 monolayers of CO [24]. The observed blueshift of $10\text{-}20\text{ cm}^{-1}$ could be explained by the presence of residual O on the Ru(001) surface. Hoffmann *et al.* [79] have shown that coadsorption of CO on Ru(001) at 85 K, with 0.3-0.5 monolayers of O preadsorbed at 300 K, leads to IR bands in the $2070\text{-}2080\text{ cm}^{-1}$ range. A model which could reproduce spectra (f)-(g) of Fig.6.20 is the $(2 \times 1)\text{-O}$ structure, containing 0.5 monolayers of O. CO adsorption onto the $(2 \times 1)\text{-O}$ layer leads to a single CO band, which shifts continuously with increasing CO coverage, from 2062 cm^{-1} to 2078 cm^{-1} [79]. In terms of this particular coadsorbate structure, the 2062 cm^{-1} shoulder in the tail of the 2077 cm^{-1} band is naturally interpreted as arising from regions of low CO coverage on $(2 \times 1)\text{-O}$ phase on the Ru(001) clusters, while the 2070 cm^{-1} band would correspond to a higher CO coverage on the same phase. We assign the 2077 cm^{-1} cm band to the CO-saturated $(2 \times 1)\text{-O}$ phase on the Ru(001) clusters (see also Fig.2.e in [79]).

We shall try in the following to exploit the rather detailed structural information contained in the STM image of the reduced surface (Fig.6.19.a) in order to explain the main features of the RAIR spectrum of CO probe molecules adsorbed on this surface under high CO pressure (Fig.6.20, curve g). We shall assume that the CO molecules contributing to the IR absorption signal are chemisorbed exclusively on the Ru clusters, which are not uniform in size but are more or less extended. To explain the $10\text{-}20\text{ cm}^{-1}$ upward shift of the IR frequency, compared to the case of a saturated CO layer on the clean Ru(001) surface, we have to assume the presence of O atoms in the vicinity of our CO probe molecules. This condition is fulfilled due to the rich oxygen content of the heavily reduced surface, shown by the HRCLS spectrum (Fig.6.19.b).

Less clear is the position of the O atoms, relatively to the CO probe molecules adsorbed on the Ru clusters. Since the Ru clusters were found to consist of only one layer of Ru atoms, the O atoms located in the substrate immediately *under* the Ru cluster could shift the CO stretch frequency almost as effectively as the O atoms adsorbed *on* the Ru cluster, in the immediate vicinity of the vibrating CO molecules. However, under strongly reducing conditions we have observed an IR band at 2044 cm^{-1} (Fig.6.20, curve e) which is similar to the IR band of CO on *bulk* Ru(001) [78]. Following this observation, we are inclined to assume that the upward frequency shifts of $10\text{-}20\text{ cm}^{-1}$ observed in spectra (f)-(g) should be attributed to O adsorbed on the Ru clusters rather than to O atoms located

underneath the Ru clusters. A possible explanation for the origin of O on the Ru clusters would be the diffusion of O, from the oxide layers underneath the surface, during annealing (520 K) in the absence of CO.

We are now in a position to discuss, based on the previous observations, the main features of the RAIR spectrum of CO adsorbed on the heavily reduced $\text{RuO}_2(110)/\text{Ru}(001)$ film (Fig.6.20, curve g). Since CO adsorption took place at gas pressures as high as 3×10^{-3} mbar CO, we can assume that each Ru cluster supports the maximal CO coverage it can accommodate. The closely packed CO molecules adsorbed on the same Ru cluster are subject to intense dipole-dipole coupling, resulting into a single narrow IR band. The remarkably narrow band (10 cm^{-1}) points to a good ordering of the adsorbates in the vicinity of each vibrating CO molecule, in agreement with an assignment to CO adsorbed on well ordered, one-layer thin Ru clusters, which mimic the $\text{Ru}(001)$ surface of a bulk crystal.

As apparent in Fig.6.20, the bands (f)-(g) are strongly asymmetric, with a pronounced low frequency tail indicative of an inherent degree of disorder in the CO adsorbate. Since both the intensity and the position of the collective IR band of CO molecules adsorbed on the same Ru cluster shifts upwards with increasing CO coverage, it is likely that this low frequency tail is due to the large dispersion of CO coverages supported on Ru clusters of very different size. The large distance (few 10 Å) between neighboring Ru clusters precludes the dipole-dipole coupling between CO molecules adsorbed on *different* Ru clusters. Each Ru cluster contributes therefore independently to the total IR absorption signal, a circumstance which would explain the asymmetric shape of these bands.

Summary

The reduction of the epitaxially grown $\text{RuO}_2(110)/\text{Ru}(001)$ film, previously observed by *in situ* SXRD [53], was nicely confirmed by our RAIRS experiments. The conditions for the reduction process have turned out to be similar to those found in the SXRD experiment. Exposure to 3×10^{-3} mbar CO at 420 K has led to the gradual disappearance of the $\text{RuO}_2(110)$ -related CO stretch band (2072 cm^{-1}) within 50 minutes. RAIR spectra recorded in the final phase of the reduction process, i.e. on the heavily reduced $\text{RuO}_2(110)/\text{Ru}(001)$ film, indicate the presence of exposed surfaces similar to $\text{Ru}(001)$. More precisely, STM evi-

dence [54] suggests that these exposed Ru(001) surfaces are in fact thin, extended clusters of Ru covering a rough residual layer of RuO₂.

Previous HRCLS data [54] indicate the existence of oxygen on the heavily reduced RuO₂(110)/Ru(001) film, in the form of buried RuO₂ domains. RAIR spectra of CO probe molecules adsorbed at 100 K, after annealing the heavily reduced RuO₂(110)/Ru(001) film to 520 K, are consistent with the presence of about 0.5 monolayers of O on the exposed Ru(001) surfaces. The presence of O on the Ru clusters manifests as a 10-20 cm⁻¹ upward shift in the stretch frequency of adsorbed CO probe molecules.

Chapter 7

In situ RAIRS of the CO oxidation reaction over the RuO₂(110) model catalyst

One of the strengths of IR spectroscopy, decisive for our surface science approach to the catalyst under working conditions, is that acquisition of IR spectra in a limited high pressure range, not currently accessible by other standard UHV techniques, does not require any refinement of the technique beyond the methods applied earlier in this work. Starting with the lower 10^{-2} mbar range, absorption by CO molecules from the gas phase in our reaction cell has quickly surpassed the absorption signal from the CO molecules on the sample surface, indicating that more sophisticated techniques, like phase-modulated RAIRS, are eventually required. Nevertheless, it was possible to exploit the (non-polarized) RAIRS technique, as applied in the present work under typical UHV conditions, to monitor the *in situ* state of the RuO₂(110) model catalyst during the CO oxidation reaction, in the relatively extended 10^{-7} - 10^{-2} mbar pressure domain. Surprisingly enough, our previous results over CO adsorption on RuO₂(110) under UHV conditions naturally fit the context of the present chapter, suggesting an interpretative scheme based upon assigning, to IR bands measured *in situ* during the CO oxidation reaction, the characteristic frequencies of different *ordered* CO_{br}/CO_{ot} phases on RuO₂(110). For each ordered CO_{br}/CO_{ot} phase the characteristic frequencies were either computed, from an approximate dipole-dipole coupling model, or directly measured in UHV experiments.

Following the standard preparation prescription described in Chap.4.4, the $\text{Ru}(001)$ sample was sputtered at 1000 K and subsequently glown in 1×10^{-7} mbar oxygen. After evacuation of the oxygen and cooling of the sample to room temperature, a LEED pattern characteristic of a well ordered $\text{O}(2 \times 2)/\text{Ru}(001)$ structure was observed. The sample was transferred to the UHV/HP cell, which was operated as a batch reactor by closing its gate valves to the turbo-molecular pump and to the analysis chamber. The isolated UHV/HP cell was filled with 1×10^{-4} mbar O_2 and the sample was oxidized at 620 K for 35 minutes. The result was a $\text{RuO}_2(110)$ oxide film covering the entire sample, no additional $\text{O}(1 \times 1)/\text{Ru}(001)$ domains being observed by LEED. The as-grown oxide layer was checked by RAIRS, saturation with CO at 100 K producing the characteristic CO stretching line at 2123 cm^{-1} (Fig.4.6) indicative of CO adsorbed on the well ordered stoichiometric $\text{RuO}_2(110)$ surface. By rapidly annealing the sample to 700 K in 2×10^{-7} mbar O_2 the characteristic CO peak could be additionally enhanced, indicating an improved local ordering of the $\text{RuO}_2(110)$ film.

After the preparation of the oxide film, the UHV/HP cell was evacuated to 1×10^{-9} mbar base pressure in about three hours. After flash-annealing the sample to 500 K, in order to desorb molecules adsorbed from the residual gas, a background RAIR spectrum was recorded for use as reference to all spectra of the present series. The spectra were recorded in the domain (1800-4000) at 4 cm^{-1} resolution by averaging of 300 scans, recording of each spectrum taking 216 seconds. The sample was continuously cooled with liquid nitrogen and simultaneously heated by electron bombardment on its backside. The sample temperature was kept constant about 350 K, small temperature fluctuations being effectively compensated by finely adjusting the rate of electron bombardment. The gases were introduced into the UHV/HP cell through manually operated leak valves. The total pressure in the UHV/HP cell was monitored by a Penning gauge working in the range 10^{-9} - 10^{-3} mbar. The composition of the reactant feed was regulated by accurately increasing the partial pressure of each reactant. In the 10^{-9} - 10^{-4} mbar domain the UHV/HP cell was operated as a flow reactor, being continuously pumped while feeding the reactants.

7.1 In situ RAIRS in the 10^{-7} - 10^{-6} mbar domain

The stretch frequency of CO molecules adsorbed at the catalyst surface (1800 - 2200 cm^{-1}) was monitored by RAIRS, in situ during the CO oxidation reaction, beginning with the high vacuum domain (Fig.7.1). The stoichiometric $\text{RuO}_2(110)$ clean surface was kept under an oxidizing reactant feed of 1×10^{-7} mbar O and 1×10^{-7} up to 2×10^{-7} mbar CO for about 40 minutes. The corresponding spectra are identical (Fig.7.1.a) showing only a very weak (0.07%) band at 1867 cm^{-1} , close to the IR band usually observed with symmetric bridging CO_{br} (1870 - 1890 cm^{-1}).

The absence of CO bands at higher frequency suggests that the 1f-cus Ru sites do not accommodate an on-top CO_{ot} species long-lived enough to be detected. The coverage of 1f-cus Ru sites by a stable O_{ot} species can not be inferred from the RAIR spectrum. However, the absence of IR intensity in the 2140 - 2150 cm^{-1} domain (see also Chap.6.2.2) indicates that, if a stable O_{ot} species is present, the 1f-cus Ru sites are far from being saturated with O_{ot} . More precisely, many 1f-cus Ru sites remain accessible for O_2 and CO adsorption and the CO oxidation reaction can continue. The reaction would follow either the CO_{ot} - O_{ot} or the CO_{ot} - O_{br} path (hence no stable CO_{ot}) rather than the CO_{br} - O_{ot} path, which would explain the long residence time of isolated CO_{br} even under oxidizing conditions, manifested in the 1867 cm^{-1} band.

A more exact picture of the O-coverage, under the same reaction conditions, is given by HREELS measurements [81] which, compared to RAIRS measurements, possess the advantage that the frequency range of molecule-substrate vibrations can be routinely measured. The authors in Ref. [81] have found that, exposing the $\text{RuO}_2(110)$ surface to 2×10^{-7} mbar CO and 1×10^{-7} mbar O_2 at 350 K, following evacuation of the reactants (not an in situ measurement) the HREELS spectrum showed the presence of CO_{br} (corresponding to the band at 1867 cm^{-1} in our experiment) but no vibrations specific of O_{ot} and O_{br} were detected (Fig.5.b in Ref.[81]). This result shows that CO_{ot} reacts efficiently with both O_{ot} and O_{br} while CO_{br} is slightly less active in the oxidation reaction, which would explain its longer residence time at the surface and its subsequent detection by RAIRS.

Remaining in the 10^{-7} mbar domain, the stable state (a) achieved by the model catalyst can be altered by keeping the 2×10^{-7} mbar CO flux constant and switching off the oxygen flux. After evacuation of the oxygen, the intense

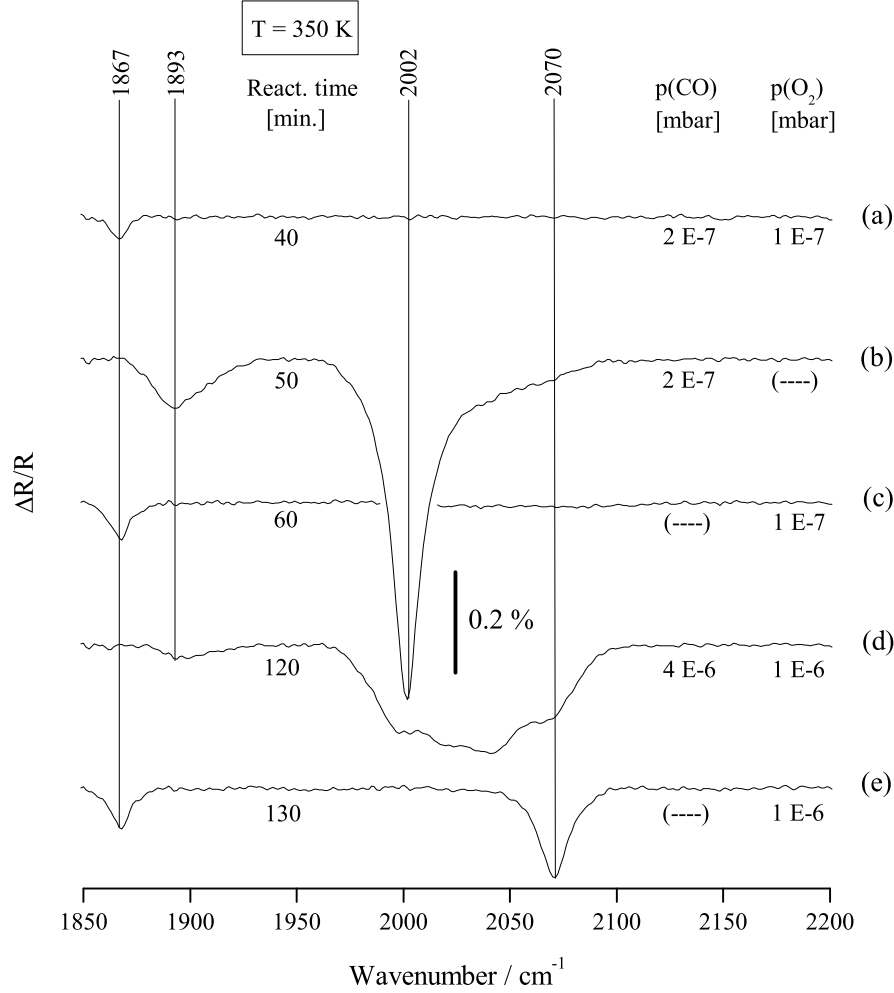


Figure 7.1: In situ RAIRS spectra of the $\text{RuO}_2(110)$ model catalyst during the CO oxidation reaction at 10^{-7} - 10^{-6} mbar. a) small number of symmetric CO_{br} (1867 cm^{-1}) and no CO_{ot} , b) symmetric CO_{br} (1893 cm^{-1}), asymmetric CO_{br} (2002 cm^{-1}) and no CO_{ot} , c) same as in (a), d) areas with different local CO_{ot} coverages, from sparse (2002 cm^{-1}) to densely packed (2070 cm^{-1}), e) symmetric CO_{br} (1867 cm^{-1}) and densely packed $\text{CO}_{br}/\text{CO}_{ot}$ clusters (2070 cm^{-1}). The densely packed $\text{CO}_{br}/\text{CO}_{ot}$ clusters are inert in the CO oxidation reaction (e). They can be formed only after a stable CO_{ot} species has been accommodated (d) at 4×10^{-6} mbar CO.

line at 2002 cm^{-1} in Fig.7.1.b shows that the O_{br} species, characteristic of stoichiometric $\text{RuO}_2(110)$, was completely replaced by asymmetric CO_{br} while the 1f-cus Ru sites are still vacant. The broad band at 1893 cm^{-1} in Fig.7.1.b indicates that a minority of the CO_{br} species is in the symmetric bridging positions, a disorder effect which arises when CO densely populates the bridge sites (see also Chap.6.1.1.)

At this point, as long as no significant coverage by on-top CO_{ot} has yet occurred, the state of the catalyst surface can still be brought back to Fig.7.1.a by dosing oxygen in excess. Switching off the CO flux and restoring the 1×10^{-7} mbar O_2 flux, the RAIR spectrum Fig.7.1.c turns identical to spectrum Fig.7.1.a, exhibiting a single CO stretch line at 1867 cm^{-1} due to sparse, symmetric CO_{br} .

By increasing the reactants pressure to the lower 10^{-6} mbar domain, qualitatively new features of CO adsorption at the $\text{RuO}_2(110)$ model catalyst surface are observed in the RAIRS. Under reducing conditions, while dosing 4×10^{-6} mbar CO and 1×10^{-6} mbar O_2 , the RAIR spectrum (Fig.7.1.d) shows a diffuse band in the $2000\text{-}2070\text{ cm}^{-1}$ domain. The existence of a CO_{ot} species, randomly distributed over the catalyst surface, is confirmed by RAIRS if we consider that the diffuse $2000\text{-}2070\text{ cm}^{-1}$ band is composed of individual IR absorption lines due to CO molecules oscillating in regions with very different *local* CO coverages. Due to the strong dipole-dipole coupling between oscillating CO molecules, regions with complete rows of CO_{br} but low CO_{ot} coverage contribute IR absorption intensity in the range $2000\text{-}2040\text{ cm}^{-1}$ while densely packed $\text{CO}_{br}/\text{CO}_{ot}$ groups contribute intensity at higher frequencies.

Like in the case of the 1867 cm^{-1} band, it is not clear how the CO species responsible for the 2070 cm^{-1} band can populate the catalyst surface at 350 K even under a purely oxidizing flux of 1×10^{-6} mbar O_2 . Moreover, the 1867 cm^{-1} and 2070 cm^{-1} bands turn out to be dominant at higher reactant pressures, under both stoichiometric and oxidizing reaction conditions. The corresponding species of adsorbed CO molecules, which may be characterised as inert towards oxidation in the 350-400 K range, shall prove typical for the CO oxidation reaction over the $\text{RuO}_2(110)$ model catalyst in the $10^{-6}\text{-}10^{-2}$ mbar pressure range.

Summary

We have discussed the *in situ* RAIRS spectra of CO species adsorbed at the RuO₂(110) model catalyst surface during the CO oxidation reaction at 350 K in the 10⁻⁷-10⁻⁶ mbar range. Under stoichiometric and oxidizing gas feed in the lower 10⁻⁷ mbar range, the RAIR spectrum presents only one band (1867 cm⁻¹) which we have assigned to the CO_{br} species, slightly less active in the oxidation reaction as CO_{ot}. No stationary CO_{ot} population was detected, presumably due to the high activity of CO_{ot} toward recombination with O_{ot} and O_{br}. Exposure of the RuO₂(110) surface to a purely reducing feed of 2 × 10⁻⁷ mbar CO has led to the complete replacement of O_{br} by CO_{br} (2002 cm⁻¹) but again, no stationary CO_{ot} was detected. In the absence of a stable CO_{ot} species, the CO_{br} molecules (2002 cm⁻¹) could subsequently be oxidized by exposing the surface to 1 × 10⁻⁷ mbar O₂. The regime of CO adsorption changes beginning with the lower 10⁻⁶ mbar range. Under a reducing reactant feed of 4 × 10⁻⁶ mbar CO, RAIRS evidence indicates that areas of the catalyst surface become densely covered by CO (2000-2070 cm⁻¹) after accommodation of a randomly distributed stationary CO_{ot} species. Exposure at 350 K to a purely oxidizing feed of 1 × 10⁻⁶ mbar O₂ did not lead to the oxidation of the CO molecules in the densely covered areas (2070 cm⁻¹).

7.2 In situ RAIRS in the 10^{-6} - 10^{-2} mbar domain

The RAIRS measurements discussed in the last section have shown that CO adsorption on the RuO₂(110) model catalyst surface, under a reducing gas feed in the lower 10^{-6} mbar range, leads to the formation of areas with a high local CO coverage which, due to the strong dipole-dipole coupling between the compactly grouped CO molecules, are characterised by a collective IR frequency band at high frequency (2070 cm^{-1}). From a chemical point of view, these densely covered areas are characterised by their low activity towards oxidation, as shown by the stability of the 2070 cm^{-1} band even under a purely oxidizing feed at 10^{-6} mbar. The current section is dedicated to *in situ* RAIRS investigations of the CO species on the model catalyst surface, under reaction conditions in the 10^{-6} - 10^{-2} mbar domain. It will become apparent that, under stoichiometric and oxidizing reactant feed, the picture proposed in the previous section for CO adsorption in the 10^{-6} mbar range remains qualitatively valid up to 10^{-2} mbar.

7.2.1 RuO₂(110) model catalyst under stoichiometric feed of CO and O₂

Recording of each series of RAIR spectra at high pressure was done by keeping a constant O₂ partial pressure and successively setting the CO partial pressure to 1, 2, 4 and 10 times the O₂ partial pressure. For the next series of spectra the O₂ partial pressure was increased one order of magnitude, and the CO pressure was again set to 1, 2, 4 and 10 times the O₂ partial pressure. For the specified reactant feeds, RAIRS measurements were performed *in situ* during the CO oxidation reaction, from 1×10^{-6} mbar to 1×10^{-2} mbar O₂ partial pressure. In the pressure range 10^{-4} - 10^{-2} mbar the UHV/HP cell was operated as a batch reactor (Chap.2.1.3). RAIR spectra were recorded with 4 cm^{-1} resolution by averaging of 300 scans, recording of each spectrum taking 216 seconds.

In the following, we shall present the RAIR spectra grouped according to the composition of the reactant feed, in order to emphasize their similarities over the extended 10^{-7} - 10^{-3} mbar pressure range. The RAIR spectra recorded at 350 K under $p(\text{CO}) = 2\text{ }p(\text{O}_2)$ gas feed are plotted in Fig.7.2. It becomes apparent from the first sight that the spectra remain similar under a variation of the pressure by four orders of magnitude. Over the entire pressure range, a

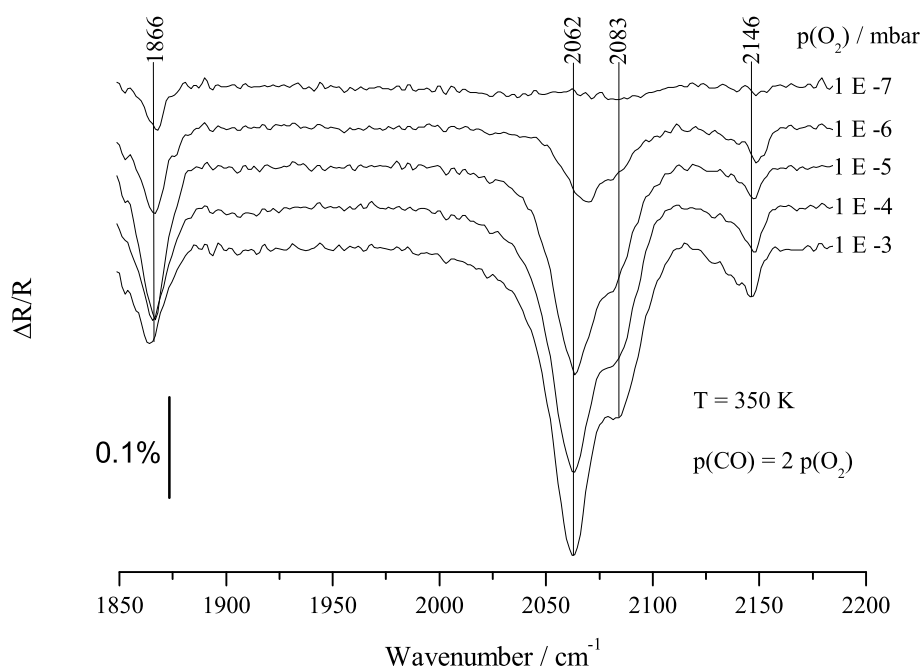


Figure 7.2: *In-situ* RAIR spectra of the $\text{RuO}_2(110)$ surface during the CO oxidation reaction at 350 K. The reactants were fed with $p(\text{CO}) = 2 p(\text{O}_2)$ at partial pressures ranging from 10^{-7} mbar to 10^{-3} mbar.

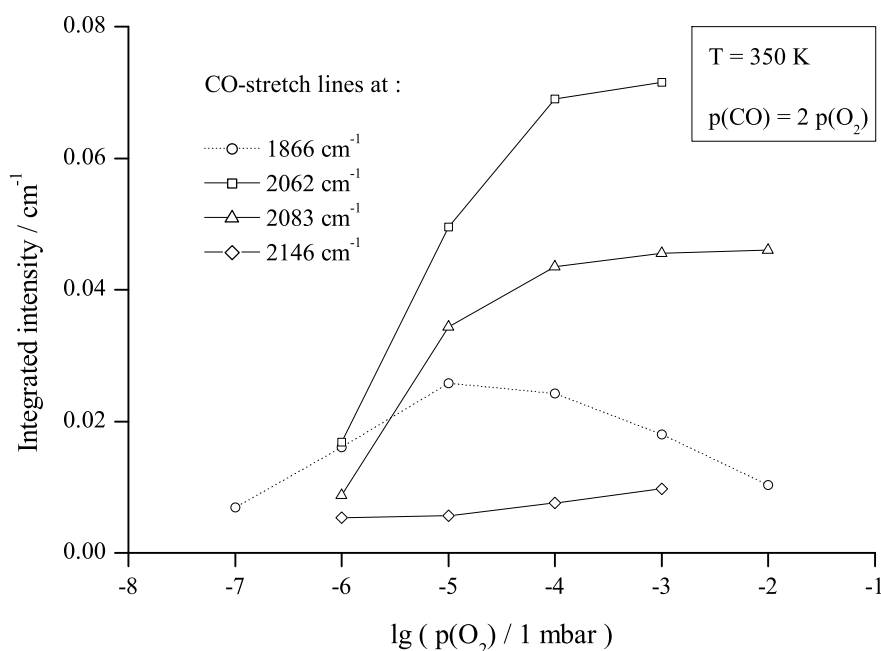


Figure 7.3: Integrated intensities of the individual IR lines of Fig.7.2. At higher CO partial pressures, enhanced adsorption of CO into areas with lower local CO coverage (signal at 1866 cm^{-1} decreasing) contributes to an increase of the densely covered $\text{CO}_{br}/\text{CO}_{ot}$ domains (signals at 2062 cm^{-1} and 2083 cm^{-1} increase).

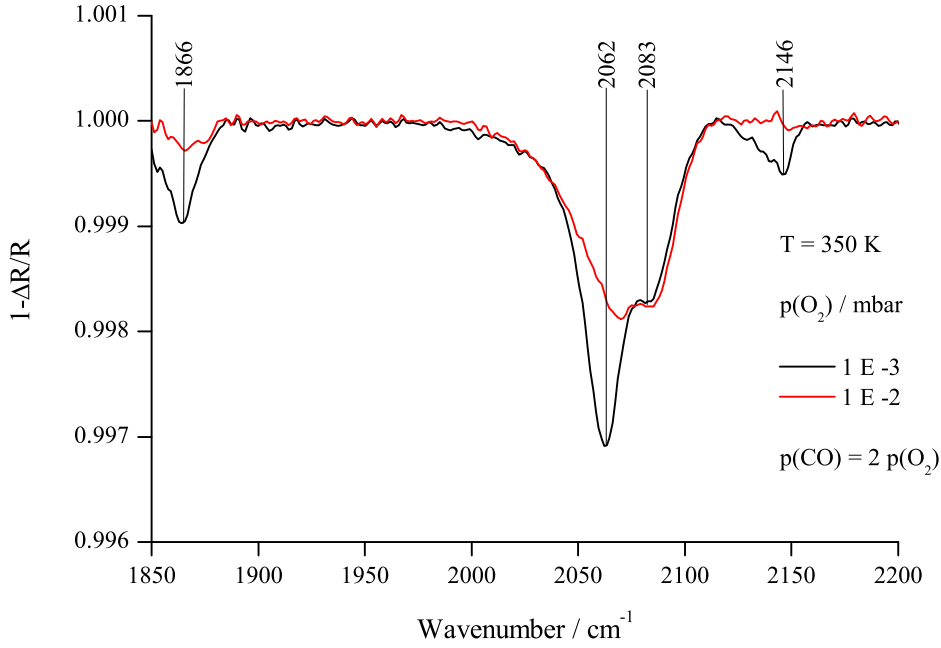


Figure 7.4: *In situ* RAIRS spectra of the $\text{RuO}_2(110)$ model catalyst under $p(\text{CO}) = 2 p(\text{O}_2)$ with 10^{-3} - 10^{-2} mbar O_2 partial pressure. The loss of intensity in the 2062 cm^{-1} band indicates a more efficient adsorption of O_2 into areas densely covered by CO, while areas with maximal CO coverage (2083 cm^{-1}) remain unaffected.

prominent feature is the 1866 cm^{-1} band, assigned to symmetric bridging CO molecules, each doubly coordinated to a pair of neighboring 2f-cus Ru atoms [64]. In the 10^{-6} - 10^{-3} mbar range we observe an IR band at 2146 cm^{-1} which, based on the CO adsorption experiments under UHV presented in Chap.6.2.2, we assign to isolated CO molecules adsorbed on O-rich areas of the $\text{RuO}_2(110)$ surface. The CO molecules responsible for the 2146 cm^{-1} band are presumably adsorbed on top 1f-cus Ru sites, being closely surrounded by O_{br} and O_{ot} . In this case the CO molecules act as IR probes testing the presence of adsorbed O at the catalyst surface. RAIRS can not detect the adsorbed O atoms due to the low frequency of the O-Ru mode ($500\text{-}600 \text{ cm}^{-1}$).

With increasing reactant pressure, the most marked changes were seen in the intensities of the 2062 cm^{-1} and 2083 cm^{-1} bands (Fig.7.3). These bands emerged under stoichiometric feed at 1×10^{-6} mbar O_2 partial pressure, increased between 10^{-6} - 10^{-4} mbar O_2 and became practically saturated at 10^{-4} - 10^{-3} mbar O_2 stoichiometric feed. We note that in the 10^{-6} - 10^{-3} mbar range the variation of the 2062 cm^{-1} and 2083 cm^{-1} bands was correlated, the integrated intensity

of the 2083 cm⁻¹ band remaining about 60% of that of the 2062 cm⁻¹ band (see also Fig.7.11). This correlation was lost after further increasing the O₂ partial pressure to 1×10^{-2} mbar while keeping a stoichiometric reactant feed, when a pronounced decrease in the intensity of the 2062 cm⁻¹ band was observed while the 2083 cm⁻¹ band remained unaffected (Fig.7.4). Due to the increasing IR absorption by CO molecules in the gas phase, we could not further follow the variation of the 2062 cm⁻¹ band at higher pressure.

Based on our study of CO adsorption on the reduced RuO₂(110) surface under UHV conditions (Chap.6.1.2), where CO bands in the 2016-2086 cm⁻¹ range can be observed, we propose to assign the 2062 cm⁻¹ and 2083 cm⁻¹ bands to ordered CO_{br}/CO_{ot} phases on RuO₂(110). We propose that these phases emerge spontaneously, conditioned by the reaction mechanism, on areas of the RuO₂(110) model catalyst characterized by a higher local CO coverage. Within these areas, no O_{ot} or O_{br} are present whereas CO occupies, to a large extent, both the bridge and the on-top positions.

Under UHV conditions, the 2083 cm⁻¹ band is characteristic of complete rows of CO_{br} alongside rows of 1f-cus Ru sites completely occupied by CO_{ot}, a phase denoted by CO_{br}/CO_{ot}. Assignment of the 2062 cm⁻¹ band is less straightforward. Upon considering the dipole-dipole interaction in ordered CO_{br}/CO_{ot} layers on RuO₂(110), modeling of the IR spectra suggests that the 2062 cm⁻¹ band is due to CO molecules vibrating in densely covered areas, where on average 2/3 of the 1f-cus Ru sites are occupied by CO_{ot} (see also Chap.7.3.2). Adsorption of O₂ on the surface requires a pair of vacant *neighboring* on-top sites [82]. Since only one on-top site out of three is vacant, there are no sufficient pairs of neighboring on-top sites in order to accommodate O₂ molecules from the gas phase directly into these areas. This circumstance could explain the stability of the CO species characterised by the 2062 cm⁻¹ band, *in situ* under stoichiometric and oxidizing reactant feed over the 10⁻⁶-10⁻³ mbar range. A representation of the *in situ* state of the RuO₂(110) model catalyst during the CO oxidation reaction, along the guidelines of the argument sketched above, is given in Fig.7.5.

The simplest mechanism for the oxidation of CO molecules in the blocked areas (2062 cm⁻¹ and 2083 cm⁻¹) implies reaction with O molecules at the area perimeter, a process which under the present conditions is very slow, as illustrated by the RAIRS oxidation experiment in Fig.7.6. Prior to the experiment, areas of the RuO₂(110) surface have been densely covered by CO after exposure at

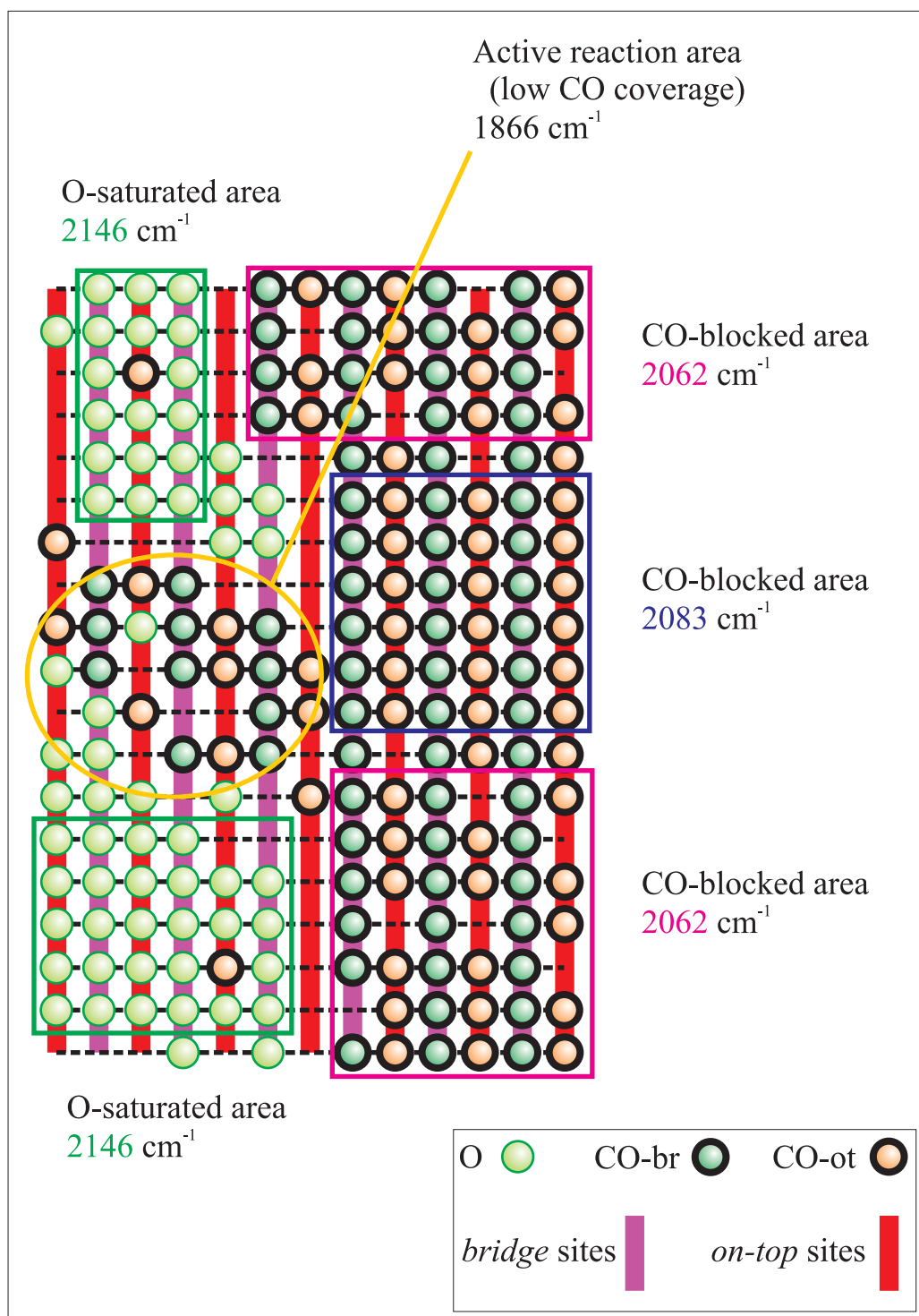


Figure 7.5: Proposed model of the $\text{RuO}_2(110)$ surface *in situ* during the CO oxidation reaction. Reaction conditions: $p(\text{CO}) = 2 p(\text{O}_2)$ in the 10^{-6} - 10^{-3} mbar range at 350 K. The corresponding RAIR spectra are plotted in Fig.7.2.

400 K to a reducing reactant flow with $p(\text{CO}) = 3 p(\text{O}_2)$ at 6×10^{-6} mbar CO partial pressure. The resulting RuO₂(110) surface exhibits locally: i) rows of saturated CO_{br} together with rows of vacant 1f-cus Ru sites, characterised by a weak IR band at 2001 cm⁻¹ and ii) areas with rows of saturated CO_{br} but with very different local CO_{ot} coverages, whose individual IR frequencies are combined into a single band centered at 2057 cm⁻¹. From the relatively high position of the central frequency, due presumably to a strong dipole-dipole coupling between closely packed CO molecules, we conclude that in most of these areas the coverage of the on top sites by CO is between 50% and 66%, values which would correspond to IR bands at about 2050 cm⁻¹ and 2060 cm⁻¹ respectively. This CO-precovered RuO₂(110) surface was subsequently exposed at 400 K to a purely oxidizing feed of 2×10^{-6} mbar O₂. The *in situ* RAIR spectrum shows a single CO band at 2071 cm⁻¹ which, although continuously diminishing, takes as long as 30 minutes to completely disappear, regardless of the strongly oxidizing conditions. This observation clearly indicates that the CO species characterized by the 2071 cm⁻¹ band is practically inactive during the CO oxidation reaction, acting more like a catalytic poison to the areas it occupies rather than as an active reactant. We could say that the catalyst is partially poisoned by one of the reactants.

To rationalize the *in situ* presence of inactive CO species at the RuO₂(110) model catalyst surface during the CO oxidation reaction under strongly oxidizing conditions, we propose to assign the CO bands with frequencies as high as 2060-2080 cm⁻¹ to collective vibration modes of CO molecules located in areas which are practically blocked for O₂ adsorption, due to a sufficiently high CO_{ot} local coverage (at least 2/3 of the 1f-cus Ru sites, for example). These CO molecules can only react with O along the perimeter of the area they occupy. There are essentially two mechanisms by which O atoms can be supplied to the frontier of CO-blocked areas. First, O₂ can adsorb into the immediate vicinity of the frontier, provided there is a sufficient number of pairs of neighboring vacant on-top sites. Second, O₂ can adsorb into a different region of the RuO₂(110) surface and subsequently approach the CO-blocked areas through diffusion along the rows of 1f-cus Ru sites. Assuming that under strongly oxidizing conditions the RuO₂(110) surface is richly covered by O, except for the CO-blocked areas, it is likely that the rate of CO oxidation equals in fact the rate of O diffusion.

To test this hypothesis, we have studied the time dependence of the integrated intensity of the 2071 cm⁻¹ CO band under oxidizing conditions (Fig.7.7).

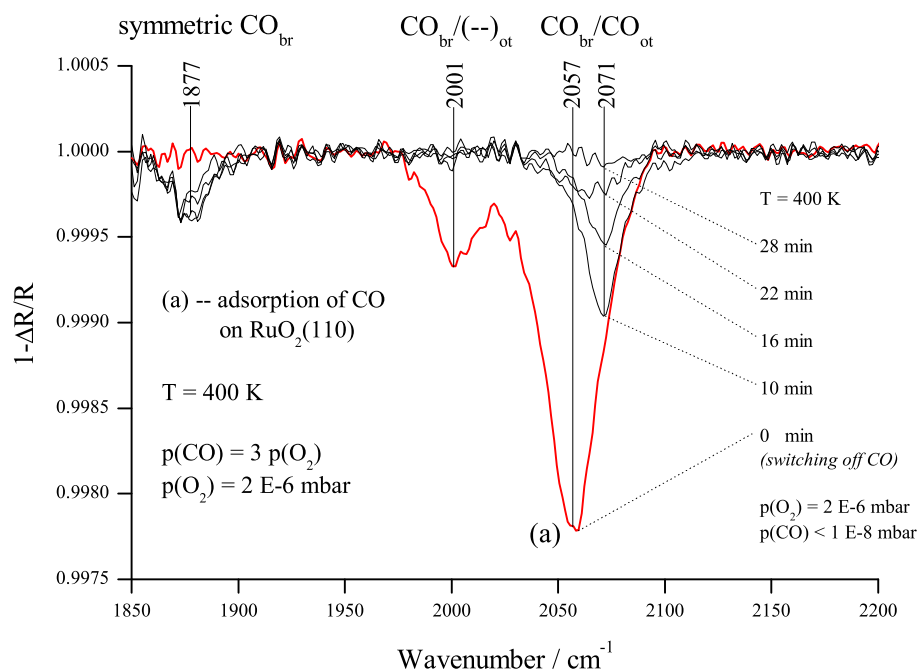


Figure 7.6: RAIR spectra showing the partial self-poisoning of the $\text{RuO}_2(110)$ model catalyst by the reactant CO. Previously adsorbed CO (curve *a*) was exposed to 2×10^{-6} mbar O_2 at 400 K. Residual CO species (2071 cm^{-1}) were detected for 30 minutes after switching to purely oxidizing conditions.

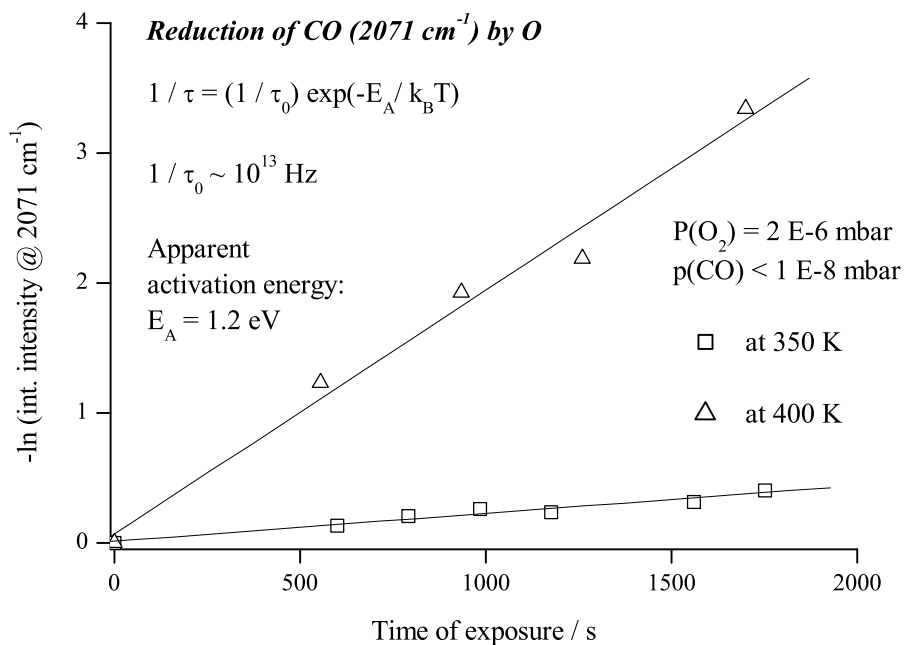


Figure 7.7: Integrated intensities of the 2071 cm^{-1} CO band, plotted against the time of exposure to 2×10^{-6} mbar O_2 at 350 K and 400 K. For the CO oxidation process in Fig.7.6, an apparent activation energy of $1.2 \pm 0.1 \text{ eV}$ was inferred.

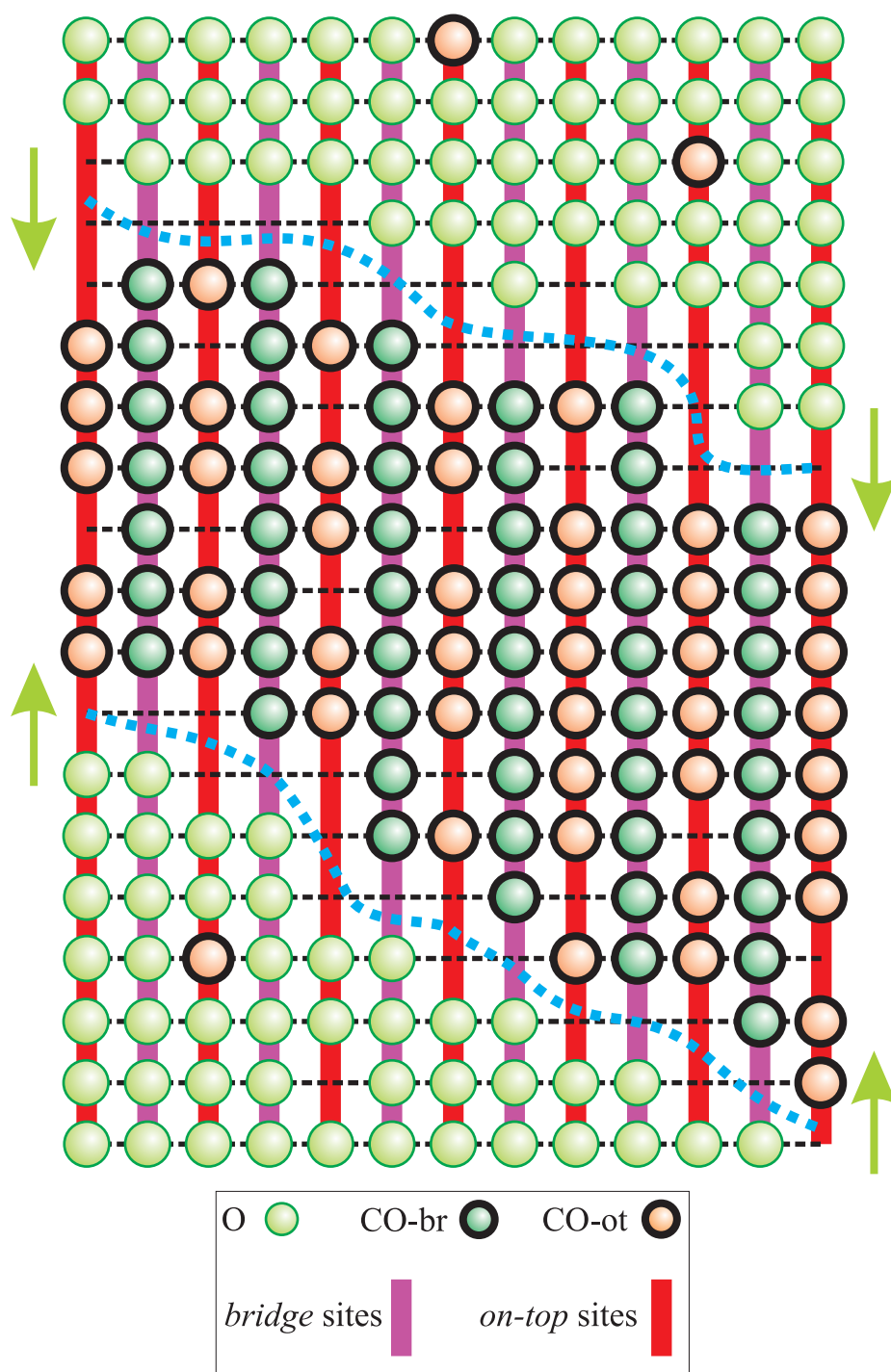


Figure 7.8: Segregation of the reactants on the $\text{RuO}_2(110)$ surface during the CO oxidation reaction. Under the strongly oxidizing conditions of Fig.7.6 the CO-blocked areas (2071 cm^{-1}) are encircled by O-saturated areas. The reaction is confined to the narrow stripe (blue curve) separating the areas, where O atoms are delivered through diffusion along the [001] direction (green arrows).

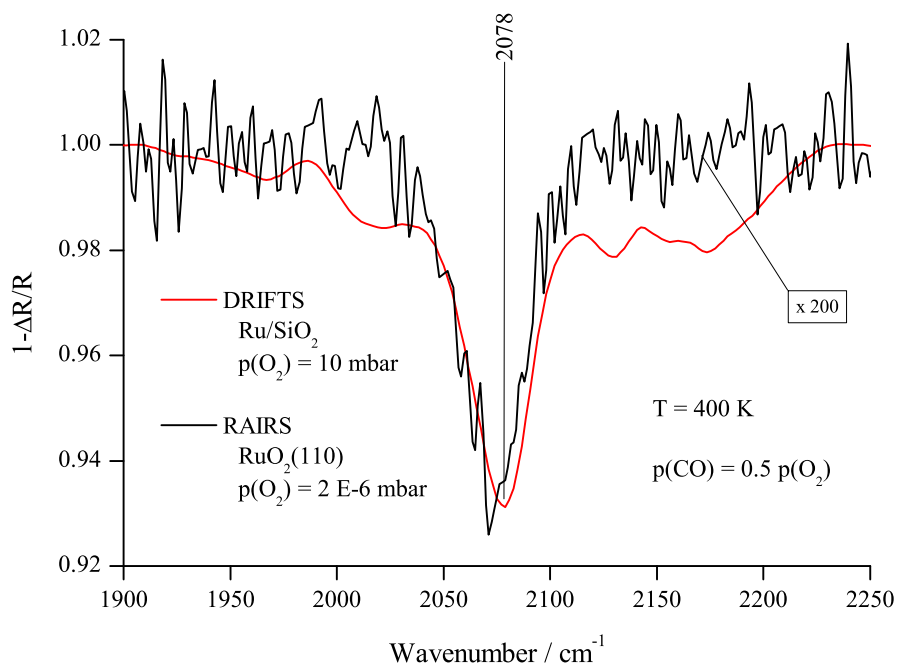


Figure 7.9: Comparison of *in situ* IR reflectivity spectra of Ru-based catalysts during the CO oxidation reaction: DRIFTS of a Ru/SiO₂ supported catalyst (red curve, [12]) and RAIRS of the RuO₂(110) model catalyst (black curve) at 400 K with $p(\text{CO}) = 0.5 p(\text{O}_2)$. The O₂ partial pressures were 10 mbar (DRIFTS) and 2×10^{-6} mbar (RAIRS).

Assuming a frequency factor of 10^{13} Hz for the rate constant of the CO oxidation reaction, we have found an apparent activation energy of 1.2 ± 0.1 eV, in excellent agreement with the activation energy of 1.2 eV for O diffusion along the rows of 1f-cus Ru sites computed by Over *et al.* [65]. A representation of the RuO₂(110) surface during oxidation of the CO molecules in the blocked areas, under an excess of oxygen in the gas phase, is given in Fig.7.8.

We note that the existence of an inactive CO 'spectator' species at the Ru-based catalyst surface, characterised by an IR band in the 2070-2080 cm⁻¹ range, is a more general phenomenon and not restricted to the chosen model catalyst, namely the epitaxially grown RuO₂(110) film on the monocrystalline Ru(001) surface. Diffuse reflectance IR spectroscopy (DRIFTS) studies performed *in situ* during the CO oxidation reaction over finely divided Ru catalysts, consisting of nanometer size Ru particles supported on MgO and SiO₂, have shown that the CO-stretch region of the IR spectrum is actually dominated by a similar CO band, at 2067 cm⁻¹ and 2078 cm⁻¹ respectively [12]. The DRIFT spectra were

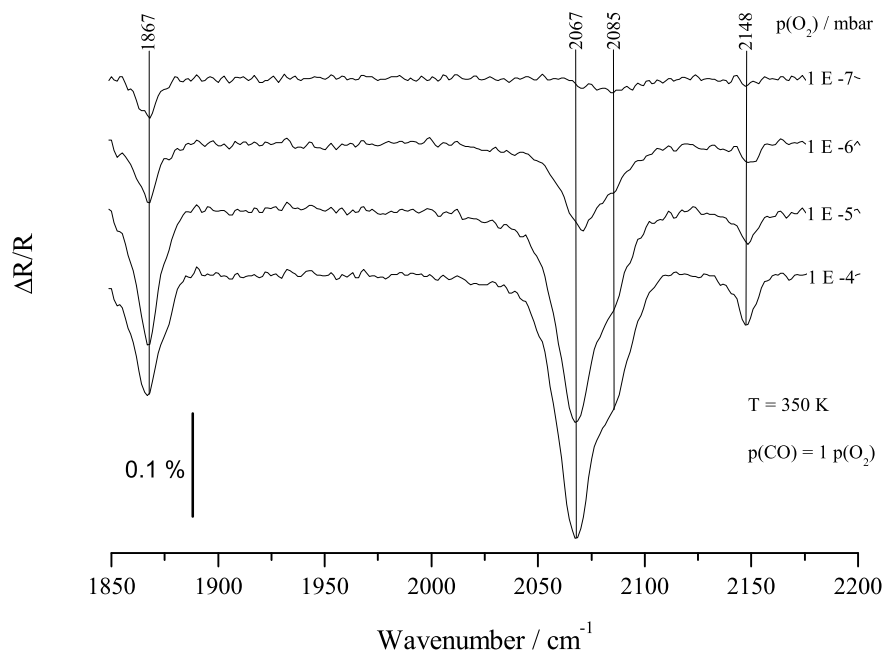


Figure 7.10: *In-situ* RAIR spectra of the RuO₂(110) surface during the CO oxidation reaction at 350 K. The reactants were fed with $p(\text{CO}) = p(\text{O}_2)$ at partial pressures ranging from 10^{-7} mbar to 10^{-4} mbar.

recorded at 423 K under a strongly oxidizing reactant feed with $p(\text{CO}) = 0.5 p(\text{O}_2)$ at 5–35 mbar CO and O₂ partial pressure. For comparison we consider the equivalent RAIR spectra of CO on the RuO₂(110) model catalyst, recorded at 400 K with $p(\text{CO}) = 0.5 p(\text{O}_2) = 1 \times 10^{-6}$ mbar. The similarity between the IR bands of CO adsorbed *in situ* on the supported Ru/SiO₂ catalyst (DRIFTS) and those on the RuO₂(110) model catalyst (RAIRS) (Fig.7.9), indicates that for Ru-based catalysts both the materials and the pressure gap are successfully bridged in the context of IR spectroscopy.

7.2.2 RuO₂(110) model catalyst under oxidizing reaction conditions

In the discussion of *in situ* RAIR spectra of the RuO₂(110) model catalyst we have concentrated on the state of the surface under stoichiometric ($p(\text{CO}) = 2 p(\text{O}_2)$) reactant feed. For a more complete picture, we shall now discuss the *in situ* state of the model catalyst under the excess of one of the reactants. The RAIR spectra in Fig.7.10 were recorded under oxidizing reaction conditions with $p(\text{CO}) = p(\text{O}_2)$

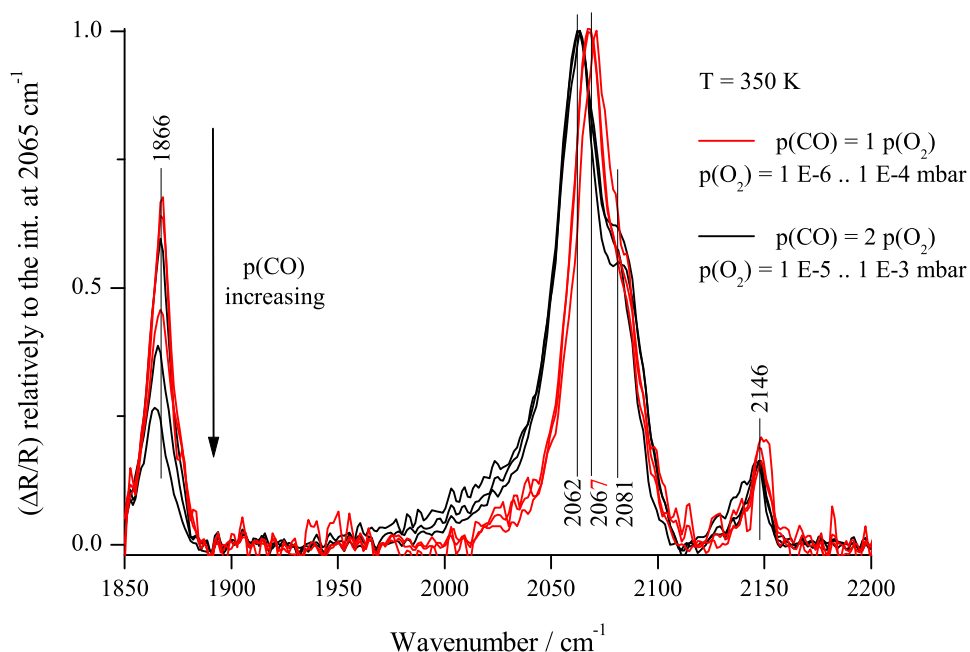


Figure 7.11: Comparison of *in situ* RAIR spectra of the $\text{RuO}_2(110)$ model catalyst under oxidizing (red curves) and stoichiometric (black curves) reaction conditions. The spectra were normalized relatively to the intensity of the main CO band, located at 2067 cm^{-1} and 2062 cm^{-1} respectively.

and 10^{-7} - 10^{-4} mbar O_2 partial pressure. Similarly the case of stoichiometric feed (Fig.7.2), in the 10^{-7} - 10^{-6} mbar domain we note the emergence of two bands at 2067 cm^{-1} and 2085 cm^{-1} . In the 10^{-6} - 10^{-4} mbar range the RAIR spectra are similar to each other, like in the case of stoichiometric feed. The relatively intense bands at 1867 cm^{-1} and 2148 cm^{-1} accentuate the similarity to RAIR spectra recorded under stoichiometric feed. The differences between the oxidizing and the stoichiometric regime in the 10^{-6} - 10^{-3} mbar range, as well as the similarity of the spectra recorded under reactant feeds of the same composition, are shown in a common plot of the corresponding RAIR spectra, normalized relatively to the intensities of the main band at 2067 cm^{-1} (oxidizing conditions) and at 2062 cm^{-1} (stoichiometric conditions) (Fig.7.11).

7.3 Characteristic vibration frequencies of ordered CO_{br}/CO_{ot} phases on RuO₂(110)

In the previous sections we have discussed in some detail the *in situ* RAIR spectra of the RuO₂(110) model catalyst during the CO oxidation reaction at high reactant pressure, more exactly at 350 K in the 10⁻⁷-10⁻³ mbar range. In order to achieve an interpretation of the experimental results, we have made the fundamental assumption that the CO bands detected *in situ* under oxidizing and stoichiometric reaction conditions, most of them laying the 2060-2085 cm⁻¹ domain, are attributable to high coverage CO_{br}/CO_{ot} phases formed on RuO₂(110). This assumption is natural since UHV experiments have shown that the CO_{br}/CO_{ot} phases formed on the reduced RuO₂(110) surface under increasing CO coverage are characterised by IR bands in the 2000-2086 cm⁻¹ domain. On the other hand, the most straightforward *Ansatz* for the discussion of the IR bands observed under reaction conditions would have been an analogy with ordered coadsorbate phases on RuO₂(110), consisting of both CO *and* O. The most critical aspect of our interpretation, based on adsorbates consisting exclusively of CO, is therefore the implied absence, even during an excess of oxygen in the gas phase, of O adsorbed in the immediate vicinity of CO molecules. There are however experimental reasons which could justify the omission of O from the models we shall propose for the *in situ* structure of the adsorbates on the model catalyst surface. Referring the reader to our experiments concerning the coadsorption of CO and O on the RuO₂(110) surface under UHV conditions (Chap.6.2) we note that the characteristic IR frequencies of the studied CO-O coadsorbates are, within a margin of about 20 cm⁻¹, either too low (2000-2046 cm⁻¹) or too high (2100-2150 cm⁻¹) to interfere with the characteristic domain (2060-2085 cm⁻¹) of the CO bands observed *in situ* during the CO oxidation reaction (Fig.7.12). Returning to our fundamental interpretative assumption, it becomes important to estimate the characteristic IR frequencies of specific ordered CO_{br}/CO_{ot} phases on RuO₂(110) in order to make assignments of the IR bands observed *in situ* during the CO oxidation reaction on the RuO₂(110) model catalyst. The present section is devoted to the calculation of IR frequencies, characteristic of selected ordered CO_{br}/CO_{ot} phases formed on the reduced RuO₂(110) surface, by considering a model of the dipole-dipole coupling between the vibrating CO molecules.

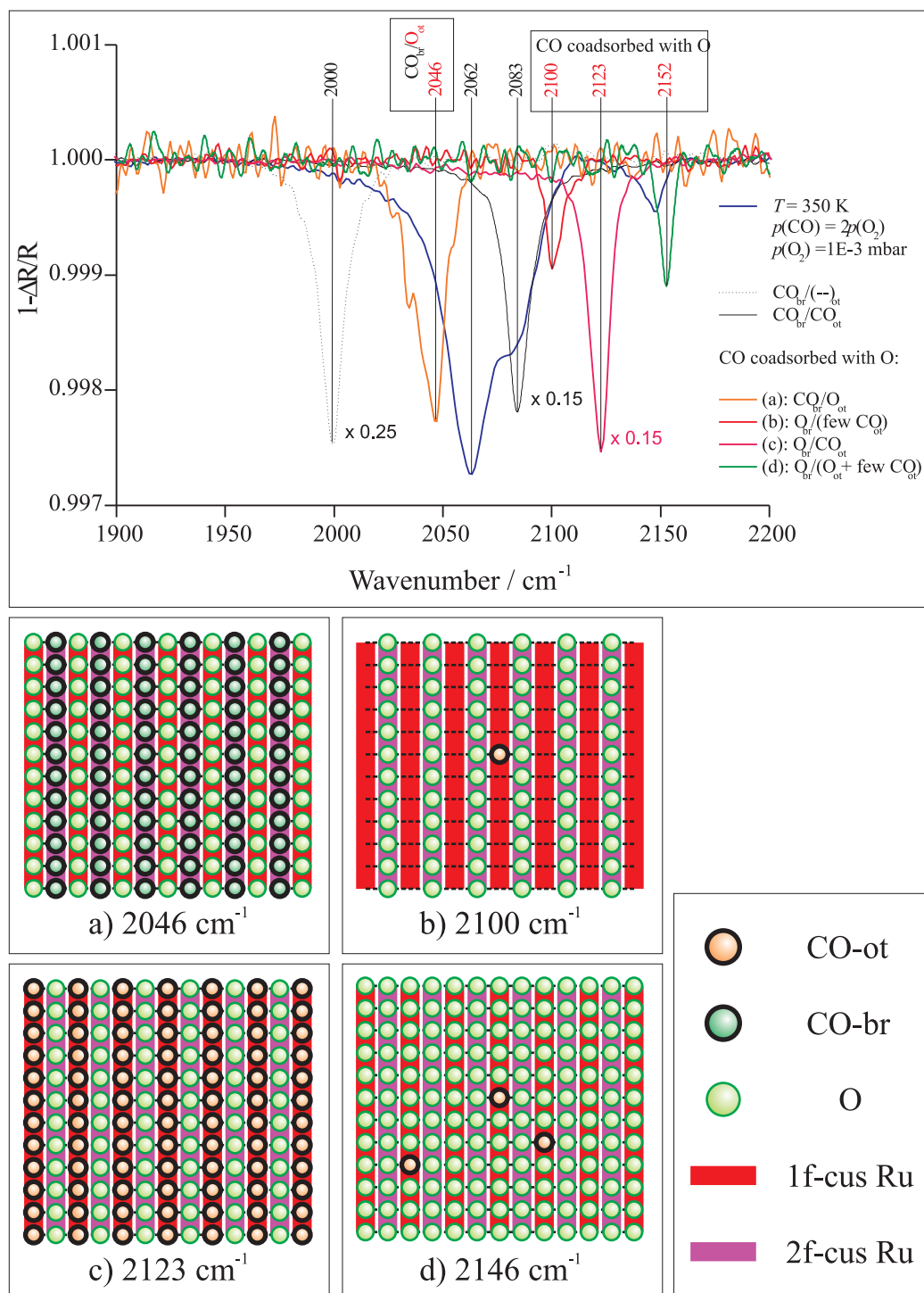


Figure 7.12: The IR bands measured for several CO-O coadsorbate structures on $\text{RuO}_2(110)$ (insets *a* – *d*) fall outside the 2060–2085 cm^{-1} domain, characteristic of the bands of CO on the $\text{RuO}_2(110)$ surface *in situ* during the CO oxidation reaction (blue curve).

7.3.1 Vibrational polarizabilities of isolated CO molecules adsorbed on RuO₂(110)

The current subsection is dedicated to the estimation of the parameters of the vibrational polarizability of CO molecules adsorbed on the reduced RuO₂(110) surface. We are interested in finding appropriate values for the molecular polarizability parameters α_V and Ω of Eq.7.3 for the CO_{br} and CO_{ot} species. For this purpose we shall refer to the CO adsorption experiment on the reduced RuO₂(110) surface under UHV conditions, described in Fig.6.3 Chap.6.1.1. The experiment consists in monitoring by RAIRS the gradual adsorption of CO on the reduced RuO₂(110) surface, at 110 K and 3×10^{-9} mbar CO pressure. Prior to the adsorption experiment, the reduced r-RuO₂(110) surface surface is characterised by an IR band at 2000 cm⁻¹, corresponding to rows of bridge sites saturated by CO, singly coordinated to the underlaying 2f-cus-Ru sites, alongside vacant 1f-cus-Ru sites. The gradual filling of these vacant sites by CO leads to the development of an intense IR band, which shifts from 2016 cm⁻¹, at low CO_{ot} coverage, up to 2086 cm⁻¹ at saturation CO_{ot} coverage. Parallel to the evolution of this high frequency band, a downward shift of about 10-15 cm⁻¹ and a weakening of the original 2000 cm⁻¹ band are observed. The evolution of the two bands, marked in Fig.7.13, can be understood as the result of the coupled vibrations of the two different types of molecular oscillators, CO_{br} and CO_{ot}. By setting up a dynamical model of the coupled vibrations of the two types of adsorbed CO molecules, we can match the positions of the low frequency band (ω_l) and high frequency band (ω_h) predicted by the model, with the values obtained directly from the CO adsorption experiment, obtaining thus an estimate of the molecular polarizability parameters α_V and Ω for both species of CO molecules.

Dynamical model for the vibrations of the coupled CO_{br} and CO_{ot} species on the reduced RuO₂(110) surface

The RAIR spectrum of the adsorbed CO layer, as function of the frequency ω of the exciting light, is given by Eq.3.15 [36]

$$\left(\frac{\Delta R}{R}\right)(\omega) = -\frac{16\pi}{c} \left(\frac{N}{A}\right) \left(\frac{\sin^2 \varphi}{\cos \varphi}\right) \omega \text{Im } \tilde{\alpha}(\omega)$$

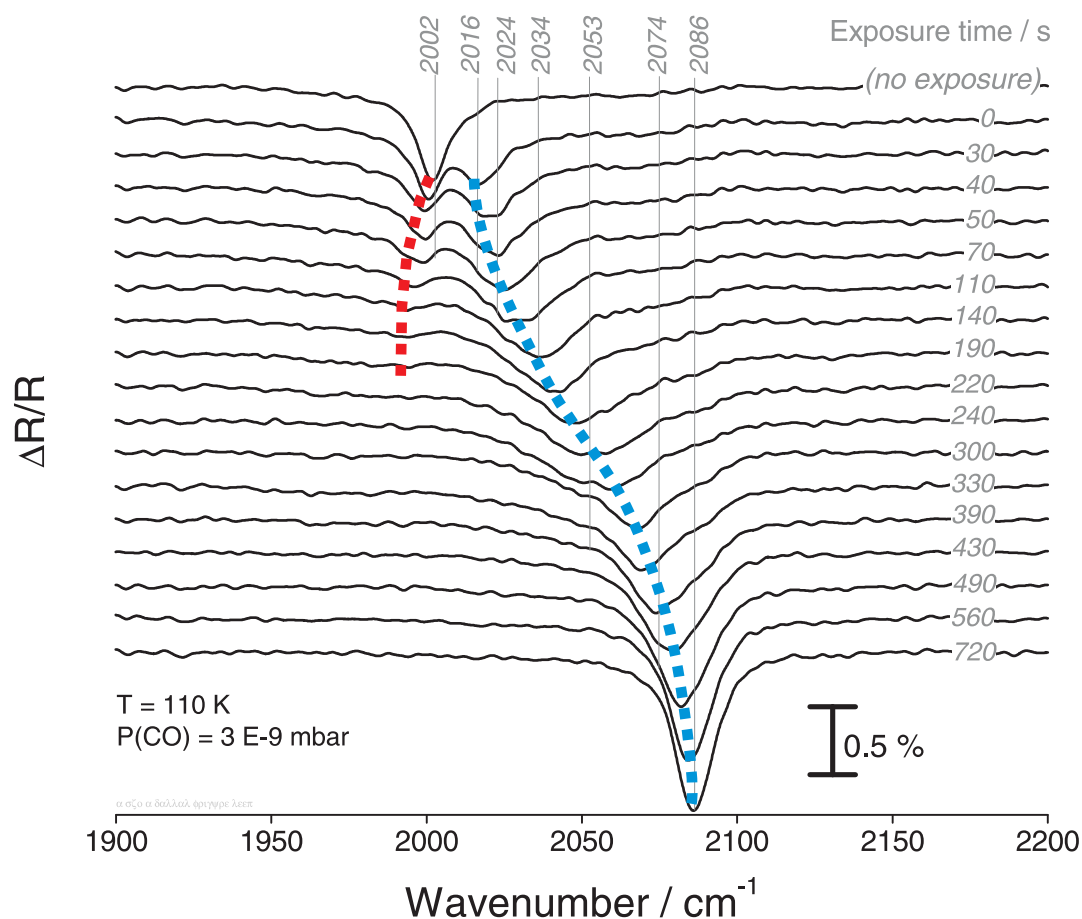


Figure 7.13: The RAIR spectrum of the $\text{CO}_{br}/\text{CO}_{ot}$ adsorbed layer on the reduced $\text{r-RuO}_2(110)$ surface is characterised by two IR bands. The high frequency band (blue trace) shifts from 2016 cm^{-1} up to 2086 cm^{-1} with increasing intensity. The low frequency band (red trace) shifts $10\text{-}15 \text{ cm}^{-1}$ downwards with diminishing intensity. The observed development of the IR bands is due to the coupled vibrations of two types of molecular oscillators, CO_{br} and CO_{ot} .

where c is the speed of light in vacuum, N is the number of molecules adsorbed over a surface area A of the sample, φ is the angle of incidence of the light beam relatively to the surface normal and $\tilde{\alpha}(\omega)$ is the *effective* vibrational polarizability of a CO molecule in the fully coupled layer, defined according to

$$\sum_i \hat{p}_i = N \tilde{\alpha}(\omega) \hat{E}^{ext} \quad , \quad (7.1)$$

where the sum extends over all sites \mathbf{x}_i of the selected area occupied by adsorbed CO molecules. Since the vibrational dipole moment of the CO molecule adsorbed at site \mathbf{x}_i is simply

$$\hat{p}_i = \alpha_i(\omega) \hat{E}_i^{loc} \quad ,$$

we can rewrite Eq.7.1 as [39]

$$\tilde{\alpha}(\omega) = \frac{1}{N \hat{E}^{ext}} \sum_i \alpha_i(\omega) \hat{E}_i^{loc} \quad . \quad (7.2)$$

The effective polarizability $\tilde{\alpha}$ of the CO molecule, coupled by dipole-dipole forces with all other CO molecules in the CO_{br}/CO_{ot} adsorbed layer, is obtained from Eq.7.2 after insertion of the local electric field \hat{E}_i^{loc} corresponding to the specified structure of the CO_{br}/CO_{ot} adsorbed layer and computed from the dynamical equation Eq.3.61. For the vibrational polarizabilities α_i of isolated CO molecules we shall adopt the following lorentzian parametrizations

$$\begin{aligned} \alpha_i^{br}(\omega) &= \alpha_V^{br} \frac{\Omega_{br}^2}{\Omega_{br}^2 - \omega^2 - i\omega\delta} \\ \alpha_j^{ot}(\omega) &= \alpha_V^{ot} \frac{\Omega_{ot}^2}{\Omega_{ot}^2 - \omega^2 - i\omega\delta} \end{aligned} \quad (7.3)$$

for CO molecules adsorbed in *bridge* and *on-top* sites respectively. For both species of adsorbed CO molecules, α_V denotes the vibrational polarizability, Ω denotes the stretch frequency of the molecule and δ denotes the width (FWHM) of the lorentzian vibrational line, typically in the range 10-30 cm⁻¹.

In the present treatment we are going to consider only a simplified model of the dynamics of adsorbed CO molecules, which would lead to a simplified version of the general dynamical equation Eq.3.61. The parameters we are going to treat as negligible are: i) the part of the dipole-dipole potential due to the electro-

static images of the molecular dipoles, ii) the electronic polarizability α_e of the adsorbed molecules and iii) the short range chemical coupling χ between neighboring molecules. With these simplifications, the dynamical equation Eq.3.61 is reduced to

$$\hat{E}_i^{loc} + \sum_{j \neq i} v(|\mathbf{x}_i - \mathbf{x}_j|) \alpha_j(\omega) \hat{E}_j^{loc} = \hat{E}_i^{ext} \quad (7.4)$$

where the interaction potential of a pair of CO molecules

$$v(|\mathbf{x}_i - \mathbf{x}_j|) = \frac{1}{|\mathbf{x}_i - \mathbf{x}_j|^3}$$

corresponds to the usual through-vacuum interaction potential of a pair of parallel dipoles (Eq.3.55). The sum in Eq.7.4 extends over all sites \mathbf{x}_j occupied by CO on the reduced $\text{RuO}_2(110)$ surface. The dynamical equation Eq.7.4 has to be solved for the local field \hat{E}_i^{loc} by considering the particular arrangement of CO molecules within the $\text{CO}_{br}/\text{CO}_{ot}$ layer. This would constitute a problem at intermediate gas exposure, when CO adsorption on the reduced $\text{RuO}_2(110)$ surface at 110 K leads to the formation of a disordered $\text{CO}_{br}/\text{CO}_{ot}$ layer, through a random occupation of the on-top sites, which would require the use of rather elaborate approximation schemes.

Vibration of CO molecules in a saturated $\text{CO}_{br}/\text{CO}_{ot}$ layer

The most suitable example to start a discussion of the dynamics of coupled CO molecules is a saturated CO layer on the reduced $\text{RuO}_2(110)$ surface. The adsorbate layer consists of saturated rows of CO_{br} and saturated rows of CO_{ot} , which form a perfectly ordered adsorbate structure (Fig.7.14). The elementary cell of the ordered $\text{CO}_{br}/\text{CO}_{ot}$ layer contains one CO_{br} and one CO_{ot} molecule. Taking into account i) that the wavelength of the IR radiation is much larger than the dimensions of the adsorbate and ii) that the adsorbate presents translational symmetry, it follows that over the entire lattice, the local electric field \hat{E}_i^{loc} takes the same value at similar sites

$$\hat{E}_i^{loc} = \begin{cases} \hat{E}_{br}^{loc} & \text{if } \mathbf{x}_i \text{ is a } \textit{bridge} \text{ site,} \\ \hat{E}_{ot}^{loc} & \text{if } \mathbf{x}_i \text{ is an } \textit{on-top} \text{ site.} \end{cases} \quad (7.5)$$

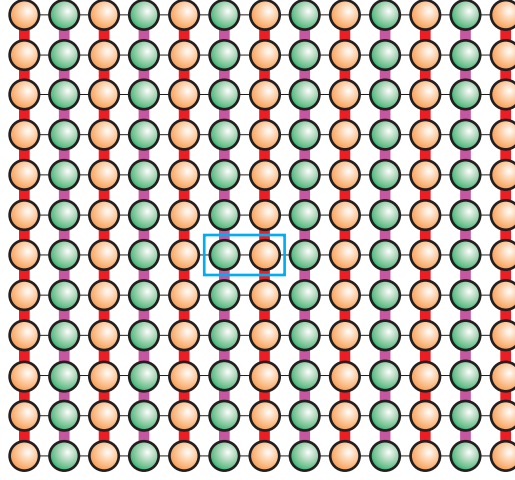


Figure 7.14: Saturated CO_{br}/CO_{ot} layer on the reduced RuO₂(110) surface. The elementary cell of the ordered adsorbate structure (blue rectangle) contains one CO_{br} and one CO_{ot} molecule.

In order to find the effective polarizability $\tilde{\alpha}(\omega)$ (Eq.7.2) of the saturated CO layer, we have to solve Eq.7.4 for the two values \hat{E}_{br}^{loc} and \hat{E}_{ot}^{loc} of the local electric field

$$\left. \begin{aligned} \hat{E}_{br}^{loc} + \sum_{j \neq 1} v(|\mathbf{x}_1 - \mathbf{x}_j|) \alpha_j(\omega) \hat{E}_j^{loc} &= \hat{E}^{ext} \\ \hat{E}_{ot}^{loc} + \sum_{j \neq 2} v(|\mathbf{x}_2 - \mathbf{x}_j|) \alpha_j(\omega) \hat{E}_j^{loc} &= \hat{E}^{ext} \end{aligned} \right\}, \quad (7.6)$$

where \hat{E}^{ext} is the value of the external field of the IR radiation and \mathbf{x}_1 and \mathbf{x}_2 denote, respectively, the *bridge* site and the *on-top* site in the marked elementary cell. Separation of the sums according to the two types of adsorption sites leads to

$$\left. \begin{aligned} \hat{E}_{br}^{loc} + [C_{11} \alpha^{br}(\omega) \hat{E}_{br}^{loc} + C_{12} \alpha^{ot}(\omega) \hat{E}_{ot}^{loc}] &= \hat{E}^{ext} \\ \hat{E}_{ot}^{loc} + [C_{21} \alpha^{br}(\omega) \hat{E}_{br}^{loc} + C_{22} \alpha^{ot}(\omega) \hat{E}_{ot}^{loc}] &= \hat{E}^{ext} \end{aligned} \right\}, \quad (7.7)$$

where the coefficients C denote the sums of the dipole-dipole interaction potential v over the sublattice consisting only from the *bridge* sites

$$\begin{aligned} C_{11} = C_{22} &= \sum_{j \neq 1} v(|\mathbf{x}_1 - \mathbf{x}_j|) \quad (\text{Fig.7.15.a}) \\ C_{12} = C_{21} &= \sum_j v(|\mathbf{x}_2 - \mathbf{x}_j|) \quad (\text{Fig.7.15.b}) \quad . \end{aligned} \quad (7.8)$$

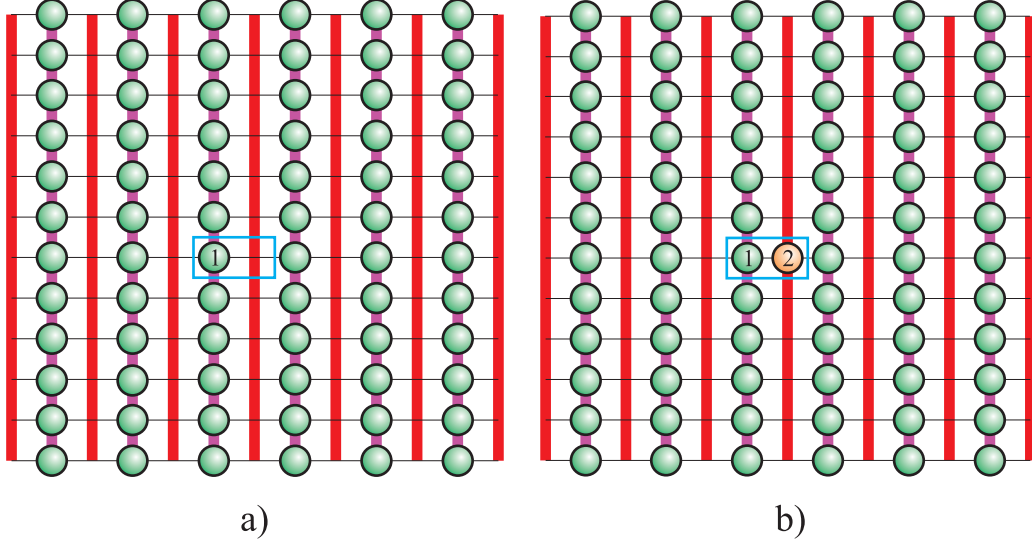


Figure 7.15: Lattice sums (Eq.7.8) of the dipole-dipole interaction potential v between adsorbed CO molecules: a) the sum C_{11} is proportional to the energy of a CO_{br} molecule in the electrostatic field produced by the other CO_{br} molecules, b) the sum C_{12} is proportional to the energy of a CO_{ot} molecule in the electrostatic field produced by the CO_{br} molecules. The adsorbed CO molecules are considered here as rigid electric dipoles.

It shall prove useful in the following to write Eq.7.7 in matrix form

$$\begin{bmatrix} \frac{1}{\alpha^{br}(\omega)} + C_{11} & C_{12} \\ C_{21} & \frac{1}{\alpha^{ot}(\omega)} + C_{22} \end{bmatrix} \cdot \begin{bmatrix} \alpha^{br}(\omega) \hat{E}_{br}^{loc} \\ \alpha^{ot}(\omega) \hat{E}_{ot}^{loc} \end{bmatrix} = \hat{E}^{ext} \begin{bmatrix} 1 \\ 1 \end{bmatrix} \quad (7.9)$$

We note that for a finite lorentzian linewidth δ (Eq.7.3), the determinant of the matrix of coefficients

$$\begin{bmatrix} \frac{1}{\alpha^{br}(\omega)} + C_{11} & C_{12} \\ C_{21} & \frac{1}{\alpha^{ot}(\omega)} + C_{22} \end{bmatrix} \quad (7.10)$$

is nonzero for all real values of the frequency parameter ω and consequently, that the inverse of the matrix of coefficients

$$\begin{bmatrix} \frac{1}{\alpha^{br}(\omega)} + C_{11} & C_{12} \\ C_{21} & \frac{1}{\alpha^{ot}(\omega)} + C_{22} \end{bmatrix}^{-1}$$

is well defined. With the help of the inverse matrix, the solutions $\alpha^{br}(\omega) \hat{E}_{br}^{loc}$ and

$\alpha^{ot}(\omega) \hat{E}_{ot}^{loc}$ of Eq.7.9 can be explicitly expressed as

$$\begin{bmatrix} \alpha^{br}(\omega) \hat{E}_{br}^{loc} \\ \alpha^{ot}(\omega) \hat{E}_{ot}^{loc} \end{bmatrix} = \hat{E}^{ext} \begin{bmatrix} \frac{1}{\alpha^{br}(\omega)} + C_{11} & C_{12} \\ C_{21} & \frac{1}{\alpha^{ot}(\omega)} + C_{22} \end{bmatrix}^{-1} \cdot \begin{bmatrix} 1 \\ 1 \end{bmatrix} . \quad (7.11)$$

We shall next use this result to find a convenient analytical expression for the effective vibrational polarizability $\tilde{\alpha}$ (Eq.7.2) as a function of the frequency parameter ω . Considering that half of the total of N sites are bridge (on-top) sites, the effective vibrational polarizability $\tilde{\alpha}$ is

$$\tilde{\alpha}(\omega) = \frac{1}{2\hat{E}^{ext}} \left[\alpha^{br}(\omega) \hat{E}_{br}^{loc} + \alpha^{ot}(\omega) \hat{E}_{ot}^{loc} \right] .$$

Inserting the solution Eq.7.11 into the last equation, we get the final expression of the effective vibrational polarizability $\tilde{\alpha}$ of a CO molecule within the saturated CO_{br}/CO_{ot} layer

$$\tilde{\alpha}(\omega) = \frac{1}{2} \begin{bmatrix} 1 & 1 \end{bmatrix} \cdot \begin{bmatrix} \frac{1}{\alpha^{br}(\omega)} + C_{11} & C_{12} \\ C_{21} & \frac{1}{\alpha^{ot}(\omega)} + C_{22} \end{bmatrix}^{-1} \cdot \begin{bmatrix} 1 \\ 1 \end{bmatrix} . \quad (7.12)$$

We note that the mathematical form of Eq.7.12 permits an immediate generalization to ordered CO_{br}/CO_{ot} layers with many adsorbates in the unit cell, as well as an easy implementation on the computer even for more complex cases.

Vibrational polarizabilities of isolated CO_{br} and CO_{ot} molecules by the analysis of IR band positions

The positions of the two CO stretch lines of the saturated CO_{br}/CO_{ot} layer can be found from Eq.7.12. It is possible to show that they are the roots of the determinant of the matrix of coefficients Eq.7.10 in the limit of zero linewidth. Considering the explicit expressions of the vibrational polarizabilities of the CO_{br} and the CO_{ot} molecules (Eq.7.3) and setting $\delta = 0$, the two characteristic CO stretch frequencies are the roots of the second order equation in ω^2

$$(1 + C_{11} \alpha_V^{br} - \omega^2/\Omega_{br}^2) (1 + C_{22} \alpha_V^{ot} - \omega^2/\Omega_{ot}^2) = C_{12} C_{21} \alpha_V^{br} \alpha_V^{ot} . \quad (7.13)$$

This equation restricts the oscillation frequencies ω of the adsorbed layer, in the absence of excitation by an external electric field, to the two eigenfrequencies ω_l

and ω_h of the system of coupled oscillators. In the analytical mechanics of linear coupled systems Eq.7.13 is known as the secular equation.

The sums of the dipole-dipole interaction potential for quadratic lattices have been many times calculated and reported in the literature [83]. Approximating the almost quadratic lattice of the $\text{RuO}_2(110)$ structure, with constants of 3.2 Å and 3.1 Å, with a quadratic lattice of constant $a = 3.15$ Å, the values of the dipole sums are

$$\begin{aligned} C_{11} &= C_{22} = 4.04/a^3 \\ C_{12} &= C_{21} = 4.98/a^3 \quad . \end{aligned} \quad (7.14)$$

The secular equation Eq.7.13 reads then explicitly

$$\left(1 + 4.04 \frac{\alpha_V^{br}}{a^3} - \frac{\omega^2}{\Omega_{br}^2}\right) \left(1 + 4.04 \frac{\alpha_V^{ot}}{a^3} - \frac{\omega^2}{\Omega_{ot}^2}\right) = 24.80 \frac{\alpha_V^{br} \alpha_V^{ot}}{a^6} \quad . \quad (7.15)$$

The roots ω_l and ω_h of Eq.7.15 are identified with the position of the low and high frequency vibrational bands in the IR spectrum, which in the case of a saturated $\text{CO}_{br}/\text{CO}_{ot}$ layer are 1986 cm^{-1} and 2086 cm^{-1} respectively. These data would already be sufficient to calculate the vibrational polarizability parameters α_V^{br} and α_V^{ot} from Eq.7.15, if the vibration frequencies of the isolated CO molecules (singleton frequencies) Ω_{br} and Ω_{ot} were known.

The $\text{CO}_{br}/(-)_{ot}$ phase, consisting from complete rows of CO_{br} alongside vacant on-top sites, is characterised by an IR line at 2000 cm^{-1} . The effective polarizability of a CO_{br} molecule in the $\text{CO}_{br}/(-)_{ot}$ phase, containing only one CO_{br} molecule in the elementary cell, can be immediately written following the pattern of Eq.7.12

$$\tilde{\alpha}(\omega) = \frac{1}{\frac{1}{\alpha_{br}(\omega)} + C_{11}} \quad . \quad (7.16)$$

To find the vibration eigenfrequency $\tilde{\Omega}_{br}$ of the row of coupled CO_{br} molecules, we have to find the root of the denominator in Eq.7.16. In the limit of vanishing linewidth ($\delta = 0$) the result is

$$\tilde{\Omega}_{br}^2 = \Omega_{br}^2 (1 + C_{11} \alpha_V^{br}) \quad . \quad (7.17)$$

The experimental value is $\tilde{\Omega}_{br} = 2000 \text{ cm}^{-1}$.

At low CO_{ot} coverage, the isolated CO_{ot} molecules adsorbed between complete rows of CO_{br} are characterised by an IR line at 2016 cm^{-1} . In principle, a strong

dipole-dipole coupling of the isolated CO_{ot} molecules with the CO_{br} molecules should be carefully taken into account, with the possible result that the vibration frequency Ω_{ot} of the isolated CO_{ot} molecules, in the absence of the CO_{br} species, is sensibly lower than the observed value of 2016 cm⁻¹. We shall assume for simplicity $\Omega_{ot} = 2016$ cm⁻¹, consistently with the experimental value in the absence of significant dipole-dipole coupling to the CO_{br} species.

Introducing the notations

$$\begin{aligned}\gamma_{br}^2 &= \alpha_V^{br} \Omega_{br}^2 / a^3 \\ \gamma_{ot}^2 &= \alpha_V^{ot} \Omega_{ot}^2 / a^3 \\ \tilde{\Omega}_{br}^2 &= \Omega_{br}^2 \left(1 + 4.04 \frac{\alpha_V^{br}}{a^3} \right)\end{aligned}\tag{7.18}$$

we can write Eq.7.15 more explicitly as

$$\left(\tilde{\Omega}_{br}^2 - \omega^2 \right) \left(\Omega_{ot}^2 + 4.04 \gamma_{ot}^2 - \omega^2 \right) = 24.80 \gamma_{br}^2 \gamma_{ot}^2 \quad . \tag{7.19}$$

Inserting into the last expression the experimental values $\tilde{\Omega}_{br} = 2000$ cm⁻¹ and $\Omega_{ot} = 2016$ cm⁻¹ we obtain

$$\left(2000^2 - \omega^2 \right) \left(2016^2 + 4.04 \gamma_{ot}^2 - \omega^2 \right) = 24.80 \gamma_{br}^2 \gamma_{ot}^2 \quad . \tag{7.20}$$

Eq.7.20 can be seen as a second order equation in the two variables γ_{br}^2 and γ_{ot}^2 and depending on the parameter ω^2 . Inserting into Eq.7.20 a pair of frequencies of the two IR bands, ω_l^2 and ω_h^2 , simultaneously measured in a RAIRS experiment, we obtain the completely determined system of second order equations in γ_{br}^2 and γ_{ot}^2

$$\left. \begin{aligned} \left(2000^2 - \omega_l^2 \right) \left(2016^2 + 4.04 \gamma_{ot}^2 - \omega_l^2 \right) &= 24.80 \gamma_{br}^2 \gamma_{ot}^2 \\ \left(2000^2 - \omega_h^2 \right) \left(2016^2 + 4.04 \gamma_{ot}^2 - \omega_h^2 \right) &= 24.80 \gamma_{br}^2 \gamma_{ot}^2 \end{aligned} \right\} \quad . \tag{7.21}$$

For a saturated CO_{br}/CO_{ot} layer the experimental values are $\omega_l = 1988 \pm 3$ cm⁻¹ and $\omega_h = 2086$ cm⁻¹. Solution of Eq.7.21 with these values gives

$$\begin{aligned}\gamma_{br} &= 107 \pm 16 \text{ cm}^{-1} \\ \gamma_{ot} &= 243 \pm 7 \text{ cm}^{-1} \quad .\end{aligned}\tag{7.22}$$

The vibrational polarizabilities α_V of the isolated CO_{br} and CO_{ot} molecules are

found according to Eq.7.18

$$\begin{aligned}\alpha_V^{br} &= \gamma_{br}^2 a^3 / \Omega_{br}^2 \\ \alpha_V^{ot} &= \gamma_{ot}^2 a^3 / \Omega_{ot}^2 \quad .\end{aligned}$$

Using Eq.7.22 we get

$$\begin{aligned}\alpha_V^{br} &= 0.09 \pm 0.03 \text{ \AA}^3 \\ \alpha_V^{ot} &= 0.45 \pm 0.02 \text{ \AA}^3 \quad .\end{aligned}\tag{7.23}$$

We note that the vibrational polarizability α_V^{br} of the CO_{br} molecules is close to the gas phase value $\alpha_V^{gas} = 0.06 \text{ \AA}^3$ for CO molecules, while the vibrational polarizability α_V^{ot} of the CO_{ot} molecules is of the order of magnitude of CO adsorbed on other transition metals, for example $\alpha_V = 0.27 \text{ \AA}^3$ for CO on Cu(100) [73].

The results of the current section may be summarized by giving explicitly the frequency dependent vibrational polarizabilities according to Eq.7.3

$$\begin{aligned}\alpha^{br}(\omega)/a^3 &= \frac{107^2}{1988^2 - \omega^2 - i\omega\delta} \\ \alpha^{ot}(\omega)/a^3 &= \frac{243^2}{2016^2 - \omega^2 - i\omega\delta}\end{aligned}\tag{7.24}$$

where the frequency parameter ω is given in cm^{-1} and the lorentzian linewidth is $\delta \sim 20 - 30 \text{ cm}^{-1}$.

7.3.2 Simulated IR spectra of ordered $\text{CO}_{br}/\text{CO}_{ot}$ phases. Comparison with in situ RAIR spectra.

Within the proposed dynamical model, Eq.7.24 together with Eq.7.12 form the basis for the evaluation of the vibration frequency of other ordered $\text{CO}_{br}/\text{CO}_{ot}$ phases, characterised by a high local CO coverage, like those observed *in situ* on the $\text{RuO}_2(110)$ surface during the CO oxidation reaction. During the discussion of the *in situ* RAIR spectra, we have assigned the important band at 2062 cm^{-1} to a dense $\text{CO}_{br}/\text{CO}_{ot}$ phase consisting of saturated CO_{br} and with CO_{ot} occupying on average 2/3 of the on top sites (Fig.7.16.a). As an example of application of the proposed dynamical model, we shall compute the vibration eigenfrequency of this dense $\text{CO}_{br}/\text{CO}_{ot}$ phase. The elementary cell (Fig.7.16.b) contains three CO_{br} and two CO_{ot} molecules. For the dipole sums C entering the matrix of

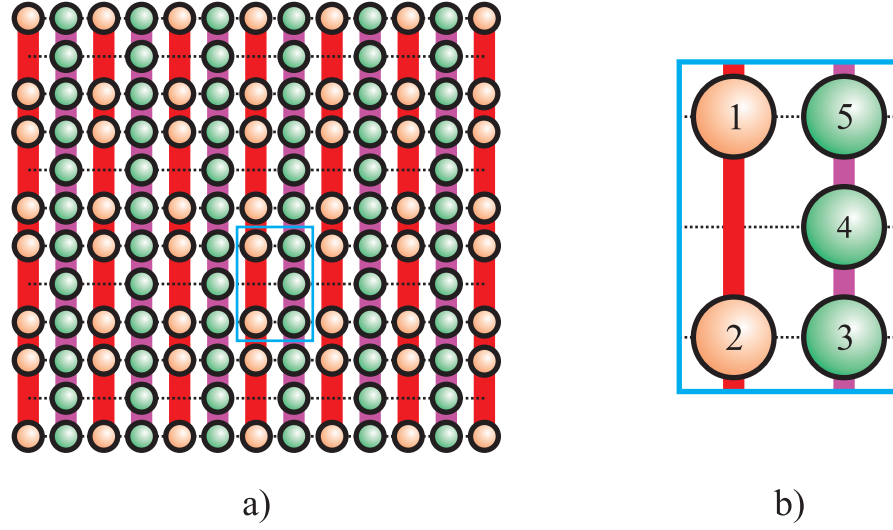


Figure 7.16: An ordered $\text{CO}_{br}/\text{CO}_{ot}$ phase with $2/3$ of the on top sites occupied by CO_{ot} (a). The elementary unit cell (b) contains three CO_{br} and two CO_{ot} molecules.

coefficients

$$\begin{pmatrix} \frac{1}{\alpha_{ot}} + C_{11} & C_{12} & C_{13} & C_{14} & C_{15} \\ C_{21} & \frac{1}{\alpha_{ot}} + C_{22} & C_{23} & C_{24} & C_{25} \\ C_{31} & C_{32} & \frac{1}{\alpha_{br}} + C_{33} & C_{34} & C_{35} \\ C_{41} & C_{42} & C_{43} & \frac{1}{\alpha_{br}} + C_{44} & C_{45} \\ C_{51} & C_{52} & C_{53} & C_{54} & \frac{1}{\alpha_{br}} + C_{55} \end{pmatrix} \quad (7.25)$$

the following symmetry relations are found, by directly evaluating the dipole sums

$$\begin{aligned} C_{11} &= C_{22} = C_{33} = C_{44} = C_{55} = 0.66 \\ C_{12} &= C_{34} = C_{35} = C_{45} = 1.69 \\ C_{13} &= C_{14} = C_{24} = C_{25} = 1.25 \\ C_{23} &= C_{15} = 2.47 \quad , \end{aligned} \quad (7.26)$$

with the same equalities holding for the coefficients under the principal diagonal.

Inserting the coefficients C of Eq.7.26 into the matrix of coefficients Eq.7.25, the effective polarizability $\tilde{\alpha}(\omega)$ of the CO molecule, coupled in the layer presented in Fig.7.16.a, is easily written following the pattern of Eq.7.12. The IR spectrum obtained by this method is plotted in Fig.7.17 curve (b), the principal line being

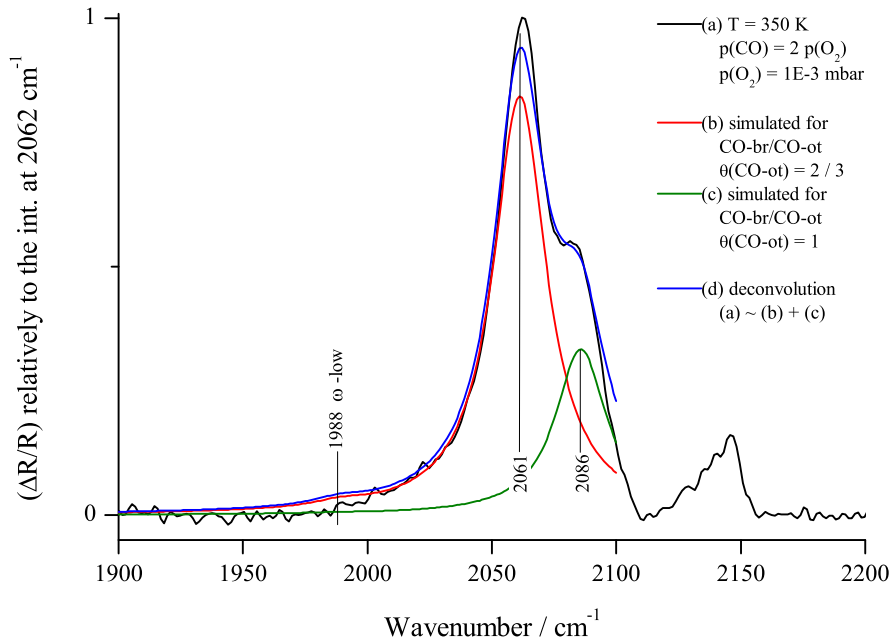


Figure 7.17: The *in situ* RAIR spectrum of the $\text{RuO}_2(110)$ model catalyst (a) is deconvoluted (d) with the simulated IR spectra of the $\text{CO}_{br}/\text{CO}_{ot}$ phase with 66% occupation by CO_{ot} (b) and of the saturated $\text{CO}_{br}/\text{CO}_{ot}$ phase (c).

located at 2061 cm^{-1} and a second weak line at 1988 cm^{-1} , corresponding to the singleton frequency of the CO_{br} molecules. For comparison, the IR spectrum of a saturated $\text{CO}_{br}/\text{CO}_{ot}$ layer is plotted in Fig.7.17 curve (c), being simulated with the same expressions Eq.7.24 of the vibrational polarizabilities. The intensities of curves (b) and (c) were adjusted in order that they form a deconvolution of the RAIR spectrum measured *in situ* during the CO oxidation reaction on the $\text{RuO}_2(110)$ catalyst surface. A good fit of the flanks of the *in situ* RAIR spectrum was obtained by assuming a lorentzian linewidth $\delta = 25 \text{ cm}^{-1}$ for both bands.

The results presented in the current section show that our discussion of the *in situ* RAIR spectra is consistent with a dynamical interpretation of the IR spectra.

Chapter 8

Summary and Outlook

As part of the present thesis, a complex ultrahigh vacuum (UHV) system for *in situ* IR spectroscopic studies of model catalysts was designed, commissioned and made operational. The UHV system was conceived as an extension to the Bruker IFS 120 HR high resolution fourier transform infrared spectrometer (FTIR) in use at the Physical Chemistry department of the University of Giessen. The interface between the UHV system and the FTIR spectrometer is formed by an UHV reaction chamber with high pressure capabilities equipped with IR-transparent viewports. The setup allows the preparation and *in situ* IR-spectroscopic study of model catalysts over an extended pressure range (10^{-10} -1 mbar) at temperatures in the 100-1200 K range.

The model catalyst studied in the present thesis was an ultrathin $\text{RuO}_2(110)$ film epitaxially grown on the $\text{Ru}(001)$ surface. The adsorption and oxidation of CO on the model catalyst was studied by *in situ* reflection-absorption IR spectroscopy (RAIRS) in the spectral region of the C-O bond stretch vibrations ($1800\text{-}2200\text{ cm}^{-1}$) at pressures in the range 10^{-10} - 10^{-2} mbar.

Two distinct kinds of Ru atoms are accessible for CO adsorption on the $\text{RuO}_2(110)$ surface. With respect to their six-fold coordination in the bulk, these Ru atoms are one-fold (1f-cus-Ru) and two-fold (2f-cus-Ru) undercoordinated. CO molecules bind over the 1f-cus-Ru atoms in an on-top geometry (CO_{ot}). CO molecules can also occupy bridge sites over pairs of 2f-cus-Ru atoms (CO_{br}). The $\text{RuO}_2(110)$ surface with all bridge sites occupied by CO_{br} is referred to as *mildly reduced*. On the pristine or *stoichiometric* $\text{RuO}_2(110)$ surface the bridge sites are occupied by oxygen (O_{br}).

The RuO₂(110) surface was prepared and characterized by the RAIR spectrum of CO_{ot} test molecules. Since the principal CO band at 2123 cm⁻¹ was found very sensitive to the cleanliness and ordering of the sample surface, we took its intensity as an indicator of the quality of the sample surface. With residual gas pressures in the range $1\text{--}5 \times 10^{-9}$ mbar in the IR spectroscopic cell under working conditions, the cleanliness of the sample surface during the UHV experiments has constantly been an issue. Accordingly, we have maximized the intensity of the 2123 cm⁻¹ band prior to each experiment by annealing the sample to 700 K in 10⁻⁷ mbar oxygen. The consequent application of this quality check has proved decisive for the reproducibility of our RAIR spectra.

In a series of time-resolved adsorption experiments under UHV conditions we have studied the evolution of the RAIR spectra with increasing CO coverage. The frequency of the IR band of CO_{ot} molecules increases in the ranges 2101–2123 cm⁻¹ on the stoichiometric RuO₂(110) surface, and 2016–2086 cm⁻¹ on the reduced RuO₂(110) surface, when the coverage increases from isolated on-top CO molecules to the saturation coverage. Using the theory of dipole-dipole coupling, we have analyzed the observed shifts of the CO stretch frequency and estimated the dipole moments of the CO_{br} and CO_{ot} molecules. We have subsequently used these data in the analysis of the *in situ* RAIR spectra under reaction conditions.

The motivation of the present thesis has been the study of the CO oxidation reaction over the RuO₂(110) model catalyst by *in situ* RAIRS. We have monitored the reaction at 350 K in the 10⁻⁷–10⁻² mbar range, by feeding the reactants in the ratios $p(\text{CO}) = 2 p(\text{O}_2)$ (stoichiometric) and $p(\text{CO}) = p(\text{O}_2)$ (oxidizing).

Under stoichiometric and oxidizing gas feed at $p(\text{O}_2) = 10^{-7}$ mbar, the RAIR spectrum presents only one band at 1867 cm⁻¹, which we have assigned to the bridging CO_{br} species. No stable CO_{ot} population was detected, presumably due to the high activity of CO_{ot} in the reaction with O.

A stable CO_{ot} population has been accommodated at $p(\text{O}_2) \sim 10^{-6}$ mbar after dosing CO in excess. Dosing $p(\text{CO}) = 4 p(\text{O}_2)$ the RAIRS spectrum consisted of several overlapping IR bands in the 2000–2070 cm⁻¹ range. We have assigned these bands to a RuO₂(110) surface covered by clusters of CO molecules with different local coverages, from loose (2000 cm⁻¹) to densely packed (about 2070 cm⁻¹). The existence of densely packed CO clusters indicates that a stable on-top CO population has been accommodated at the surface. Conversely, since adsorption of O₂ requires vacant on-top sites, a stable on-top CO population may

block the on-top sites for O_2 adsorption, contributing essentially to the formation of compact agglomerations of CO molecules.

In the $p(\text{O}_2) = 10^{-6}$ - 10^{-3} mbar range the reactants were fed in a stoichiometric ratio. The principal IR bands are centered at 2062 cm^{-1} and 2083 cm^{-1} and remain fixed over the indicated pressure range. We have assigned the two IR bands to densely packed clusters of CO molecules. Since the adsorption of an O_2 molecule requires two neighboring vacant on-top sites, oxygen cannot adsorb into these areas. Only CO molecules at the perimeter of these clusters can react with neighboring O molecules, in a process limited by the high activation barrier of CO and O diffusion (see below). We have obtained similar RAIR spectra under oxidizing reaction conditions.

To test this hypothesis, we have exposed a high-coverage CO layer to 10^{-6} mbar oxygen at 400 K. A CO phase characterized by an IR band at 2070 cm^{-1} , which we have assigned to clusters of densely packed CO molecules, has vanished only after 30 minutes of oxygen exposure. From an analysis of the intensity of the 2070 cm^{-1} band, an activation energy of 1.2 eV for the reaction of this CO phase with the oxygen molecules has been inferred, in excellent agreement with the DFT-computed activation energy for the diffusion of on-top O across the $\text{RuO}_2(110)$ surface (1.2 eV [65]).

Our *in situ* RAIRS experiments suggest that under stoichiometric and oxidizing feed in the 10^{-6} - 10^{-3} mbar range, areas of the $\text{RuO}_2(110)$ surface are covered by clusters of densely packed CO molecules, characterized by IR bands in the 2060 - 2080 cm^{-1} range. Although RAIRS cannot detect adsorbed O directly, our spectra indicate the existence of densely packed clusters of O atoms on the $\text{RuO}_2(110)$ surface. Based on our UHV experiments on the adsorption of CO on the O-precovered $\text{RuO}_2(110)$ surface, we have assigned the 2146 cm^{-1} band, observed *in situ* during the reaction, to CO molecules trapped within dense clusters of O atoms. The oxidation of the aggregated CO molecules is very slow due the high activation energies for CO and O diffusion on the $\text{RuO}_2(110)$ surface. We can say that this practically inactive CO species is partly poisoning the catalyst surface.

The existence of densely packed CO clusters at a Ru-based model catalyst surface, characterised by an IR band in the 2070 - 2080 cm^{-1} range, is not associated with a particular form of the model catalyst. Assmann *et al.* [11, 12] have performed *in situ* diffuse reflectance IR spectroscopy (DRIFTS) studies of

the CO oxidation reaction over nanometer-size Ru clusters supported on MgO and SiO₂ and have shown that the CO-stretch region of the IR spectrum is actually dominated by similar CO bands, at 2067 cm⁻¹ and 2078 cm⁻¹ respectively. We consider thus the pressure and material gaps in the oxidation of CO over Ru-based catalysts as bridged, from the point of view of IR spectroscopy.

We shall next review those results of the present thesis which are not directly related to the oxidation of CO over the RuO₂ model catalyst. In Chap.6.4 we have studied *in situ* the reduction of the RuO₂ epitaxial film under CO exposure. The reduction process has been previously studied by different methods (TDS [76], STM and HRCLS [54], SXRD [53]).

Wendt *et al.* [76] have observed that after removing all bridging O atoms from the stoichiometric RuO₂(110) surface by exposure to CO at 300 K, the resulting mildly reduced RuO₂(110) surface could no longer produce CO₂ when exposed to CO below 400 K. Wendt *et al.* have found that annealing the sample to 570 K reactivates the mildly reduced RuO₂(110) surface, which they have attributed to the repopulation of the bridge sites by O atoms liberated from the RuO₂ structure. The proposal of Wendt *et al.* has been confirmed by STM studies [54]. We present a series of RAIR spectra which illustrate the gradual repopulation of the bridging O species on the reduced RuO₂(110) surface, upon annealing the sample in the 330-600 K range. Our RAIRS results closely parallel the STM studies of Over *et al.* [54].

The heavy reduction of the epitaxially grown RuO₂(110) film on Ru(001), previously observed by *in situ* SXRD [53], was nicely confirmed by our *in situ* RAIRS experiments at high pressure. The conditions for the reduction process have turned out to be similar to those found in the SXRD experiment. Exposure to 3×10^{-3} mbar CO at 420 K has led to the vanishing of the RuO₂(110)-related CO stretch band (2072 cm⁻¹) within 50 minutes. RAIR spectra recorded in the final phase of the reduction process indicate, on the heavily reduced RuO₂(110) film, the presence of CO adsorbed on the Ru(001) surface. STM images [54] suggest that this Ru(001) surface consists in fact of thin, extended clusters of Ru covering a rough layer of residual RuO₂. HRCLS data [54] indicate the existence of large quantities of oxygen on the heavily reduced RuO₂(110) film, mostly within buried RuO₂ domains.

We have annealed the heavily reduced RuO₂(110) film to 520 K and measured the RAIR spectra of CO probe molecules, adsorbed after cooling the sample to

100 K. Our results are consistent with the presence of 0.5 monolayers of O on the Ru(001) clusters. The presence of O on the Ru(001) clusters manifests as a 10-20 cm^{-1} upward shift in the stretch frequency of the coadsorbed CO probe molecules. The CO band was thus measured at 2070-2077 cm^{-1} instead of 2060 cm^{-1} , the value measured for a CO-saturated Ru(001) surface [24].

We have undertaken steps in the direction of the simulation of RAIR spectra of CO test molecules. For this purpose, we have presented the standard theory of RAIR spectra for adsorbates with dipole-dipole couplings within the more general framework of linear response theory. We have made the presented formalism accessible for potential users by implementing it as a computer program. We have obtained the necessary parameters, the singleton frequencies and the dynamic dipole moments of the adsorbed CO molecules, from evaluation of RAIRS data on CO adsorption under UHV conditions. In combination with Monte-Carlo simulations of the structure of adsorbed layers under reaction conditions, our program could be used in a computer 'experiment' to establish a correspondence between the microscopic reaction mechanism and the *in situ* RAIR spectrum.

In the present thesis we have built a complex UHV system coupled with *in situ* RAIR spectroscopy and demonstrated its possibilities in the study of the CO oxidation reaction over the $\text{RuO}_2(110)$ model catalyst, in the pressure range 10^{-7} - 10^{-2} mbar. The high pressure limit of 10^{-2} mbar has been set by the intensifying absorption of IR radiation in the gas phase. For *in situ* RAIRS studies of model catalysts at higher pressure we see the necessity to implement phase-sensitive spectroscopic methods with our setup. Due to the availability of high quality photoelastic modulators (PEM), phase-modulated RAIRS (PM-RAIRS) [84] seems an attractive solution.

Appendix A

Life cycle of a catalyst

Although the catalyst does not appear in the net balance of the catalyzed reaction, it may nevertheless be strongly affected during the catalytic process. One can properly speak of a catalyst *life cycle*: preparation, activation, deactivation, regeneration and decommissioning [1, 2].

Commercial catalysts are robust and economical but also complex. Support materials with 100-400 m²/g specific surface area are prepared from alumina, silica, carbon or metal (Mg, Zr, Ti, V) oxides. These materials have well defined microstructures and behave as active components of the catalyst. The supported particles are prepared by deposition of transition metal atoms or ions into the micropores of the support, which upon heating and reduction agglomerate to metal particles 10-100 Å in size, with virtually all their atoms located on the surface. More than one metal component may be used, many successful catalysts being bimetallic systems. Additives that are electron donors (alkali metals) or electron acceptors (halogens) are adsorbed on the metal particles or on the oxide support to modify the bond strengths of the coadsorbed reactants. This structural complexity allows the catalyst many thousands of hours of stable activity and high selectivity in the production of the desired molecules [2].

The catalyst as prepared or as bought is yet another precursor of the catalyst as used in a reaction. Prior to use, it must be activated *in situ*, for example by the removal of oxygen from the surface layers. Activation is in fact the last stage in the preparation of the catalyst. After the start of a run with an activated catalyst, slow changes in its surface structure are the norm. In a process called *reconstruction*, the catalyst may adapt its structure to the catalyzed reaction.

For instance, during ammonia synthesis over iron-based catalysts, nitrogen and ammonia molecules induce a reconstruction of the iron clusters [85], manifested in the preferential growth of the (111) planes, far more active in ammonia synthesis than other iron crystal planes.

Changes in surface structure which entail unfavorable effects on catalyst performance are termed *deactivation*. This is frequently due to *poisoning* by impurity atoms which diffuse from the bulk of the metal particles or from their support, or by impurities from the feed or from the metallic components of the reactor. Iron-based catalysts in ammonia synthesis are poisoned by diffusion of oxygen from the bulk of the larger iron particles, such that it can take months of operation before the catalyst reaches its optimal performance. Poisoning of the catalyst may also occur through undesired reaction intermediates, like layers of inactive carbon (coke) formed during the catalytic cracking of hydrocarbons. In finely divided catalysts, deactivation may follow over time from the loss of specific surface area by coalescence of the catalyst particles (sintering) due to the thermodynamic drive to minimize surface free energy.

The use of a catalyst may be compromised if its deactivation cannot be circumvented by catalyst *regeneration*. In some cases, regeneration may be achieved by engineering solutions. For many catalysts, deactivation is slow enough to permit steady state operation. With rapid coking, regeneration by coke burning becomes mandatory, such that the reactors must switch frequently between running the reaction and regeneration. Regeneration by combustion of coke can lead to the agglomeration of supported metal clusters. Redispersion of the metal into nanoscopic clusters can be achieved with the help of oxygen and chlorine. Regeneration is often the key to success in practical heterogeneous catalysis, and has to be considered right from the beginning of a catalyst development program [1].

If a deactivated catalyst cannot be regenerated, the catalyst must be disposed of within the rules of environmental protection. Today it is necessary to achieve safe decommission at the end of the life cycle of any catalyst.

Appendix B

Reflection of light at metal surfaces

In the present Appendix we shall briefly review, within the approximation of classical electrodynamics [86], the phenomenon of reflection of light at metal surfaces. The reader might find the following derivation as a useful summary of the basic electromagnetic-optical formulas mentioned in the text of this thesis or in the cited RAIRS literature.

Electromagnetic wave in a dielectric medium

Let us first consider a plane, monochromatic wave of light propagating through a nonmagnetic, transparent medium. In the original Maxwell equations

$$\text{curl } \mathbf{H} - \frac{1}{c} \frac{\partial \mathbf{D}}{\partial t} = \frac{4\pi}{c} \mathbf{j} \qquad \text{curl } \mathbf{E} + \frac{1}{c} \frac{\partial \mathbf{B}}{\partial t} = 0$$

$$\text{div } \mathbf{D} = 4\pi\rho \qquad \text{div } \mathbf{B} = 0$$

we put $\rho = 0$ and $\mathbf{j} = 0$ as there are no free macroscopic charges or currents in the medium. A plane monochromatic wave of light is represented by the electromagnetic fields

$$\mathbf{E}(t, \mathbf{x}) = \mathbf{E}(\omega, \mathbf{k}) \exp(-i\omega t + i \mathbf{k} \cdot \mathbf{x}) \qquad (\text{B.1})$$

$$\mathbf{B}(t, \mathbf{x}) = \mathbf{B}(\omega, \mathbf{k}) \exp(-i\omega t + i \mathbf{k} \cdot \mathbf{x}) \qquad (\text{B.2})$$

where the amplitudes $\mathbf{E}(\omega, \mathbf{k})$ and $\mathbf{B}(\omega, \mathbf{k})$ are in general complex. In addition, we have to consider the pair of medium-specific fields

$$\mathbf{D}(t, \mathbf{x}) = \mathbf{D}(\omega, \mathbf{k}) \exp(-i\omega t + i \mathbf{k} \cdot \mathbf{x})$$

$$\mathbf{H}(t, \mathbf{x}) = \mathbf{H}(\omega, \mathbf{k}) \exp(-i\omega t + i \mathbf{k} \cdot \mathbf{x})$$

which encode the polarization and the magnetization response of the medium and are related to the fundamental electromagnetic fields

$$\mathbf{D}(\omega, \mathbf{k}) = \epsilon(\omega) \mathbf{E}(\omega, \mathbf{k}) \quad (\text{B.3})$$

$$\mathbf{H}(\omega, \mathbf{k}) = \mathbf{B}(\omega, \mathbf{k}). \quad (\text{B.4})$$

The frequency-dependent complex dielectric function $\epsilon(\omega)$ in Eq.B.3 accounts for the polarizability of the medium in the IR domain, while Eq.B.4 shows the non-magnetic nature of the medium. The Maxwell equations reduce now to

$$\mathbf{k} \times \mathbf{B} + \frac{\omega}{c} \epsilon(\omega) \mathbf{E} = 0 \quad (\text{B.5}) \quad \mathbf{k} \times \mathbf{E} - \frac{\omega}{c} \mathbf{B} = 0 \quad (\text{B.7})$$

$$\epsilon(\omega) \mathbf{k} \cdot \mathbf{E} = 0 \quad (\text{B.6}) \quad \mathbf{k} \cdot \mathbf{B} = 0 \quad (\text{B.8})$$

where the boldface capitals stand for the amplitudes $\mathbf{E}(\omega, \mathbf{k})$ and $\mathbf{B}(\omega, \mathbf{k})$ respectively. Eqs.B.6 and B.8 show the transversal character of the electromagnetic field in the optically isotropic medium (as ϵ was assumed a scalar) and are implicit once Eqs.B.5 and B.7 are put. Either \mathbf{E} or \mathbf{B} may now be eliminated between Eqs.B.5 and B.7 to get the mathematical consistency condition

$$c^2 \mathbf{k}^2 = \omega^2 \epsilon(\omega) \quad (\text{B.9})$$

which ensures that an electromagnetic wave can propagate in the medium. We note that in order that Eq.B.9 holds for a general complex dielectric function ϵ we have to assume complex wavevectors \mathbf{k} , i.e. the wave will loss intensity as it propagates trough the medium.

Boundary conditions at the frontier of two dielectric media

A monochromatic plane wave propagating from medium \mathcal{A} into a medium \mathcal{B} , characterised by a different dielectric function, is represented by two distinct

solutions of the Maxwell equations, valid in the bulk of each respective medium. The two separate solutions have to be matched along the frontier by imposing continuity conditions on the four electromagnetic fields $\mathbf{E}, \mathbf{B}, \mathbf{D}, \mathbf{H}$ when crossing from medium \mathcal{A} into medium \mathcal{B} , namely

$$\mathbf{n} \times \mathbf{H}_{\mathcal{A}} = \mathbf{n} \times \mathbf{H}_{\mathcal{B}} \quad (\text{B.10}) \qquad \mathbf{n} \times \mathbf{E}_{\mathcal{A}} = \mathbf{n} \times \mathbf{E}_{\mathcal{B}} \quad (\text{B.12})$$

$$\mathbf{n} \cdot \mathbf{D}_{\mathcal{A}} = \mathbf{n} \cdot \mathbf{D}_{\mathcal{B}} \quad (\text{B.11}) \qquad \mathbf{n} \cdot \mathbf{B}_{\mathcal{A}} = \mathbf{n} \cdot \mathbf{B}_{\mathcal{B}} \quad (\text{B.13})$$

where \mathbf{n} is the surface normal unit vector at the frontier and the subscripts denote the side of the frontier on which the field is evaluated. The conditions of Eqs.B.10 and B.11 hold in the absence of free currents or charges confined to the immediate vicinity of the frontier.

The Fresnel amplitude coefficients

To specify the boundary conditions for the case of monochromatic plane waves we introduce the incident, reflected and transmitted waves, respectively

$$\begin{aligned} \mathbf{E}_i(t, \mathbf{x}) &= \mathbf{E}_i(\omega, \mathbf{k}_i) \exp(-i\omega t + i \mathbf{k}_i \cdot \mathbf{x}) \\ \mathbf{E}_r(t, \mathbf{x}) &= \mathbf{E}_r(\omega, \mathbf{k}_r) \exp(-i\omega t + i \mathbf{k}_r \cdot \mathbf{x}) \\ \mathbf{E}_t(t, \mathbf{x}) &= \mathbf{E}_t(\omega, \mathbf{k}_t) \exp(-i\omega t + i \mathbf{k}_t \cdot \mathbf{x}) . \end{aligned}$$

In medium \mathcal{A} the total electric field is the sum of the fields of the incident wave and of the reflected wave while in medium \mathcal{B} only the electric field of the transmitted wave is present. In the boundary conditions we have to replace

$$\mathbf{E}_{\mathcal{A}}(t, \mathbf{x}) = \mathbf{E}_i(t, \mathbf{x}) + \mathbf{E}_r(t, \mathbf{x}) \quad (\text{B.14})$$

$$\mathbf{E}_{\mathcal{B}}(t, \mathbf{x}) = \mathbf{E}_t(t, \mathbf{x}) \quad (\text{B.15})$$

together with similar decompositions for the fields $\mathbf{B}, \mathbf{D}, \mathbf{H}$. Since the boundary conditions are valid at each instant and at each point of the frontier, the temporal and spatial variation of the fields at the boundary has to be the same. The first condition to be imposed on the three waves is therefore the equality of their phase factors on the frontier plane

$$\mathbf{k}_i \cdot \mathbf{x} = \mathbf{k}_r \cdot \mathbf{x} = \mathbf{k}_t \cdot \mathbf{x} \text{ whenever } \mathbf{n} \cdot \mathbf{x} = 0. \quad (\text{B.16})$$

As a consequence, the three wavevectors $\mathbf{k}_i, \mathbf{k}_r, \mathbf{k}_t$ and the surface normal \mathbf{n} lie all in the same plane. Condition Eq.B.16 further implies that the wavevectors obey the law of reflection and Snell's law of refraction. After eliminating the magnetic field \mathbf{B} by Eq.B.7 the boundary conditions read

$$\mathbf{k}_i \times \mathbf{E}_i(\omega, \mathbf{k}_i) + \mathbf{k}_r \times \mathbf{E}_r(\omega, \mathbf{k}_r) = \mathbf{k}_t \times \mathbf{E}_t(\omega, \mathbf{k}_t) \quad (\text{B.17})$$

$$\mathbf{n} \times (\mathbf{E}_i(\omega, \mathbf{k}_i) + \mathbf{E}_r(\omega, \mathbf{k}_r)) = \mathbf{n} \times \mathbf{E}_t(\omega, \mathbf{k}_t) \quad (\text{B.18})$$

$$\epsilon_{\mathcal{A}}(\omega) \mathbf{n} \cdot (\mathbf{E}_i(\omega, \mathbf{k}_i) + \mathbf{E}_r(\omega, \mathbf{k}_r)) = \epsilon_{\mathcal{B}}(\omega) \mathbf{n} \cdot \mathbf{E}_t(\omega, \mathbf{k}_t). \quad (\text{B.19})$$

The set of boundary conditions Eqs.B.17-B.19 is solved for the transmitted field \mathbf{E}_t and for the reflected field \mathbf{E}_r in terms of the incident field \mathbf{E}_i . By defining the Fresnel amplitude coefficients t and r

$$\begin{aligned} E_t^{(p)} &= t^{(p)} E_i^{(p)} & E_r^{(p)} &= r^{(p)} E_i^{(p)} \\ E_t^{(s)} &= t^{(s)} E_i^{(s)} & E_r^{(s)} &= r^{(s)} E_i^{(s)} \end{aligned}$$

the result is written as

$$t^{(p)} = \frac{2\sqrt{\epsilon} \cos(\varphi)}{\epsilon \cos(\varphi) + \sqrt{\epsilon - \sin^2(\varphi)}} \quad (\text{B.20})$$

$$t^{(s)} = \frac{2 \cos(\varphi)}{\cos(\varphi) + \sqrt{\epsilon - \sin^2(\varphi)}} \quad (\text{B.21})$$

$$r^{(p)} = \frac{\epsilon \cos(\varphi) - \sqrt{\epsilon - \sin^2(\varphi)}}{\epsilon \cos(\varphi) + \sqrt{\epsilon - \sin^2(\varphi)}} \quad (\text{B.22})$$

$$r^{(s)} = \frac{\cos(\varphi) - \sqrt{\epsilon - \sin^2(\varphi)}}{\cos(\varphi) + \sqrt{\epsilon - \sin^2(\varphi)}} \quad (\text{B.23})$$

where φ is the angle of incidence of the incoming wave and $\epsilon = \epsilon_{\mathcal{B}}/\epsilon_{\mathcal{A}}$.

Starting from the Fresnel formulas, the components of the local electric field at a vacuum-metal interface may now be written

$$\begin{aligned}
 \mathcal{E}_x &= E_i^{(s)} + E_r^{(s)} = \frac{2 \cos(\varphi)}{\cos(\varphi) + \sqrt{\epsilon - \sin^2(\varphi)}} E_i^{(s)} \\
 \mathcal{E}_y &= [E_i^{(p)} - E_r^{(p)}] \cos(\varphi) = \frac{2 \cos(\varphi) \sqrt{\epsilon - \sin^2(\varphi)}}{\epsilon \cos(\varphi) + \sqrt{\epsilon - \sin^2(\varphi)}} E_i^{(p)} \\
 \mathcal{E}_z &= [E_i^{(p)} + E_r^{(p)}] \sin(\varphi) = \frac{\epsilon \sin(2\varphi)}{\epsilon \cos(\varphi) + \sqrt{\epsilon - \sin^2(\varphi)}} E_i^{(p)}
 \end{aligned} \tag{B.24}$$

The absolute value of the dielectric function of metals is large in the IR domain ($|\epsilon| \gg 1$). For a not too flat angle of incidence ($\varphi < 87^\circ$) the components of the local electric field simplify to

$$\begin{aligned}
 \mathcal{E}_x &= (2/\sqrt{\epsilon}) \cos(\varphi) E_i^{(s)} \\
 \mathcal{E}_y &= (2/\sqrt{\epsilon}) E_i^{(p)} \\
 \mathcal{E}_z &= 2 \sin(\varphi) E_i^{(p)} \quad .
 \end{aligned} \tag{B.25}$$

We note that for metals the components of the field parallel to the surface are suppressed by a factor $1/\sqrt{\epsilon}$. A typical example is Pt(111) with $\epsilon = -120 + 340i$ at 2000 cm^{-1} and $1/|\sqrt{\epsilon}| \sim 5\%$. At flat angles of incidence the contribution of the s -polarized field is further diminished by a geometric factor, which in the typical case $\varphi = 80^\circ$ is about 14%, the actual value of the s -polarized field at the surface being less than 1% of the amplitude of the incident s -polarized wave. Only the normal component of the local electric field is undiminished, its value being about twice the amplitude of the incident p -polarized wave.

Energy fluxes, reflection and transmission coefficients.

We shall start our discussion of the IR absorption spectra of chemisorbed molecular layers by a recapitulation of the concept of flux of electromagnetic energy, as given in the classical theory of electrodynamics [86]. A plane monochromatic wave of light of frequency ω , propagating in direction k through a transparent

medium, is represented by the electromagnetic fields (see also App.B)

$$\mathbf{E}(t, \mathbf{x}) = \mathbf{E}(\omega, \mathbf{k}) \exp(-i\omega t + i \mathbf{k} \cdot \mathbf{x}) \quad (\text{B.26})$$

$$\mathbf{H}(t, \mathbf{x}) = \mathbf{H}(\omega, \mathbf{k}) \exp(-i\omega t + i \mathbf{k} \cdot \mathbf{x}) \quad (\text{B.27})$$

where the amplitudes $\mathbf{E}(\omega, \mathbf{k})$ and $\mathbf{H}(\omega, \mathbf{k})$ are in general complex. The quantity or flux of electromagnetic energy which propagates through the unit surface in unit time is given by the Poynting vector (Ref.[86], p.307)

$$\mathbf{S}(t, \mathbf{x}) = \frac{c}{4\pi} \mathbf{E}(t, \mathbf{x}) \times \mathbf{H}(t, \mathbf{x}). \quad (\text{B.28})$$

For monochromatic plane waves of complex amplitude, a more convenient definition of the energy flux is the so-called complex Poynting vector

$$\mathbf{S} = \frac{c}{8\pi} \mathbf{E}^*(\omega, \mathbf{k}) \times \mathbf{H}(\omega, \mathbf{k}) \quad (\text{B.29})$$

whose real part is the time-average of the standard Poynting vector

$$\text{Re}(\mathbf{S}) = \frac{1}{T} \int_0^T \mathbf{S}(t, \mathbf{x}) dt. \quad (\text{B.30})$$

After eliminating $\mathbf{H}(\omega, \mathbf{k})$ by Eq.B.7 we get

$$\mathbf{S} = \frac{c^2}{8\pi\omega} \{ \mathbf{k} |\mathbf{E}(\omega, \mathbf{k})|^2 - \mathbf{E}(\omega, \mathbf{k}) (\mathbf{k} \cdot \mathbf{E}^*(\omega, \mathbf{k})) \}.$$

If medium \mathcal{B} is absorptive then the imaginary component of the wavevector \mathbf{k}_t is oriented normal to the frontier. In this case it can be shown that the flux of energy propagating through the unit surface of the frontier into medium \mathcal{B} reduces to

$$\text{Re}(\mathbf{n} \cdot \mathbf{S}_t) = \frac{c^2}{8\pi\omega} |\mathbf{E}_t(\omega, \mathbf{k}_t)|^2 \text{Re}(\mathbf{n} \cdot \mathbf{k}_t). \quad (\text{B.31})$$

Using Eq.B.9 to express $\mathbf{n} \cdot \mathbf{k}$ for the incident, reflected and transmitted waves, the respective fluxes of electromagnetic energy propagating through the unit surface

of the frontier are the real parts of

$$\mathbf{n} \cdot \mathbf{S}_i = \frac{c}{8\pi} |\mathbf{E}_i(\omega, \mathbf{k}_i)|^2 \sqrt{\epsilon_{\mathcal{A}}} \cos(\varphi) \quad (\text{B.32})$$

$$\mathbf{n} \cdot \mathbf{S}_r = \frac{c}{8\pi} |\mathbf{E}_r(\omega, \mathbf{k}_r)|^2 \sqrt{\epsilon_{\mathcal{A}}} \cos(\varphi) \quad (\text{B.33})$$

$$\mathbf{n} \cdot \mathbf{S}_t = \frac{c}{8\pi} |\mathbf{E}_t(\omega, \mathbf{k}_t)|^2 \sqrt{\epsilon_{\mathcal{B}}} \cos(\psi) . \quad (\text{B.34})$$

Of direct physical relevance are the ratios of transmitted- and reflected- to the incident energy flux, also known as transmission and reflection coefficients of a surface

$$T = \frac{\text{Re}(\mathbf{n} \cdot \mathbf{S}_t)}{\text{Re}(\mathbf{n} \cdot \mathbf{S}_i)} \quad R = \frac{\text{Re}(\mathbf{n} \cdot \mathbf{S}_r)}{\text{Re}(\mathbf{n} \cdot \mathbf{S}_i)} . \quad (\text{B.35})$$

For s polarization they are

$$T_s = |t^{(s)}|^2 \frac{\text{Re}(\sqrt{\epsilon - \sin^2(\varphi)})}{\cos(\varphi)} \quad (\text{B.36})$$

$$R_s = |r^{(s)}|^2 \quad (\text{B.37})$$

while for p polarization

$$T_p = |t^{(p)}|^2 \frac{\text{Re}(\epsilon^* \sqrt{\epsilon - \sin^2(\varphi)})}{|\sqrt{\epsilon}|^2 \cos(\varphi)} \quad (\text{B.38})$$

$$R_p = |r^{(p)}|^2 . \quad (\text{B.39})$$

The energy conservation law at the separation surface of the two media requires

$$T + R = 1 , \quad (\text{B.40})$$

a condition satisfied by Eqs.B.36-B.39 in conjunction with the Fresnel amplitude coefficients Eqs.B.20-B.23. \square

Appendix C

Quantum theory of IR absorption

In the current Appendix we present the quantum mechanical theory of IR absorption by a general polarizable system. In particular, this could be a layer of chemisorbed molecules. We put the emphasis on the linear-response properties of the absorbing system, which entails a discussion based on the formalism of Green functions. The Green functions are a powerful instrument of the theory of many-electron systems and have well defined properties, for example by satisfying the Dyson equation, which make them useful in approaching even complicated problems [87]. Following the treatment in Ref. [88], this presentation intends to highlight a couple of physical concepts, which could be of interest for an understanding of IR absorption in chemisorbed layers.

Energy absorption by a polarizable system

Let us briefly consider the quantum mechanical description of the molecular adsorbate. We assume that the adsorbate is characterised by the ground state wave function ψ_0 satisfying the unperturbed Schrödinger equation

$$H_0 \psi_0 = \mathcal{E}_0 \psi_0 \tag{C.1}$$

where H_0 is the total Hamilton operator of the adsorbate. We are next interested to find a simple expression for the energy absorption in the adsorbate under the influence of the electric field of the IR wave.

Let the adsorbate initially be, in the absence of the external field, in the ground state ψ_0 . The field is turned on and after having exposed the adsorbate

for a time \mathcal{T} it is turned off, such that the adsorbate can return into the ground state ψ_0 after having lost (mainly through dissipation into the substrate) the energy acquired during the exposure. The condition that the external field vanishes both in the initial and final states ensures that the adsorbate is an isolated system characterised by a well defined energy (i.e. the ground state energy). The energy Q absorbed by the adsorbate during the exposure is given by the Hellmann-Feynman formula

$$Q = \int_0^{\mathcal{T}} \langle \psi(t) | \partial V / \partial t | \psi(t) \rangle dt \quad (\text{C.2})$$

where the time dependent wave function ψ is the exact solution of the Schrödinger equation in the time-dependent external field

$$i\hbar \frac{\partial \psi}{\partial t} = (H_0 + V(t)) \psi \quad . \quad (\text{C.3})$$

The potential energy V corresponds to an electric dipole in external field

$$V(t) = -\mathbf{p} \cdot \mathbf{E}(t, 0) \quad (\text{C.4})$$

where \mathbf{p} is the total dipole moment of the adsorbate, a time-independent operator. Considering that the electric field at the surface is oriented practically along the normal direction, Eq.C.4 will subsequently be written

$$V(t) = -p E_z(t)$$

where p is the normal component of the total dipole moment operator. Eq.C.2 reads now

$$Q = - \int_0^{\mathcal{T}} \langle \psi(t) | p | \psi(t) \rangle \left(\frac{\partial E_z}{\partial t} \right) dt \quad . \quad (\text{C.5})$$

Within the framework of linear response theory the average value of the dipole moment operator is connected to the time dependent electric field through a linear relationship, its most general form being

$$\langle \psi(t) | p | \psi(t) \rangle = \int_0^t \alpha(t') E_z(t - t') dt' \quad . \quad (\text{C.6})$$

The last equation, actually a *definition* of the polarizability $\alpha(t)$ of the adsorbed system, shows that the current value of the dipole moment is a weighted super-

position of contributions due to the past influences of the external field. As a consequence of this explicit cause-effect relationship between the external field and the induced dipole moment, the polarizability α is a highly relevant physical quantity, from both a theoretical as well as an experimental point of view (see footnote 1).

We shall denote the average value of the dipole moment operator

$$p(t) = \langle \psi(t) | p | \psi(t) \rangle \quad . \quad (\text{C.7})$$

It will prove useful to continue the discussion by taking into account not the real time quantities $p(t)$, $\alpha(t)$ and $E_z(t)$ but rather their Fourier transformed counterparts. The Fourier transform of a physical quantity $f(t)$ is defined as

$$f(\omega) = \int_{-\infty}^{+\infty} f(t) e^{i\omega t} dt \quad . \quad (\text{C.8})$$

If $f(t)$ is real then its Fourier transform has the property

$$f^*(\omega) = f(-\omega) \quad . \quad (\text{C.9})$$

The linear functional relationship Eq.C.6 is reduced now to

$$p(\omega) = \alpha(\omega) E_z(\omega) \quad . \quad (\text{C.10})$$

Here $\alpha(\omega) = \alpha'(\omega) + i\alpha''(\omega)$ is the complex polarizability¹ of the adsorbate. Since the polarizability $\alpha(t)$ is real it follows by Eq.C.9 that $\alpha'(\omega)$ and $\alpha''(\omega)$ are respectively even and odd functions

$$\alpha'(-\omega) = \alpha'(\omega) \quad \alpha''(-\omega) = -\alpha''(\omega) \quad . \quad (\text{C.11})$$

¹The causal dependence of p on E_z as expressed by Eq.C.6 requires $\alpha'(\omega)$ and $\alpha''(\omega)$ to be connected through the Kramers-Kronig relations. In principle it is possible to get all the information contained in $\alpha'(\omega)$ from measurements on $\alpha''(\omega)$ only.

We apply the Fourier representation of the quantity $f(t)$

$$f(t) = \frac{1}{2\pi} \int_{-\infty}^{+\infty} f(\omega) e^{-i\omega t} d\omega \quad (\text{C.12})$$

to $p(t)$, $\alpha(t)$ and $E_z(t)$ and insert these into Eq.C.5 to get

$$Q = -\frac{i}{2\pi} \int_{-\infty}^{+\infty} \omega \alpha(\omega) E_z(-\omega) E_z(\omega) d\omega$$

which, by considering the parity of the integrand and Eq.C.11, is reduced to

$$Q = \frac{1}{\pi} \int_0^{\infty} \omega \alpha''(\omega) |E_z(\omega)|^2 d\omega \quad . \quad (\text{C.13})$$

The simple formula Eq.C.13, valid only for an external perturbation of finite duration, relates energy absorption in a polarizable system (adsorbate) to the imaginary part $\alpha''(\omega)$ of its dynamical polarizability. Although our discussion was started in a quantum mechanical setting, we could have equally well derived Eq.C.13 within the classical electrodynamics of macroscopic media.

Energy absorption under an external harmonic perturbation

Most interesting from the point of view of spectroscopy is to write Eq.C.13 for the special case of a monochromatic wave of frequency ω . As mentioned in the opening discussion, we need first to switch the wave on and subsequently off in order to expose the adsorbate only for a finite duration \mathcal{T} . The switching has to be done adiabatically in order to preserve the monochromatic character of the wave. The switching process is therefore characterised by a much lower frequency than the frequency of the IR wave (adiabaticity condition)

$$\omega \gg 1/\mathcal{T} \quad . \quad (\text{C.14})$$

With the typical IR value $\omega/c = 1000 \text{ cm}^{-1}$ a process of duration $\mathcal{T} = 10^{-12} \text{ s}$ would already qualify as adiabatic, so that in practice all experimental procedures are well within the adiabatic regime. From an experimental point of view, the frequency of the IR wave is set by the mirror of a Michelson interferometer in slow

translation through the position of maximum wave intensity, recording of FTIR spectra being thus an illustrative example of the type of adiabatic process we are going to discuss.

Let us consider a strictly monochromatic, linear polarized plane wave propagating in vacuum

$$\begin{aligned}\mathbf{E}(t, \mathbf{x}) &= E \mathbf{e}_z \cos(\omega[t - \mathbf{e}_y \cdot \mathbf{x}/c]) \\ \mathbf{B}(t, \mathbf{x}) &= E \mathbf{e}_x \cos(\omega[t - \mathbf{e}_y \cdot \mathbf{x}/c])\end{aligned}$$

where E is the real amplitude of the wave and \mathbf{e}_x , \mathbf{e}_y , \mathbf{e}_z are the unit vectors of a right handed orthogonal frame. The simplest realization of a quasi monochromatic pulse is a gaussian modulation of the pure monochromatic wave

$$\begin{aligned}\mathbf{E}_{\mathcal{T}}(t, \mathbf{x}) &= E \mathbf{e}_z \cos(\omega[t - y/c]) e^{-\frac{\pi}{2} \left(\frac{t-y/c}{\mathcal{T}}\right)^2} \\ \mathbf{B}_{\mathcal{T}}(t, \mathbf{x}) &= E \mathbf{e}_x \cos(\omega[t - y/c]) e^{-\frac{\pi}{2} \left(\frac{t-y/c}{\mathcal{T}}\right)^2}\end{aligned}\tag{C.15}$$

where for simplicity the gaussian pulse was centered at $t = 0$. The total energy (per cm^2) transported by the gaussian pulse is

$$\begin{aligned}\frac{c}{4\pi} \int_{-\infty}^{+\infty} |\mathbf{E}_{\mathcal{T}}(t, \mathbf{x}) \times \mathbf{B}_{\mathcal{T}}(t, \mathbf{x})| dt &= \frac{c}{4\pi} E^2 \int_{-\infty}^{+\infty} \cos^2(\omega[t - y/c]) e^{-\pi \left(\frac{t-y/c}{\mathcal{T}}\right)^2} dt \\ &= \frac{c}{8\pi} E^2 \mathcal{T} \left(1 + e^{-\frac{1}{\pi} (\mathcal{T}\omega)^2}\right) .\end{aligned}$$

Under the adiabaticity condition Eq.C.14 the second term vanishes, the total energy transported by the gaussian pulse being equal to the energy transported on average during \mathcal{T} by the pure monochromatic wave.

Assuming that the incident wave is a gaussian pulse of the type of Eq.C.15, the local electric field at the surface is written

$$E_z(t) = 1/2 \left(\mathcal{E}_z e^{-i\omega t} + \mathcal{E}_z^* e^{+i\omega t} \right) e^{-\frac{\pi}{2} \left(\frac{t}{\mathcal{T}}\right)^2}\tag{C.16}$$

where the amplitude \mathcal{E}_z is proportional to the sum of the amplitudes of the incident and reflected waves

$$\mathcal{E}_z = [1 + r^{(p)}] \sin(\varphi) E_i^{(p)} ,\tag{C.17}$$

its explicit form being given in Eq.B.24. The Fourier transform of the field (Eq.C.16) is

$$E_z(\omega') = \mathcal{T}/\sqrt{2} \left(\mathcal{E}_z e^{-\frac{1}{2\pi}[T(\omega-\omega')]^2} + \mathcal{E}_z^* e^{-\frac{1}{2\pi}[T(\omega+\omega')]^2} \right) ,$$

whereby in the expression of the field square modulus

$$\begin{aligned} 2|E_z(\omega')|^2 = \mathcal{T}^2 |\mathcal{E}_z|^2 & \left(e^{-\frac{1}{\pi}[T(\omega-\omega')]^2} + e^{-\frac{1}{\pi}[T(\omega+\omega')]^2} \right) \\ & + \mathcal{T}^2 (\mathcal{E}_z^2 + \mathcal{E}_z^{*2}) e^{-\frac{1}{\pi}[T^2(\omega^2+\omega'^2)]} \end{aligned}$$

the term on the second line vanishes by the adiabaticity condition Eq.C.14. The identity

$$(\mathcal{T}/\pi) e^{-\frac{1}{\pi}(\mathcal{T}x)^2} \rightarrow \delta(x) ,$$

holding in the adiabatic limit, leads to the final expression of the field square modulus

$$|E_z(\omega')|^2 = (\pi/2) |\mathcal{E}_z|^2 \mathcal{T} (\delta(\omega - \omega') + \delta(\omega + \omega')) . \quad (\text{C.18})$$

Inserting the last equation into Eq.C.13 we get the *power* absorbed on the average by the polarizable system under the influence of the monochromatic wave

$$Q/\mathcal{T} = (1/2) |\mathcal{E}_z|^2 \omega \alpha''(\omega) . \quad (\text{C.19})$$

Quantum mechanical expression of the polarizability

The foregoing discussion of the absorbed energy was essentially classical. The expression of the complex polarizability $\alpha(\omega)$ is found by inserting in the definition

$$p(t) = \langle \psi(t) | p | \psi(t) \rangle$$

the exact solution of the Schrödinger equation in external field Eq.C.3 and by identifying the linear contributions in E_z . Instead of the exact solution we shall

take its approximation to first order in the external field E_z

$$\psi(t) = \exp\left(-\frac{i}{\hbar}H_0t\right)\left(1 + \frac{i}{\hbar}\int_0^t \hat{p}(t') E_z(t') dt'\right)\psi_0 \quad (\text{C.20})$$

where \hat{p} denotes the dipole moment operator in the so-called *interaction picture*

$$\hat{p}(t) = \exp(+iH_0t/\hbar) p \exp(-iH_0t/\hbar) \quad . \quad (\text{C.21})$$

Eq.C.20 is a normalized solution of Eq.C.3 with the initial value ψ_0 , valid to first order in the external field E_z . The mean value of the dipole moment operator p corresponding to the wave function Eq.C.20 is, to same accuracy

$$\langle \psi(t) | p | \psi(t) \rangle = \langle \psi_0 | p | \psi_0 \rangle + \frac{i}{\hbar} \int_0^t \langle [\hat{p}(t), \hat{p}(t')] \rangle E_z(t') dt' \quad (\text{C.22})$$

where the mean value commutator expression is explicitly

$$\langle [\hat{p}(t), \hat{p}(t')] \rangle = \langle \psi_0 | \hat{p}(t) \hat{p}(t') | \psi_0 \rangle - \langle \psi_0 | \hat{p}(t') \hat{p}(t) | \psi_0 \rangle \quad . \quad (\text{C.23})$$

Starting from the fact that ψ_0 is the ground state of the system (Eq.C.1) it may be shown that

$$\langle [\hat{p}(t), \hat{p}(t')] \rangle = \langle [\hat{p}(t-t'), \hat{p}(0)] \rangle \quad . \quad (\text{C.24})$$

Making abstraction of the static dipole moment $\langle \psi_0 | p | \psi_0 \rangle$, comparison of Eq.C.22 to Eq.C.6 leads to the identification of the dynamic dipole moment²

$$\alpha(t) = \frac{i}{\hbar} \theta(t) \langle [\hat{p}(t), \hat{p}(0)] \rangle \quad (\text{C.25})$$

where the θ function³ was introduced to emphasise strict causality. We are next interested to derive the complex polarizability $\alpha(\omega)$ from Eq.C.25.

The vibrating adsorbate loses energy by its inherent coupling to the elementary excitations of the substrate, for example through excitation of phonons or electron-hole pairs. For this reason, the vibrationally excited states of the adsorbate are not stationary states of well defined energy but rather energy levels

²Eq.C.25 is known as the Kubo formula [89].

³The Heaviside unit-step function $\theta(t)$ is 0 for $t < 0$ and 1 for $t > 0$.

of finite lifetime (quasilevels). Notwithstanding this difficulty, we shall associate each vibrationally excited state ψ_n an energy value E_n through the stationary Schrödinger equation

$$H_0 \psi_n = E_n \psi_n \quad . \quad (\text{C.26})$$

Assuming that the excited states ψ_n form a complete set of wave functions for the vibrating adsorbate

$$\sum_{n=0}^{\infty} |\psi_n\rangle \langle \psi_n| = 1$$

we can write the identity

$$\langle \psi_0 | \hat{p}(t) \hat{p}(0) | \psi_0 \rangle = \sum_{n=0}^{\infty} \langle \psi_0 | \hat{p}(t) | \psi_n \rangle \langle \psi_n | \hat{p}(0) | \psi_0 \rangle$$

which by the definition of \hat{p} (Eq.C.21) can be further simplified

$$\langle \psi_0 | \hat{p}(t) \hat{p}(0) | \psi_0 \rangle = \sum_{n=0}^{\infty} |\langle \psi_0 | p | \psi_n \rangle|^2 e^{-it(E_n - E_0)/\hbar} \quad .$$

The explicit expression of the polarizability Eq.C.25

$$\alpha(t) = \frac{2}{\hbar} \theta(t) \sum_{n=1}^{\infty} |\langle \psi_n | p | \psi_0 \rangle|^2 \sin((E_n - E_0) t / \hbar) \quad (\text{C.27})$$

puts in evidence the important connection between the polarizability α of the adsorbate, which describes in a macroscopic and phenomenological way the dispersion and absorption of electromagnetic energy, and the quantum mechanical matrix elements of the total electric dipole moment p of the adsorbate, a microscopic quantity.

Frequency-dependent polarizability

To compute the Fourier transform $\alpha(\omega)$ of Eq.C.27 let us introduce the following representation⁴ of the unit-step function

$$\theta(t) = \frac{1}{2\pi i} \int_{-\infty}^{+\infty} \frac{e^{i\omega' t}}{\omega' - i\gamma} d\omega' \quad (\text{C.28})$$

where γ is a small positive parameter. We have to compute

$$\int_{-\infty}^{+\infty} \theta(t) \sin(\omega_n t) e^{i\omega t} dt = \frac{1}{2\pi i} \int_{-\infty}^{+\infty} \frac{d\omega'}{\omega' - i\gamma} \int_{-\infty}^{+\infty} \sin(\omega_n t) e^{i(\omega+\omega')t} dt \quad (\text{C.29})$$

where $\omega_n = (E_n - E_0)/\hbar$. Using

$$\int_{-\infty}^{+\infty} \sin(\omega_n t) e^{i(\omega+\omega')t} dt = i\pi[\delta(\omega + \omega' - \omega_n) - \delta(\omega + \omega' + \omega_n)] \quad (\text{C.30})$$

we get

$$\int_{-\infty}^{+\infty} \theta(t) \sin(\omega_n t) e^{i\omega t} dt = \frac{1}{2} \left\{ \frac{1}{\omega_n - \omega - i\gamma} + \frac{1}{\omega_n + \omega + i\gamma} \right\} \quad (\text{C.31})$$

The Fourier transform of the polarizability Eq.C.27 reads

$$\alpha(\omega) = \frac{1}{\hbar} \sum_{n=1}^{\infty} |\langle \psi_n | p | \psi_0 \rangle|^2 \left\{ \frac{1}{\omega_n - \omega - i\gamma} + \frac{1}{\omega_n + \omega + i\gamma} \right\} \quad (\text{C.32})$$

Eq.C.32 provides the reason why the lorentzian parametrization of the polarizability of an adsorbed molecule is usually a very good approximation. \square

⁴For positive γ the integrand has a pole in the upper half complex plane. For $t < 0$ one has to close the integration contour trough the lower half plane excluding the pole, which gives a vanishing integral. For $t > 0$ the integration contour is closed trough the upper half plane including the pole, the integral being thus $e^{-\gamma t} \approx 1$.

Appendix D

One-dimensional adsorbates

Our discussion of the adsorption of CO on the stoichiometric RuO₂(110) surface, at 110 K under UHV conditions, has shown that the succession of IR lines developing with increasing CO-coverage of the on top sites can be satisfactorily explained by the hypothesis that absorption of the IR radiation takes place not in the individual CO molecules, but rather in one dimensional aggregates, consisting of a few CO_{ot} molecules coupled through dipole-dipole forces. Since the existence of the short chains of neighboring CO_{ot} molecules, vibrating under their reciprocal dipole-dipole couplings, could be put in evidence by RAIRS, we find it of interest to sketch a statistical theory of these systems. The benefits of a statistical theory are predictions concerning for example the intensity of the particular IR bands and the interaction energy between CO_{ot} molecules, which can be easily tested against the available RAIRS data.

Let us consider a row of N neighboring on-top sites on which n CO_{ot} molecules are adsorbed at random positions. The CO_{ot} molecules form chains consisting of different numbers of molecules. We are interested to find the average number of chains consisting of exactly k molecules, considering that in the absence of pairwise interactions between the CO molecules the configurations of the CO adsorbate appear with the same probability. We note that in the physically relevant limit of large N we have to keep the coverage $\theta = n/N$ constant.

The total number of configurations W into which n adsorbates can be distributed over N sites is

$$W = \binom{N}{n} = \frac{N!}{n!(N-n)!} \quad .$$

We shall specify a configuration $\{a\} = \{a_1, \dots, a_k, \dots, a_n\}$ of the n adsorbates by giving the number a_k of groups of k adsorbates for each value of k . The numbers a_k are then subject to the constraint

$$\sum_{k=1}^n k a_k = n. \quad (\text{D.1})$$

The total number g of distinct chains, irrespective of their size, is

$$g = \sum_{k=1}^n a_k, \quad ,$$

which takes values between 1 and n when the a_k 's satisfy the constraint Eq.D.1.

Let us evaluate the number of different structures $w(\{a\})$ characterised by the same configuration $\{a\}$. To get the g groups distinctly separated we need to have at least one free ad-site between each two neighboring groups, i.e. the number of free ad-sites $N - n$ has to be at least $g - 1$. This condition may fail at higher coverages, where eventually just few groups can be formed. If the number of free ad-sites is large enough to allow for a complete separation of all groups, we may consider distributing the excess of $(N - n) - (g - 1)$ free ad-sites into the $g + 1$ free zones delimited by the g groups.¹ Next we have to consider that there are $g!$ more ways to realize the configuration $\{a\}$ because the order in which the g groups succeed each other is immaterial (no interaction between them). Finally, since permutations of groups of the same size do not lead to distinct configurations, we have to divide by the number $a_1! a_2! \dots a_n!$ of these permutations

$$w(\{a\}) = \frac{g!}{a_1! a_2! \dots a_n!} \binom{N - n + 1}{g}.$$

Because of the closure relation

$$\sum_{\{a\}} w(\{a\}) = W$$

¹ *Combinations with repetition*: the number of ways p identical objects can be distributed among m distinct containers is $\binom{m+p-1}{p}$.

we define the probability of configuration $\{a\}$ as

$$P(\{a\}) = \frac{w(\{a\})}{W}. \quad (\text{D.2})$$

We are now in position to evaluate the average number $\langle a_k \rangle$ of groups of k adsorbates at given coverage. We have to compute

$$\langle a_k \rangle = \sum_{\{a\}} a_k P(\{a\})$$

by summing over all possible sets $\{a\}$ obeying the constraint Eq.D.1 to get the exact result

$$\langle a_k \rangle = \frac{N - n + 1}{\binom{N}{n}} \binom{N - 1 - k}{n - k}$$

which may be checked to satisfy the constraint Eq.D.1. Using Stirling's approximation $\ln(n!) \approx n \ln(n) - n$ we get

$$\langle a_k \rangle \approx (N - n) \left(1 - \frac{n}{N}\right) \left(\frac{n}{N}\right)^k$$

which may finally be written as a function of the coverage θ only

$$\lim_{N \rightarrow \infty} \frac{\langle a_k \rangle}{N} = (1 - \theta)^2 \theta^k, \quad (\text{D.3})$$

which is the solution to the problem formulated at the beginning of the current section. Summation of the geometric series

$$\sum_{k=1}^{\infty} k(1 - \theta)^2 \theta^k = \theta$$

shows that Eq.D.3 satisfies indeed the constraint Eq.D.1. \square

Appendix E

Program for the computation of RAIR spectra

On the following pages we list the program used for the computation of the RAIR spectra presented in Chap.5. The program has been written in Pascal, and compiled and executed with the Free Pascal compiler¹. Running of the program as listed produces ASCII output files with the spectra of CO_{ot} on the stoichiometric RuO₂(110) surface, at coverages from 0.05 to 0.45, increasing with 0.02.

¹The compiler is available under the GNU license at www.freepascal.org

```

program SPECTIM; {simulation of RAIR spectra}

uses graph, crt, sysutils, variants;

const
    M=40;
    DM=4900;
    epsilon=1E-14;

    Lower=2080;
    Higher=2150;
    Step=1;

    trc=0.001;

var T: Array[1..M,1..M] of integer;
    countr, num1, num2, old1, old2, CO2: longint;
    sigma, oldsigma, w, Yco, Dco, Ro, COVER: real;

A,B,A1,P1: Array [1..DM,1..DM] of double;
X,Y,F,G: Array [1..DM] of double;

ba: Array[1..2,1..DM] of integer;
bd: Array[1..DM] of integer;

ii,jj,kk,ll, numero, gilgul:integer;
aa,bb,cc,freq, Vibb:real;

first, second, ident: string;

gd,gm: integer;

    PathToDriver : string;
    fileout, data, status: text;

procedure coverage;
var i,j,r,s: integer;
begin
    num1:=0;
    num2:=0;

    for i:=1 to M do
    for j:=1 to M do
    begin
        case T[i,j] of
            1: num1:=num1+1;
            2: num2:=num2+1
        end
    end;
    end;

end;

{ spectroscopy : }

function kroneck(a,b: integer):real;
var i, j, p, q: integer;
begin
    i:= 1 + Trunc((a-trc)/M); p:= 1 + Trunc((b-trc)/M);
    j:= a - M*(i-1);      q:= b - M*(p-1);

    if (i=p) and (j=q) then kroneck:=1
    else kroneck:=0;

```



```

end;

function VV(a,b: integer):real;
var i, j, p, q, t, u: integer;
    r,s,DL: real;
begin
    DL:=0.31746;    { distance to jellium edge d=1 A,
                    lattice constant a = 3.15 A,
                    DL= d/a }

    i:= 1 + Trunc((a-trc)/M); p:= 1 + Trunc((b-trc)/M);
    j:= a - M*(i-1);      q:= b - M*(p-1);

    VV:=0;

    for t:=-10 to 10 do
    for u:=-10 to 10 do
    begin
        r:= Sqrt( (i-p-t*M)*(i-p-t*M) + (j-q-u*M)*(j-q-u*M) );
        s:= Sqrt( (i-p-t*M)*(i-p-t*M) + (j-q-u*M)*(j-q-u*M) + 4*DL*DL );

        if r > epsilon then VV:=VV+1/r/r/r+1/s/s/s-12*DL*DL/s/s/s/s/s;
        end;

    end;

function swapo(r,s:integer):boolean;
var i: integer;
begin
    swapo:=true;

```

```

procedure swap(p,q: integer);
var i, j: integer;
    st: real;
begin
    st:=F[p];
    F[p]:=F[q];
    F[q]:=st;

    st:=G[p];
    G[p]:=G[q];
    G[q]:=st;

    for i:= 1 to DM do
    begin
        st:=A[p,i];
        A[p,i]:=A[q,i];
        A[q,i]:=st;

        st:=B[p,i];
        B[p,i]:=B[q,i];
        B[q,i]:=st;
    end;
end;

```

```

function swapo(r,s:integer):boolean;
var i: integer;
begin
    swapo:=true;

```

{ Here begins the equation solving EQ-ENGINE. It solves inhomogeneous linear equations with complex coefficients, by using the method of lower triangular gaussian elimination. }

```

if A[r,s]*A[r,s]+B[r,s]*B[r,s] < epsilon then
begin
  i:=r;
  if r < DM then
    repeat i:=i+1 until (A[i,s]*A[i,s]+B[i,s]*B[i,s] > epsilon) or
    (i=DM);
  if A[i,s]*A[i,s]+B[i,s]*B[i,s] > epsilon then swap(i,r)
  else swapo:=false;
end;
end;

function polaris(Dim:integer):real;
var i, j, k, q: integer;
    sum1,sum2,mdl,pp,qq,xx,yy: double;
    sw: boolean;
begin {0}
  if Dim < 2 then begin
    writeln('WARNING: Dimension of System of Eqs. is lower than 2. ');
    Dim:=2; end;
  sw:=true;

  for k:= 1 to Dim-1 do
    begin {1}
      sw:=swapo(k,k);
      if sw then
        begin
          for i:= k+1 to Dim do
            begin
              { A[i,j]:=A[k,k]*A[i,j]-A[i,k]*A[k,j]; }
              xx:=A[i,j];
              A[i,j]:=A[k,k]*F[i]-B[k,k]*G[i]-(A[i,k]*F[k]-B[i,k]*G[k]);
              G[i]:=B[k,k]*xx+A[k,k]*G[i]-(B[i,k]*F[k]+A[i,k]*G[k]);

              for j:= k+1 to Dim do
                begin
                  { A[i,j]:=A[k,k]*A[i,j]-A[i,k]*A[k,j]; }
                  xx:=A[i,j];
                  A[i,j]:=A[k,k]*A[i,j]-B[k,k]*B[i,j]-(A[i,k]*A[k,j]-
                    B[i,k]*B[k,j]);
                  B[i,j]:=B[k,k]*xx+A[k,k]*B[i,j]-
                    (B[i,k]*A[k,j]+A[i,k]*B[k,j]);
                end;
              A[i,k]:=0;
              B[i,k]:=0;
            } now normalize pivots to 1 : }
          end;
        end;
      end;
    end;
  end;

  function polaris(Dim:integer):real;
  var i, j, k, q: integer;
      sum1,sum2,mdl,pp,qq,xx,yy: double;
      sw: boolean;
  begin {0}
    if Dim < 2 then begin
      writeln('WARNING: Dimension of System of Eqs. is lower than 2. ');
      Dim:=2; end;
    sw:=true;

    for k:= 1 to Dim-1 do
      begin {1}
        sw:=swapo(k,k);
        if sw then
          begin
            for i:= k+1 to Dim do
              begin
                { F[i]:=A[k,k]*F[i]-A[i,k]*F[k]; }
                xx:=F[i];
                F[i]:=A[k,k]*F[i]-B[k,k]*G[i]-(A[i,k]*F[k]-B[i,k]*G[k]);
                G[i]:=B[k,k]*xx+A[k,k]*G[i]-(B[i,k]*F[k]+A[i,k]*G[k]);

                for j:= k+1 to Dim do
                  begin
                    { A[i,j]:=A[k,k]*A[i,j]-A[i,k]*A[k,j]; }
                    xx:=A[i,j];
                    A[i,j]:=A[k,k]*A[i,j]-B[k,k]*B[i,j]-(A[i,k]*A[k,j]-
                      B[i,k]*B[k,j]);
                    B[i,j]:=B[k,k]*xx+A[k,k]*B[i,j]-
                      (B[i,k]*A[k,j]+A[i,k]*B[k,j]);
                  end;
                    A[i,k]:=0;
                    B[i,k]:=0;
                  } now normalize pivots to 1 : }
                end;
              end;
            end;
          end;
        end;
      end;
    end;
  end;

```

```

pp:=A[i,k+1];
qq:=B[i,k+1];

mdl:=pp*pp+qq*qq;

if mdl > epsilon then
begin
xx:=F[i];
yy:=G[i];
F[i]:=(xx*pp+yy*qq)/mdl;
G[i]:=(yy*pp-xx*qq)/mdl;
for q:= k+1 to Dim do
begin
xx:=A[i,q];
A[i,q]:=(A[i,q]*pp+B[i,q]*qq)/mdl;
B[i,q]:=(B[i,q]*pp-xx*qq)/mdl;
end;
end;

{ ended normalization }
{3} end;

end;

end;

end; {1}
end {2}
end;

if A[Dim,Dim]*A[Dim,Dim]+B[Dim,Dim]*B[Dim,Dim] < epsilon
then sw:=false;

if sw then
begin {2}
X[Dim]:=F[Diml];
Y[Dim]:=G[Dim];

for k:= 2 to Dim do
begin
sum1:=0; for i:= Dim+2-k to Dim do
sum1:=sum1+(A[Dim+1-k,i]*X[i]-B[Dim+1-k,i]*Y[i]);

sum2:=0; for i:= Dim+2-k to Dim do
sum2:=sum2+(B[Dim+1-k,i]*X[i]+A[Dim+1-k,i]*Y[i]);

pp:=A[Dim+1-k,Dim+1-k];
qq:=B[Dim+1-k,Dim+1-k];
mdl:=pp*pp+qq*qq;

X[Dim+1-k]:=((F[Dim+1-k]-sum1)*pp+(G[Dim+1-k]-
sum2)*qq)/mdl;
Y[Dim+1-k]:=((G[Dim+1-k]-sum2)*pp-(F[Dim+1-k]-
sum1)*qq)/mdl;

{ X[Dim+1-k]:=(F[Dim+1-k]-sum)/A[Dim+1-k,Dim+1-k]; }

end;

end {2}
end {2}
end;

```



```

    ba[1,num]:=M*(i-1)+j;
    ba[2,num]:=3;
end;
    {all O have code 3}

end;

initia0:=num;

if num > 0 then for i:= 1 to num do
begin
    F[i]:=1; G[i]:=0;

    r:=ba[1,i];

    for j:= 1 to num do
    begin
        s:=ba[1,j];

        P1[i,j]:= kroneck(r,s);
        A1[i,j]:= VV(r,s);

    end;

end;

end; {0}

procedure initia(num:integer);
var i, j, k: integer;

    omega , vibe , omega0:real;      sum:real;
    omega1, vibe1, delta :real;
    omega2, vibe2, alpha :real;
    omega3, vibe3, gg : real;
    cup, rea, ima, ff : real;
    elpol,numitor:real;
begin {0}

    omega0:=800;      gg:=Sqr(0); {CO-substrate mode freq}
    omega1:=1986;    vibe1:=sqr(110);  delta:= 7;  {br-CO}
    omega2:=2098;    vibe2:=sqr(205);    {ot-CO}
    omega3:=600;     vibe3:=sqr(100);    {O - all}

    elpol:=0.025;
    ff:=freq;

    if num > 0 then for i:= 1 to num do
    begin
        F[i]:=1; G[i]:=0;

        case ba[2,i] of
        1: begin omega:=omega1; vibe:=vibe1; cup:=gg*gg end;
        2: begin omega:=omega2; vibe:=vibe2; cup:=gg*gg end;
        3: begin omega:=omega3; vibe:=vibe3; cup:=0  end;
        end;

        numitor:=vibe+elpol*(omega*omega-ff*ff);
        rea:=(omega*omega-ff*ff)/numitor;
        ima:=-omega*delta*vibe/(numitor*numitor);

```

```

for j:= 1 to num do
begin
  A[i,j]:= A1[i,j] + P1[i,j] * rea;
  B[i,j]:= ima * P1[i,j];
end;

end;

end;

begin
  gd:=detect; { highest possible resolution }
  gm:=0; { not needed, auto detection }
  PathToDriver:='C:\PP\BGI'; { path to BGI fonts, drivers aren't
  needed }

  InitGraph(gd,gm,PathToDriver);
  if GraphResult<>grok then halt;

  assign(status,'Z:\Farkas,Artila\focus\STATUS.dat');

  Randomize;

  for gilgul:= 1 to 20 do

    BEGIN

      initialize(0.05+gilgul*0.020);

      countr:=1;
      num1:=0;
      num2:=0;

```

```

Str(gilgul,ident);

first:=concat('Z:\Farkas,Atrila\focus\Adsorbate_',ident,'.dat');
second:=concat('Z:\Farkas,Atrila\focus\Spectrum_',ident,'.dat');

    assign(fileout,first);
    assign(data, second);

vitalize1;

coverage;

rewrite(fileout);

writeln(fileout);
writeln(fileout,'Size of table :','M,'*M);
writeln(fileout,'Impacts / Site:', countr/sqr(M));
writeln(fileout,'Nr. CO moles.:', ' ',num1);
writeln(fileout);
writeln(fileout,'      yCO :', Yco);
writeln(fileout,'      Dco :', Dco);
writeln(fileout,'      Ro  :', Ro );
writeln(fileout);
writeln(fileout,'Coverage by CO:', num1 / Sqr(M));
writeln(fileout,'Coverage by O:', num2 / Sqr(M));
writeln(fileout,'Coverage by __:', 1-(num1+num2) / Sqr(M));
writeln(fileout);

COVER:=num1 / Sqr(M);

for ii:=1 to M do begin writeln;

```

```

    for jj:=1 to M do
        write(fileout,T[ii,jj], ' '); writeln(fileout); end;

    close(fileout);
    rewrite(data);

    numero:=initia0;

    for ii:=1 to Trunc((Higher-Lower)/Step) do
        begin
            freq:=Lower+ii*Step;
            initia(numero);
            sigma:=polaris(numero);
            writeln(data,freq,' ',COVER*sigma);
            kk:=Trunc(300*sigma);
            putpixel(ii,200+kk,2);

            rewrite(status);
            write(status,'Just calculated frequency ',freq,' cm-1. ');
            close(status);

        end;
        close(data);

    END;

    Closegraph;

end.

```


Bibliography

- [1] H. Knözinger G. Ertl and J. Weitkamp, editors. *Handbook of Heterogeneous Catalysis*, chapter Principles of Heterogeneous Catalysis, by M. Boudart, pages 1–13. Wiley VCH, 1997.
- [2] G. A. Somorjai. *Introduction to Surface Chemistry and Catalysis*. John Wiley & Sons Inc., 1st edition, 1994.
- [3] G. Ertl and J. Küppers. *Low energy electrons and surface chemistry*. VCH Weinheim, 1985.
- [4] P. Stoltze and J. K. Norskov. Bridging the "pressure gap" between ultrahigh-vacuum surface physics and high-pressure catalysis. *Phys. Rev. Lett.*, 55(22):2502–2505, November 1985.
- [5] L. M. Aparicio and J. A. Dumesic. Ammonia synthesis kinetics: Surface chemistry, rate expressions, and kinetic analysis. *Top. Catal.*, 1(3):233–252, September 1994.
- [6] N. W. Cant, P. C. Hicks, and B. S. Lennon. Steady-state oxidation of carbon monoxide over supported noble metals with particular reference to platinum. *J. Catal.*, 54(3):372–383, October 1978.
- [7] C. H. F. Peden and D. W. Goodman. Kinetics of CO Oxidation over Ru(0001). *J. Phys. Chem.*, 90:1360–1365, 1986.
- [8] H. Over, Y. D. Kim, A. P. Seitsonen, S. Wendt, E. Lundgren, M. Schmid, P. Varga, A. Morgante, and G. Ertl. Atomic-Scale Structure and Catalytic reactivity of the RuO₂(110) surface. *Science*, 287:1474–1476, 2000.
- [9] H. Over and M. Muhler. Catalytic CO oxidation over ruthenium - bridging the pressure gap. *Progr. Surf. Sci.*, 72:3–17, 2003.

- [10] J. Assmann, V. Narkhede, N. A. Breuer, M. Muhler, A. P. Seitsonen, M. Knapp, D. Crihan, A. Farkas, G. Mellau, and H. Over. Heterogeneous oxidation catalysis on ruthenium: bridging the pressure and materials gaps and beyond. *J. Phys.: Condens. Matter*, 20:184017, 2008.
- [11] J. Assmann, E. Löffler, A. Birkner, and M. Muhler. Ruthenium as oxidation catalyst: bridging the pressure and material gaps between ideal and real systems in heterogeneous catalysis by applying DRIFT spectroscopy and the TAP reactor. *Catalysis Today*, 85:235–249, 2003.
- [12] J. Assmann, V. Narkhede, L. Khodeir, E. Löffler, O. Hinrichsen, A. Birkner, H. Over, and M. Muhler. On the nature of the active state of supported ruthenium catalysts used for the oxidation of carbon monoxide: steady-state and transient kinetics combined with *in situ* infrared spectroscopy. *J. Phys. Chem. B*, 108(38):14634–14642, September 2004.
- [13] F. M. Hoffmann. Infrared reflection-absorption spectroscopy of adsorbed molecules. *Surf. Sci. Rep.*, 3:107–192, 1983.
- [14] Y. J. Chabal. Surface infrared spectroscopy. *Surf. Sci. Rep.*, 8(5-7):211–357, May 1988.
- [15] J. W. Niemantsverdriet. *Spectroscopy in Catalysis*. Wiley VCH, 2000.
- [16] P. R. Griffiths and J. A. de Haseth. *Fourier Transform Infrared Spectrometry*. John Wiley & Sons, 1986.
- [17] P. Hollins and J. Pritchard. Infrared studies of chemisorbed layers on single crystals. *Progress in Surface Science*, 19(4):275–349, 1985.
- [18] R. P. Eischens, S. A. Francis, and W. A. Pliskin. The effect of surface coverage on the spectra of chemisorbed CO. *J. Phys. Chem.*, 60:194–201, 1955.
- [19] R. J. Bell. *Introductory Fourier Transform Spectroscopy*. Academic Press, New York and London, 1972.
- [20] A. C. S. van Hell, editor. *Advanced Optical Techniques*, chapter by A. Firard and P. Jacquinot, pages 71–109. North Holland, Amsterdam, 1967.

- [21] P. Fellgett. A propos de la théorie du spectrometre interférentiel multiplex. *J. Phys. Radium*, 19:187–191, 1958.
- [22] P. R. Griffiths, C. T. Foskett, and R. Curbelo. Rapid scan infrared fourier transform spectroscopy. *Applied Spectroscopy Reviews*, 6(1):31–77, 1972.
- [23] R. G. Greenler. Infrared study of adsorbed molecules on metal surfaces by reflection techniques. *J. Chem. Phys.*, 44(1):310–315, January 1966.
- [24] H. Pfnur, D. Menzel, F. M. Hoffmann, A. Ortega, and A. M. Bradshaw. High resolution vibrational spectroscopy of CO on Ru(001): The importance of lateral interactions. *Surf. Sci.*, 93(2-3):431–452, March 1980.
- [25] G. E. Thomas and W. H. Weinberg. The vibrational spectrum and adsorption site of CO on the Ru(001) surface. *J. Chem. Phys.*, 70:1437–1439, 1979.
- [26] J. D. E. McIntyre and D. E. Aspnes. Differential reflection spectroscopy of very thin surface films. *Surf. Sci.*, 24:417–434, 1971.
- [27] H. P. Myers. *Introductory solid state physics*. Taylor & Francis, 1990.
- [28] R. J. H. Clark and R. E. Hester, editors. *Spectroscopy of Surfaces*, chapter by A. M. Bradshaw and E. Schweizer. John Wiley & Sons, Chichester, 1988.
- [29] G. Blyholder. Molecular orbital view of chemisorbed carbon monoxide. *J. Phys. Chem.*, 68:2772–2778, 1964.
- [30] H. Ibach and G. A. Somorjai. Evidence for the weakening of the C-O bond upon coadsorption with hydrocarbons. *Appl. of Surf. Sci.*, 3:293–296, 1979.
- [31] M. Gerloch and E. C. Constable. *Transition Metal Chemistry*. Wiley VCH, 1994.
- [32] E. Shustorovich and H. Sellers. The UBI-QEP method: A practical theoretical approach to understanding chemistry on transition metal surfaces. *Surf. Sci. Rep.*, 31(1-3):1–119, 1998.
- [33] H. Sellers. Relationship among force constants implied by the principle of bond-order conservation in chemisorbed systems. *J. Phys. Chem.*, 98:968–971, 1994.

- [34] S. Efrima and H. Metiu. The role of the electrostatic interaction in shifting the vibrational frequencies for two adsorbed molecules. *Surf. Sci.*, 109(1):109–126, August 1981.
- [35] H. Ibach and D. L. Mills. *Electron energy loss spectroscopy and surface vibrations*. Academic Press, 1982.
- [36] B. N. J. Persson. Absorption of photons by molecules adsorbed on metal surfaces. *Solid State Commun.*, 30(3):163–166, April 1979.
- [37] M. Moskovits and J. E. Hulse. Frequency shifts in the spectra of molecules adsorbed on metals, with emphasis on the infrared spectrum of adsorbed CO. *Surf. Sci.*, 78:397–418, 1978.
- [38] F. A. Cotton and C. S. Kraihanzel. Vibrational Spectra and Bonding in Metal Carbonyls. I. Infrared Spectra of Phosphine-substituted Group VI Carbonyls in the CO Stretching Region. *J. Am. Chem. Soc.*, 84(23):4432–4438, December 1962.
- [39] M. W. Severson, C. Stuhlmann, I. Villegas, and M. J. Weaver. Dipole–dipole coupling effects upon infrared spectroscopy of compressed electrochemical adlayers: Application to the Pt(111)/CO system. *J. Chem. Phys.*, 103(22):9832–9843, December 1995.
- [40] S. Efrima and H. Metiu. Vibrational frequencies of a chemisorbed molecule: The role of the electrodynamic interactions. *Surf. Sci.*, 92:433–452, 1980.
- [41] G. W. Ford and W. H. Weber. Electromagnetic interactions of molecules with metal surfaces. *Phys. Rep.*, 113:195–287, 1984.
- [42] J. A. Appelbaum and D. R. Hamann. Variational calculation of the image potential near a metal surface. *Phys. Rev. B*, 6(4):1122–1130, August 1972.
- [43] N. D. Lang and W. Kohn. Theory of metal surfaces: Induced surface charge and image potential. *Phys. Rev. B*, 7(8):3541–3550, April 1973.
- [44] B. N. J. Persson and A. Liebsch. Collective vibrational modes of isotopic mixtures of CO on Cu(111) and Cu(001). *Surf. Sci.*, 110(2):356–368, 1981.

- [45] B. N. J. Persson. Indirect vibrational coupling between adsorbed molecules. *Surf. Sci.*, 116(3):585–595, May 1982.
- [46] R. Blume, M. Havecker, S. Zafeirotos, D. Teschner, E. Kleimenov, A. Knop-Gericke, R. Schlogl, A. Barinov, P. Dudin, and M. Kiskinova. Catalytically active states of Ru(0001) catalyst in CO oxidation reaction. *J. Catal.*, 239(2):354–361, April 2006.
- [47] M. Lindroos, H. Pfnur, G. Held, and D. Menzel. Adsorbate induced reconstruction by strong chemisorption: Ru(001)- $p(2 \times 2)$ -O. *Surf. Sci.*, 222(2-3):451–463, November 1989.
- [48] H. Pfnur, G. Held, M. Lindroos, and D. Menzel. Oxygen induced reconstruction of a close-packed surface: A LEED IV study on Ru(001)- $p(2 \times 1)$ O. *Surf. Sci.*, 220(1):43–58, October 1989.
- [49] Y. D. Kim, S. Wendt, S. Schwegmann, H. Over, and G. Ertl. Structural analyses of the pure and cesiated Ru(0001)- (2×2) -3O phase. *Surf. Sci.*, 418(1):267–272, November 1998.
- [50] C. Stampfl, S. Schwegmann, H. Over, M. Scheffler, and G. Ertl. Structure and Stability of a High-Coverage (1×1) Oxygen Phase on Ru(0001). *Phys. Rev. Lett.*, 77(16):3371–3374, October 1996.
- [51] A. Boettcher and H. Niehus. Oxygen adsorbed on oxidized Ru(0001). *Phys. Rev. B*, 60:14396–14404, 1999.
- [52] H. Over and A. P. Seitsonen. Oxidation of metal surfaces. *Science*, 297:2003–2004, 2002.
- [53] Y. B. He, M. Knapp, E. Lundgren, and H. Over. Ru(0001) model catalyst under oxidizing and reducing reaction conditions: *in-situ* high pressure surface X-ray diffraction study. *J. Phys. Chem. B*, 109:21825–21830, 2005.
- [54] H. Over, A. P. Seitsonen, E. Lundgren, M. Schmid, and P. Varga. Experimental and simulated STM images of stoichiometric and partially reduced RuO₂(110) surfaces including adsorbates. *Surf. Sci.*, 515:143–156, 2002.
- [55] Y. D. Kim. *Atomic-Scale Structure and Catalytic Reactivity of RuO₂*. PhD thesis, Freie Universität Berlin, 2000.

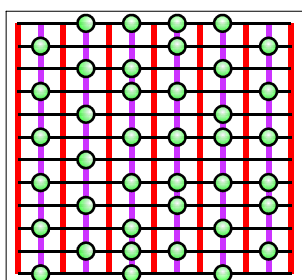
- [56] M. Knapp. *Die Schlüsselrolle des Wasserstoffs im Reaktionsverhalten einer oxidischen Katalysatoroberfläche am Beispiel von RuO₂(110)*. PhD thesis, Justus-Liebig-Universität Giessen, 2006.
- [57] C. H. F. Peden. Surface science of catalysis. Number 483 in ACS Symp. Ser., page 143, 1992.
- [58] H. Over, M. Knapp, E. Lundgreen, A. P. Seitsonen, M. Schmid, and P. Varga. Visualization of Atomic Processes on Rutheniumdioxide using Scanning Tunneling Microscopy. *Chem. Phys. Chem*, 5:167–174, 2004.
- [59] J. Assmann, D. Crihan, M. Knapp, E. Lundgren, E. Löffler, M. Muhler, V. Narkhede, H. Over, M. Schmid, A. P. Seitsonen, and P. Varga. Understanding the structural deactivation of ruthenium catalysts on an atomic scale under both oxidizing and reducing conditions. *Angew. Chem. Int. Ed.*, 44:917–920, 2005.
- [60] J. T. Kiss and R. D. Gonzalez. Catalytic oxidation of carbon monoxide over ruthenium/silicon dioxide. An *in situ* infrared and kinetic study. *J. Phys. Chem.*, 88(5):892–897, 1984.
- [61] U. Diebold. The surface science of titanium dioxide. *Surf. Sci. Rep.*, 48:53–229, 2003.
- [62] Y. D. Kim, H. Over, G. Krabbes, and G. Ertl. Identification of RuO₂ as the active phase in CO oxidation on oxygen-rich ruthenium surfaces. *Topics in Catal.*, 14:95–100, 2001.
- [63] J. P. LaFemina. Total energy computations of oxide surface reconstructions. *Crit. Rev. Surf. Chem.*, 3:297–386, 1994.
- [64] A. P. Seitsonen, Y. D. Kim, M. Knapp, S. Wendt, and H. Over. CO adsorption on the reduced RuO₂(110) surface: Energetics and structure. *Phys. Rev. B*, 65(3):035413, December 2001.
- [65] H. Over, A. P. Seitsonen, E. Lundgren, M. Schmid, and P. Varga. Direct imaging of catalytically important processes in the oxidation of CO over RuO₂(110). *J. Am. Chem. Soc.*, 123:11807–11808, 2001.

- [66] C. Y. Fan, J. Wang, K. Jacobi, and G. Ertl. The oxidation of CO on RuO₂(110) at room temperature. *J. Chem. Phys.*, 114:10058–10062, 2001.
- [67] P. Mars and D. W. van Krevelen. *Chem. Eng. Sci.*, 3:41, 1954.
- [68] C. Doornkamp and V. Ponc. The universal character of the Mars and van Krevelen mechanism. *Journal of Molecular Catalysis A: Chemical*, 162(1-2):19–32, November 2000.
- [69] M. A. Morris, M. Bowker, and D. A. King. Kinetics of adsorption, desorption and diffusion at metal surfaces. In C. H. Bamford, C. F. H. Tipper, and R. G. Compton, editors, *Simple processes at the gas-solid interface*, volume 19 of *Comprehensive chemical kinetics*. Elsevier, 1984.
- [70] K. Christmann. *Introduction to Surface Physical Chemistry*. Topics in Physical Chemistry. Springer, 1991.
- [71] P. Kisliuk. The sticking probabilities of gases chemisorbed on the surfaces of solids. *J. Phys. Chem. Solids*, 3:95–101, 1957.
- [72] P. J. Flory. *J. Am. Chem. Soc.*, 58(10):1877–1885, 1936.
- [73] B. N. J. Persson and R. Ryberg. Vibrational interaction between molecules adsorbed on a metal surface: The dipole-dipole interaction. *Phys. Rev. B*, 24(12):6954–6970, December 1981.
- [74] E. Escalona Platero, S. Colluccia, and A. Zecchina. Dipole coupling and chemical shifts in CO overlayers adsorbed on NiO. *Surf. Sci.*, 171(3):465–482, 1986.
- [75] U. A. Paulus, Y. Wang, K. Jacobi, and G. Ertl. CO adsorption on the reduced RuO₂(110) surface. *Surf. Sci.*, 547(3):349–354, December 2003.
- [76] S. Wendt. *Komplexe Redox-Chemie auf der RuO₂(110)-Oberfläche*. PhD thesis, Freie Universität Berlin, 2002.
- [77] D. Crihan. *HCl-Oxidation auf RuO₂(110): Neuartiger Deacon Prozess*. PhD thesis, Justus-Liebig-Universität Giessen, 2007.

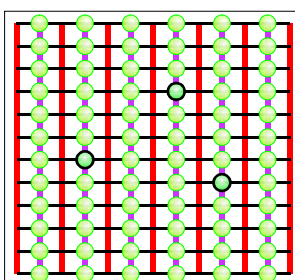
- [78] C. H. F. Peden, D. W. Goodman, M. D. Weisel, and F. M. Hoffmann. *In-situ* FT-IRAS study of the CO oxidation reaction over Ru(001) : I. Evidence for an Eley-Rideal mechanism at high pressures? *Surf. Sci.*, 253:44–58, 1991.
- [79] F. M. Hoffmann, M. D. Weisel, and C. H. F. Peden. *In-situ* FT-IRAS study of the CO oxidation reaction over Ru(001) : II. Coadsorption of carbon monoxide and oxygen. *Surf. Sci.*, 253:59–71, 1991.
- [80] Lj. Atanasoska, W. E. O’Grady, R. T. Atanasoski, and F. H. Pollak. The surface structure of RuO₂: A LEED, Auger and XPS study of the (110) and (100) faces. *Surf. Sci.*, 202(1-2):142–166, 1988.
- [81] J. Wang, C. Y. Fan, K. Jacobi, and G. Ertl. The kinetics of CO oxidation on RuO₂(110). *J.Phys.Chem. B*, 106:3422–3427, 2002.
- [82] S. Wendt, A. P. Seitsonen, and H. Over. Catalytic activity of RuO₂(110) in the oxidation of CO. *Catal. Today*, 85:167–175, 2003.
- [83] B. R. A. Nijboer and F. W. de Wette. The internal field in dipole lattices. *Physica*, 24(1-5):422–431, 1958.
- [84] T. Buffeteau, B. Desbat, and J. M. Turlet. Polarization Modulation FT-IR Spectroscopy of Surfaces and Ultra-thin Films: Experimental Procedure and Quantitative Analysis. *Appl. Spectrosc.*, 45(3):380–389, 1991.
- [85] E. Dragulis and R. I. Jaffee, editors. *The Physical Basis for Heterogeneous Catalysis*, chapter by M. Boudart, H. Topsoe and J. A. Dumesic. Plenum Press, New York, 1975.
- [86] J. D. Jackson. *Classical electrodynamics*. John Wiley & Sons, 1998.
- [87] A. Fetter and J. D. Walecka. *Quantum Theory of Many Particle Systems*. McGraw Hill, 1971.
- [88] L. D. Landau and E. M. Lifshitz. *Statistische Physik*. Akademie Verlag Berlin, 1970.
- [89] R. Kubo. *J. Phys. Soc. Japan*, 12:570–586, 1957.

Synoptic Table

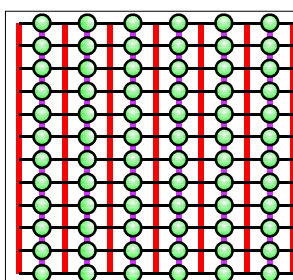
of
the vibrational bands of CO on RuO₂(110)



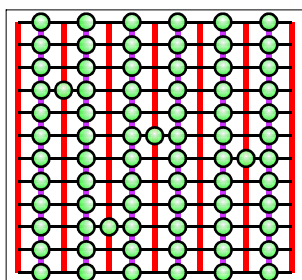
$\text{CO}_{\text{br}}^{\text{II}} / (--)_{\text{ot}}$
1867-1893 cm^{-1}



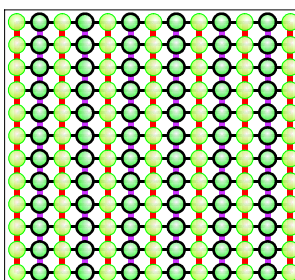
$(\text{O}_{\text{br}} + \text{CO}_{\text{br}}^{\text{sg}}) / (--)_{\text{ot}}$
1953 cm^{-1}



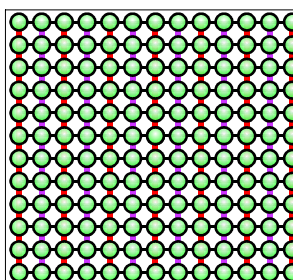
$\text{CO}_{\text{br}} / (--)_{\text{ot}}$
1992-2002 cm^{-1}



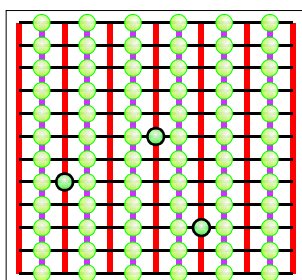
$\text{CO}_{\text{br}} / \text{CO}_{\text{ot}}^{\text{sg}}$
2 bands:
2000 cm^{-1} , 2016 cm^{-1}



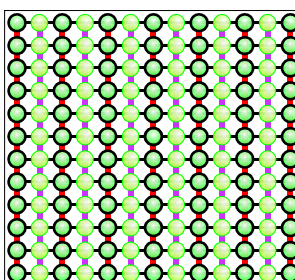
$\text{CO}_{\text{br}} / \text{O}_{\text{ot}}$
2033-2046 cm^{-1}



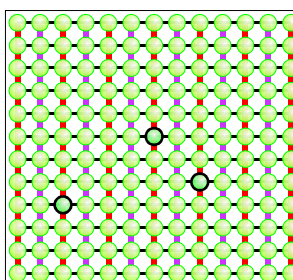
$\text{CO}_{\text{br}} / \text{CO}_{\text{ot}}$
2016 -2086 cm^{-1}



$\text{O}_{\text{br}} / \text{CO}_{\text{ot}}^{\text{sg}}$
2101 cm^{-1}



$\text{O}_{\text{br}} / \text{CO}_{\text{ot}}$
2101-2123 cm^{-1}



$\text{O}_{\text{br}} / (\text{O}_{\text{ot}} + \text{CO}_{\text{ot}}^{\text{sg}})$
2146-2152 cm^{-1}

CO
 O

1f-cus Ru
 2f-cus Ru